The Dissertation Committee for Lisa Michelle Richards Certifies that this is the approved version of the following dissertation:

Laser Speckle Contrast Imaging for Intraoperative Monitoring of Cerebral Blood Flow

Committee:

Andrew Dunn, Supervisor

Douglas Fox, Jr.

Henry Grady Rylander, III

James Tunnell

Stanislav Emelianov

Laser Speckle Contrast Imaging for Intraoperative Monitoring of Cerebral Blood Flow

by

Lisa Michelle Richards, B.S.E.; M.S.E.

Dissertation

Presented to the Faculty of the Graduate School of

The University of Texas at Austin

in Partial Fulfillment

of the Requirements

for the Degree of

Doctor of Philosophy

The University of Texas at Austin

December 2015

Dedication

To my family and Jason.

Acknowledgements

First and foremost, I would like to acknowledge my advisor, Dr. Andrew Dunn, for his patience, guidance, and support during my graduate studies. All of the advice and helpful discussions regarding my project taught me how to be a better researcher, both during data acquisition and presentation. I am also thankful for the encouragement and for pushing me to overcome the obstacles that seemed insurmountable at the time. I would not have accomplished any of my major achievements in graduate school without your support. I am truly grateful to have had the opportunity to work with you for the past 6+ years, and am looking forward to the future.

I am also very grateful to the NeuroTexas doctors, nurses, and research staff at St. David's Medical Center for their support during the clinical studies. Thank you especially to our collaborator and my committee member Dr. Douglas Fox for your dedication to the project, and for your feedback about the instrument design and imaging data. Thank you to Dr. James Waldron for your help with data collection in the phase II study. Also, thank you to Kaelyn Kappeler and Sergio Michel Avila for handling patient accrual and regulatory documents. Thank you as well to the NeuroTexas surgical nursing staff, who provided support for the neurosurgical microscopes during each clinical case.

I am also very thankful to Dr. Grady Rylander, Dr. James Tunnell, and Dr. Stas Emelianov for serving on my committee. Your feedback about my project helped me adjust my research approach to make the project more impactful. Your comments also helped me see the project from a different perspective, which helped me understand how my work fits into the big picture. Thank you for all of your help and guidance, and for taking the time to critically assess my project. I greatly appreciate your support, and have truly enjoyed working with you during my graduate career.

Thank you to my current and former lab-mates for all of your assistance and support over the years. Thank you especially to Dr. Ashwin Parthasarathy, Dr. Erica Towle, and Dr. Shams Kazmi for your support with the clinical project. Thank you to Shams as well for your support with the multi-camera comparison project, and for your advice, encouragement, and general help with problem solving. Thank you to Dr. Mitch Davis for helpful discussions about dynamic light scattering theory, and to Colin Sullender for improving functionality of the speckle image acquisition software. Thank you to my undergraduate research assistants: Katherine Olin (speckle size measurements), Janel Davis (webcam study), Pawan Mannava (microfluidic studies, EM-CCD study), Jake George (laser comparison study), and Nazariy Shaydyuk (clinical image registration). These projects would not have been possible without your help.

Thank you to my mentors from high school and college that helped me get to this point. My high school Physics teacher, Dr. Guy Letteer, inspired my excitement about the sciences and encouraged me to pursue Biomedical Engineering in college. My advisor from Duke University, Dr. Nimmi Ramanujam, showed me the potential impact of optical devices in the operating room and inspired me to apply to graduate school.

Finally, thank you to my family for their unconditional love, support, and encouragement. Thank you to my parents, Doug and Nancy, for pushing me to work hard and take risks, for believing in me and being my biggest cheerleaders, and for always being there when I need it the most. Thank you to my brother and sister, Matt and Christie, for keeping me grounded, for inspiring me to excel, and for always making me laugh. Thank you to Auntie Ellen and Uncle Tom for being an incredible support system in Austin and for always making me feel like I'm one of your own kids. Lastly, thank you to Jason for all of your love and support. You push me to be a better version of myself everyday, and I am incredibly lucky to have you in my life.

Laser Speckle Contrast Imaging for Intraoperative Monitoring of Cerebral Blood Flow

Lisa Michelle Richards, Ph.D.

The University of Texas at Austin, 2015

Supervisor: Andrew K. Dunn

Ensuring adequate blood flow during surgical procedures is crucial, as prolonged ischemia can result in tissue death and lead to poor clinical outcomes. This is especially important during neurosurgery, since the brain relies on a constant supply of cerebral blood flow (CBF) to maintain normal function. Intraoperative blood flow monitoring tools are essential to detect ischemia in a timely manner, and allow surgical correction before the onset of irreversible brain injury. Laser speckle contrast imaging (LSCI) is an optical imaging method that provides blood flow maps with high spatiotemporal resolution, and overcomes many of the limitations of current intraoperative monitoring technologies. The objective of this dissertation is to demonstrate that LSCI is an effective tool for blood flow monitoring during neurosurgery, and to optimize and improve LSCI technology for clinical use.

This research has two primary elements: assessing the LSCI instrumentation components in a controlled laboratory setting, and evaluating the clinical performance of LSCI during neurosurgery. The laboratory study aims to determine the optimal specifications for the clinical instrument design, using controlled static and microfluidic flow experiments. Two of the main components of the LSCI instrument are the camera used for recording, and the laser used for coherent illumination of the tissue. Thus, a

broad camera and laser comparison was performed spanning a wide array of available hardware options to determine which specifications are the most important for reliable and highly sensitive flow measurements. The two-phase clinical study aims to demonstrate the performance and utility of LSCI in a neurosurgical setting as a potential tool for real-time, continuous, and noninvasive image guidance. These studies demonstrate that LSCI can produce blood flow maps consistent with expected physiological trends, and show the impact of instrument design and image acquisition techniques on image quality and quantitative flow assessment. The results from both the laboratory and clinical studies can be used to design a more sensitive and robust LSCI system, which increases its value as an intraoperative tool for monitoring blood flow. LSCI has the potential to be the next generation of neurosurgical image guidance for blood flow visualization, and the work presented in this dissertation can accelerate its clinical adoption.

Table of Contents

List of Tables

List of Figures

Chapter 1: Introduction

Maintaining adequate blood flow during surgical procedures is critical, as prolonged ischemia can result in tissue death and lead to poor clinical outcomes. Vascular injury can result if a surgeon inadvertently occludes a vessel and does not repair the blockage quickly. This is especially important during neurosurgery, since the brain relies on a constant supply of cerebral blood flow (CBF) to deliver vital nutrients and maintain normal function [1]. Any reduction in CBF for a prolonged time period puts the patient at risk for irreversible ischemic brain injury that can lead to functional deficits, or even death. Thus, monitoring CBF during neurosurgery is critical, allowing the surgeon be rapidly alerted to an ischemic event. CBF monitoring can help minimize post-operative complications by enabling and guiding potential life-saving neurological interventions.

The availability of real-time blood flow monitoring can help improve surgical outcomes for a wide variety of neurosurgical procedures. Monitoring CBF is particularly important during high-risk cerebrovascular procedures, such as aneurysm clipping or vessel bypass, where the surgeon is operating directly on the blood vessels [2, 3]. The surgeon must be able to assess whether blood flow has returned to pre-surgical levels in parent and branching vessels, and identify residual stenosis or occlusion to reduce the risk of irreversible ischemic brain damage. For procedures that require removal of diseased brain tissue, such as tumor resection or epilepsy, monitoring CBF can be used to localize areas of eloquent brain tissue relative to the pathology. This localization of brain activity can be achieved based on the tight coupling between neural activity and CBF, known as neurovascular coupling [4, 5]. Functional brain mapping allows surgeons to maintain a

balance between sufficient resection of pathological tissue and preservation of motor, language, and sensory function.

1.1 Clinically Available Blood Flow Monitoring Techniques

Several intraoperative blood flow monitoring tools have been developed and evaluated in recent years to aid surgeons, with a summary of techniques in clinical use and under clinical evaluation shown in Table 1.1. Each technique has its own strengths and weaknesses, and none are completely reliable as a stand-alone method. Prospective studies have confirmed that methods provide complementary information with higher certainty gained from employing multiple techniques [2]. Any combination of intraoperative techniques that provides the detection of blood flow reduction can alter the course of the surgery and reduce complication rates, including stroke and the need for subsequent surgeries.

1.1.1 Non-Optical Techniques

For cerebrovascular procedures, such as aneurysm clipping, blood flow monitoring techniques can be used to guide clip placement. The gold standard monitoring technique is digital subtraction angiography (DSA) [6, 7], which involves X-ray based visualization of cerebral vasculature by subtracting images recorded before and after the injection of a radiopaque contrast agent. Despite the fact that visualization can take up to 30 minutes, imaging can identify residual stenosis, occlusion, and residual aneurysm after clip placement [8]. Computed tomography angiography (CTA) and dynamic perfusion CT (PCT) are other X-ray based techniques that require a contrast agent, but can be performed faster (<10 minutes) and can detect residual perfusion deficits [9]. Disadvantages for these techniques include the exposure to ionizing X-rays, injection of a contrast agent, and a limited number of repeated imaging sessions.

Magnetic resonance angiography (MRA) allows assessment of cerebral vasculature without using ionizing radiation or a contrast agent, and diffusion-weighted magnetic resonance imaging (MRI) can identify tissue with potentially reversible ischemia [10]. This technique can also be performed relatively fast (<10 minutes) and is safer for the patient. However, image artifacts near the aneurysm clips can make interpretation difficult, and a special operating room setup is required to ensure both patient and staff safety.

Microvascular Doppler sonography uses a micro-probe to measure absolute velocities in blood vessels, and can provide a timecourse of the flow profile for advanced evaluation [11, 12]. This is useful during aneurysm surgery because it allows surgeons to identify residual flow in an aneurysm and to ensure that clip placement maintains sufficient arterial supply [11]. This technique is advantageous because it is safe, fast to perform, and low-cost, but is typically limited to point measurements and must be physically placed in contact with the vessel for recording. Another similar technique is ultrasound-based transit time flowmetry, which uses a perivascular flow probe that must be placed around the vessel [13, 14]. The technique senses an ultrasound wave that bounces between two transducers off a reflector on the opposite side, and can provide time courses of absolute flow velocities in real-time. Because the probe must be placed around the vessel, it cannot be used to examine the aneurysm sac, but can be used to assess parent or major artery patency. The probe can typically only be used for a limited vessel diameter range (1.5 – 3 mm [14]), and could potentially injure the vessel during use. Thermal Diffusion flowmetry produces a continuous and quantitative measure of blood flow [15-17]. This technique uses a probe with a heated and non-heated plate that measures the temperature gradient by the Peltier thermoelectric effect. Thermal Diffusion flowmetry provides a timecourse of parenchymal blood flow, usually in

relative measures or in mL/100 g/min using a calibration, and can provide flow status information during temporary artery occlusion in aneurysm procedures. Despite its benefits, this technique only samples a limited tissue volume and small spatial areas under the probe, which may not accurately represent the perfusion across the entire field.

1.1.2 Optical Techniques

Indocyanine green angiography (ICGA) is a fluorescence-based optical imaging technique that involves injection of ICG dye, illumination of the vasculature with near infrared light (785 – 800 nm), and subsequent recording of ICG fluorescence emission (820 – 835 nm) [18, 19]. The plasma half-life of ICG dye is 3 – 4 minutes, and can be repeated in 10-minute intervals 2-3× during the procedure [20]. Complications from ICG dye are low, since the dye is cleared by the liver, but is contraindicated in patients with an iodine allergy. The technology has also been integrated into surgical microscopes for rapid evaluation and ease of use [21-23]. This technique has gained increasing popularity because it allows immediate visualization of blood perfusion in the surgical field of view. Recent advances in quantitative analysis software allow computation of hemodynamic parameters during procedures, including maximum fluorescence intensity, rise time, time to peak fluorescence, and cerebral blood flow index [24]. Limitations of ICGA include: all quantitative information must be extracted from the initial wash-in of the dye, and repeated injections can reduce the maximum fluorescence intensity. Unfortunately, the utility of these fluorescence-based parameters for quantitatively assessing perfusion or flow is questionable, and poor agreement was found with other flow metrics in a recent study [25].

Other optical techniques currently under clinical evaluation are based on coherent dynamic light scattering (DLS), which can be used to detect the motion of particles

without an exogenous contrast agent. DLS techniques utilize either the Doppler effect or time-varying speckle, which are different approaches of looking at the same phenomena [26]. Both techniques are inherently based on the principle of the Doppler effect, which results in the change in frequency of a coherent light wave when there is relative motion between the source and detector.

Laser Doppler Flowmetry (LDF) involves illuminating the tissue with a coherent light source, recording the back-scattered light, and analyzing the frequency spectrum. LDF was historically performed using fiber optics for imaging point locations, but now is typically performed using scanning mirrors to build up an image from multiple point locations [27]. The need for mechanical scanning increases acquisition times, with scan times up to ~5 minutes in commercial systems rendering a modest 256 x 256 pixel image [28]. Full-field LDF instruments have also been developed [29, 30], with scan times up to 14 frames per second (fps) for a 480 x 480 pixel image. Despite fairly slow acquisition speeds, LDF has been tested in clinical studies with promising results during direct bypass procedures using a commercial laser Doppler scanner [31]. A custom LDF system operating at 1.5 fps has also been used for functional mapping of the cortex, which found functional activation areas consistent with functional MRI and electrostimulation [32].

Laser speckle contrast imaging (LSCI) is another technique based on Doppler-shifted scattered light, and offers significant advantages in temporal resolution compared to LDF. Because rapid processing techniques are available for LSCI [33], the temporal resolution of a LSCI is determined by the frame rate of the camera, which can be >200 fps for high-speed cameras available today. A thorough introduction to LSCI is provided in the next section.

Table 1.1: Characteristics of clinically available and emerging blood flow monitoring techniques for neurosurgery* [3, 10].

Modality	Depth Penetration	Field of View	Temporal Resolution	Spatial resolution	Frequency	Contrast Agent?	Interruption, Cost
DSA	Superficial, Deep	3D Full-field	Single time point	High (<1 mm)	1-2 times	Yes	High
CTA	Superficial, Deep	3D Full-field	Single time point	High (<1 mm)	1-2 times	Yes	High
MRA	Superficial, Deep	3D Full-field	Single time point	High (~mm)	1-2 times	Optional	High
ICGA	Superficial	2D Full-field	Real-time (wash-in)	High (μm)	Repeatable (>10 min.)	Yes	Low
Micro-Doppler Ultrasound	Superficial	Point measurement	Real-time	N/A	Repeatable	No	Low
Transit Time Flowmetry (US)	Superficial	Point measurement	Real-time	N/A	Repeatable	No	Low
Thermal Diffusion Flowmetry	Superficial	Point measurement	Real-time	N/A	Continuous	No	Low
Laser Speckle Contrast Imaging	Superficial	2D Full-field	Real-time	High (μm)	Continuous	No	Low

*DSA = Digital Subtraction Angiography, CTA = Computed Tomography Angiography, MRA = Magnetic Resonance Angiography, ICGA = Indocyanine Green Angiography, US = ultrasound-based, N/A = not applicable (not imaging based)

1.2 Laser Speckle Contrast Imaging for Monitoring Cerebral Blood Flow

Laser speckle contrast imaging (LSCI) is a full-field optical imaging method that can provide an instantaneous map of blood flow in real-time by imaging time-varying laser speckle. LSCI was first demonstrated by Fercher and Briers in 1981 using film single-exposure photography of retinal blood flow [34]. Because images were recorded on film and required processing of the film negative to view blood flow information, the technique suffered from poor temporal resolution and was not feasible as a clinical monitoring tool. However, a digital version was developed in the 1990's with the arrival of CCD cameras and faster computers. This made real-time visualization feasible and was first demonstrated by imaging bulk perfusion in the skin [35, 36]. The first demonstrated use of LSCI for imaging CBF dynamics in rodents was in 2001 [37], and has since become widely adopted by neuroscience researchers in animal studies of stroke [38, 39], cortical spreading depression [40, 41], and functional activation [42, 43].

1.2.1 Laser Speckle Imaging Theory

Laser speckle is a random interference pattern produced when coherent light scatters from a rough surface (on the scale of an optical wavelength) or a random, inhomogeneous medium. Scattered photons travel slightly different path lengths, resulting in constructive and destructive interference from de-phased coherent light waves. When this scattered light is imaged, a 2D random intensity pattern is produced at the detector. This is known as subjective speckle [44] and consists of bright spots of highly constructive interference, dark spots of highly destructive interference, and a continuum of intensity values in between randomly distributed throughout the image plane. Originally called "granularity" because of its grainy appearance, speckle is often considered unwanted noise and techniques were developed for reducing speckle formed

in images [26]. However, researchers began studying speckle theory and developing practical applications of the phenomena in the 1970's [45].

One of the most common applications of laser speckle imaging is detecting motion within a sample. When an object moves in the imaging plane, the speckle pattern fluctuates in time as a result of phase shifts in the backscattered light. The same is true for a random medium made up of individual moving scatterers, such as particles in a fluid or red blood cells in vasculature. When imaging a time-varying speckle pattern, the camera integrates the temporal intensity fluctuations during the exposure time. If the image is recorded with an exposure time longer than the time scale of the speckle intensity fluctuations (typically <1 ms for biological tissues), this integration results in blurring of the speckle pattern. Areas of higher motion have more rapid intensity fluctuations, resulting in more blurring of the speckles during the camera exposure time, and vice versa. Since the motion of the scattering particles is encoded in the dynamics of the speckle pattern, a measure of blood flow can be obtained by quantifying the spatial blurring of speckle pattern. This is accomplished by calculating the local speckle contrast, K, defined as the ratio of the standard deviation, σ_s, to the mean intensity of pixels values, $\langle I \rangle$, in a small region of the acquired image [36],

$$K(T) = \frac{\sigma_s(T)}{\langle I \rangle}, \tag{1.1}$$

where T is the exposure time of the camera. The speckle contrast image is a spatially resolved map of the local speckle contrast calculated by computing this ratio at every pixel from the surrounding $N \times N$ pixel region and sliding this window across the raw image. The window size must be carefully chosen to ensure it is large enough to provide an accurate estimate of the speckle contrast with good statistics and small enough to preserve reasonable spatial resolution of the image. N is always an odd integer, so that

the result can be assigned to the center pixel. The minimum window size is 3×3, where 9 pixels make up the local neighborhood, and could go on up to include the entire image, which would be called the global speckle contrast. Empirical studies up to a window size of 13×13 have been compared (169 pixels), and show that the median speckle contrast continues to increase with window size, but that 7×7 (49 pixels) sits near a bend in the curve approaching the asymptote [46]. Thus, $N = 7$ is typically selected as an appropriate window size, and is used throughout this dissertation. Theoretically, speckle contrast ranges between 0 and 1 when the speckle pattern is fully developed and sampled properly. A fully developed speckle pattern comes from polarized light with uniformly distributed phases and a negative exponential distribution of speckle intensities [47]. Proper sampling of the speckle pattern requires satisfying the Nyquist criterion to ensure maximum theoretical speckle contrast, meaning that the speckle size should be at least twice the size of the camera pixel for proper sampling of the speckle pattern [48]. The upper speckle contrast limit $K = 1$ indicates no blurring and therefore no motion in the sample. The lower limit $K = 0$ means that the scatterers are moving fast enough to average out all of the speckles.

A typical example of a raw speckle image and the computed speckle contrast are shown in Figure 1.1, which was taken from a mouse cerebral cortex under normal physiological conditions. The raw speckle image illustrates the grainy appearance of the speckle pattern, with some regions appearing more blurred than others. The speckle contrast image, computed directly from the raw speckle image using Equation 1.1, represents a 2D map of motion occurring in the tissue, which is primarily due to blood flow. Areas of higher baseline flow, such as large vessels, have lower K values and appear red in the speckle contrast image while areas of lower baseline flow with unresolved vasculature, such as the tissue parenchyma, appear blue. In the parenchyma,

speckle contrast values relate to flow in the underlying microvasculature, which includes slower flows from smaller vessels or capillaries.

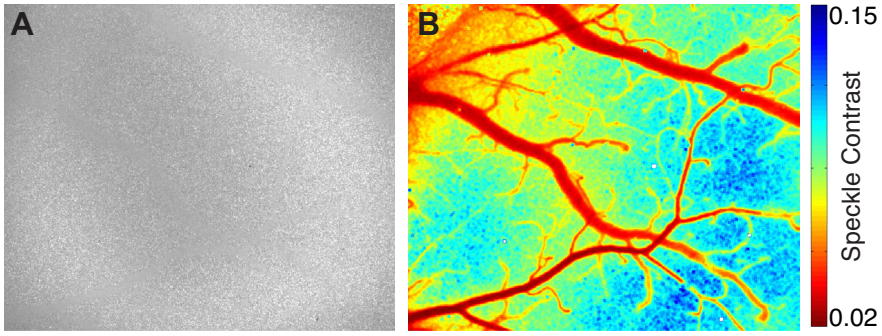

Figure 1.1: Example of a raw speckle contrast image taken from a mouse cerebral cortex (A) and the corresponding speckle contrast image (B), which represents an instantaneous map of blood flow. Speckle contrast values are inversely related to flow, with faster flows shown in red and slower flows shown in blue. The field of view is ~3 mm.

Although speckle contrast values are indicative of the magnitude of motion in the sample, they are not linearly proportional to speed or flow. The exact quantitative relationship between speckle contrast and underlying flow is a complex function that is still an ongoing area of research [49, 50]. To quantitatively relate speckle contrast values to the underlying flow or speed, the theory of correlation functions from dynamic light scattering can be used to calculate the speckle correlation time, τ_c, which is the characteristic decay time of the speckle autocorrelation function [51]. The autocorrelation function quantifies the similarity of a signal with a time-shifted version of itself [26, 51]. The probability that the signal at the shifted time will be similar to the value recorded at an earlier time decreases as the time interval increases. The probability of similarity also decreases the more rapidly the signal changes, which results in a shorter correlation time. The temporal fluctuations of speckles can be quantified using the electric field autocorrelation function $g_1(\tau)$. Because $g_1(\tau)$ is difficult to measure, the

intensity autocorrelation function $g_2(\tau)$ is recorded and can be related to $g_1(\tau)$ using the Siegert relation [34],

$$g_2(\tau) = 1 + \beta \left| g_1(\tau) \right|^2 \quad . \tag{1.2}$$

Here, β is a normalization term that accounts for speckle averaging due to mismatch between speckle size and pixel size, polarization of the light source vs. the detector, and the finite coherence of the light source [52]. The original relationship between *K(T)* and τ_c was first proposed by Fercher and Briers in 1981 [34] and is given by,

$$K(T, \tau_c) = \left(\frac{1 - e^{-2x}}{2x} \right)^{1/2} \quad , \tag{1.3}$$

where $x = T / \tau_c$. This expression is calculated by approximating $g_1(\tau)$ with a negative exponential function, which assumes a Lorentzian velocity distribution [34]. Recently, a more accurate expression has been proposed by Banyopadhyay *et al* [53] to account for speckle averaging effects and is given by,

$$K(T, \tau_c) = \left(\beta \frac{e^{-2x} - 1 + 2x}{2x^2} \right)^{1/2} \quad . \tag{1.4}$$

This expression corresponds to the single scattering regime where photons are scattered from particles undergoing diffusive dynamics (Brownian motion, Lorentzian velocity distribution), and to the multiple scattering regime where photons are scattered from particles undergoing ballistic dynamics (bulk flow, Gaussian velocity distribution) [53]. These underlying assumptions about the scattering regime and sample velocity distribution affect the accuracy of the quantitative relationship between τ_c and the velocity of the moving particles (red blood cells) [49, 50, 54]. Despite these potential shortcomings, Equation 1.4 has been widely adopted for relating measured speckle contrast with relative blood flow [55, 56], and will be used throughout this dissertation.

Using simplifying assumptions, the speckle correlation time τ_c is inversely related to the speed of the moving particles ($1/\tau_c \propto$ speed) [26, 36, 57]. This means that a smaller τ_c corresponds to faster moving red blood cells in tissue. Thus, the measured speckle contrast values are converted to correlation time using Equation 1.4 and relative blood flow changes can be calculated by computing the change in τ_c from a baseline value [37]. Multiple studies have shown a strong correlation between the speckle inverse correlation time ($ICT = 1/\tau_c$) and absolute measures of cerebral blood flow [38, 39], which further supports this approximation for measuring relative blood flow changes with LSCI.

1.2.2 Instrumentation

One reason why LSCI continues to gain popularity as a tool for imaging blood flow is that it requires relatively simple instrumentation. The required hardware for LSCI consists of a coherent light source such as a laser diode for illuminating the tissue, a camera for detection of the backscattered light, and imaging optics to focus the light onto the camera sensor. A traditional laboratory LSCI setup is shown in Figure 1.2.

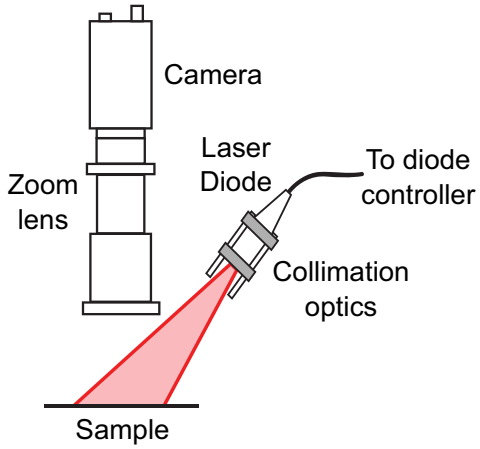

Figure 1.2: Traditional laboratory LSCI setup consisting of a laser diode, imaging optics, and a camera.

The coherent light source is the first major component of an LSCI system, and is required for generation of a speckle pattern. The laser diode output is expanded using collimation optics to illuminate the area of interest. Although uniform laser illumination is always preferred, uneven illumination can still be used for imaging because the speckle contrast calculation includes normalization by the mean intensity within each $N \times N$ pixel window (Equation 1.1). The incident angle of the laser light relative to the sample may vary widely across setups, ranging from near normal to oblique depending on the application. Typically, the laser wavelength is selected in the red to near-infrared range (600 – 850 nm), where tissue hemoglobin absorption is low and scattering dominates. High absorption levels will reduce the mean recorded speckle intensity significantly over larger vasculature, which can impact the accuracy of subsequently calculated flow measures. Because LSCI is typically not light limited, low power laser diodes within the safety limit for tissue exposure can be used. The maximum permissible exposure (MPE) to a laser beam on skin tissue is $0.2\ \mathrm{W/cm^2}$ for a visible laser diode (<700 nm), and $0.2 * 10^{2(\lambda - 0.7)}$ for wavelengths (λ, μm) <1.05 μm [58]. Although not all tissues have the same exposure limits, this is typically used as a general guideline for safe laser powers for use with LSCI.

The camera is the second major component of an LSCI system, required for recording the speckle pattern. The specifications of cameras used in LSCI systems vary widely in the literature, and researchers tend to use any available camera in their laboratory. It is generally accepted that a standard CCD or CMOS camera can be used [55, 59]. CCD (charge-coupled device) and CMOS (complementary metal-oxide silicon) detectors are two types of image sensors that accumulate electronic charge in each pixel proportional to the number of absorbed photons. The main difference between the sensors is the conversion from electronic charge to voltage, which occurs at an output

node after transfer to a storage region for CCD sensors and inside each individual pixel for CMOS sensors [60]. Although CCDs have historically been associated with superior image quality, modern CMOS sensors often outperform CCDs and are typically the standard for high volume consumer cameras. High dynamic range, cooled CCD cameras are usually not required because LSCI systems tend to have high light levels, meaning the majority of noise arises from shot noise [56]. Dynamic range refers to the difference between the brightest and darkest intensity levels, or the pixel saturation and noise threshold. A sensor has high dynamic range when it can record very low light levels and bright signals simultaneously. Cooling a CCD sensor reduces the dark noise, which is a source of noise arising from thermally generated electrons across the entire pixel (even outside the photosensitive area) [60]. The rate of thermal electron generation at a certain temperature is called the dark current, which increases as temperature rises. Dark noise follows Poisson statistics and is equal to the number of thermally generated electrons within the camera exposure time, or $\sqrt{(\text{dark current}) * (\text{exposure time})}$. Thus, cooling the CCD becomes important in low-light level applications where exposure times are typically longer. Photon noise arises from the random arrival of photons, also governed by Poisson statistics, and is equivalent to $\sqrt{\text{signal}}$. Photon noise is unavoidable, but can be reduced by collecting more photons with a longer exposure time or by increasing light levels incident upon the sensor. Shot noise encompasses noise sources with a statistical variation and is a combination of both dark noise and photon noise. Read noise is a source of electronic noise that arises from the circuitry of the sensor, mainly from the on-chip amplifier, during the process of converting electronic charge into a voltage signal. This noise usually includes both white noise and frequency dependent noise, and dominates under low-light level conditions. At longer exposure times or with sufficient light levels, the image is considered shot noise limited, or photon noise limited if CCD

cooling is used to minimize dark noise. Since all of these noise types vary with time, they are considered temporal noise sources and frame averaging is common practice to improve the signal-to-noise (SNR).

Although CCD and CMOS cameras are typically used interchangeably for LSCI, the spectral properties of the sensor are important to consider. Most LSCI systems utilize a monochrome sensor, which record images in grayscale. However, these sensors still have a spectral response and are more sensitive to certain wavelength ranges than others. The spectral response is usually given in terms of the quantum efficiency (QE), which measures how efficient the sensor is at producing electronic charge from incident photons (ranges from 0 – 1, or 0 – 100%). Most standard front-illuminated CCD sensors have a maximum QE around 50% in the visible wavelength range, with a much lower QE in the near-infrared (NIR) range (<20%). This is because incoming light must pass through polysilicon gates to reach the photosensitive region, which reflect and absorb a fraction of photons (reduces the overall QE). Back-illuminated CCD sensors eliminate this issue by illuminating a thinned silicon layer that absorbs photons and allows them to diffuse to the photosensitive region, resulting in high QE >90%. These sensors are typically also high dynamic range and offer cooling to enable imaging in low-light levels with excellent sensitivity, making them fairly expensive. CMOS sensors generally have lower QE than CCDs because they have smaller fill factors. The fill factor is the ratio of the photosensitive area to the pixel area. However, fill factors can be improved using microlenses placed on top of every pixel, which helps image nearly all input photons onto the detector when the design is properly optimized. High sensitivity, NIR-enhanced CMOS sensors are also available with improved QE ranging from 40 – 65% from 400 – 800 nm, and dropping below 20% above 900 nm [61]. These sensors are typically

similarly priced to front-illuminated CCDs, and offer an excellent option for NIR imaging with improved QE.

Other than the sensor type and spectral response, camera selection involves choosing from a wide array of specifications that affect the image quality and performance. Analog voltage signals must be quantized into discrete levels, and the accuracy of this quantization depends on the number of unique levels available. The camera bit depth quantifies how many discrete output levels the analog-to-digital converter can produce. For example, an 8-bit camera has 2^8 gray levels (256), while a 16-bit camera has 2^{16} gray levels (65536). The bit depth of the sensor must have more gray levels than the dynamic range to resolve each signal electron (after accounting for the noise floor) [60]. Thus, higher dynamic range cameras typically have higher bit depths. However, the number of gray levels should not be significantly larger than the dynamic range, or the sensor will be dynamic range limited.

The camera frame rate is another important parameter that determines how fast the camera can acquire images, and is usually reported as frames per second, or fps. The maximum frame rate is limited by one of three factors: the time it takes to read the data for a frame from the sensor to the image buffer (readout speed), the camera exposure time, or the time it takes to transfer a frame from the camera to the host computer [61]. The longest of these three time factors determines the maximum achievable frame rate. The readout speed usually reduces with the height of the frame, thus recording a smaller sub-region (fewer pixels) on the camera sensor increases the frame rate. Long exposure times will reduce the maximum frame rate, while very short exposure times are typically readout speed limited. Frame transmission time depends on the bandwidth assigned to the camera, which usually depends on the type of camera interface, as well as the amount of data that must be transferred per frame (number of pixels). Higher bandwidth means

that more image data can be transferred to the computer per second (usually in megabytes per second). The major machine vision interfaces in ascending maximum bandwidth are USB 2.0, FireWire, Gigabit Ethernet (GigE), USB 3.0, and Camera Link [62]. Increasing frame rate order does not necessarily follow the interface order, since the amount of image data depends on the sensor resolution. However, as you would expect, cameras with lower bandwidth generally cannot achieve the same maximum frame rate as cameras with higher bandwidth connections (i.e. USB 2.0 cameras cannot run as fast as USB 3.0 cameras).

Other camera parameters of interest are the sensor size, pixel size, and optical size. The sensor size refers to the pixel resolution, and is usually listed in terms of horizontal × vertical pixels. Standard resolution typically includes sensor sizes up to 2 MB, including VGA (~640 × 480 pixels), wide VGA (~768 × 480 pixels), and HD resolution (~1280 × 720 pixels). High resolution includes sensor sizes > 2 MB, including full HD (~1920 × 1080 pixels), QSXGA resolution (~2560 × 2048 pixels), or higher pixel density. As sensor resolution increases, higher image data is transferred per frame, which either requires a higher bandwidth interface or results in a lower maximum frame rate. Pixel size refers to the horizontal and vertical size of each detector element in physical units, and is usually calculated as the center-to-center spacing between pixels (known as pitch) [60]. The photosensitive area of the pixel is a fraction of this pixel size, specified by the fill factor. Pixels are usually square, and can range from ~2 × 2 μm up to ~16 × 16 μm. The physical size of the camera sensor can be calculated simply by multiplying the pixel size (μm/pixel) by the number of pixels in each dimension. The physical size of the camera can be classified by the optical format, which is the standard area-scan sensor size. Some commons formats include: 1/8", ¼", 1/3" ½", 2/3", 1", and larger. For these formats, the diagonal dimension is 2, 4, 6, 8, 11, and 16 mm,

respectively [60]. Camera manufacturers tend to round to the nearest standard value, meaning that arrays of slightly different diagonals may be labeled as the same format. Thus, the optical format does not represent the true sensor dimensions, which can be calculated exactly using the pixel size and resolution. This rounding is usually performed to match standard imaging lenses, which also use the optical format specification to specify image size in the focal plane. To avoid image degradation at the edges (vignetting), the optical format of the lens should be greater than or equal to the optical format of the sensor.

The imaging optics used to focus the scattered light onto the camera sensor is the last major component of an LSCI system. This component also varies widely in the literature, since LSCI systems can have vastly different fields of view (a few millimeters up to several centimeters). Fixed focal length camera lenses with *f*/# control are commonly used (Nikon Inc., Canon Inc., or similar) [42, 63], since the aperture is an important parameter for controlling the speckle size. Variable zoom lenses are also common, such as VZM Zoom lens (0.75× – 3×, Edmund Optics Inc.) [38] and Navitar® 6000/ 7000 [64], since the field-of-view (FOV) can be easily adjusted between a wide range. Commercial LSCI systems from Moor Instruments Inc. (moorFLPI-2) and Perimed Instruments AB (PeriCam PSI) both use variable zoom lenses as well to allow imaging of both small and large FOV with the same instrument. LSCI systems can also be easily added on to an existing microscope system that uses objective lenses for higher magnification studies [65, 66]. The type of imaging lens chosen is typically governed by the magnification (*M*) and flexibility required for the given imaging application.

The other main optical parameter to consider when selecting the imaging lenses for LSCI is the numerical aperture, or *f*/#, which determines both the system resolution and speckle size. The numerical aperture (NA) is defined as $n\sin\theta_{\max}$, where n is the

refractive index of the medium and $\theta_{\max}$ is the half-angle of the maximum acceptance cone of light for the lens. Usually, $n = 1.0$ for air with fixed focal length lenses, variable zoom lenses, and air immersion microscope objectives used in LSCI. The refractive index is higher for water or oil immersion microscope objectives, but these are not commonly used for LSCI since a larger working distance is usually required for laser illumination. The numerical aperture is closely related to the *f*/# (f-number) defined as f/D, where f is the effective focal length of the lens and D is the entrance pupil diameter. The entrance pupil of an imaging system is the image of the aperture stop seen from the object, and the aperture stop is an element that limits the amount of light reaching the image. The *f*/# is also referred to as the speed of a lens, since a smaller *f*/# (larger aperture) requires a shorter camera exposure time. Thus, the relationship between NA and *f*/# is shown in Equation 1.5 below, assuming $n = 1.0$ for air,

$$NA = n\sin\theta_{\max} \approx \frac{nD}{2f} \rightarrow f/\# = \frac{1}{2NA} \ . \tag{1.5}$$

Since both parameters provide the same information, only one is typically used to specify the lens. Typically, NA is used for microscope objectives while *f*/# is more common for camera lenses used in photography.

The resolution of an imaging system depends on the NA and the wavelength of light. The image of a point source through a circular aperture is a diffraction pattern, made up by a central maximum circular spot known as an Airy disk surrounded by fainter concentric circular rings. The size of the Airy disk corresponds to the first minimum of $J_1(u)$, a Bessel function of the first kind order one, which represents the location of the first dark ring around the central bright spot. The radius, r, of the Airy disk is given by,

$$r = 1.22\frac{\lambda f}{D} = 0.61\frac{\lambda}{NA} \ , \tag{1.6}$$

where λ is the wavelength of light [67]. This radius represents the resolution limit of an imaging system, since two adjacent points are just resolved when their Airy disks are separated by a distance = r. This is critical for LSCI because the speckle size is defined as the diffraction-limited spot size for the lens system, and thus is determined entirely by the aperture of the optical system used for imaging [26]. For a single-lens system, the speckle size is given by $1.22\lambda(1+M)f/\#$, which is adapted for imaging geometries from Equation 1.6 [44]. Assuming that the speckle size is given by the diameter of an Airy disk, a similar definition for speckle size would be $2.44\lambda(1+M)f/\#$, or even $2.44\lambda M f/\#$ depending on the lens system [68, 69]. A version of the speckle size expression is commonly used to calculate the speckle size for LSCI systems [37, 55, 70]. Because there is not an agreed upon consensus about the correct expression, and because the expression is not the same for more complex lens systems, the speckle size can also be experimentally measured for a given imaging system [71]. This allows the user to be more confident in their LSCI system's speckle size. Knowing the speckle size for a given LSCI system is critical to ensure proper sampling of the speckle pattern on the camera sensor. As mentioned in Section 1.2.1, the speckle size should be at least twice the size of the camera pixel for proper sampling of the speckle pattern [48], and the user can ensure this criteria is met by proper setting of the aperture or *f*/# of the lens system. The speckle size is inversely related to the aperture size, meaning that a smaller aperture (larger *f*/#) will produce larger speckles.

1.2.3 Clinical Translation

Because visual access to tissue is required due to superficial sampling (penetration depth ~700 μm [72]), LSCI is well suited for use during neurosurgery when the brain tissue is already exposed. Translating LSCI to a surgical setting has certain

design requirements to ensure the technology is a useful intraoperative monitoring tool. First and foremost, the use of intraoperative imaging technology should be beneficial to the surgeon, to the patient's safety during the procedure, and to the surgical outcome [73]. To benefit the surgeon, the technology must provide critical surgical assessment not available from direct visualization of the surgical field to assist with surgical decision-making. For the patient's safety, the imaging technology should ideally allow real-time visualization with minimal interruption to the procedure, should be noninvasive and allow continuous monitoring, and should use non-ionizing radiation [74]. To improve surgical outcomes, the technology must be able to identify residual stenosis or occlusion to help prevent undetected problems that could lead to debilitating post-operative results [75]. LSCI has the potential to meet all requirements for patient safety, which allows consideration for clinical translation. LSCI can also provide specific advantages over currently available intraoperative blood flow monitoring tools that may make the technique preferable for many applications. Compared to ICG angiography, LSCI does not require the injection of a contrast agent and can be used as a continuous monitoring tool. Compared to Doppler ultrasound based techniques, LSCI is a non-contact and full-field imaging technique, which means that the surgeon can visualize blood flow in the entire surgical field in real-time. Although ultrasound-based techniques provide absolute measures of blood flow, contact with the vessel of interest is required, and vessels must be investigated sequentially, which can be time consuming. The benefit to the surgeon must be examined intraoperatively using a broad set of clinical studies as well as direct comparison with existing monitoring techniques. The impact of surgical outcome is the last evaluation translation step, where prospective studies are performed to examine ability to affect patient treatment.

1.3 RESEARCH GOALS

The overall goal of this research is to demonstrate that LSCI is an effective tool for monitoring blood flow during surgery, and to optimize and improve LSCI technology for clinical use. Although this research is broadly applicable to any surgical application, this project focuses on the use of LSCI during neurosurgery. This research has two primary components: examining each of the main hardware components in a laboratory setting to determine the optimal specifications for clinical instrument design, and investigating LSCI clinically in a neurosurgical setting.

In the laboratory setting, the first objective is to assess the performance of the laser diode used for illumination and determine which lasers have both sufficient coherence length and stability to perform flow measurements. Coherence length is measured using a Michelson interferometer and stability is examined using a static sample, since a constant speckle contrast value is expected for a non-moving sample. The second objective is to assess the performance of the camera used for recording the speckle images and determine what specifications are most important for reliable, highly sensitive flow measurements. This is tested primarily in microfluidic studies, where both linearity to flow changes and sensitivity to small, transient flow changes can be examined in a controlled manner.

In the clinical setting, the first objective is to adapt LSCI for intraoperative use, to assess LSCI during brain tumor resection procedures, and to develop a paradigm to compensate for unavoidable physiological motion artifacts. The second objective is to optimize the hardware and image acquisition techniques to improve image quality and to enable quantitative CBF assessment for surgical guidance. By optimizing instrument design both in the clinical and laboratory setting, the goal is to make LSCI reliable and sensitive enough to guide surgical decision-making.

1.4 REFERENCES

[1] C. J. Kirkness, "Cerebral blood flow monitoring in clinical practice," *AACN Clinical Issues,* **16**(4), pp. 476-487 (2005).

[2] A. Gruber, C. Dorfer, H. Standhardt, G. Bavinzski, and E. Knosp, "Prospective comparison of intraoperative vascular monitoring technologies during cerebral aneurysm surgery," *Neurosurgery,* **68**(3), pp. 657-673; discussion 673 (2011).

[3] S. Bacigaluppi, M. Fontanella, P. Manninen, A. Ducati, G. Tredici, and F. Gentili, "Monitoring techniques for prevention of procedure-related ischemic damage in aneurysm surgery," *World Neurosurgery,* **78**(3-4), pp. 276-288 (2012).

[4] C. Iadecola, "Neurovascular regulation in the normal brain and in Alzheimer's disease," *Nature Reviews Neuroscience,* **5**(5), pp. 347-360 (2004).

[5] H. Girouard and C. Iadecola, "Neurovascular coupling in the normal brain and in hypertension, stroke, and Alzheimer disease," *Journal of Applied Physiology,* **100**(1), pp. 328-335 (2006).

[6] T. W. Vitaz, M. Gaskill-Shipley, T. Tomsick, and J. M. Tew, Jr., "Utility, safety, and accuracy of intraoperative angiography in the surgical treatment of aneurysms and arteriovenous malformations," *American Journal of Neuroradiology,* **20**(8), pp. 1457-1461 (1999).

[7] V. L. Chiang, P. Gailloud, K. J. Murphy, D. Rigamonti, and R. J. Tamargo, "Routine intraoperative angiography during aneurysm surgery," *Journal of Neurosurgery,* **96**(6), pp. 988-992 (2002).

[8] T. D. Alexander, R. L. Macdonald, B. Weir, and A. Kowalczuk, "Intraoperative angiography in cerebral aneurysm surgery: a prospective study of 100 craniotomies," *Neurosurgery,* **39**(1), pp. 10-17; discussion 17-18 (1996).

[9] C. Schichor, W. Rachinger, D. Morhard, S. Zausinger, T. J. Heigl, M. Reiser, and J. C. Tonn, "Intraoperative computed tomography angiography with computed tomography perfusion imaging in vascular neurosurgery: feasibility of a new concept," *Journal of Neurosurgery,* **112**(4), pp. 722-728 (2010).

[10] G. R. Sutherland, T. Kaibara, C. Wallace, B. Tomanek, and M. Richter, "Intraoperative assessment of aneurysm clipping using magnetic resonance angiography and diffusion-weighted imaging: technical case report," *Neurosurgery,* **50**(4), pp. 893-897; discussion 897-898 (2002).

[11] E. Marchese, A. Albanese, L. Denaro, A. Vignati, E. Fernandez, and G. Maira, "Intraoperative microvascular Doppler in intracranial aneurysm surgery," *Surgical Neurology,* **63**(4), pp. 336-342; discussion 342 (2005).

[12] E. Z. Kapsalaki, G. P. Lee, J. S. Robinson, 3rd, A. A. Grigorian, and K. N. Fountas, "The role of intraoperative micro-Doppler ultrasound in verifying proper clip placement in intracranial aneurysm surgery," *Journal of Clinical Neuroscience,* **15**(2), pp. 153-157 (2008).

[13] H. J. Kirk, P. J. Rao, K. Seow, J. Fuller, N. Chandran, and V. G. Khurana, "Intra-operative transit time flowmetry reduces the risk of ischemic neurological deficits in neurosurgery," *British Journal of Neurosurgery,* **23**(1), pp. 40-47 (2009).

[14] S. Amin-Hanjani, G. Meglio, R. Gatto, A. Bauer, and F. T. Charbel, "The utility of intraoperative blood flow measurement during aneurysm surgery using an ultrasonic perivascular flow probe," *Neurosurgery,* **58**(4 Suppl 2), pp. ONS-305-312; discussion ONS-312 (2006).

[15] N. Ogata, J. Y. Fournier, H. G. Imhof, and Y. Yonekawa, "Thermal diffusion blood flow monitoring during aneurysm surgery," *Acta Neurochirurgica,* **138**(6), pp. 726-731 (1996).

[16] Y. Kubo, K. Ogasawara, N. Tomitsuka, Y. Otawara, S. Kakino, and A. Ogawa, "Revascularization and parent artery occlusion for giant internal carotid artery aneurysms in the intracavernous portion using intraoperative monitoring of cerebral hemodynamics," *Neurosurgery,* **58**(1), pp. 43-49 (2006).

[17] C. Thome, P. Vajkoczy, P. Horn, C. Bauhuf, U. Hubner, and P. Schmiedek, "Continuous monitoring of regional cerebral blood flow during temporary arterial occlusion in aneurysm surgery," *Journal of Neurosurgery,* **95**(3), pp. 402-411 (2001).

[18] T. Desmettre, J. M. Devoisselle, and S. Mordon, "Fluorescence properties and metabolic features of indocyanine green (ICG) as related to angiography," *Survey of Ophthalmology,* **45**(1), pp. 15-27 (2000).

[19] M. L. Landsman, G. Kwant, G. A. Mook, and W. G. Zijlstra, "Light-absorbing properties, stability, and spectral stabilization of indocyanine green," *Journal of Applied Physiology,* **40**(4), pp. 575-583 (1976).

[20] A. Raabe, J. Beck, R. Gerlach, M. Zimmermann, and V. Seifert, "Near-infrared indocyanine green video angiography: a new method for intraoperative assessment of vascular flow," *Neurosurgery,* **52**(1), pp. 132-139; discussion 139 (2003).

[21] A. Raabe, P. Nakaji, J. Beck, L. J. Kim, F. P. Hsu, J. D. Kamerman, V. Seifert, and R. F. Spetzler, "Prospective evaluation of surgical microscope-integrated intraoperative near-infrared indocyanine green videoangiography during aneurysm surgery," *Journal of Neurosurgery,* **103**(6), pp. 982-989 (2005).

[22] J. G. de Oliveira, J. Beck, V. Seifert, M. J. Teixeira, and A. Raabe, "Assessment of flow in perforating arteries during intracranial aneurysm surgery using intraoperative near-infrared indocyanine green videoangiography," *Neurosurgery,* **61**(3 Suppl), pp. 63-72; discussion 72-63 (2007).

[23] R. Dashti, A. Laakso, M. Niemela, M. Porras, and J. Hernesniemi, "Microscope-integrated near-infrared indocyanine green videoangiography during surgery of intracranial aneurysms: the Helsinki experience," *Surgical Neurology,* **71**(5), pp. 543-550; discussion 550 (2009).

[24] M. A. Kamp, P. Slotty, B. Turowski, N. Etminan, H. J. Steiger, D. Hanggi, and W. Stummer, "Microscope-integrated quantitative analysis of intraoperative indocyanine green fluorescence angiography for blood flow assessment: first

experience in 30 patients," *Neurosurgery,* **70**(1 Suppl Operative), pp. 65-73; discussion 73-64 (2012).
[25] V. Prinz, N. Hecht, N. Kato, and P. Vajkoczy, "Flow 800 Allows Visualization of Hemodynamic Changes After Extracranial-to-Intracranial Bypass Surgery but Not Assessment of Quantitative Perfusion or Flow," *Operative Neurosurgery,* **10**(2), pp. 231-239 (2013).
[26] J. D. Briers, "Laser Doppler, speckle and related techniques for blood perfusion mapping and imaging," *Physiological Measurement,* **22**(4), pp. R35-66 (2001).
[27] T. J. Essex and P. O. Byrne, "A laser Doppler scanner for imaging blood flow in skin," *Journal of Biomedical Engineering,* **13**(3), pp. 189-194 (1991).
[28] K. R. Forrester, C. Stewart, J. Tulip, C. Leonard, and R. C. Bray, "Comparison of laser speckle and laser Doppler perfusion imaging: measurement in human skin and rabbit articular tissue," *Medical & Biological Engineering & Computing,* **40**(6), pp. 687-697 (2002).
[29] A. Serov, B. Steinacher, and T. Lasser, "Full-field laser Doppler perfusion imaging and monitoring with an intelligent CMOS camera," *Optics Express,* **13**(10), pp. 3681-3689 (2005).
[30] M. Leutenegger, E. Martin-Williams, P. Harbi, T. Thacher, W. Raffoul, M. Andre, A. Lopez, P. Lasser, and T. Lasser, "Real-time full field laser Doppler imaging," *Biomedical Optics Express,* **2**(6), pp. 1470-1477 (2011).
[31] H. Nakase, T. Kaido, S. Okuno, T. Hoshida, and T. Sakaki, "Novel intraoperative cerebral blood flow monitoring by laser-Doppler scanner," *Neurologia Medico-Chirurgica (Tokyo),* **42**(1), pp. 1-4 (2002).
[32] A. Raabe, D. Van De Ville, M. Leutenegger, A. Szelenyi, E. Hattingen, R. Gerlach, V. Seifert, C. Hauger, A. Lopez, R. Leitgeb, M. Unser, E. J. Martin-Williams, and T. Lasser, "Laser Doppler imaging for intraoperative human brain mapping," *NeuroImage,* **44**(4), pp. 1284-1289 (2009).
[33] W. J. Tom, A. Ponticorvo, and A. K. Dunn, "Efficient processing of laser speckle contrast images," *IEEE Transactions on Medical Imaging,* **27**(12), pp. 1728-1738 (2008).
[34] A. F. Fercher and J. D. Briers, "Flow Visualization by Means of Single-Exposure Speckle Photography," *Optics Communications,* **37**(5), pp. 326-330 (1981).
[35] J. D. Briers and S. Webster, "Quasi real-time digital version of single-exposure speckle photography for full-field monitoring of velocity or flow fields," *Optics Communications,* **116**(1-3), pp. 36-42 (1995).
[36] J. D. Briers and S. Webster, "Laser speckle contrast analysis (LASCA): a nonscanning, full-field technique for monitoring capillary blood flow," *Journal of Biomedical Optics,* **1**(2), pp. 174-179 (1996).
[37] A. K. Dunn, H. Bolay, M. A. Moskowitz, and D. A. Boas, "Dynamic imaging of cerebral blood flow using laser speckle," *Journal of Cerebral Blood Flow & Metabolism,* **21**(3), pp. 195-201 (2001).
[38] C. Ayata, A. K. Dunn, Y. Gursoy-Özdemir, Z. Huang, D. A. Boas, and M. A. Moskowitz, "Laser speckle flowmetry for the study of cerebrovascular physiology

in normal and ischemic mouse cortex," *Journal of Cerebral Blood Flow & Metabolism,* **24**(7), pp. 744-755 (2004).

[39] A. J. Strong, E. L. Bezzina, P. J. B. Anderson, M. G. Boutelle, S. E. Hopwood, and A. K. Dunn, "Evaluation of laser speckle flowmetry for imaging cortical perfusion in experimental stroke studies: quantitation of perfusion and detection of peri-infarct depolarisations," *Journal of Cerebral Blood Flow & Metabolism,* **26**(5), pp. 645-653 (2005).

[40] C. Ayata, H. K. Shin, S. Salomone, Y. Ozdemir-Gursoy, D. A. Boas, A. K. Dunn, and M. A. Moskowitz, "Pronounced hypoperfusion during spreading depression in mouse cortex," *Journal of Cerebral Blood Flow & Metabolism,* **24**(10), pp. 1172-1182 (2004).

[41] H. Bolay, U. Reuter, A. K. Dunn, Z. Huang, D. A. Boas, and M. A. Moskowitz, "Intrinsic brain activity triggers trigeminal meningeal afferents in a migraine model," *Nature Medicine,* **8**(2), pp. 136-142 (2002).

[42] T. Durduran, M. G. Burnett, G. Yu, C. Zhou, D. Furuya, A. G. Yodh, J. A. Detre, and J. H. Greenberg, "Spatiotemporal quantification of cerebral blood flow during functional activation in rat somatosensory cortex using laser-speckle flowmetry," *Journal of Cerebral Blood Flow & Metabolism,* **24**(5), pp. 518-525 (2004).

[43] A. K. Dunn, A. Devor, A. M. Dale, and D. A. Boas, "Spatial extent of oxygen metabolism and hemodynamic changes during functional activation of the rat somatosensory cortex," *NeuroImage,* **27**(2), pp. 279-290 (2005).

[44] A. E. Ennos, "Speckle Interferometry," in *Laser Speckle and Related Phenomena*, J. C. Dainty, Ed., Berlin: Springer-Verlag, 1975, pp. 203-253.

[45] J. C. Dainty, *Laser speckle and related phenomena*. Berlin; New York: Springer-Verlag, 1975.

[46] D. D. Duncan, S. J. Kirkpatrick, and R. K. Wang, "Statistics of local speckle contrast," *Journal of the Optical Society of America A,* **25**(1), pp. 9-15 (2008).

[47] J. W. Goodman, "Statistical Properties of Laser Speckle Patterns," in *Laser Speckle and Related Phenomena*, J. C. Dainty, Ed., Berlin: Springer-Verlag, 1975, pp. 9-75.

[48] S. J. Kirkpatrick, D. D. Duncan, and E. M. Wells-Gray, "Detrimental effects of speckle-pixel size matching in laser speckle contrast imaging," *Optics Letters,* **33**(24), pp. 2886-2888 (2008).

[49] D. D. Duncan and S. J. Kirkpatrick, "Can laser speckle flowmetry be made a quantitative tool?," *Journal of the Optical Society of America A,* **25**(8), pp. 2088-2094 (2008).

[50] D. Briers, D. D. Duncan, E. Hirst, S. J. Kirkpatrick, M. Larsson, W. Steenbergen, T. Stromberg, and O. B. Thompson, "Laser speckle contrast imaging: theoretical and practical limitations," *Journal of Biomedical Optics,* **18**(6), pp. 066018 (2013).

[51] Bruce J. Berne and Robert Pecora, *Dynamic light scattering: with applications to chemistry, biology, and physics*, Dover ed. Mineola, N.Y.: Dover Publications, 2000.
[52] P. A. Lemieux and D. J. Durian, "Investigating non-Gaussian scattering processes by using nth-order intensity correlation functions," *Journal of the Optical Society of America A,* **16**(7), pp. 1651-1664 (1999).
[53] R. Bandyopadhyay, A. S. Gittings, S. S. Suh, P. K. Dixon, and D. J. Durian, "Speckle-visibility spectroscopy: A tool to study time-varying dynamics," *Review of Scientific Instruments,* **76**(9), pp. 093110 (2005).
[54] J. C. Ramirez-San-Juan, R. Ramos-Garcia, I. Guizar-Iturbide, G. Martinez-Niconoff, and B. Choi, "Impact of velocity distribution assumption on simplified laser speckle imaging equation," *Optics Express,* **16**(5), pp. 3197-3203 (2008).
[55] D. A. Boas and A. K. Dunn, "Laser speckle contrast imaging in biomedical optics," *Journal of Biomedical Optics,* **15**(1), pp. 011109 (2010).
[56] A. K. Dunn, "Laser speckle contrast imaging of cerebral blood flow," *Annals of Biomedical Engineering,* **40**(2), pp. 367-377 (2012).
[57] R. Bonner and R. Nossal, "Model for laser Doppler measurements of blood flow in tissue," *Applied Optics,* **20**(12), pp. 2097-2107 (1981).
[58] "American National Standard for the Safe Use of Lasers," in *ANSI Z136.1-2007*: Laser Institute of America, 2007.
[59] M. Draijer, E. Hondebrink, T. van Leeuwen, and W. Steenbergen, "Review of laser speckle contrast techniques for visualizing tissue perfusion," *Lasers in Medical Science,* **24**(4), pp. 639-651 (2009).
[60] Gerald C. Holst and Terrence S. Lomheim, *CMOS/CCD sensors and camera systems*, 2nd ed. Winter Park, FL; Bellingham, WA: JCD Publishing; SPIE, 2011.
[61] "Basler ace: User's Manual for GigE Vision Cameras," Basler AG, http://www.baslerweb.com, 2014.
[62] René von Fintel, "Comparison of the Most Common Digital Interface Technologies in Vision Technolog: Camera Link, USB3 Vision, GigE Vision, FireWire [White Paper]," Basler AG, http://www.baslerweb.com, 2013.
[63] J. Kim, J. Oh, and B. Choi, "Magnetomotive laser speckle imaging," *Journal of Biomedical Optics,* **15**(1), pp. 011110 (2010).
[64] R. A. DeFazio, W. Zhao, X. Deng, A. Obenaus, and M. D. Ginsberg, "Albumin therapy enhances collateral perfusion after laser-induced middle cerebral artery branch occlusion: a laser speckle contrast flow study," *Journal of Cerebral Blood Flow & Metabolism,* **32**(11), pp. 2012-2022 (2012).
[65] T. P. Obrenovitch, S. Chen, and E. Farkas, "Simultaneous, live imaging of cortical spreading depression and associated cerebral blood flow changes, by combining voltage-sensitive dye and laser speckle contrast methods," *NeuroImage,* **45**(1), pp. 68-74 (2009).
[66] A. I. Srienc, Z. L. Kurth-Nelson, and E. A. Newman, "Imaging retinal blood flow with laser speckle flowmetry," *Frontiers in Neuroenergetics,* **2**(128), pp. 1-10 (2010).

[67] Eugene Hecht, *Optics*, 4th ed. Reading, Mass.: Addison-Wesley, 2002.
[68] R. J. Adrian and C. S. Yao, "Pulsed laser technique application to liquid and gaseous flows and the scattering power of seed materials," *Applied Optics,* **24**(1), pp. 44-52 (1985).
[69] C. D. Meinhart and S. T. Wereley, "The theory of diffraction-limited resolution in microparticle image velocimetry," *Measurement Science and Technology,* **14**(7), pp. 1047-1053 (2003).
[70] K. R. Forrester, J. Tulip, C. Leonard, C. Stewart, and R. C. Bray, "A laser speckle imaging technique for measuring tissue perfusion," *IEEE Transactions on Biomedical Engineering,* **51**(11), pp. 2074-2084 (2004).
[71] Y. Piederrière, J. Cariou, Y. Guern, B. Le Jeune, G. Le Brun, and J. Lotrian, "Scattering through fluids: speckle size measurement and Monte Carlo simulations close to and into the multiple scattering," *Optics Express,* **12**(1), pp. 176-188 (2003).
[72] M. A. Davis, S. M. S. Kazmi, and A. K. Dunn, "Imaging depth and multiple scattering in laser speckle contrast imaging," *Journal of Biomedical Optics,* **19**(8), pp. 086001 (2014).
[73] O. Goren, S. J. Monteith, M. Hadani, M. Bakon, and S. Harnof, "Modern intraoperative imaging modalities for the vascular neurosurgeon treating intracerebral hemorrhage," *Neurosurgical Focus,* **34**(5), pp. E2 (2013).
[74] P. Nakaji, "Laser speckle flow imaging of cerebral blood flow," *World Neurosurgery,* **82**(6), pp. e697-698 (2014).
[75] R. M. Starke and A. S. Dumont, "Intraoperative imaging and assessment of cerebral blood flow in cerebrovascular surgery: hybrid operating rooms, intraoperative angiography and magnetic resonance imaging, Doppler ultrasound, cerebral blood flow probes, endoscopic assistance, indocyanine green videography, and laser speckle contrast imaging," *World Neurosurgery,* **82**(6), pp. e693-696 (2014).

Chapter 2: LSCI Laser Comparison

Laser diodes used for speckle imaging must be single longitudinal mode (SLM), or single frequency. The spectral width of the laser is an indication of whether the laser is operating in single or multiple longitudinal modes. A single mode laser will have a narrow spectral line width at the operating wavelength, while multimode lasers will have multiple peaks with a broader width around the center wavelength. The spectral width is closely related to the coherence length of the laser diode, which is a critical parameter in LSCI since coherent interference is required for speckle visibility. The coherence length, l_c, is the distance required for two oscillating light waves from the same source to get out of phase, or become uncorrelated. It is inversely related to the bandwidth of the source, $l_c \propto c/\Delta v$, where c is the speed of light in a vacuum and Δv is the frequency spread of the source (similar to spectral width). Thus, highly monochromatic sources with narrow line widths (SLM) have longer coherence lengths. To ensure all photons detected by the camera interfere coherently, the coherence length must be greater than the maximum optical path length (OPL) within the scattering medium detected by the camera [1]. When $l_c \rightarrow OPL$ or $l_c < OPL$, the speckle pattern becomes partially destroyed, resulting in incoherent detection at the camera and leading to a reduction in the contrast of the recorded speckle pattern [2]. This reduces the β value and affects the decay rates of $g_2(\tau)$, which could lead to inaccurate interpretation of the flow dynamics of a sample.

The laser source for LSCI has wide variation across the field, including wavelength range, power levels, longitudinal mode, manufacturer, and cost. Each of these parameters can have an effect on the imaging performance, and thus thorough assessment is required to determine how to properly select a laser source for LSCI. Another parameter that is not usually a specification available from the manufacturer is

the diode stability over time. This refers to the temporal variations in spatial intensity of the laser illumination during operation, which is a critical parameter for use in LSCI. During the course of the experiment, the intensity distribution of the diode must remain the same so that all measured changes in speckle contrast arise from flow, rather than from the instrument itself. Thus, identifying diodes with the lowest overall noise, as well as experimental parameters that can reduce noise are important. Cost of the diode doesn't directly affect imaging performance, but could affect the quality of the diode and subsequent stability over time. Low-cost is not necessarily a requirement for clinical translation of LSCI, but could help increase adoption in laboratory research settings. This would continue to advance LSCI development and application, which is why it is included as a parameter here.

The objective of this chapter is to perform a broad laser comparison sampling diodes that span the range of available parameters. This includes testing diodes from 635 – 850 nm wavelengths with 5 – 300 mW power levels from two manufacturers spanning a wide range of diode costs. The coherence length of the diodes is measured to assess the longitudinal mode of the laser in Section 2.1, and the stability of the diodes is quantified in an imaging setting in Section 2.2. Both long coherence length and high stability (low noise) is the desired performance for LSCI.

2.1 Coherence Length Study

For this study, a broad assessment of the coherence lengths of several diodes spanning the range of commonly used wavelengths for LSCI (600 – 850 nm) was performed. The assessment includes traditional diodes (Thorlabs Inc.) using standard mounting equipment and laser diode controllers as well as low-cost alternative options (AixiZ LLC) that require a simple power supply for operation. The goal was to

determine which diodes have a long enough to coherence length to perform LSCI imaging, and which low-cost diodes, if any, could provide comparable performance.

2.1.1 Visible Laser Diodes

A standard Michelson interferometer was used to measure the coherence length of the visible diodes included in this comparison, with a schematic shown in Figure 2.1. The traditional diodes were mounted in a temperature-controlled housing (LDM21, Thorlabs Inc.), yet the temperature was not controlled for this study. The laser diode controller (LDC205C, Thorlabs Inc.) was used to control the diode current level. A 635 nm diode (HL6322G, Thorlabs Inc.) was examined at its standard operating current. A 660 nm diode (HL6545MG, Thorlabs Inc.) was examined at both its threshold and operating current levels. An aspheric lens (Thorlabs Inc.) was used to collimate the diode output, and the lens selected was adjusted on a case-by-case basis, since each diode had differing divergences. For the low-cost diodes (AH635-35-3-1 and AH650-10-123, AixiZ LLC), a DC power supply was set to 3.2V output to power the diodes, and the low-cost aspheric lens that comes with the diode was used for collimation. Two beam steering mirrors (M1 and M2) were used to guide the laser into a 50:50 non-polarizing cube beamsplitter. This split the laser into two paths toward mirrors M3 and M_{fixed}, which were then re-combined, expanded with a lens, and imaged onto an 8-bit camera (MV1-D1312(I)-100, PhotonFocus AG). Mirror M3 was placed on a translation stage to vary the optical path difference (OPD) between the two beams, which adds a phase difference between the two beams. When properly aligned, a back-reflection from mirror M_{fixed} travels back into the laser diode cavity, causing fluctuations in the diode intensity. The angle of mirror M_{fixed} was adjusted slightly after alignment to position the back-reflection away from the diode output to improve stability.

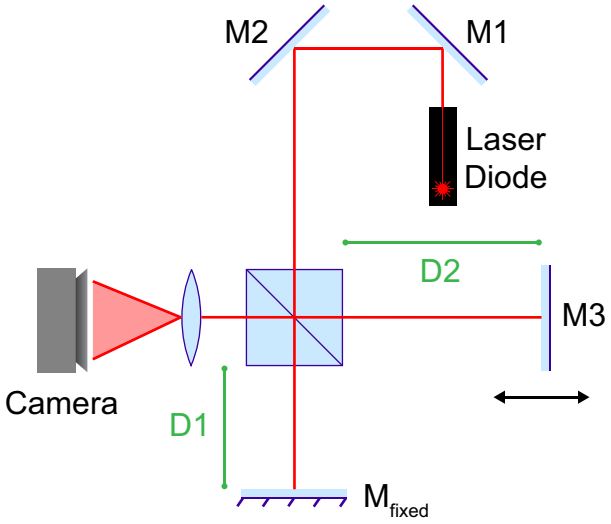

Figure 2.1: Schematic of the Michelson Interferometer design used to measure the coherence length of the visible laser diodes. The OPD between mirrors M3 and M_{fixed} is given by 2*(D2-D1).

When the beams re-combined, the interference produced a fringe pattern consisting of constructive and destructive interference bands, or rings, which was imaged by the camera. For this study, imaging optics were not required and the lens was simply used to increase the size of the fringe pattern on the detector. The camera exposure time was kept at 7 ms for the entire study, and neutral density filters were placed in front of the camera to avoid saturating pixels. This was required since the diodes studied had a wide range of optical powers. The visibility V of the interference pattern was quantified by measuring the minimum and maximum intensities of the pattern, given by

$$V = \frac{I_{max} - I_{min}}{I_{max} + I_{min}}, \tag{2.1}$$

and is a measure of the contrast of the fringe pattern. The coherence length of the laser is defined as the OPD required for the visibility to reach a threshold value of $1/\sqrt{2}$. For this study, the visibility was measured using a line profile drawn across the fringe pattern visible on the camera image. A line profile was used rather than a 2D calculation across

the image because the size of the fringe pattern was not equal across the diodes, and did not always fill the detector. Incorporating dark pixels outside the fringe pattern artificially increases the visibility result, which in turn leads to inaccuracy in the calculation of the coherence length. To measure the coherence length, the two mirrors M3 and M_{fixed} were placed at equal distance from the beam splitter to start (OPD = 0), and images were recorded for visibility measurements to confirm $V = 1$ for correct spacing. Then, mirror M3 was translated using a precision micrometer stage and 2000 images were recorded at each distance until the visibility was confirmed to be less than the threshold value. The mirror was translated both closer and farther from the beamsplitter from the OPD = 0 position for the 635 nm diode pair and just farther from the beamsplitter for the 650/ 660 nm diode pair.

The visibility results versus OPD and representative fringes for both the maximum and threshold visibility are shown for the 635 nm diode pair in Figure 2.2. As shown from the representative fringes (Figure 2.2B and 2.2D), the fringes at maximum visibility have perfectly dark destructive fringes, while the fringes at the threshold have partially overlapping constructive and destructive interference that appears as a blurring of the fringe pattern. This low contrast indicates that the diode had a limited coherence length. If the OPD was increased enough, the fringe pattern would vanish, or wash out, completely and a single uniform intensity spot would be imaged onto the detector. These fringes were parallel to each other, which indicated slight misalignment of the mirrors. This misalignment may have resulted in a slight error in the resulting coherence length calculation. This was tolerable for this study, since the magnitude of the coherence length was more important rather than its exact value. The plots in Figure 2.2A and 2.2C show the visibility of the fringes calculated from the yellow line profile drawn across the fringe pattern. The data points are plotted as the mean and standard deviation over the

2000 recorded images. The blue line shows the total distance required for the visibility to drop below the threshold value on either side of equal mirror separation. The coherence length is equal to half this distance, which is 1.23 mm for the traditional HL6322G and 0.73 mm for the low-cost alternative AH635-35-3-1. Both of these diodes have a fairly short coherence length, which could be an issue for some LSCI applications.

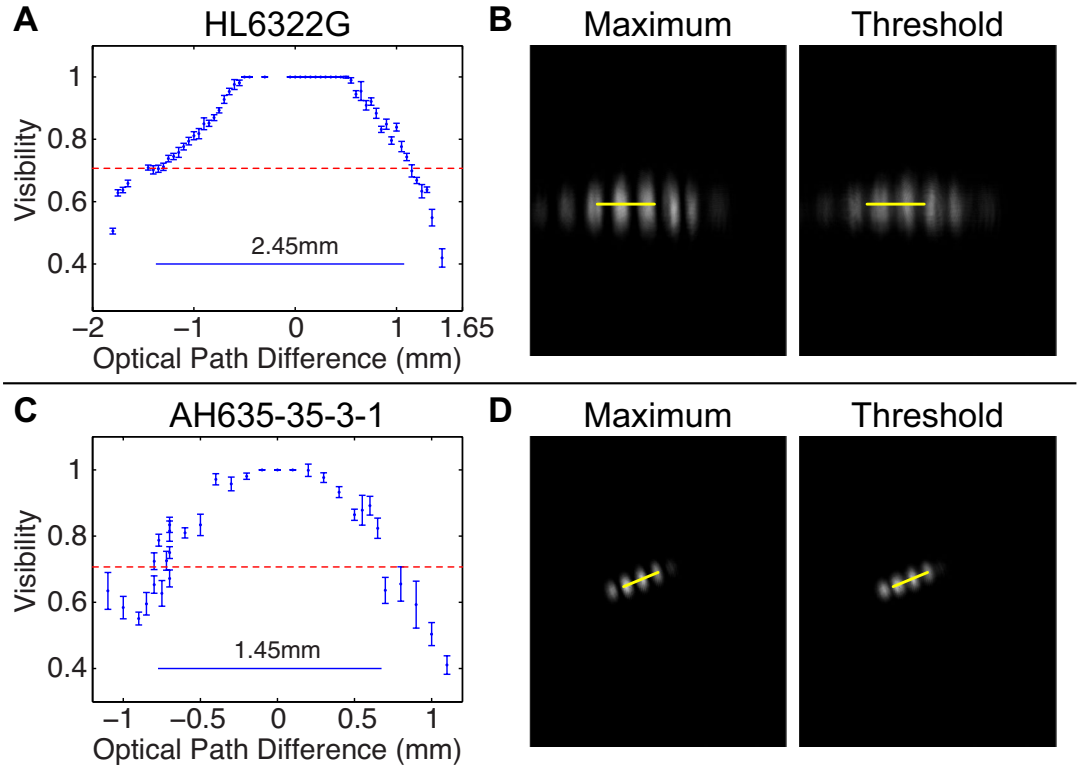

Figure 2.2: Visibility *versus* OPD for the 635 nm traditional diode HL6322G (A) and low-cost alternative AH635-35-3-1 (C). The dotted red line represents the visibility threshold where the coherence length is defined. The blue line represents the total distance required for the diode to pass this threshold on both sides of the OPD = 0 position. The coherence length is equal to half this length. Representative fringe patterns at the maximum ($V = 1$) and threshold ($V = 0.707$) visibility, as well as the image profile used for visibility calculation (yellow line) are shown for the traditional diode (B) and low-cost alternative (D).

The visibility results versus OPD and representative fringes for both the maximum and threshold visibility are shown for the 660/ 650 nm diode pair in Figure 2.3. For the traditional diode HL6545MG, results are shown for both the threshold and operating current, since different coherence lengths were measured for each. As seen from the fringe pattern images, fewer bright and dark fringes were imaged for this pair, with only 1 – 2 visible on the camera. This could be related to different placement of the expanding lens between the two measurements. For this diode pair, images were recorded only one-way from the maximum visibility position (OPD = 0); therefore, the coherence length is defined as the OPD required for the visibility to drop below the threshold value. For the traditional HL6545MG, the coherence length was actually longer for the threshold current value (80 mA) at 8.25 mm than it was at the operating current value (170 mA) at 7.5 mm. This difference is important to note, since the current level of the diode is often adjusted to control the laser power. Since this can affect the coherence of the diode, it would be recommended to control the power using neutral density filters and run the diode at the same current level for consistency. For low-cost alternative AH650-10-123, the coherence length was an order of magnitude less than the traditional diode at only 0.24 mm, which is a stark difference to the 635 nm low-cost alternative. The coherence length of the 650 nm low-cost diode is less than the typical penetration depth of light for LSCI imaging in a microvasculature imaging geometry (0.7 mm) [3], which means that some of the light that returns to the sensor may not be coherent. This will be more of an issue for parenchyma tissue rather than blood vessels, since a larger percentage of light sampling blood vessels travel a shorter distance [3]. Thus, the user would need to decide if the coherence length of the 650 nm diode would be sufficient for their desired application.

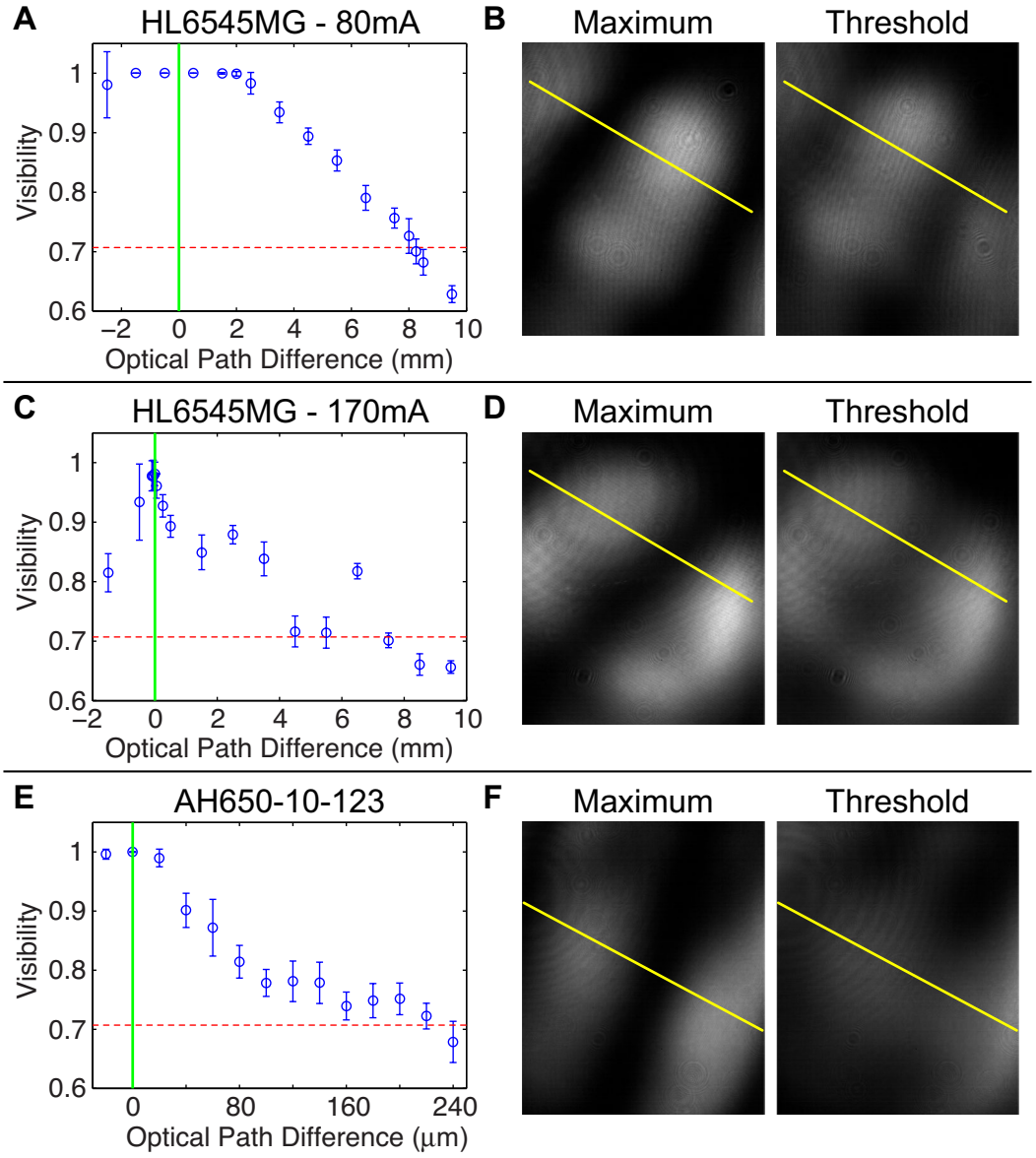

Figure 2.3: Visibility *versus* OPD for the 660 nm traditional diode HL6545MG at 80 mA (A) and 170 mA (C), as well as the 650 nm low-cost alternative AH650-10-123 (E). The dotted red line represents the visibility threshold where the coherence length is defined. The green line represents the OPD = 0 position where maximum visibility was measured. The coherence length is equal to the OPD where the visibility drops below the threshold value. Representative fringe patterns at the maximum ($V = 1$) and threshold ($V = 0.707$) visibility, as well as the image profile used for visibility calculation (yellow line) are shown for the traditional diode at 80 mA (B) and 170 mA (D) as well as the low-cost alternative (F).

2.1.2 NIR Laser Diodes

To measure the coherence length of the NIR laser diodes, initial testing was performed using the same setup in Figure 2.1. However, the coherence length was much longer than what was measurable with the translation stage, and thus a modified setup was used, shown in Figure 2.4. Here, the translating mirror M_{last} was placed at a much farther distance relative to the beamsplitter to increase the OPD. This was performed using multiple mirrors traversing back and forth on the optical table, but is shown with a single mirror for illustration purposes. Because the primary path of the laser is now along a much longer distance, adjusting the angle of the beam to steer the back-reflection off the diode output was no longer an option. Thus, a Faraday isolator was used to prevent back-reflections from traveling back into the laser cavity to improve stability. Because the isolator had a limited aperture smaller than the collimated beam, a 2× beam shrinker was used to reduce the beam size before the isolator. Following the steering mirrors M1 and M2, the beam size was then expanded N×, where N was either 3 or 4 depending on the initial diode output size. This beam expander was used to increase the Rayleigh range of the diode, which increased the distance that the diode remained collimated. The maximum OPD possible with available table space was ~10 m. A longer distance could have been possible using a fiber-based interferometer design, but the exact coherence length >10 m is not important for clinical LSCI applications.

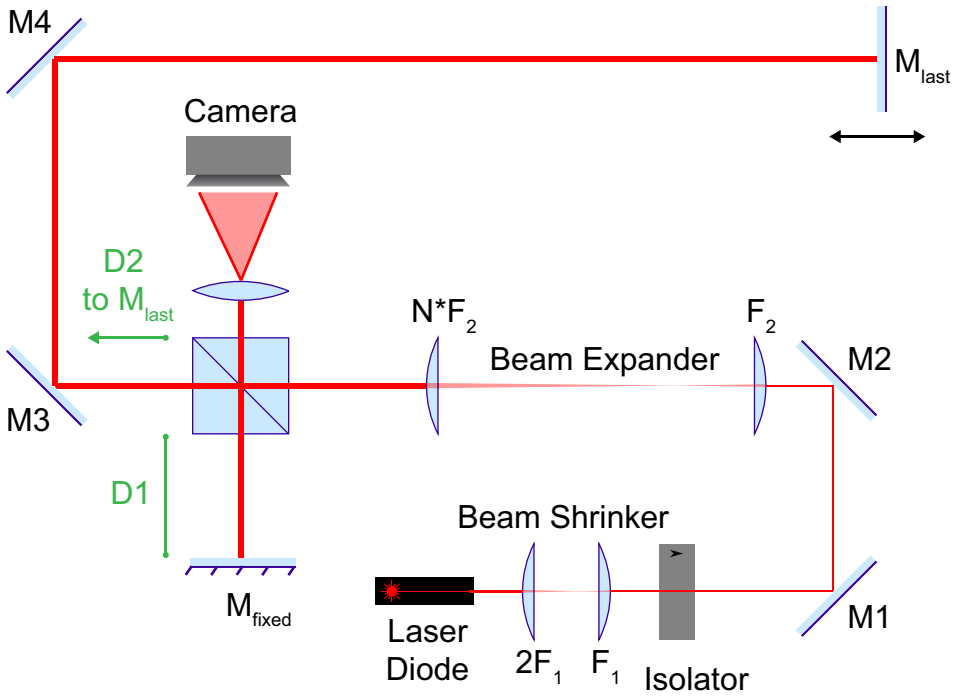

Figure 2.4: Schematic of the Michelson Interferometer design used to measure the coherence length of the NIR laser diodes. The interferometer portion of the setup is the same. Here, the OPD was calculated between mirrors M_{fixed} and M_{last}, given by 2*(D2-D1). A Faraday isolator was used to prevent reflections from traveling back into the laser diode cavity, and a beam expander was used to increase the Rayleigh range. M_{last} is a representative mirror, where in fact multiple mirrors traveling back and forth along the optical table were used to increase the optical path difference.

Multiple diodes operating at two different NIR wavelengths were evaluated, 785 nm and 850 nm, and all diodes had an average visibility >0.707 at an OPD >10 m over 2000 recorded images. Thus, these diodes had a coherence length three orders of magnitude longer than the longest coherence length of the visible diodes measured in Section 2.1.1. Multiple diode models were tested at 785 nm, since this is a common wavelength choice, with three traditional diodes (DL7140-201S, L785P090, and L785-SH300, Thorlabs Inc.) and two low-cost diodes (AH780-601230 and

AH780-150123, AixiZ LLC). The fringe pattern at the mean visibility measured is shown for two of the traditional diodes and low-cost diodes in Figure 2.5, along with the profile used for measuring the visibility. Both traditional diodes were examined at their standard operating currents, and both low-cost diodes were powered using a DC power supply set to 3.2V. These images were recorded at the distances listed in the next section in Table 2.1, with the actual visibility measured also listed in the table. The fringes had excellent visibility, even at a very long distance, indicating a coherence length longer than the maximum OPD measured. The noise in the visibility measurement (standard deviation) was ≤1.6% across all four diodes, which was excellent stability in the fringe pattern. Because optical path lengths >10 m will never be encountered in a clinical setting, all of the NIR diodes had sufficiently long coherence length, making them excellent choices for LSCI imaging. Both the traditional and low-cost alternatives have equally long coherence length, suggesting that the low-cost alternatives could be an acceptable option for LSCI imaging studies.

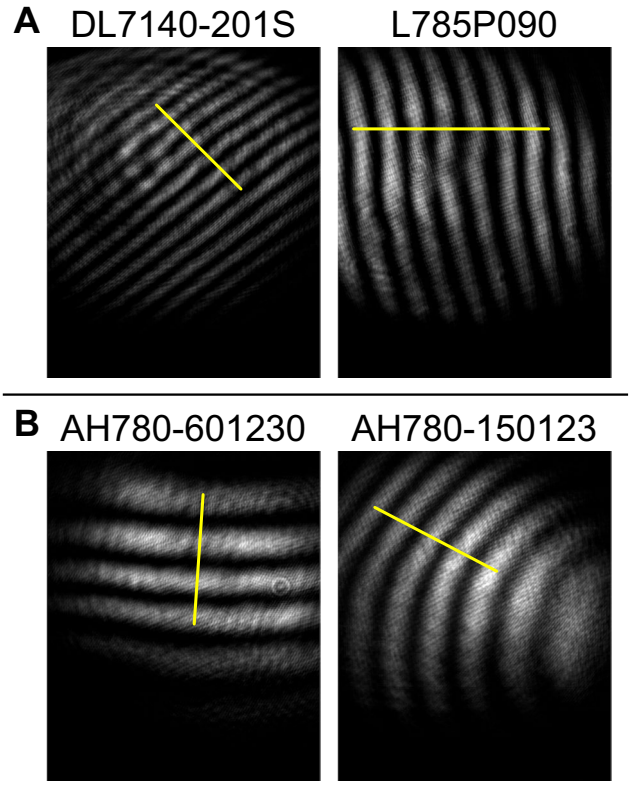

Figure 2.5: Fringe patterns and image profiles used for measuring visibility are shown for two traditional 785 nm laser diode models DL7140-201S and L785P090 (A) as well as two low-cost 780 nm diode alternatives AH780-601230 and AH780-150123 (B). These images correspond to the mean visibility measured, and were all measured at >10 m OPD.

The high power diode L785-SH300 shown in Figure 2.6 was included in this study because it was also used for the phase II clinical study presented in Chapter 6. For this diode, the visibility was measured at three current levels, 100 mA near the threshold current, 300 mA, and 425 mA (operating current), since the current level was adjusted between this range during the clinical measurements. Because this diode was high power (300 mW), a temperature controller (TED200C, Thorlabs Inc.) was used to regulate the temperature of the diode at 10.5 kΩ (~24°C). This study showed that the visibility of the laser diode reduced as the current level decreased, with a mean visibility of 0.997 at

425 mA, 0.968 at 300 mA, and 0.882 at 100 mA. The noise in the visibility measurement also increased from 2% for the operating current to around 6% for the lower current values. Although all of these visibility values are above the threshold, the coherence of the diode is clearly altered by changing the current level, and suggests that a shorter coherence length would be measured using a lower current. This result agreed with the finding from the visible diode study that the coherence length varies with current; however, in this case, the coherence length decreases with current. Overall, the result confirms that neutral density filters are preferred for controlling the laser power to maintain a consistent coherence level.

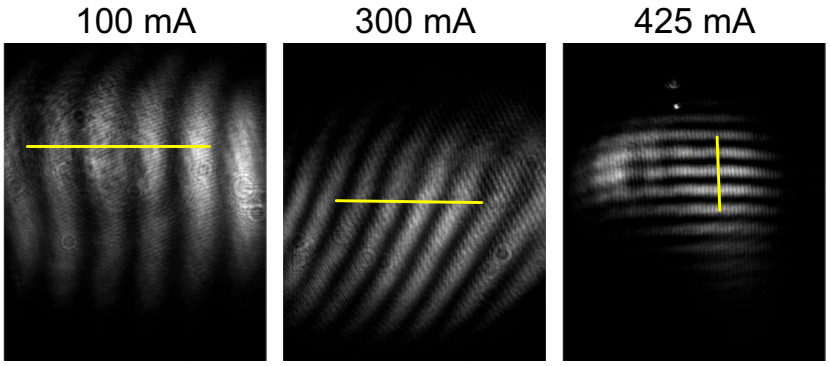

Figure 2.6: Fringe patterns and image profiles used for measuring visibility are shown for the high power traditional diode L785-SH300 at three different current levels. The visibility of the fringe pattern reduces as the current level is decreased. These images correspond to the mean visibility measured, and were all measured at >10 m OPD.

Finally, an 850 nm diode pair was evaluated, with the fringe patterns shown in Figure 2.7. Similar to the 785 nm diodes, both the traditional diode (L850P010, Thorlabs Inc.) and low-cost alternative diode (AH-850-51230, AixiZ LLC) at 850 nm had excellent visibility at >10 m. These diodes did have higher noise in the visibility measurements, at 5.5% for the traditional diode and 7.9% for the low-cost alternative.

Because of the higher noise for the low-cost alternative, the traditional diode might be preferred for this wavelength depending on the application.

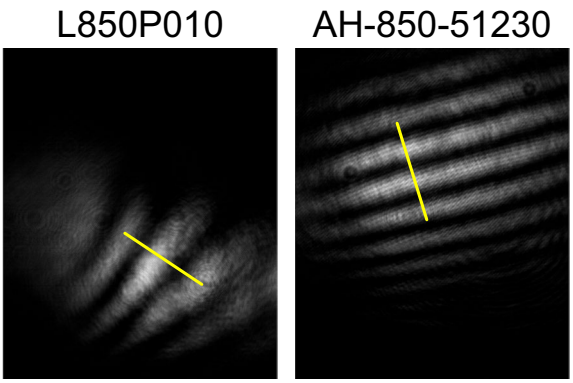

Figure 2.7: Fringe patterns and image profiles used for measuring visibility are shown for the 850 nm diode pair, with the traditional diode L850P010 on the left and the low-cost alternative AH-850-51230 on the right. These images correspond to the mean visibility measured, and were all measured at >10 m OPD.

2.1.3 Discussion

A summary of the coherence length results from both the visible and NIR diodes is shown in Table 2.1. For the visible wavelength range, the HL6545MG had the longest coherence length at 8.5 cm (threshold current) and the low cost alternative AH650-10-123 had the lowest coherence length at 0.24 mm. The visible low-cost alternatives had shorter coherence length and higher noise in the visibility measurements relative to their traditional counterparts. However, all of the visible diodes had fairly low noise ≤2.6%, averaged across all OPD positions measured. For the NIR wavelength range, all traditional and low-cost diodes had a coherence length >10 m, with the exact OPD measured listed in Table 2.1 and the mean visibility measured provided as well. The diode with the highest visibility was the traditional DL7140-201S diode at 785 nm, which was measured to be at maximum $V = 1$, with no variation across the recorded set.

Unfortunately, this diode has recently been discontinued and is now superceded by model L785P090, which still had excellent performance with a visibility of 0.998 and noise of 1.5%. The low-cost 780 nm alternatives at 60 mW and 150 mW also had excellent visibilities >0.975, with noise ≤1.6%. This indicates essentially equivalent performance between the traditional and low-cost alternative diodes, which could be beneficial if a lower cost system was required. The higher power 785 nm diode had comparable performance at its operating current with a visibility of 0.997 and noise of 2.0%, but visibility decreased and noise increased as the current level was decreased towards the threshold value. The results suggest that the diode should be run at its operating current for maximum coherence length, and that the current level should be kept constant for consistency in the coherence length across recordings. Finally, the 850 nm diode pair had slightly lower mean visibility and noticeably higher noise in the visibility recordings compared to the other NIR diodes. For this wavelength, the traditional diode may be preferred over the low-cost diode to improve stability, since it had slightly lower noise levels. Interestingly enough, the actual cost of the diode alone is less for the 850 nm traditional option, but the mounting and controller make this option more expensive.

Table 2.1: Coherence length results for both traditional and inexpensive illumination options, ranging from 635 nm – 850 nm. For NIR diodes, the coherence length is greater than the longest optical path difference measured, with the average visibility provided for reference. Noise = average standard deviation of visibility across 2000 data points, converted to %. Total price includes price of mount (Thorlabs LDM21, AixiZ mount included) and laser diode controller or power supply (Thorlabs LDC205C, AixiZ A-PS-32-500m). DC = discontinued, superceded by model number L785P090.

Model	Vendor	λ (nm)	Power (mW)	Current (mA)	Coherence Length	Stability (Noise %)	Price (Diode)	Price (Total)
HL6322G	Thorlabs	635	15	85	1.23 mm	1.0	$88	$1407
AH635-35-3-1	Aixiz	635	25	-	0.73 mm	2.6	$32.50	$42.30
HL6545MG	Thorlabs	660	120	80	8.25 mm	1.6	$58	$1377
				170	7.50 mm	2.4		
AH650-10-123	Aixiz	650	10	-	0.24 mm	2.5	$12.00	$21.80
DL7140-201S	Thorlabs	785	70	120	>10.38 m (1.00)	0	$40.70 (DC)	$1359.70
L785P090	Thorlabs	785	90	120	>10.42 m (0.998)	1.5	$41.45	$1360.50
L785-SH300	Thorlabs	785	300	100	>10.01 m (0.882)	5.8	$450	$2737*
				300	>10.01 m (0.968)	6.2		
				425	>10.01 m (0.997)	2.0		
AH780-601230	Aixiz	780	60	-	>10.43 m (0.998)	1.6	$12	$21.80
AH780-150123	Aixiz	780	150	-	>10.38 m (0.975)	1.4	$32	$41.80
L850P010	Thorlabs	850	10	50	>10.02 m (0.961)	5.5	$22.60	$1341.60
AH-850-51230	Aixiz	850	5	-	>10.15 m (0.953)	7.9	$29	$38.80

* = Temperature controller used to reduce fluctuations and improve stability. Added cost of $968 included in total price.

2.2 LASER STABILITY STUDY

For this study, a sampling of two of the most commonly used wavelengths was examined with LSCI to investigate its performance in an imaging setting. The traditional and low-cost alternative diode pairs for 660 nm (HL6545MG and AH650-10-123) and 785 nm (L785P090 and AH780-601230) were studied. To investigate the stability of the diodes in an imaging configuration, all diodes imaged a static sample for around 30 minutes. This study also demonstrates differences among the speckle contrast of the raw speckle patterns recorded from each camera. The theoretical maximum for a fully evolved, polarized speckle pattern is $K = 1$ [4], but is typically much lower in practice. The speckle contrast is expected to be lower for diodes with a shorter coherence length [2], and thus the measured K values are used to corroborate the results from Section 2.1.

2.2.1 Instrumentation and Study Design

A simple single-camera LSCI setup was used to measure the mean speckle contrast and stability over time for a sampling of the diodes studied in the Section 2.1. Figure 2.8 shows a schematic of the setup, where the camera was a monochrome CCD camera (Basler Pilot piA640-210gm, Basler AG), the laser diode was swapped between different models as part of the study, and the imaging optics were two Nikon AF-Nikkor fixed focal length ($f = 50$ mm) lenses (represented as boxes) for 1:1 imaging. The CCD camera was controlled using the Basler Pylon API (Basler AG) using custom software, with a fast speckle contrast routine implemented for live display during acquisition [5]. The camera was run using 5 ms exposure time, since this is one of the most commonly used exposure times for *in vivo* microvasculature studies [6]. The Nikon F-mount was adapted to C-mount to connect with the camera (Bower GBCMN, B&H Photo). The Nikon lenses were placed in tandem for 1:1 imaging, and both were set to infinity focus.

This setup was first reported by Ratzlaff *et al* [7] and was used because it provided high light collection efficiency and because it allowed for easy control of the *f*/#. For this study, a speckle size ≥1 pixel size was desired, since this was achievable for the rest of the hardware comparisons performed in this dissertation. Although the speckle size should be twice the size of the camera pixel for proper sampling [8], matched speckle size/ pixel size ratio is most important for relative comparisons, which will be used exclusively. The pixel size for the CCD camera was 7.4 μm. Based on measurements of the speckle size using the 1:1 tandem lens configuration, the speckle size was most closely related to the expression $1.22\lambda f/\#M$. Given a magnification $M = 1$, the CCD camera required an *f*/# of 11 for a speckle size of approximately 1.20 pixels for the visible diodes and an *f*/# of 8 for a speckle size of approximately 1.03 pixels for the NIR diodes. The *f*/# was changed to the appropriate setting on the lens closest to the sample, and the aperture was left all the way open (*f*/# = 1.8) on the lens closest to the camera.

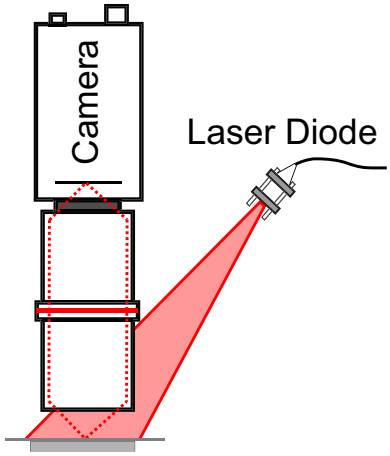

Figure 2.8: LSCI setup schematic for the laser diode stability study. This is essentially the same as Figure 1.2, with a modification in the imaging optics. Here the two boxes represent Nikon AF-Nikkor $f = 50$ mm lenses placed in tandem for 1:1 imaging, and the red line represents a red filter. The sample shown is a tissue phantom made from PDMS with added scattering, bonded to a glass slide.

The traditional diodes were mounted in a temperature-controlled housing (LDM21, Thorlabs Inc.). The laser diode controller (LDC205C, Thorlabs Inc.) was used to set the diode to its operating current level (170 mA for HL6545MG, and 120 mA for L785P090). Stability was tested with and without a temperature controller (TEC) (TED200C, Thorlabs Inc.), which was set to 10.75 kΩ (~23.4°C) when used. For the low-cost diodes (AH650-10-123 and AH780-601230), a DC power supply set to output 3.2V was used to power the diodes. All diodes were allowed to run at the operating levels for 1 hour before recording. Bare diodes without collimating optics were set to illuminate the sample with oblique illumination, shown in Figure 2.8. The divergence angle of the diodes was sufficient to illuminate the entire imaging region. The raw image histogram was matched across all diodes to allow relative comparison (peak = 37, histogram range = 255). This histogram peak was limited by the NIR diodes, which started to saturate the camera detector with higher peak values.

The static sample used in this study was a homogenous tissue phantom. This sample was chosen over a traditional static sample such as a reflectance standard, since it more closely represents the tissue samples of interest in the clinic. The phantom consisted of poly dimethyl siloxane (PDMS) with 1.8 mg titanium dioxide (TiO_2) per gram of PDMS added to generate a scattering background that mimicked tissue optical properties. The concentration of TiO_2 corresponds to a reduced tissue scattering $\mu_s' = 8\ cm^{-1}$ [9], which is within the normal range for extravascular tissue scattering of brain tissue (gray matter) measured *in vitro* for the visible-NIR wavelength range [10]. Absorption was not added to the phantom for simplicity, since the small absorption coefficient in this wavelength range ($\mu_a = 0.2\ cm^{-1}$) would have a minimal effect on imaging. To fabricate the phantom, Dow Corning Sylgard® 184 PDMS was used, which is a 10:1 base-to-curing agent mixture by weight. From an optical imaging standpoint,

cured PDMS is advantageous because it is optically clear, which ensures that the optical scattering of the phantom is known and controllable from the added TiO_2. From a practical standpoint, cured PDMS is solid yet flexible and doesn't degrade over time, which makes the phantoms easy to work with and long lasting. Enough PDMS was measured to fill a 100 mm diameter, 25 mm height polystyrene petri dish for a 1.5 – 2 cm thick phantom, and then TiO_2 was added based on the total PDMS weight. The PDMS mixture was vigorously mixed for 15 minutes to ensure even distribution of the TiO_2 in the phantom. Because mixing added air bubbles to the mixture, centrifugation (3000 *G*, 10 minutes) was then performed to de-gas the sample and remove any TiO_2 clumps. The sample was then carefully poured into the petri dish, and then placed in a vacuum chamber to remove any remaining bubbles. Finally, the PDMS was cured at 70°C for approximately 45 minutes and allowed to cool. The cured PDMS was removed from the petri dish using a spatula and a ~1"x1" square was cut from the middle. The flat side of the PDMS (against the petri dish) was then oxygen plasma bonded to a glass slide. Although this step wasn't required for a static sample, it was used for all future phantoms fabricated for this dissertation, and thus was used here for consistency. The glass slide also enabled easy mounting of the sample for imaging, and was simpler to keep clean.

2.2.2 Image Display and Stability Visualization

Raw images were converted to speckle contrast using Equation 1.1 with a 7×7 pixel window. By incorporating rapid processing techniques into the custom software [5], the speckle contrast images were computed and displayed in real-time during the procedure. In post-processing after the completion of the experiments, speckle contrast images were converted to correlation time, τ_c, using Equation 1.4, where $T = 5$ ms exposure time and $\beta = 1$, which strictly allows computations of relative flow

changes. Although this study involves imaging a static sample, relative flow was still calculated using the same procedure that will be used in all future chapters for comparison. Relative flow was defined as the inverse correlation time relative to a baseline value, which is given by the ratio of an average baseline τ_c and the τ_c values at all remaining time points (flow = $\tau_{c,\,\text{baseline}} / \tau_{c,\,\text{current}}$) [11, 12]. To visualize the stability of the diodes over time, 3 overlapping ROIs were defined in the center of the image FOV with different pixel areas. The average speckle contrast for the ROI was calculated, and then converted to τ_c. The average τ_c over the entire recording (~30 minutes) was used as the baseline for each ROI, putting the average relative flow at 1, or 100% of baseline. For these plots, 30-frame temporal averaging was performed across all trials. Since the camera was run at full speed (~150 fps average), this corresponds to ~0.2 second averaging window. Since the sample imaged is completely static, any visualization of "relative flow" changes is in reality due to spatial fluctuations in the laser output. This allows visualization of the stability of the laser over time in an imaging setup.

2.2.3 Visible Laser Diodes

For the visible laser diodes, a summary of the LSCI imaging results and stability plots are shown in Figure 2.9. All raw images had the same histogram peak (37), yet all speckle contrast images had slightly different mean values. One interesting point to note is that the mean speckle contrast value for the low-cost diode (0.24 mm coherence length) was actually higher than the mean speckle contrast value for the traditional diode (7.5 mm coherence length at the operating current). The reverse trend is usually expected, with a higher speckle contrast value for diodes with a longer coherence length. However, the difference in the mean speckle contrast value is not large, meaning that it could be related to differences in oblique angle illumination between the two trials. The

stability plots show the "relative flow" measured for the 3 ROIs shown in the speckle contrast image. Here, the ROIs are overlapping, so the largest blue ROI (80 × 80 pixels, 6400 pixels^2) includes the smaller red ROI (40 × 40 pixels, 1600 pixels^2) as well as the even smaller green ROI (20 × 20 pixels, 400 pixels^2). The reason for looking at different sized, overlapping ROIs is to show the effect of spatial averaging on the measured stability. For these plots, the smallest ROI in green has the maximum variability across all diodes and vice versa, the largest ROI in blue is the most stable. The red ROI in Figure 2.9C is the one exception, which has slightly less noise than the blue ROI. In this set of plots, the traditional diode, both with and without the TEC, has higher noise than the low-cost alternative. Within the traditional diode trials, the TEC does appear to lower the temporal noise, which would be beneficial for experiments that require high sensitivity.

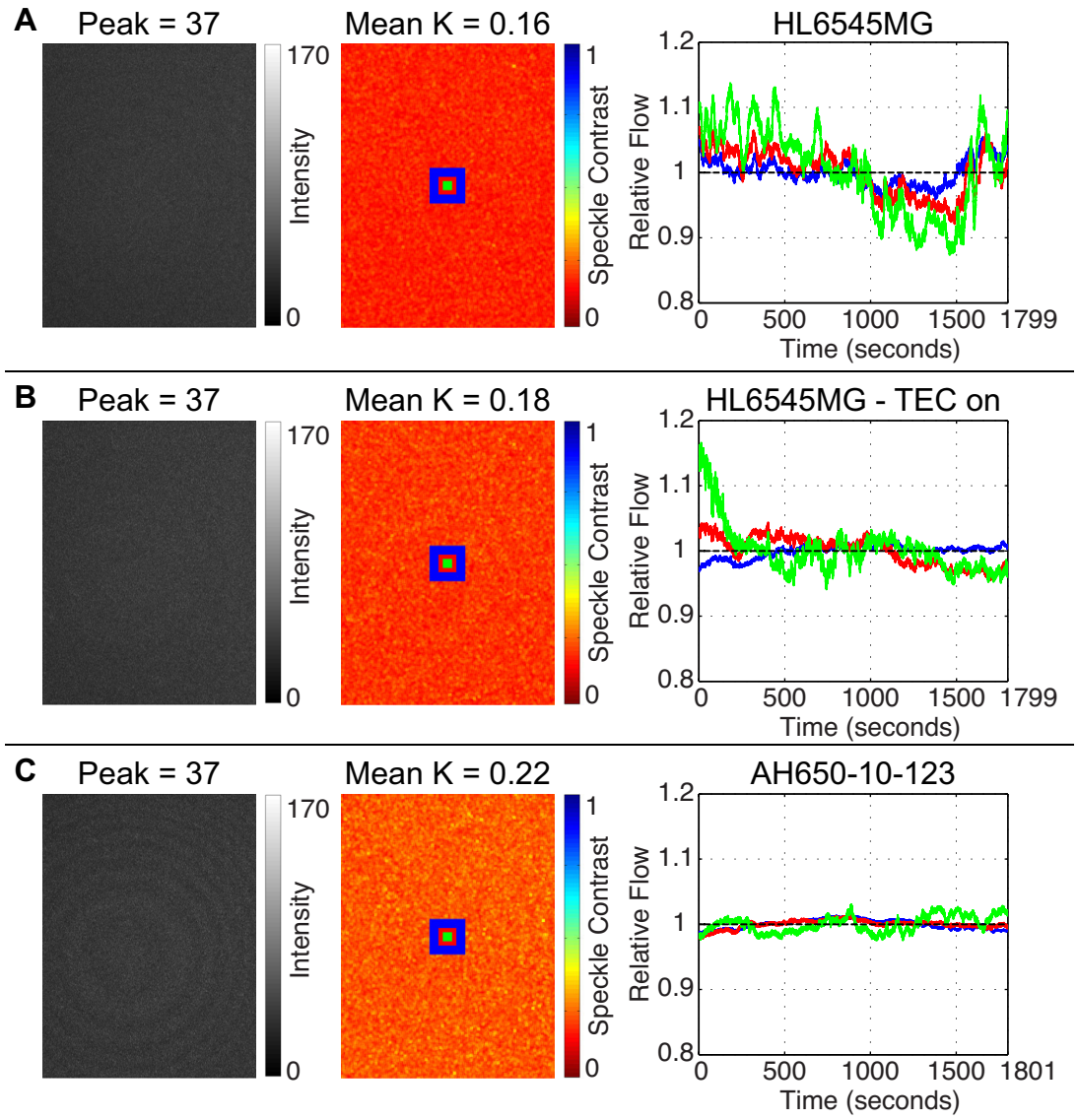

Figure 2.9: LSCI assessment of the visible laser diode pair, including the raw speckle image, the speckle contrast image with 3 ROIs shown, and the corresponding stability recordings for each ROI over 30-minute duration. The colors of the ROIs (blue, red, and green) match the colors in the plots. The traditional 660 nm diode HL6545MG is examined both (A) without temperature control to match the coherence length study and (B) with temperature control on (TEC, 10.75 kΩ, 23.4°C) to see if stability improves. The traditional diode is then compared against the performance of the low-cost 650 nm diode AH650-10-123 (C).

One important point to note regarding the visible diodes is that both are susceptible to mode hopping. This is evidenced by additional trials with both diodes shown in Figure 2.10. Mode hopping refers to when the SLM laser suddenly switches to a different resonator mode, which results in a discrete jump to a different center wavelength. This causes dramatic spatial intensity fluctuations seen by the sharp spikes in the stability plots. Mode hops are often caused by temperature shifts in the diode, which can be caused if the diode overheats, or if a temperature controller is set at a transition temperature. Most diodes come with a specification from the manufacturer showing a plot with the laser wavelength versus case temperature, and shows that the laser wavelength increases in a stair-step fashion as the temperature is increased. If the temperature is set to one of these stair-step transitions, the laser will be highly susceptible to mode hopping. This was evident with the traditional diode, where the temperature controller was set to 10.0 kΩ (25°C). When the diode was operated without the temperature controller (Figure 2.9A), the temperature reading was 9.24 kΩ (~26.8°C). Thus, the temperature setting 10.0 kΩ shifted the diode to a transition location (Figure 2.10B), while the temperature setting 10.75 kΩ (~23.4°C) (Figure 2.9B) shifted the diode back onto a stable operation level. Thus, mode hopping can be avoided with the traditional diode using the TEC at an appropriate setting. However, the mode hopping in the low-cost alternative diode is more problematic, since these diodes are traditionally powered using a DC power supply without the ability to control the drive current or temperature of the diode. It could be possible to disassemble the low-cost diode and integrate into the more expensive housing for temperature control; however, required specifications for the low-cost diode are not readily available. Thus, at that point, it would make more sense just to use the traditional diode, since the price savings using the low-cost diode with the traditional mounts and controllers would only be $76.

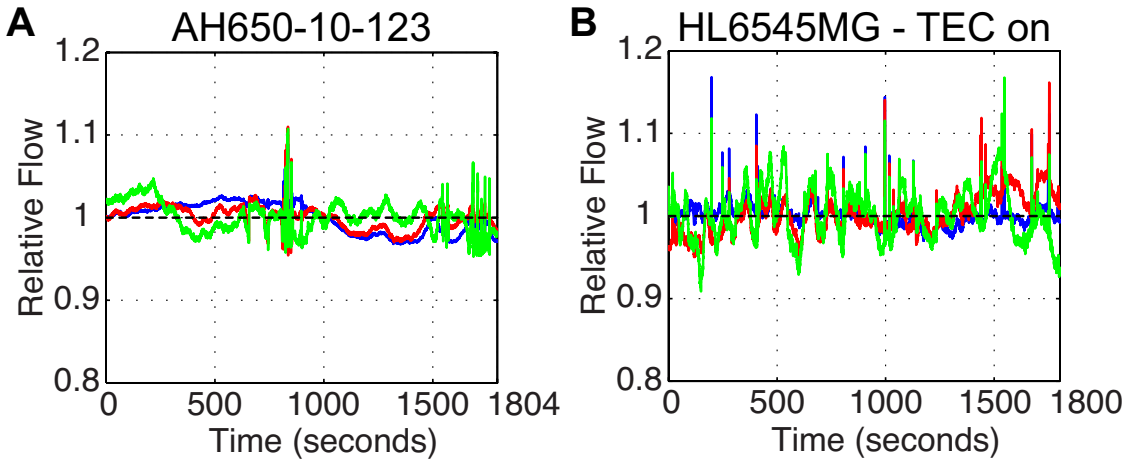

Figure 2.10: Additional stability recordings over 30-minute duration for the same ROIs shown in Figure 2.9 for (A) the low-cost alternative AH650-10-123 and (B) the traditional diode HL6545MG with a TEC setting of 10.0 kΩ (25°C), demonstrating examples of mode hopping with both diodes.

2.2.4 NIR Laser Diodes

For the NIR laser diodes, a summary of the LSCI imaging results and stability plots are shown in Figure 2.11. All raw images had the same histogram peak (37) and the same speckle contrast mean value ($K = 0.45$). For this set of diodes, both the traditional and low-cost diode alternatives had similar coherence lengths (>10 m), and this is reflected by the similarity in the speckle images. Because these diodes had a longer coherence length than the visible diodes, the mean speckle contrast value is higher in comparison ($K = 0.45$ NIR vs. $K = 0.16 – 0.22$ visible), as expected. The stability plots show that the traditional diode without the temperature controller and the low-cost diode alternative have similar noise levels, which is consistent with the noise results from the coherence length study. The TEC does lower the temporal noise of the traditional diode as shown in Figure 2.11B, which would be beneficial for experiments that require high sensitivity.

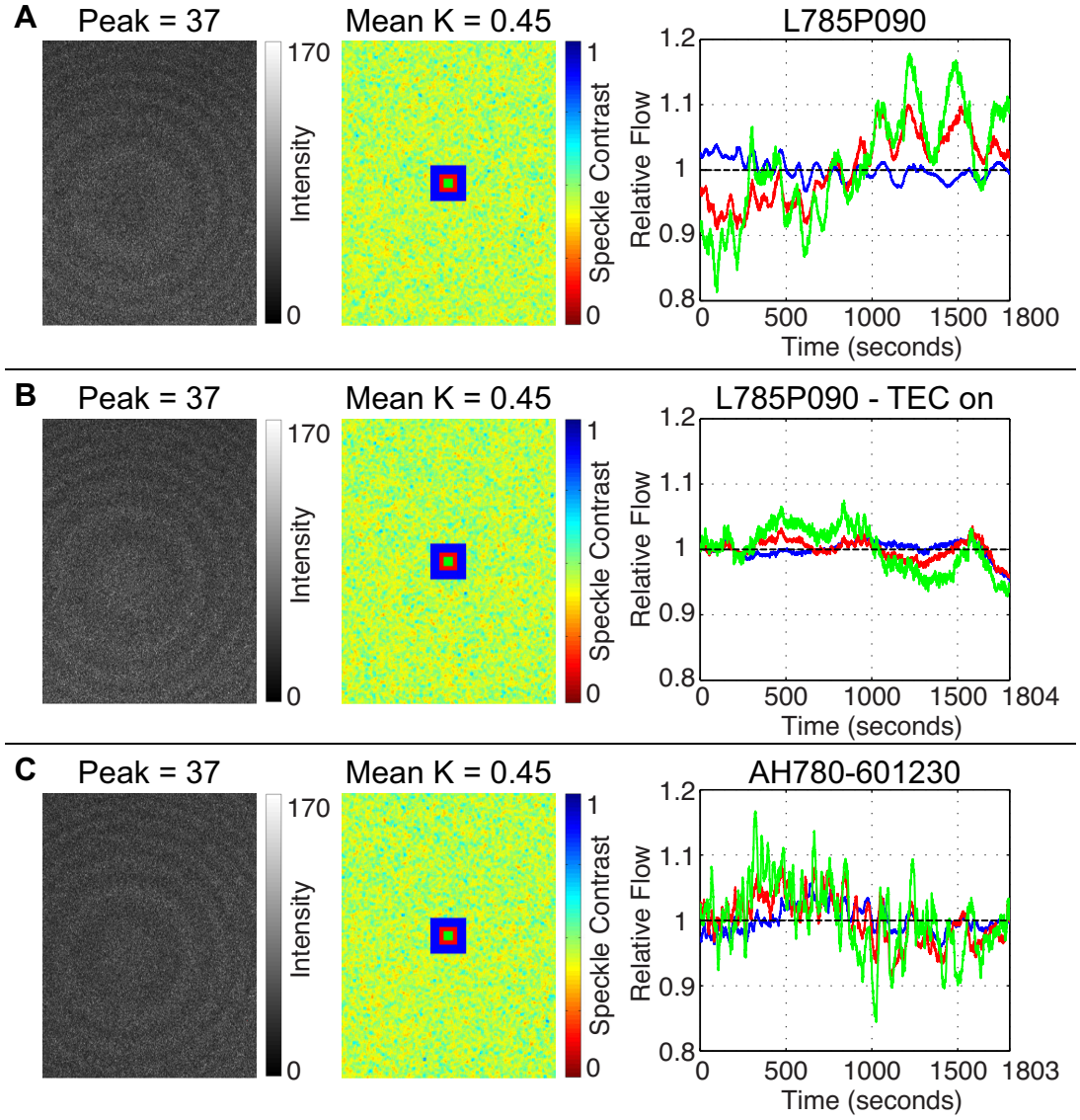

Figure 2.11: LSCI assessment of the NIR laser diode pair, including the raw speckle image, the speckle contrast image with 3 ROIs shown, and the corresponding stability recordings for each ROI over 30-minute duration. The colors of the ROIs (blue, red, and green) match the colors in the plots. The traditional 785 nm diode L785P090 is examined both (A) without temperature control to match the coherence length study and (B) with temperature control on (TEC, 10.75 kΩ, 23.4°C) to see if stability improves. The traditional diode is then compared against the performance of the low-cost 780 nm diode AH780-601230 (C).

2.2.5 Discussion

A summary of the noise quantification from the stability study in a traditional LSCI imaging setup is shown in Table 2.2. Both traditional diodes had improved stability (less noise) across all ROIs with the TEC on. The noise of the low-cost visible diode was less than the traditional alternative, even with the TEC. However, both the low-cost diode and the traditional alternative 660 nm diodes were found to be susceptible to mode hopping. The laser mode can be adjusted by changing either the drive current or the temperature setting on the TEC with the traditional diode, while there is no way to control or minimize mode hopping with the low-cost diode. Thus, it is recommended to use the traditional diode over the low-cost alternative for the visible diode pair, to reduce the risk of mode hopping unexpectedly occurring in the middle of an experiment. The noise of the low-cost NIR diode was similar to the traditional alternative with the TEC off, confirming similar performance of this diode pair in the coherence length study. However, the traditional diode with the TEC on had the lowest noise for this wavelength pair.

Table 2.2: Quantification of noise (average standard deviation of relative flow, converted to %) for both traditional and low-cost laser diode options (660 nm and 785 nm) shown in Figures 2.9 and 2.11. Noise levels are shown for each of the ROI sizes included in the stability plots for comparison. TEC = temperature controller.

Laser Diode Model	**Blue ROI (6400 pixels^2)**	**Red ROI (1600 pixels^2)**	**Green ROI (400 pixels^2)**
HL6545MG – TEC off	1.99	3.45	6.60
HL6545MG – TEC on	0.99	2.25	3.73
AH650-10-123	0.70	0.63	1.27
L785P090 – TEC off	1.53	5.15	8.12
L785P090 – TEC on	1.17	1.39	3.30
AH780-601230	1.98	3.57	5.42

2.3 CONCLUSIONS

The results from this laser comparison study show definitive trends that can be used as a starting point to guide optimal laser diode choice for LSCI instrumentation. The coherence length study showed that all NIR diodes tested (780 – 850 nm) had a very long coherence length (>10 m), which is much greater than the maximum optical path length expected for any clinical LSCI tissue sample. The traditional 660 nm visible diode also had a sufficiently long coherence length (≥7.5 mm), while the remaining visible diodes (635 – 650 nm) had much shorter coherence lengths (≤1.23 mm). Given the expected imaging depth in an LSCI imaging geometry [3], the latter visible diodes may lead to partially incoherent detection at the camera, especially over tissue regions with non-resolvable vasculature. Measurements at multiple current levels for traditional diodes across both wavelength ranges indicated that the drive current affects the coherence length of the diode, and that this variable should be kept constant across recordings to maintain the same level of coherence. The LSCI imaging study showed that the 785 nm traditional and low-cost diode pair had very similar performance in terms of stability and mean speckle contrast, indicating that the low-cost diode is a suitable option for LSCI imaging. However, even better stability is observed when the temperature controller is used with the traditional diode, making this the preferred choice when high stability is required. The 650 nm low-cost diode actually had the highest mean speckle contrast value and lowest noise overall for the visible diode set; however, its susceptibility to mode hopping and its low coherence length reduce its viability as a reliable option for LSCI imaging. The 660 nm traditional diode, operated with temperature control, provides the next best choice if a visible diode is required. Overall, all NIR diodes and the 660 nm traditional diode have sufficient coherence length for

LSCI imaging, and temperature control improves stability of the traditional diodes. If a low-cost diode is desired, one of the 780 nm options would be a good choice.

2.4 REFERENCES

[1] D. A. Boas and A. K. Dunn, "Laser speckle contrast imaging in biomedical optics," *Journal of Biomedical Optics,* **15**(1), pp. 011109 (2010).

[2] P. A. Lemieux and D. J. Durian, "Investigating non-Gaussian scattering processes by using nth-order intensity correlation functions," *Journal of the Optical Society of America A,* **16**(7), pp. 1651-1664 (1999).

[3] M. A. Davis, S. M. S. Kazmi, and A. K. Dunn, "Imaging depth and multiple scattering in laser speckle contrast imaging," *Journal of Biomedical Optics,* **19**(8), pp. 086001 (2014).

[4] J. W. Goodman, "Statistical Properties of Laser Speckle Patterns," in *Laser Speckle and Related Phenomena*, J. C. Dainty, Ed., Berlin: Springer-Verlag, 1975, pp. 9-75.

[5] W. J. Tom, A. Ponticorvo, and A. K. Dunn, "Efficient processing of laser speckle contrast images," *IEEE Transactions on Medical Imaging,* **27**(12), pp. 1728-1738 (2008).

[6] S. Yuan, A. Devor, D. A. Boas, and A. K. Dunn, "Determination of optimal exposure time for imaging of blood flow changes with laser speckle contrast imaging," *Applied Optics,* **44**(10), pp. 1823-1830 (2005).

[7] E. H. Ratzlaff and A. Grinvald, "A tandem-lens epifluorescence macroscope: hundred-fold brightness advantage for wide-field imaging," *Journal of Neuroscience Methods,* **36**(2-3), pp. 127-137 (1991).

[8] S. J. Kirkpatrick, D. D. Duncan, and E. M. Wells-Gray, "Detrimental effects of speckle-pixel size matching in laser speckle contrast imaging," *Optics Letters,* **33**(24), pp. 2886-2888 (2008).

[9] A. B. Parthasarathy, W. J. Tom, A. Gopal, X. J. Zhang, and A. K. Dunn, "Robust flow measurement with multi-exposure speckle imaging," *Optics Express,* **16**(3), pp. 1975-1989 (2008).

[10] A. N. Yaroslavsky, P. C. Schulze, I. V. Yaroslavsky, R. Schober, F. Ulrich, and H. J. Schwarzmaier, "Optical properties of selected native and coagulated human brain tissues in vitro in the visible and near infrared spectral range," *Physics in Medicine and Biology,* **47**(12), pp. 2059-2073 (2002).

[11] A. K. Dunn, H. Bolay, M. A. Moskowitz, and D. A. Boas, "Dynamic imaging of cerebral blood flow using laser speckle," *Journal of Cerebral Blood Flow & Metabolism,* **21**(3), pp. 195-201 (2001).

[12] C. Ayata, A. K. Dunn, Y. Gursoy-Özdemir, Z. Huang, D. A. Boas, and M. A. Moskowitz, "Laser speckle flowmetry for the study of cerebrovascular physiology

in normal and ischemic mouse cortex," *Journal of Cerebral Blood Flow & Metabolism,* **24**(7), pp. 744-755 (2004).

Chapter 3: Microfluidic Studies for LSCI Hardware Assessment

Microfluidic flow studies are commonly used for characterizing LSCI in a controlled setting, since the ability to differentiate different flow levels is a critical metric used to define LSCI performance. Hardware assessment requires the use of a stable and repeatable flow control system. Any variability in flow will be measured as instrument noise, and non-repeatable flow generation will introduce error for multiple cross-comparisons. Typically, studies involve the use of a flow channel embedded in a PDMS background [1], glass capillary tubing [2], or a segment of clear plastic tubing [3]. A scattering solution [1] or whole blood [2, 3] is then flowed through the channel for imaging. The velocity of the flow varies widely across studies, and usually depends on the size of the channel and the intended application. For application in rodent studies, 1 – 10 mm/s is a commonly selected range of speeds, since this corresponds to the capillary speeds measured in rodents [4]. This speed is then converted to a flow rate using the cross-sectional area of the flow channel, which can then be used to program a flow control system to deliver controlled flow rates.

Syringe pumps are commonly used for microfluidic studies, especially in the LSCI community. A review of >20 LSCI microfluidic studies all used syringe pumps from various manufacturers, with various syringe sizes and materials. Syringe pumps operate by using a pushing block to apply a mechanical force on the plunger of a syringe at a controlled speed. A stepper motor controls the velocity of the pushing block, which is calculated by the pump from the programmed syringe size and inner diameter. A lead screw rotates at the programmed rate to move the pusher block forward and produce the desired flow rates. Syringe pumps are commonly believed to provide a highly controlled flow output and are easy to use, which is why it remains the most widespread flow

control system in the community. However, syringe pumps produce oscillations in flow with varying frequency and magnitude due to the physical motion of the motor and from imperfections on the lead screw [5, 6]. Using the smallest syringe size possible for the experiment can minimize fluctuations due to very small steps of the motor, since the lead screw velocity will be higher for the same flow rates. Syringe pumps have also been shown to have slow responsivity, and take a longer time to achieve desired flow rates [7]. This is related to the compliance of the microfluidic system, including the syringe and tubing material. A plastic syringe usually has a rubber piston as part of its plunger assembly, which can introduce system compliance and reduce responsivity. A glass syringe eliminates this compliance, which results in better responsivity. High compliance reduces responsivity, but can help improve the stability of the flow system by damping flow fluctuations. Because of the trade-off between stability and responsivity, it is difficult to obtain both stable flow and fast flow response with a syringe pump flow control system.

Fluidic networks can be modeled as a resistor-capacitor electric circuit, where compliance acts as a capacitor and microfluidic resistance acts as a resistor. The flow control system contributes to the system compliance, including the syringe material for syringe pump driven flow. In addition, the material of the tubing used to connect to the microfluidic chip contributes to the compliance, where soft tubing has higher compliance and rigid tubing has lower compliance. Microfluidic resistance arises from the length and diameter of both the tubing and the microfluidic channel, where smaller diameters and longer lengths contribute to higher resistance. Similar to compliance, higher microfluidic resistance helps improve the stability of the flow system. This electrical analogy can be used to guide the fluidic system design to optimize flow stability or responsivity [8]. However, the flow control system inherently limits the best achievable flow performance.

The same studies that demonstrated the presence of syringe pump induced flow fluctuations have shown that a pressure-based flow regulation system can overcome the limitations of a syringe pump [5-7]. This involves using compressed air and a pressure regulator to pressurize a reservoir holding the solution, and then applying a controlled pressure to push solution through the microfluidic chip at constant flow rates. Pressure regulation eliminates the use of a motor altogether and can provide very stable flow rates. An absolute flow sensor can be added in-line with the inlet tubing for the microfluidic chip, and a feedback loop can be used to adjust the pressure level to achieve a desired flow rate. This is a pressure-based equivalent of a syringe pump, since it allows the user to request a desired flow rate rather than a pressure level.

Typically, thermal mass flow sensors are used to measure the low flow rates employed in microfluidics. The internal components of the sensor includes a glass capillary tube for transporting fluid, a heating element that adds a small amount of heat to the fluid, and two temperature-sensing elements, one upstream and one downstream from the heating element. With increasing mass flow, more heat is transported toward one of the sensing elements, which is directly correlated with the magnitude and direction of the flow. In the absence of flow, the heat profile is evenly distributed between the two sensing elements, and zero flow can be detected. Thermal mass flow sensors are calibrated to produce absolute flow rates for a particular fluid, usually deionized water.

The objective of this study is to compare the relative flow rates produced by a syringe pump versus pressure regulation in controlled microfluidic flow experiments. This study involves visualizing relative flow with LSCI and using the in-line flow sensor for validation. In addition, differences in stability, response time, and ability to resolve small flow changes between the two flow control systems will be assessed. The study aims to show that LSCI can visualize relative flow changes with high accuracy and that

the syringe pump is not an ideal choice for reliable and sensitive flow control in microfluidic studies. The results of this study demonstrate the optimal parameters required for robust microfluidic studies to make LSCI hardware assessment possible.

3.1 Instrumentation and Study Design

The LSCI instrumentation used for this study is identical to that described in Section 2.2.1, shown in Figure 3.1A. For this study, the 660 nm traditional laser diode (HL6545MG, Thorlabs Inc.) was used for illumination, with current settings near operating level (~200 mA) and temperature control (10.55 kΩ, ~23.8°C) used for maximum stability. For this visible diode, the CCD camera required an *f*/# of 11 for a speckle size of ~1.20 pixels. The camera exposure time was set to 0.5 ms for this study, which was determined to be the optimal exposure time for the range of flows used in this study. Here, the sample is now a microfluidic flow phantom, with a cross-section of ~460 × 460 μm and a length of ~20 mm. To read the actual flow going through the phantom, a mass flow sensor (Flow Sensor L, 30-1000 μL/min, FLU_L, Fluigent Inc.) was placed in-line between the flow control system and the phantom inlet tubing. The sensor was connected to a flow reader (Flow Board, FLB, Fluigent Inc.) to digitize the sensor output and the MAESFLO software (Fluigent Inc.) recorded the absolute flow rate. For the first study, a syringe pump (74905-04, Cole-Parmer Instrument Company LLC) was connected to the flow sensor (Figure 3.1B), and either a 3 mL or 10 mL plastic syringe (Becton, Dickinson and Company) was filled with blood-mimicking solution and flowed through the phantom at controlled rates. For the second study, a pressure control system was used to flow the solution through the phantom (Figure 3.1C). The house air line was connected to an air filter and then a regulator was used to maintain 500 mbar of clean air into the pressure controller base unit (MFCS-EZ with 69 mbar channel,

Fluigent Inc.). This controller outputted regulated air flow up to 69 mbar to a 15 mL pressurized reservoir (Fluiwell-1C, Fluigent Inc.) filled with the desired solution. Using the flow-rate control module software, the system used a feedback loop to adjust air pressure to the reservoir to achieve the desired flow rate in the flow sensor. The system constantly regulated the air flow based on the flow sensor reading, and could adjust pressures in real-time to account for any changes in system parameters, such as partial clogging in the flow line or changes in hydrostatic pressure as the reservoir emptied during the experiment. For this system, the flow sensor recorded the absolute flow rate and served as an input to the feedback loop used to control the pressure to the reservoir. After flowing through the phantom, the output line emptied the solution into a vial, with the outlet line submerged in solution during all flow measurements.

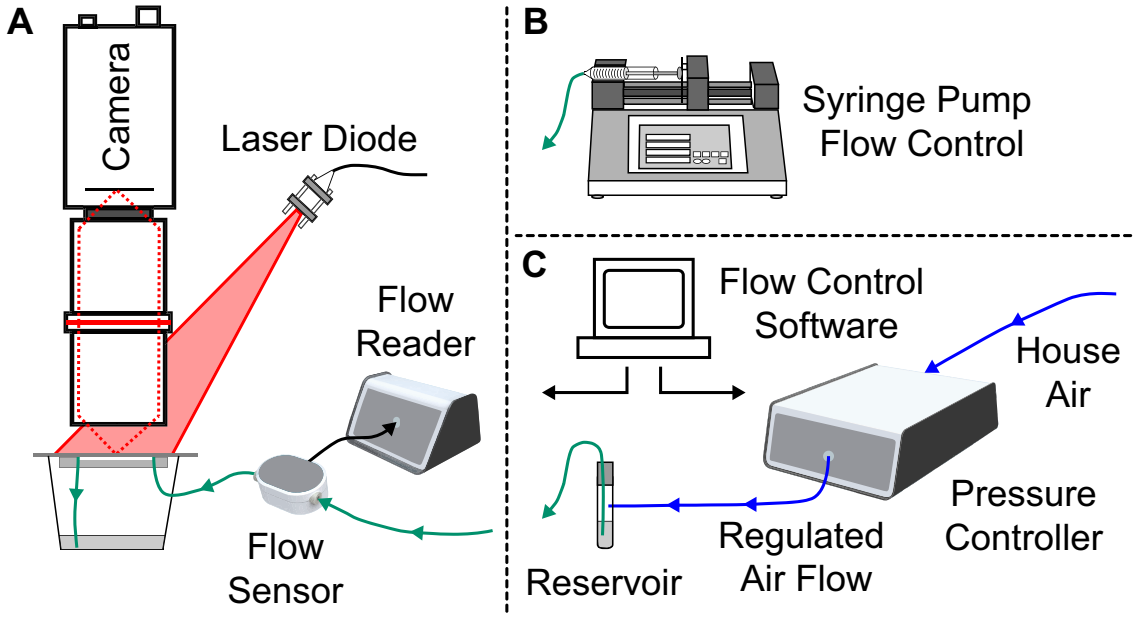

Figure 3.1: (A) LSCI setup schematic for the microfluidic flow assessment study. This is identical to the setup in Figure 2.8. Here, the sample was a microfluidic flow phantom with a 460×460 μm cross-section. A flow sensor was placed in series with the inlet line to the phantom to obtain real-time absolute flow measurements, recorded by the flow reader. (B) The first study connected a syringe pump to the inlet line as the flow control system, using either a 3 mL or 10 mL plastic syringe. (C) The second study used precisely controlled air pressure to deliver flow to the phantom. The system included house air delivery to a pressure controller, followed by regulated air flow to a reservoir which pushes liquid into the inlet line. Flow control software used a feedback loop between the flow readings and the pressure controller to regulate pressure levels in real-time to maintain desired flow levels. Blue lines represent air flow, green lines represent liquid flow, and black lines represent electronic connections.

The microfluidic flow phantom was fabricated using the same general process described for the homogenous tissue phantom in Section 2.2.1. The main difference is that a machined aluminum mold was placed in the plastic petri dish to cast the microchannel within the PDMS-TiO_2 mixture. The metal mold used is shown in Figure 3.2A, where a 1 inch long square extrusion can be seen. The cross-section of the

extrusion is ~460 × 460 μm, which becomes three walls of the microfluidic channel. The last wall is the glass slide, which is used to seal the channel and provide visible access to the flow inside. A square cross-section (1:1 aspect ratio) was desired to match the aspect ratio of the circular cross-section vascular geometries *in vivo*. A photograph of the finished phantom is shown in Figure 3.2B, where the channel is visible inside the white PDMS and the glass slide seals the surface. To flow liquid through the channel, inlet and outlet ports were attached to the side of the phantom using a 23G blunt tip needle fitted partially inside the phantom, making the usable channel length ~20 mm long. The needles were sealed in place with epoxy to form an air-tight seal at the junctions. Then, Tygon microbore tubing (Cole-Parmer Instrument Company LLC, 0.02" inner diameter) was used to connect to the blunt tip as inlet and outlet tubing. The outlet tubing drained into a vial, with the tubing end submerged, and the inlet tubing was connected to the flow sensor and then the flow control system using fluidic fittings with FEP tubing (IDEX Health and Science LLC.).

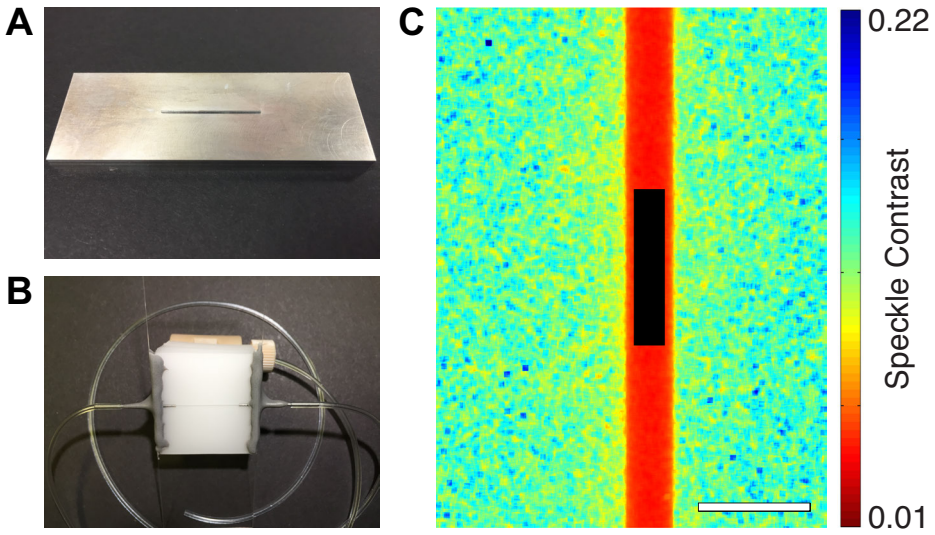

Figure 3.2: (A) Photograph of the machined aluminum mold used to cast the PDMS during fabrication of the microfluidic flow phantom. (B) Photograph of the finished microfluidic flow phantom, showing the PDMS bonded to a glass slide, with inlet and output ports secured using epoxy. Tygon tubing was secured to the inlet and output ports and connected with the rest of the system using fluidic fittings. (C) Representative speckle contrast image averaged over 15 frames showing the channel in red, along with the location of the black ROI used for analysis. Scale bar (white) = 1 mm.

A blood-mimicking colloidal mixture of suspended 1 μm diameter polystyrene microspheres (5100A, Thermo Fisher Scientific Inc.) in ultra-filtered de-ionized water was used in the flow studies. The concentration of microspheres was set to achieve a scattering coefficient $\mu_s = 243$ cm^{-1}, which was chosen to mimic the scattering properties of whole blood. Since polystyrene microspheres have a lower anisotropy than blood ($g = 0.9176$ vs. $g = 0.98$), the reduced scattering coefficient μ_s' was matched to that of flowing blood ($\mu_s' \approx 20$ cm^{-1}), assuming a hematocrit level of 50% and an oxygen saturation of >98% [9]. The corresponding scattering coefficient of the microspheres was derived using the anisotropy of the polystyrene beads and the matched reduced scattering coefficient. The solution of microspheres was freshly mixed before the experiment to

reduce aggregation of particles in the dilution. Before loading the suspension into either the syringes or the pressurized reservoir, the solution was sonicated in a glass vial to fully suspend the particles in solution. The vial was then de-gassed under vacuum to remove any bubbles that could disrupt consistent flow rates.

The blood-mimicking solution was preferred over whole blood because the flow sensor was already factory-calibrated for deionized water flow. Blood plasma is made up of buffering salts and proteins with negligible scattering, making substitution with a water-based scattering solution acceptable. Since the concentration of microspheres was very low (~0.75% by weight in the final suspension), the water calibration of the flow sensor was still valid. To confirm, flow calibration was examined using a high precision scale where the weight change due to a specific flow rate was measured after a known amount of time. Using the density of the solution, the weight was converted to a volume, and then converted to the average flow rate using the time of the trial. These experiments were used to adapt the factory calibration of the flow sensor for the synthetic blood solution.

To investigate the performance of both flow systems, identical flow tests were performed sequentially for comparison. The range of flows examined was 2.4 – 4.8 mm/s, which corresponds to 30.5 – 60.9 μL/min for this channel size. The flow endpoints were examined for a five-minute duration to visualize flow stability over time. The ability to distinguish flow changes was examined using various step sizes of one-minute duration between the two flow endpoints, including 1.2 mm/s steps (i.e. 2.4, 3.6, 4.8 mm/s), 0.4 mm/s steps (7 steps), 0.2 mm/s steps (13 steps), and 0.1 mm/s steps (25 steps). As the step size decreases, the percent change of flow for each step also decreases. For example, 1.2 mm/s step relative to a 2.4 mm/s baseline flow corresponds to a 50% increase in flow, while a 0.1 mm/s step relative to the same baseline

corresponds to a 4.2% increase in flow. Thus, by varying the step size of the flow changes, the sensitivity to incrementally smaller flow changes is investigated. Then, the effect of varying experimental parameters is explored, in particular, the impact of submerging the outlet line in fluid during the flow experiment. Finally, a quantitative assessment of the noise, response time, rise time, and settling time is performed to compare these parameters across both flow control systems.

3.2 Flow Processing and Display

Raw images were converted to speckle contrast using Equation 1.1 with a 7×7 pixel window. By incorporating rapid processing techniques into the custom software [10], the speckle contrast images were computed and displayed in real-time during the procedure. In post-processing after the completion of the experiments, speckle contrast images were converted to correlation time, τ_c, using Equation 1.4, where $T = 0.5$ ms exposure time and $\beta = 1$, which strictly allows computations of relative flow changes. Relative flow was calculated as the inverse correlation time relative to a baseline value, which is given by the ratio of an average baseline τ_c and the τ_c values at all remaining time points (flow = $\tau_{c,\,\text{baseline}} / \tau_{c,\,\text{current}}$) [11, 12]. The baseline was defined as the average τ_c for the ROI over time duration of the middle flow step of the requested flow program. For the constant flow program, this was the average τ_c for the five-minute duration of flow, for either 2.4 mm/s or 4.8 mm/s. For the stepped flow program, this was the average τ_c for the middle flow step, which was always 3.6 mm/s for a one-minute duration. To calculate the average τ_c value across all trials, a standard time range was used in the middle of the programmed step to remove any potential artifacts from the transition toward or away from that particular step. The average flow calculation excluded the first 10 seconds of the first step, since both systems tended to

overshoot the first flow change. For consistency, the average flow calculation also excluded the last 10 seconds of the last step. For any intermediate increment, the average flow excluded 5 seconds on either side of the transition times. To visualize changes in flow, all plots are shown on a relative flow scale normalized to $\tau_{c,\,\text{baseline}}$, where 1 corresponds to baseline flow (100%).

For the flow sensor recordings, all absolute flow values were converted to relative flow values using the same procedure used with the LSCI data for consistency. This allowed side-by-side comparison of the relative flows measured by both systems. Because the flow sensor was recorded on a separate clock relative to the LSCI camera, all flow programs started and ended with 30 seconds of no flow (0 mm/s). The initial rise and final fall of the flow level was used to align the timing signals across both clocks, and was then cropped out for most of the time courses shown in this chapter. For the syringe pump, trigger outputs were used to record the start and stop times of each requested flow step on the same clock as the LSCI camera exposure times using a data acquisition board (NI X-Series DAQ, USB-6341, National Instruments Inc.). For the pressure control system, the initial rise at the start of the program was used to mark the start of the flow program, and all subsequent timing was based off this first rise. After alignment of the flow sensor and LSCI timing signals, the start and end time points of each flow step were extracted to allow calculation of the average flow within each step.

3.3 Syringe Pump Flow Control

To investigate flow control with the syringe pump, the desired profile was programmed into the syringe pump, with both flow rate and time length of each step included. For each syringe size, the inner diameter of the syringe was programmed into the pump to ensure correct flow rate output (3 mL = 8.66 mm diameter,

10 mL = 14.5 mm diameter). Multiple syringe sizes were tested because this is one of the most critical variable selections for syringe pump flow control, and the impact of changing this parameter was investigated. Based on recommendations from the syringe pump manual, the force setting for the syringe pump was set to 50% for the 3 mL syringe, and was set to 100% for the 10 mL syringe. These force settings were used to overcome differing amounts of friction between the rubber plunger and the wall of the syringe, and were recommended settings for non-viscous media with Becton, Dickinson and Company plastic syringes.

The stability of the syringe pump at constant flow rates was investigated at both 2.4 mm/s and 4.8 mm/s for five-minute durations for both 3 mL and 10 mL syringe sizes, shown in Figure 3.3. Here, the red line represents the requested flow program, and shows how the actual recorded flow varied from this value. In all recorded sets, the first result to notice is the clear oscillation around the mean (requested) flow value. The frequency of the oscillation varies with the velocity of the lead screw of the syringe pump required to pump at the desired rate. Thus, looking at both syringe sizes individually, the frequency of the oscillations is higher for the 4.8 mm/s relative to the 2.4 mm/s. Comparing between syringe sizes, the frequency of oscillation is higher for the 3 mL size for both speeds, since the lead screw must rotate at a faster velocity to achieve the desired flow rate for a smaller diameter syringe. These oscillations increase the noise in the flow recording from the syringe pump. Another important result to notice is the excellent agreement between the relative flow measurement between the flow sensor and the LSCI system. This agreement confirms that the oscillations recorded here are real, since they are clearly visualized with two completely separate flow measurement systems. The remarkable agreement also shows real-time, time-resolved validation of the LSCI relative flows with an absolute flow sensor for the first time. The plots show that the shape of

both curves are the same between both recordings, and slight differences in relative flow magnitude between the two curves could be attributed to the fact that the systems are not measuring the flow at the same location in the system.

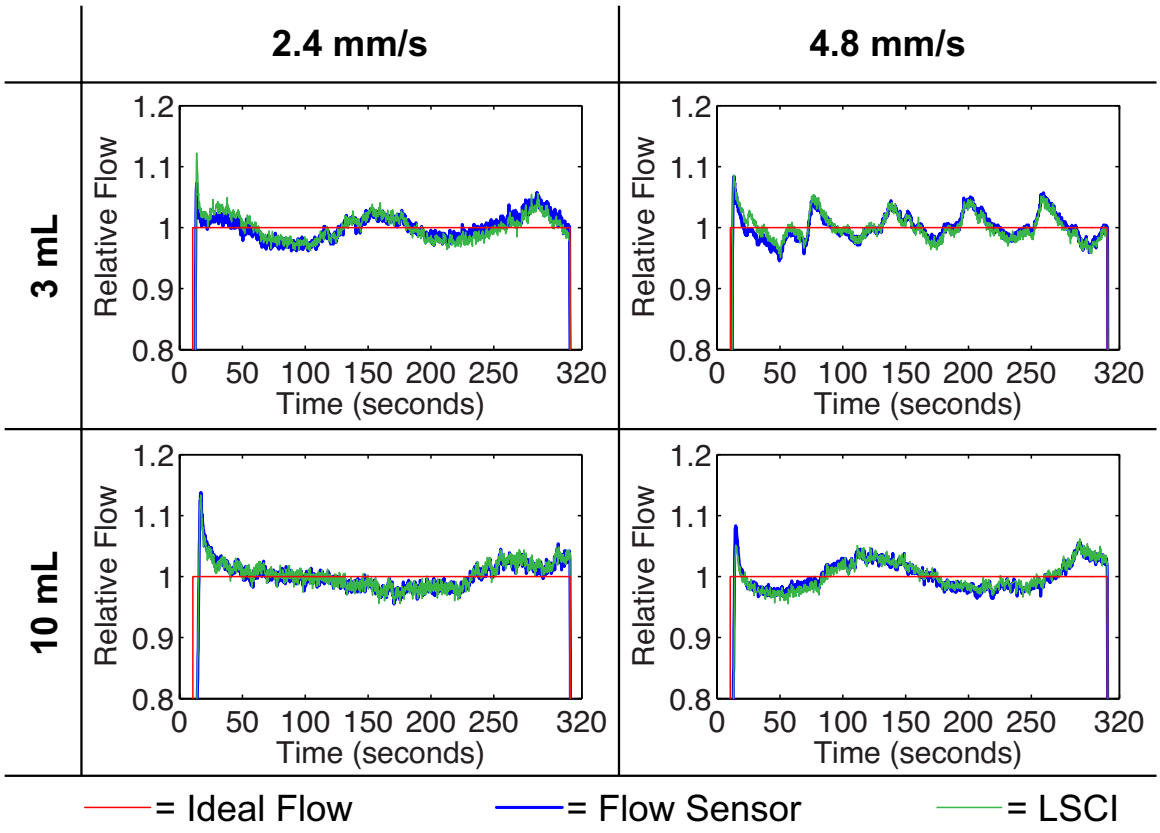

Figure 3.3: Syringe pump controlled constant flow rates at 2.4 mm/s and 4.8 mm/s for five-minute duration with both the 3 mL and 10 mL syringe sizes. The ideal flow in red represents the requested flow program, the flow sensor recording converted to relative flow is shown in blue, and the relative flow from LSCI is shown in green.

Next, the impact of these oscillations on the ability to detect relative flow changes of varying magnitude is investigated with stepped programs of various sizes, with the results for the 3 mL syringe in Figure 3.4 and results for the 10 mL syringe in Figure 3.5. Both sizes show similar results, with flow transitions between the various requested flow

rates easily discernible for the larger increment step sizes, 1.2 mm/s and 0.4 mm/s. However, the flow transitions start to become difficult to distinguish for the 0.2 mm/s step size, especially for the faster flow rates towards the end of the program. This is compounded from both increased frequency of fluctuations as well as decreasing percent change for the same step size as flow rate increases. For the 0.2 mm/s step size, the percent change relative to the average flow at the start (2.4 mm/s) is 8.3% versus 4.2% at the end (4.8 mm/s). Here, the 4.2% is similar to the maximum range of the fluctuations from the baseline seen in Figure 3.3 (average across both syringe sizes: +5.7%, -4.3%), which makes the upper end of this step size difficult to distinguish. For the 0.1 mm/s step size, the flow transitions are undetectable without the guiding red line showing the actual requested flow rate. Here, the percent change decreases from 4.2% to 2.1%, and is well within the noise level of the system fluctuations. Because the 10 mL syringe size has slower frequency oscillations due to its larger size, the shorter duration steps in Figure 3.5 appear more stable relative to the corresponding 3 mL trials. However, the period of oscillations spans multiple steps, which results in larger variation from the actual flow requested (red line) in magnitude. This is because the 10 mL is not always reaching the mean flow value within the one-minute duration of each step, and instead the fluctuations around the mean are visible for the entirety. Overall, these results clearly show that the syringe pump cannot be used to model small changes in flow with accuracy, and only larger step sizes above the noise threshold of the fluctuations can be clearly visualized.

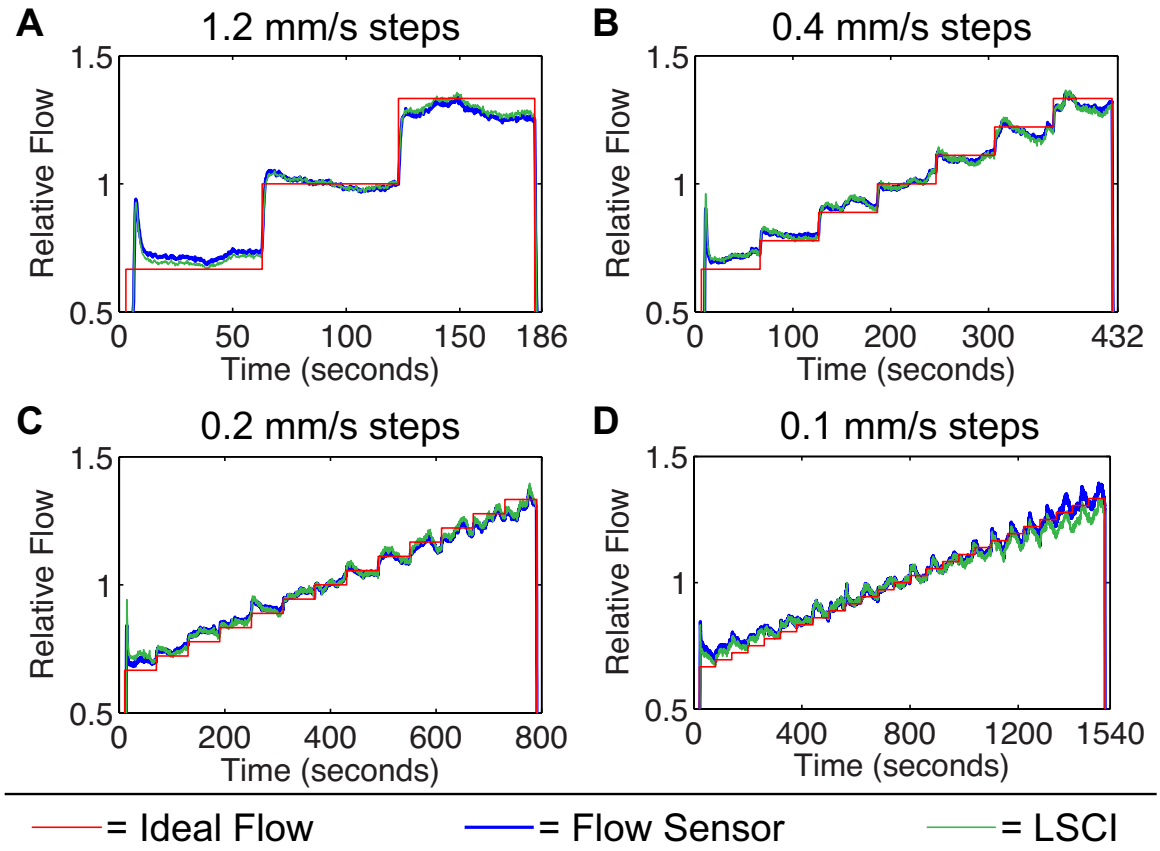

Figure 3.4: Results from the various stepped programs between 2.4 – 4.8 mm/s for the 3 mL syringe, including 1.2 mm/s steps (A), 0.4 mm/s steps (B), 0.2 mm/s steps (C), and 0.1 mm/s steps (D). The flow transitions are clearly discernible for (A, B), less obvious for (C) at the higher flow rates, and undetectable for (D).

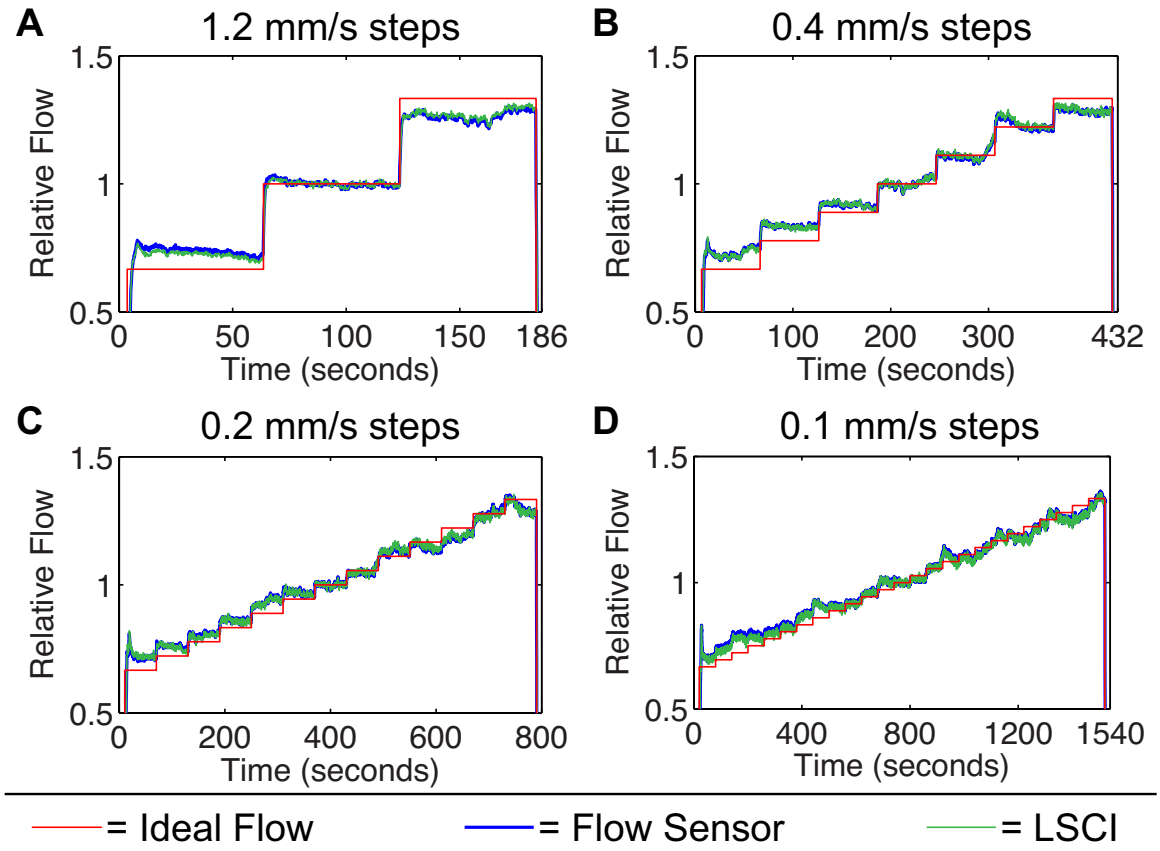

Figure 3.5: Results from the various stepped programs between 2.4 – 4.8 mm/s for the 10 mL syringe, including 1.2 mm/s steps (A), 0.4 mm/s steps (B), 0.2 mm/s steps (C), and 0.1 mm/s steps (D). Similar to the 3 mL results, the flow transitions are clearly discernible for (A, B), less obvious for (C) at the higher flow rates, and undetectable for (D).

Similar to the results from the constant flow experiments, the stepped flow profiles again show excellent agreement between the relative flow measured by the flow sensor versus the LSCI system. The only region with slight discrepancy are the higher flows in Figure 3.4D (0.1 mm/s steps with the 3 mL). Here, the shape of the two curves remains matched throughout, but the magnitude of the LSCI relative flow falls short of the flow sensor recording for the final five flows in the program. Although difficult to pinpoint the exact reason for this discrepancy, the most likely culprit was related to a

difference in the flow in the actual microfluidic channel compared to the flow in the inlet line where the flow sensor recording takes place. This difference could be related to air leakage at the inlet or outlet port of the phantom, despite efforts to ensure an airtight seal. This type of air leakage would manifest as a larger issue during faster flows, which is consistent with the results seen here. However, there is better agreement at faster flow rates for the other step sizes and for the 10 mL syringe size, meaning that the issue for the 3 mL, 0.1 mm/s step size run wasn't consistently observed across all trials. Another possible explanation for the discrepancy is that the 3 mL syringe was refilled with solution immediately prior to the 0.1 mm/s trial, due to the volume of solution required for the program. The solution was not de-gassed again prior to refill, which could have left dissolved air inside the solution. This was not an issue with the 10 mL syringe, since all four stepped programs could be completed without refill due to the higher volume.

3.4 Pressure Regulated Flow Control

To investigate flow control with the pressure system, the desired flow program was setup using the script module for the MAESFLO software (Fluigent Inc.), with both flow rate and time length of each step included. Prior to running the script, a calibration was performed to allow the system to determine the pressure orders required for the system to achieve the desired flow rates in the program, which accounts for the resistance from the tubing, microfluidic channel, and hydrostatic pressure. This calibration was saved and then re-loaded in the script program so that the software could adjust the pressure accordingly for each requested flow. The system used a feedback loop to update the pressure in real-time to account for the actual flow value recorded by the flow sensor. This was important for this study because the hydrostatic pressure changed during the course of the experiment as the reservoir holding the suspension of microspheres was

slowly emptied over the course of the experiment. The software was able to account for this change automatically, as long as the liquid level of the outlet vial was vertically higher than the liquid level of the inlet reservoir. This ensured that there was negative flow at 0 mbar, which allowed the system to apply a positive pressure to achieve 0 μL/min flow. The positive pressure value required for all flow orders simply increased over the course of the experiment as the inlet vial emptied, and was determined automatically by the software.

The stability of the pressure regulated flow control system at constant flow rates was examined at both 2.4 mm/s and 4.8 mm/s for five-minute durations, as shown in Figure 3.6A and 3.6B. Here, after the initial overshoot when flow initially starts, the flow achieves the desired flow rate quickly and maintains a stable flow value throughout the duration of the program, without any noticeable oscillations around the mean value. This improved stability carries over for the stepped programs, where the pressure system is able to clearly resolve relative flow changes of varying magnitude shown in Figure 3.6C – 3.6F. For this flow control system, the flow transitions between steps are easily distinguishable across all step sizes, making this system the preferred choice for visualizing small changes in flow. For this set of results, the agreement between the relative flows measured by the flow sensor versus LSCI is overall very good. The magnitude of the LSCI flow span is slightly less than that measured with the flow sensor, as seen from the starting and finishing steps of the programs, but the shape of both curves are almost identical. Similar to the syringe pump results, the difference in the magnitude may be due to the fact that LSCI was measuring the flow at a different location in the system. Air leakage at the phantom inlet or outlet could have reduced the flow measured by the LSCI system, while leaving the upstream flow inside the flow sensor unaffected.

Despite the minor differences between the LSCI and flow sensor curves, the results from the pressure system clearly demonstrate improved performance over the syringe pump.

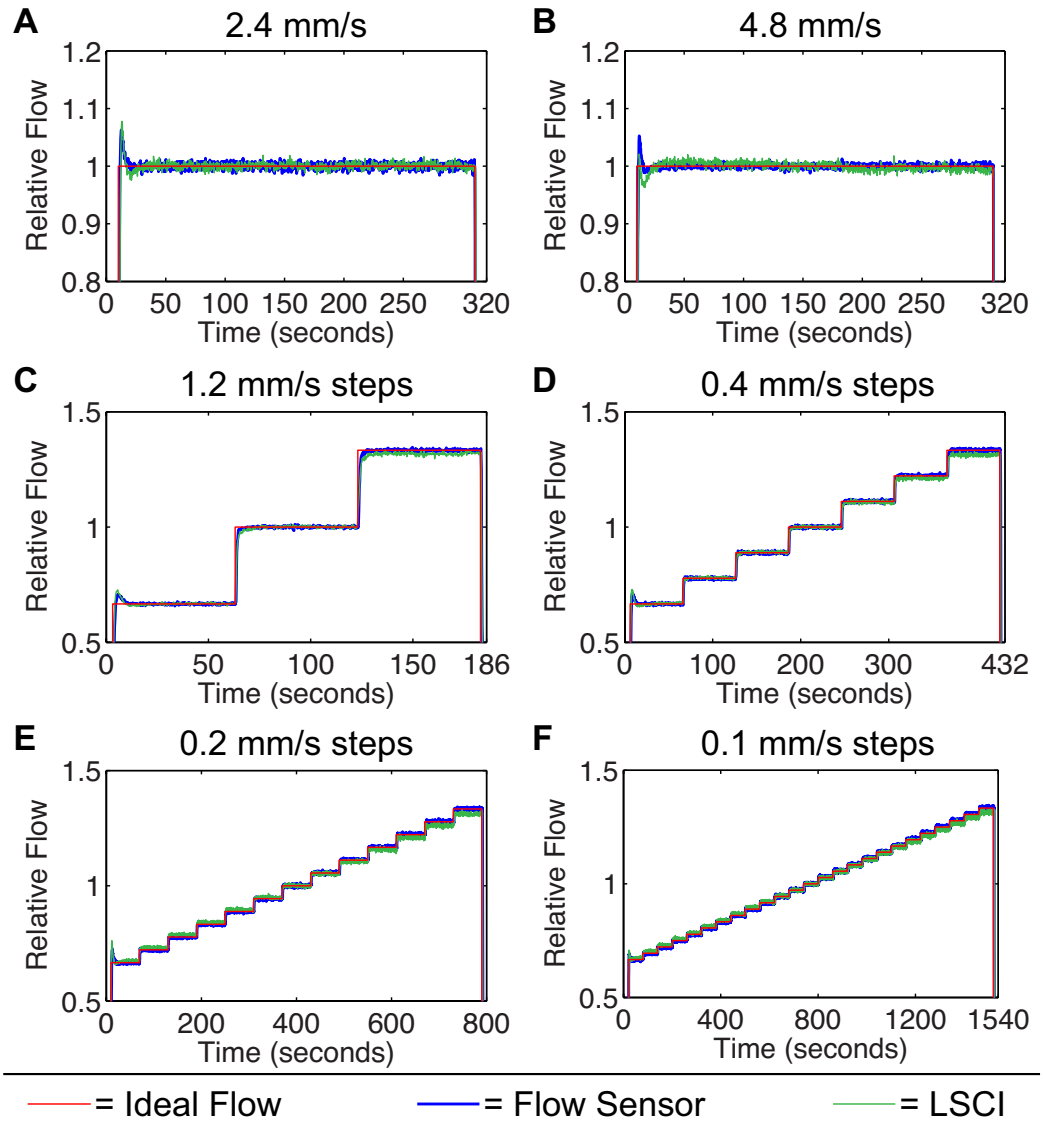

Figure 3.6: Results from pressure regulated flow system for the constant flow experiments at 2.4 mm/s (A) and 4.8 mm/s (B) for five-minute duration, which shows much more stable flow compared to the syringe pump. Results from the various stepped programs between 2.4 – 4.8 mm/s for the pressure system, including 1.2 mm/s steps (C), 0.4 mm/s steps (D), 0.2 mm/s steps (E), and 0.1 mm/s steps (F). Here, all flow transitions can be detected for every program, including the smallest 0.1 mm/s increment.

3.5 DISCUSSION

It is clear from these results the syringe pump is not an ideal flow control system due to its oscillatory behavior and associated higher noise levels. In contrast, the pressure regulated flow control can deliver flow with much more stable flow profiles, enabling visualization of much smaller changes in relative flow. A summary of the results from the various stepped programs is shown in the scatter plots in Figure 3.7, which show the average and standard deviation of the relative flow measured by LSCI plotted against the relative flow measured by the flow sensor. First and foremost, these scatter plots show excellent agreement between LSCI and flow sensor relative flows. It should be noted that this high correspondence would only be observed when the exposure time of the LSCI system is chosen for maximum sensitivity to the range of flows assessed during the experiment. For this study, the exposure time (0.5 ms) was selected for optimal performance with the flow range examined after preliminary studies at various exposure times. In the scatter plots, the only real deviation between LSCI and flow sensor predicted flows are in the 0.1 mm/s increment trial for the 3 mL syringe size. This discrepancy may have resulted from air-leakage or partial blockage in the microfluidic system, which could lead to different flows in different sections of the system where each recording took place (inlet line versus microfluidic channel). The plots also show the disparity in the spacing of the four colors identified by the four step sizes between the syringe pump and the pressure system. For both the 3 mL and 10 mL trials, the data points across all trials fall essentially on the ideal flow line, but the spacing of the points is not uniform across trials or between syringe sizes. This indicates that the syringe pump is not consistently producing the same average flow rate between different trials. In contrast, the pressure system scatter plot shows evenly spaced data points, and overlapping measurements for the flows that were repeated across different increments.

This indicates that the pressure system is reliably and repeatedly producing the same average flow rate every time, and that the system matches up well with the requested flow rates.

The noise levels are also much smaller for the pressure system in comparison to the syringe pump, which was seen visually in the time courses by much more stable flow profiles. The average standard deviation, converted to %, across the 3 mL scatter plot from all four increments is 1.6% for the flow sensor and 1.8% for the LSCI relative flows. For the 10 mL scatter plot, the average standard deviation is 1.2% for both systems, which is consistent with the previous qualitative assessment that the 10 mL stepped programs had less variation per step compared to the 3 mL trials. In contrast, the pressure system has an average standard deviation of 0.4% for the flow sensor and 0.5% for the LSCI relative flows, which is up to 4× improvement relative to the syringe pump system. It should be noted that the average noise levels for both syringe sizes are within the specification from the syringe pump manufacturer, which states that the instantaneous flow should be ±2% from the mean value. The average noise level for the pressure system is within the specification from the manufacturer as well, which indicated that the best stability achievable with this system configuration was ±0.5% from the mean value. The fact that measured noise levels are within system specifications for both systems confirms that the results shown are typical, and represent broad performance differences between the two systems. Although up to 2% noise from the syringe pump does not sound significant, the dynamic view of these fluctuations in the time courses is more telling than the numerical average noise level. Overall, the pressure system is clearly the preferred method for flow control with the greatest stability, accuracy, and repeatability.

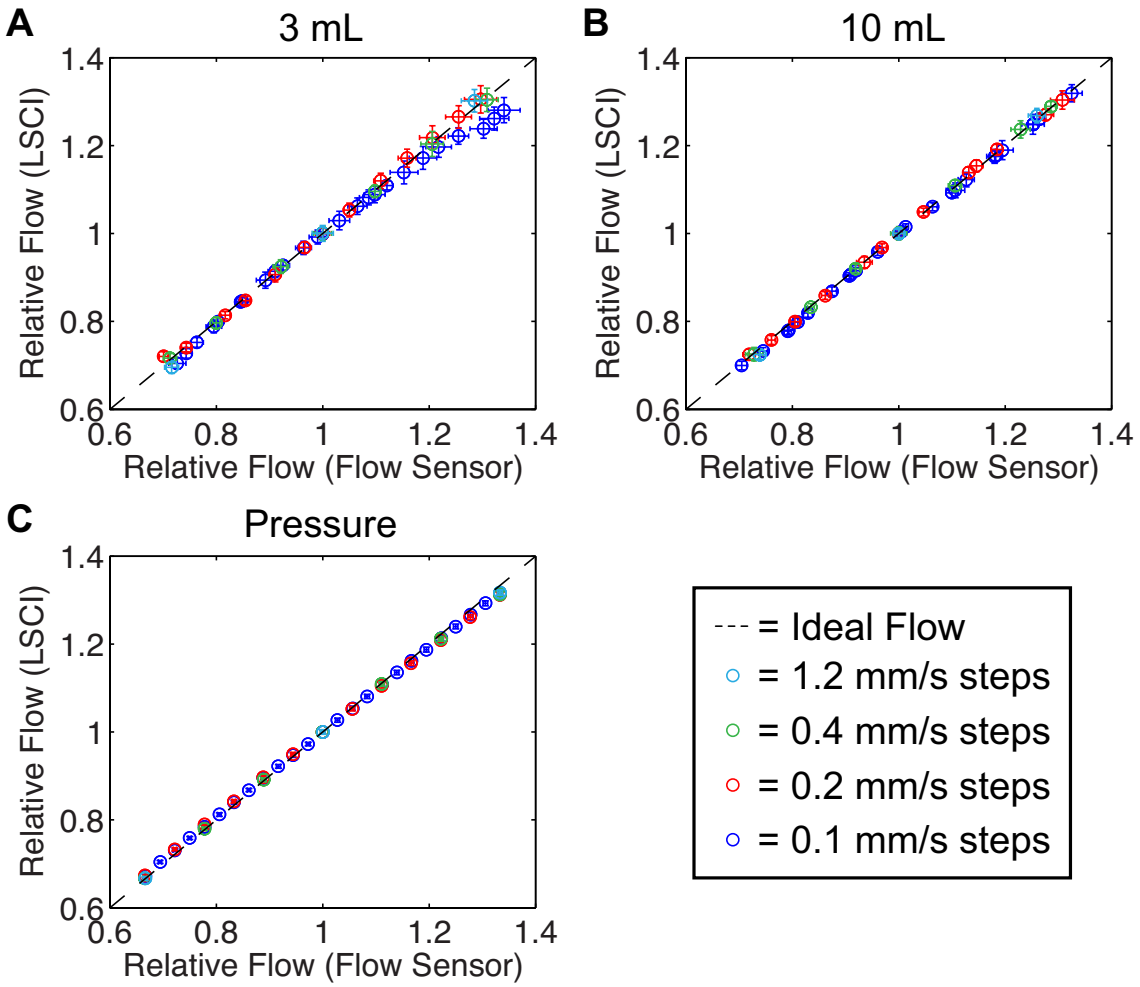

Figure 3.7: Scatter plots showing the LSCI relative flow agreement with both the flow sensor and requested (ideal) flow for each of the stepped programs shown for (A) the 3 mL syringe size from Figure 3.4, (B) the 10 mL syringe size from Figure 3.5, and (C) the pressure regulated flow control from Figure 3.6C – 3.6F. Each data point represents the average and standard deviation of a single flow step (3 steps for 1.2 mm/s increments, 7 steps for 0.4 mm/s increments, 13 for 0.2 mm/s increments, and 25 for 0.1 mm/s increments). Similar to previous figures, 3.6 mm/s was used as a baseline across all sets.

In addition to differences in stability, the two flow systems have a wide disparity in responsivity to a requested flow change. In the microfluidics community, this is usually quantified in terms of three parameters: response time, rise time, and settling

time. An illustration of these three parameters for the 2.4 mm/s constant flow rate trials across both systems is shown in Figure 3.8. The response time is the time it takes for the system to react to a command, in this case to start increasing the flow after the initial request (start trigger). Here, the cutoff point for the flow increase is defined as 10% of the difference between the requested flow and the current flow. The difference between flow rate levels is used rather than absolute calculations from the requested flow alone to make the definition more universally applicable, even for the stepped programs where flow does not always start at 0 mm/s. The rise time is the time it takes for the system to change from the requested flow to the current flow. Again, this is defined by the cutoff endpoints between 10% and 90% of the difference between the requested and current flow rates. Finally, the settling time is the time it takes for the system to reach and stay within a specified error margin of the requested flow rate from the initial start trigger. For this study, a criterion of ±6.5% of the requested flow rate was used to ensure reasonable settling times across both flow control systems. The settling time represents how long it takes for the system to achieve a stable flow rate at the newly requested flow level. For all parameters, shorter times represent better system responsivity, and are preferable for resolving rapid flow changes with better temporal accuracy. As shown by Figure 3.8, the overall responsivity of the system was the slowest for the 10 mL syringe size, improved with the 3 mL syringe size, and finally was the fastest for the pressure system. A summary of the individual numerical values for the three parameters shown in Figure 3.8 is included in Table 3.1, and a summary for the first flow rise across the entire study is included in Figure 3.9. This data includes all four stepped programs (0 – 2.4 mm/s) as well as both constant flow trials (0 – 2.4 and 0 – 4.8 mm/s). This data confirms that the same responsivity trends visible in the representative trial shown in Figure 3.8 and Table 3.1 holds across all trials performed in this study. This confirms

that the pressure system is preferable for superior responsivity across all trials, and provides the most temporally accurate representation of the requested flow change. If a syringe pump system must be used, the smaller syringe size is preferred for better responsivity.

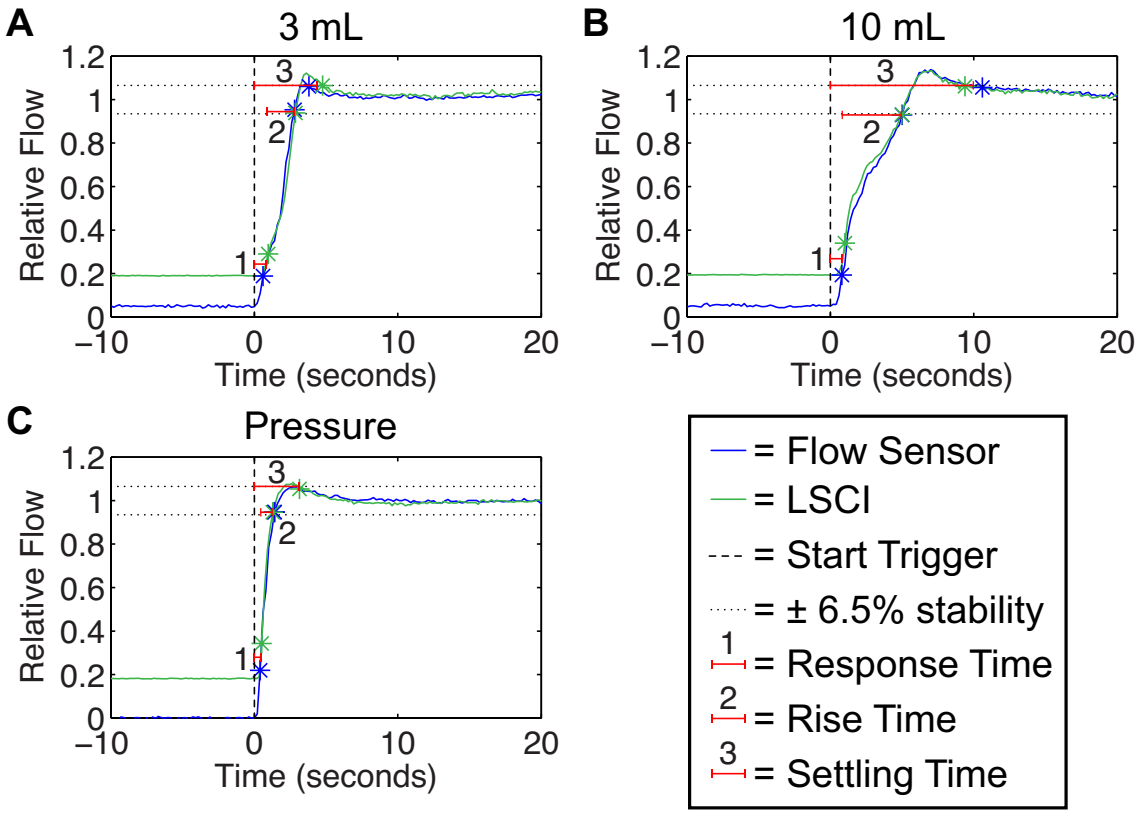

Figure 3.8: Zoomed view of the initial flow increase for the 2.4 mm/s constant flow trial for (A) the 3 mL syringe, (B) the 10 mL syringe, and (C) the pressure system. The curves are annotated to show the location of the start trigger where the flow change was requested, the criteria for the settling time (±6.5%), and illustrative definitions (red lines) for the response time (1), rise time (2), and settling time (3). The blue and green stars show the actual endpoints for (1), (2), and (3) for both the flow sensor and LSCI relative flow curves, respectively.

Table 3.1: A summary of the response time (1), rise time (2), and settling time (3) corresponding with the plots shown in Figure 3.8 for the 2.4 mm/s constant flow trials. The cutoff endpoints for each parameter are given for reference. FS = flow sensor, all times listed in seconds.

	Response Time (start trigger to 10%)		**Rise Time** (10% – 90%)		**Settling Time** (start trigger to ±6.5%)	
System	*FS*	*LSCI*	*FS*	*LSCI*	*FS*	*LSCI*
Pressure	0.4	1.114	1.0	0.771	1.4	3.748
3 mL size	0.6	0.969	2.2	1.892	3.8	4.761
10 mL size	0.8	1.009	4.2	3.975	10.6	9.384

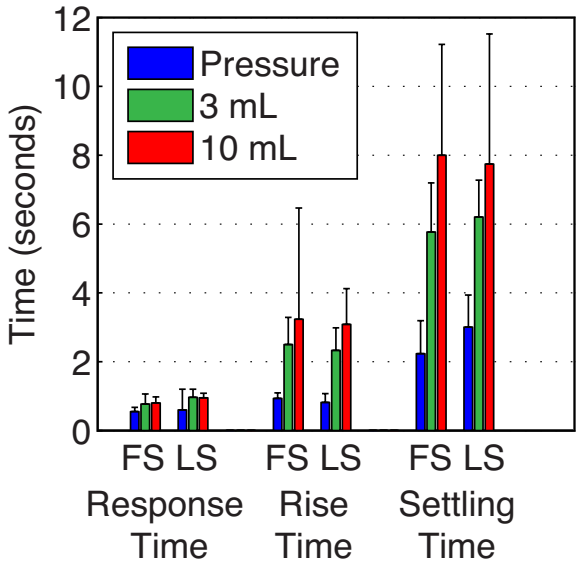

Figure 3.9: A summary of the response time, rise time, and settling time for the first flow rise across the entire study (average and standard deviation, N = 6 total trials). The trends are similar to those shown in the representative data from a single trial in Figure 3.8 and Table 3.1.

One important experimental detail that all previous plots took into account was recording the flow profiles while the outlet tubing from the phantom was submerged in solution, shown in Figure 3.1A. This was performed after visualizing the dramatic decrease in flow observed when the outlet line was elevated and the solution dripped into

the outlet vial. The release of the drop from the end of the tubing caused a large decrease in pressure, resulting in a flow decrease. This was observed with both flow control systems as shown in Figure 3.10, meaning that it is an important experimental consideration for any microfluidic setup. These trials included approximately five-minute duration with the outlet line elevated and allowed to drip into the outlet vial, followed by submersion of the outlet line in the solution for another five minutes. Thus, the large spike in relative flow corresponds to the time point where the outlet line was manually submerged in solution. Some general trends were observed from these trials. First, the magnitude of the flow decrease was larger for the syringe pump versus the pressure system. The main reason for this difference is that the pressure system has a higher compliance than the syringe pump. Therefore, high frequency perturbation, such as the release of a drop from the outlet, will be dampened more by the pressure system. Also, the frequency of the droplets was very regular within trials. This suggests that the drop reaches a similar critical volume regardless of flow rate before the size of the drop is large enough to overcome the surface tension required to release the drop from the tubing. The mean volume of the droplets can be estimated using the absolute flow rate from the flow sensor and the time between drops, and a standard deviation of $<0.5\ \mu L$ in drop volume was observed within each trial. Finally, the magnitude of the flow decrease was larger for the slower flow at 2.4 mm/s versus the faster flow 4.8 mm/s for all trials. This is likely due to the larger pressure differential generated at slower flows, since the pressure driving the flow is smaller for the slower speed. Overall, these plots demonstrate that the user should be aware of the position of the outlet line during microfluidic data acquisition, and that submersion of the outlet line is critical to eliminate rapid flow changes caused by dripping from the outlet line.

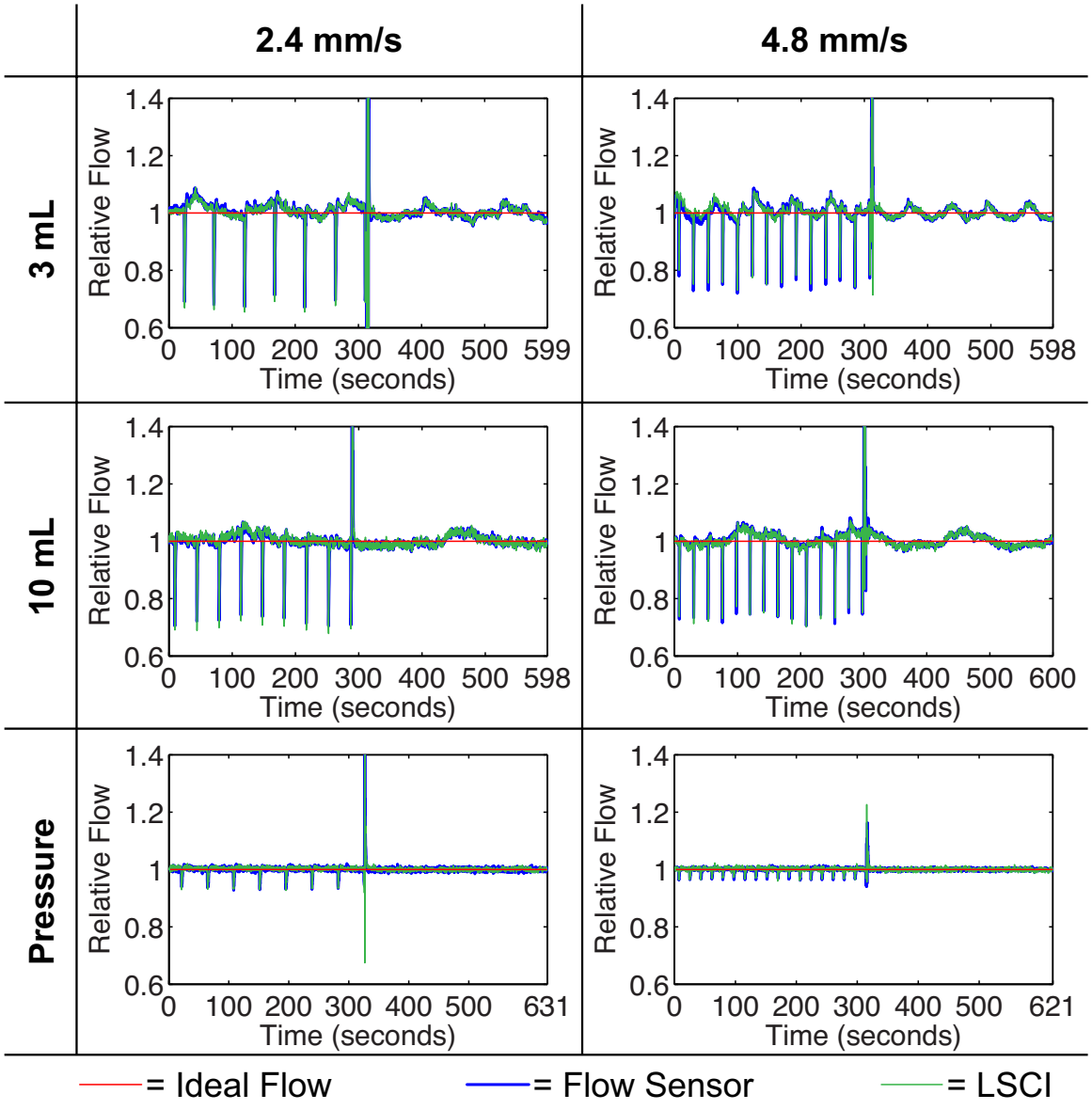

Figure 3.10: Impact of submerging the outlet tubing after the phantom, shown for both flow control systems at 2.4 mm/s and 4.8 mm/s. These trials show approximately five-minute duration of the outlet tubing dripping into the outlet vial (seen by rapid flow drops), followed by five-minute duration of the outlet tubing submerged in solution.

Overall, the pressure regulation system is superior to the syringe pump flow control system both in terms of improved stability and responsivity. However, two

disadvantages related to the pressure regulation system are its increased cost and difficulty of use in comparison to the syringe pump. The pressure regulation system used in this study was on the order of $7K, which is ~3.5× more expensive than the syringe pump model used in this study. Although there is high price variation for both types of systems depending on the vendor and specifications, the pressure regulation system tends to be more expensive. The pressure regulation system also cannot compete with the ease of use of the syringe pump, which is one of the reasons why syringe pumps are still very popular in the microfluidics community. Syringe pumps simply require filling a syringe with the solution, securing it to the pump, and programming the desired flow rate via the touchscreen. Overall, setup can be performed very quickly and without too much room for error. With the pressure regulation system, many more setup steps are involved, and much greater care must be taken to achieve performance within the specification of the device. For example, tubing lengths must be designed to achieve a certain resistance in the system such that the desired flow range (0 – 60.9 μL/min) spans the available pressure range of the system (0 – 69 mbar). This maximizes the pressure resolution within the flow range of interest to ensure maximum stability can be achieved. Also, fluidic fittings are required for connecting all system components (reservoir → flow sensor → phantom inlet). An improperly secured fitting can lead to air-leakage and reduced stability, which can be difficult to diagnose when there are 3+ connections in the system. Overall, the pressure system setup is more tedious and has much greater potential for error, which can lead to an even larger time-delay.

3.6 CONCLUSIONS

The results from these microfluidic studies demonstrate that proper choice in flow control system is critical for generating truly controlled flow profiles with high accuracy

and repeatability. The commonly used syringe pump produces flow oscillations with up to 1.8% average noise, has poor repeatability across trials, and has slow responsivity to a requested change in flow. These qualities make syringe pumps a poor choice for characterizing LSCI hardware. This study also demonstrated that LSCI has excellent relative flow agreement with a mass flow sensor. This is significant as a standalone result, and also means that LSCI picks up all dynamics of the flow generation system. Thus, all unwanted flow variations from the syringe pump flow control contributes to noise in the LSCI flow recording, making it harder to assess the performance of the instrumentation. A pressure regulated flow control system overcomes all of the limitations of the syringe pump with 4× improved stability, excellent repeatability, and 3 – 4× faster responsivity depending on the syringe size. The improved stability and responsivity enables characterization of the true LSCI hardware performance in terms of accuracy and sensitivity to small changes in flow. The improved repeatability enables multiple repeated hardware tests across a broad range of camera and laser specifications. Overall, the pressure regulated flow control system is the optimal choice for best performance in any microfluidic study, and provides a reliable controlled flow system for LSCI system characterization.

3.7 REFERENCES

[1] A. B. Parthasarathy, W. J. Tom, A. Gopal, X. J. Zhang, and A. K. Dunn, "Robust flow measurement with multi-exposure speckle imaging," *Optics Express,* **16**(3), pp. 1975-1989 (2008).

[2] B. Choi, N. M. Kang, and J. S. Nelson, "Laser speckle imaging for monitoring blood flow dynamics in the in vivo rodent dorsal skin fold model," *Microvascular Research,* **68**(2), pp. 143-146 (2004).

[3] P. Miao, Z. Chao, Y. Zhang, N. Li, and N. V. Thakor, "Entropy analysis reveals a simple linear relation between laser speckle and blood flow," *Optics Letters,* **39**(13), pp. 3907-3910 (2014).

[4] M. Tomita, T. Osada, I. Schiszler, Y. Tomita, M. Unekawa, H. Toriumi, N. Tanahashi, and N. Suzuki, "Automated method for tracking vast numbers of FITC-labeled RBCs in microvessels of rat brain in vivo using a high-speed confocal microscope system," *Microcirculation,* **15**(2), pp. 163-174 (2008).

[5] P. M. Korczyk, O. Cybulski, S. Makulska, and P. Garstecki, "Effects of unsteadiness of the rates of flow on the dynamics of formation of droplets in microfluidic systems," *Lab on a Chip,* **11**(1), pp. 173-175 (2011).

[6] Z. Li, S. Y. Mak, A. Sauret, and H. C. Shum, "Syringe-pump-induced fluctuation in all-aqueous microfluidic system implications for flow rate accuracy," *Lab on a Chip,* **14**(4), pp. 744-749 (2014).

[7] J. Zhou, K. Ren, W. Dai, Y. Zhao, D. Ryan, and H. Wu, "Pumping-induced perturbation of flow in microfluidic channels and its implications for on-chip cell culture," *Lab on a Chip,* **11**(13), pp. 2288-2294 (2011).

[8] Y. J. Kang and S. Yang, "Fluidic low pass filter for hydrodynamic flow stabilization in microfluidic environments," *Lab on a Chip,* **12**(10), pp. 1881-1889 (2012).

[9] A. Roggan, M. Friebel, K. Dörschel, A. Hahn, and G. Müller, "Optical Properties of Circulating Human Blood in the Wavelength Range 400-2500 nm," *Journal of Biomedical Optics,* **4**(1), pp. 36-46 (1999).

[10] W. J. Tom, A. Ponticorvo, and A. K. Dunn, "Efficient processing of laser speckle contrast images," *IEEE Transactions on Medical Imaging,* **27**(12), pp. 1728-1738 (2008).

[11] A. K. Dunn, H. Bolay, M. A. Moskowitz, and D. A. Boas, "Dynamic imaging of cerebral blood flow using laser speckle," *Journal of Cerebral Blood Flow & Metabolism,* **21**(3), pp. 195-201 (2001).

[12] C. Ayata, A. K. Dunn, Y. Gursoy-Özdemir, Z. Huang, D. A. Boas, and M. A. Moskowitz, "Laser speckle flowmetry for the study of cerebrovascular physiology in normal and ischemic mouse cortex," *Journal of Cerebral Blood Flow & Metabolism,* **24**(7), pp. 744-755 (2004).

Chapter 4: LSCI Camera Comparison[1]

Because of the large number of camera specifications, there are wide variations in camera choice for LSCI by researchers across the field. LSCI studies include a range from cost-effective 8-bit CMOS or CCD sensors [1-3] to expensive cooled CCD cameras, including 12-bit [4-6], 16-bit [7-9], and even 14-bit electron multiplying (EM-) CCD cameras [10, 11]. Some of these studies perform combined LSCI with other imaging techniques, such as fluorescence imaging [5, 11], which may be the driving force for the camera choice. However, most other studies that perform LSCI alone provide little justification for their camera selection.

This chapter performs two paired camera comparisons to assess a wide range of camera specifications that are expected to be most important in an LSCI setting. An 8-bit, 150 fps CCD camera was used as a reference camera in each study ($2000). The first simultaneous comparison was against a low-cost webcam (Section 4.1), which was an 8-bit, 5 fps color CMOS sensor ($35). This study compares monochrome versus color sensors, as well as performance of a low-cost camera sensor. A complete low-cost system was also evaluated to demonstrate that LSCI can be performed with very inexpensive components (Section 4.2). The second simultaneous comparison was against a high performance, back-illuminated EM-CCD camera (Section 4.3), which was a costly

[1] Portions of this chapter (Section 4.1 and 4.2) were adapted from: L. M. Richards, S. M. S. Kazmi, J. L. Davis, K. E. Olin, and A. K. Dunn, "Low-cost laser speckle contrast imaging of blood flow using a webcam," *Biomedical Optics Express,* **4**(10), pp. 2269-2283 (2013). L. M. R. built the imaging system, performed the experiments, analyzed the results, and wrote the manuscript. S. M. S. K. fabricated the 200 μm microfluidic phantom and performed the animal surgery. J. L. D. adapted the webcam for LSCI and developed software to acquire the webcam images. K. E. O. performed speckle size measurements with the tandem-lens imaging system to determine how to properly set the *f*/# for this study. A. K. D. conceived and supervised the project. All authors contributed to manuscript revisions.

16-bit, 30 fps sensor ($30K). This study compares bit depth and frame rate, as well as the impact of spatial and temporal averaging.

4.1 WEBCAM STUDY (8-BIT, COLOR CMOS, 5 FPS, $35)

Because the webcam is a color sensor, a brief introduction to the differences between color and monochrome sensors is provided. Color camera sensors are commonly used in a clinical setting, including surgical microscopes and endoscopy systems. Color visualization is usually more intuitive for the clinician and may even be critical for the procedure. Thus, demonstrating that LSCI can be performed in color cameras could make it easier for medical device companies to add-on LSCI to existing systems.

The full color spectrum is created from the additive mixing of the three primary colors: red (R), green (G), and blue (B). There are two main types of color cameras: single chip systems that consist of a color filter array on top of the sensor and three chip systems (3CCD) that image each primary color onto a different sensor using a prism setup. Single chip color sensors have individual R, G, or B color filters on top of each pixel to make each pixel most sensitive to one of the primary colors. The layout of this filter pattern varies between manufacturers, and may consist of stripes where each pixel column has a different color filter or mosaics where each 2×2 pixel region has one of each primary color filter. The latter filter arrangement is known as the Bayer matrix. For both pattern arrangements, there are usually twice as many green filters relative to red and blue filters (typically R:G:B = 1:2:1), since the human visual system is most sensitive to green light [12]. A demosaicking algorithm is used to interpolate an R, G, and B value for each individual pixel (3D matrix). The algorithm depends on the arrangement of the color filter pattern and the spectral content of the illumination source. Many

manufacturers have developed proprietary interpolation algorithms and sophisticated image processing routines to reduce color aliasing and improve color accuracy, each claiming to provide the "best" image quality [12]. Three chip systems avoid the issue of interpolation by imaging R, G, and B intensity values on three separate sensors, where a prism is used to direct each wavelength region to the appropriate sensor using coatings and color filters [12]. Since each pixel has separately measured R, G, and B values, more accurate color representation is possible. Because of high cost, 3CCD systems are used where high quality color visualization is required (often for medical imaging applications) while single chip sensors are used for low-cost, consumer applications.

Webcams are single-chip color sensors with a Bayer filter arrangement. By default, webcams are designed to stream video in RGB color mode using a manufacturer-specific interpolation algorithm. The webcam sensor used in this study also allowed streaming of the raw Bayer data, which provides a 1D matrix containing the brightness of each individual pixel. Both operating modes were tested in this study, with the red color plane used for color mode and the red-filtered pixels used for Bayer mode during calculation of the speckle contrast values. Because of the arrangement of the Bayer matrix of filters on the webcam sensor, Bayer mode effectively reduces the number of pixels by 75%, but this mode provides pixel intensity values that closely match the measurement provided by traditional monochrome cameras. Figure 4.1 shows an illustration of RGB color mode versus Bayer mode data extraction, as well as the pixels used for speckle contrast calculation in each mode.

Recently, a consumer-grade color camera (digital single-lens reflex, or dSLR) was used to perform LSCI and was shown to provide similar maps of blood flow relative to a scientific-grade monochrome camera [13]. The main differences in this study are the price of the color sensor ($35 versus ~$2000) and the bit depth (8-bit versus 14-bit). In

this section, a webcam was evaluated as a potential camera sensor for imaging flow in an *in vitro* phantom as well as *in vivo* in a mouse cerebral cortex by directly comparing images recorded simultaneously from a high performance monochrome CCD camera.

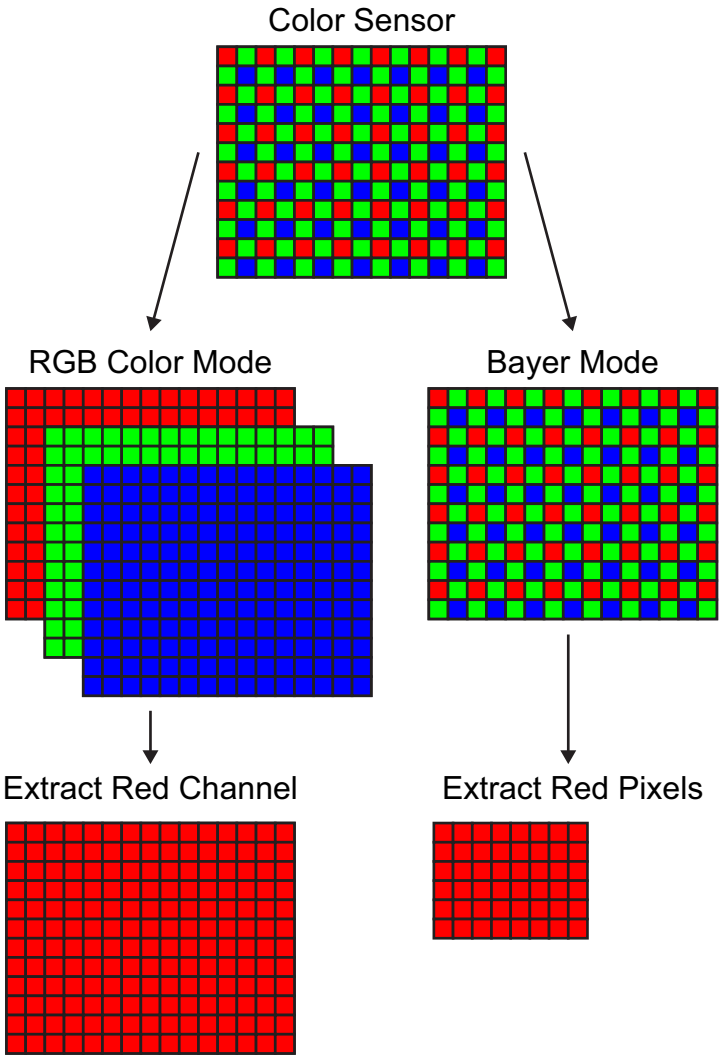

Figure 4.1: Schematic of a color camera sensor with a Bayer filter matrix. Two image acquisition modes are possible: RGB color mode, where an R, G, and B color value is extracted for each individual pixel, and Bayer Mode, where the raw intensity for each pixel is saved. For calculation of the speckle contrast, only the red channel is used for RGB color mode, and only the red filtered pixels are used for Bayer mode.

4.1.1 Instrumentation

To validate that low-cost camera sensors can be used for LSCI, a two-camera setup was used to allow simultaneous imaging with a monochrome CCD camera (Basler Pilot piA640-210gm, Basler AG, $2000) and a color webcam (Webcam C500, Logitech Inc., $35). A schematic of the two-camera setup is shown in Figure 4.2A. The imaging optics were the same as previous studies in Chapters 2 and 3, with the addition of a 50:50 beamsplitter (BSW30, Thorlabs Inc.) in between the first and second lens to split the light between two camera arms. The webcam sensor was disassembled from its housing and the wide-field lens was removed and replaced with an S-mount lens holder (PT-LH010M, M12 Lenses Inc.). An S-mount to C-mount adapter (63-974, Edmund Optics Inc.) was used to connect with the imaging optics. Once again, using camera lenses (Nikon Inc., AF-Nikkor, $f = 50$ mm) provided high light collection efficiency [14] and allowed individual control of the *f*/# for each camera arm. For this setup, the *f*/# was controlled using the lens closest to the camera, and the aperture on the common lens closest to the sample was left all the way open (*f*/# = 1.8). A 660 nm, 120 mW laser diode (ML101J27, Thorlabs Inc.) was mounted in a temperature-controlled housing (LDM21, Thorlabs Inc.) and expanded using an aspheric lens to evenly illuminate the sample. This laser diode model was the older version of the traditional diode HL6545MG studied in Chapter 2, and had the same specifications. For the animal study, a 532 nm laser (AixiZ LLC, 200 mW) was used in combination with Rose Bengal to induce a localized occlusion in a photothrombotic stroke model. The green laser was attenuated using neutral density filters so that ~14 mW reached the tissue surface. A long focal length plano-convex lens was used to focus the beam to a small spot on the imaging field of view. To reduce the green light that reached the camera sensors, a red filter (Edmund Optics Inc., R-60 Long pass filter, 2") was placed in front of the first lens.

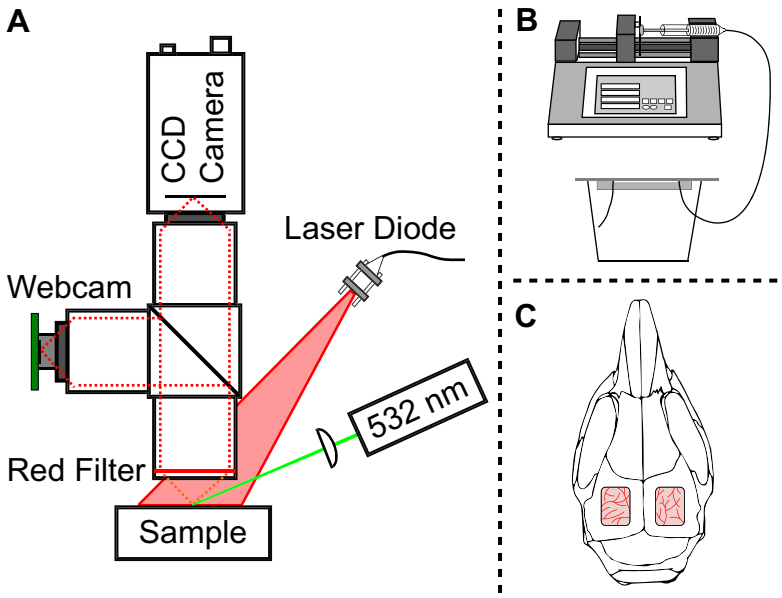

Figure 4.2: (A) Schematic of the two-camera setup for simultaneous LSCI with a CCD camera and a webcam using traditional optics and illumination components. A 50-50 beamsplitter separated the light between the two imaging arms. The 532 nm laser was only used for the animal study. (B) A microfluidic flow phantom was used for *in vitro* validation and different flow levels were controlled using a syringe pump. (C) *In vivo* validation was performed using a mouse prepared with bi-lateral cranial windows. Adapted from [15].

The speckle size was matched as closely as possible between the two cameras to provide a fair comparison. Similar to previous studies, a speckle size ≥1 pixel size was desired, since this was achievable using the low-cost setup described in Section 4.2. The pixel size for the webcam CMOS sensor was calculated to be 2.8 μm, and the pixel size for the CCD camera was 7.4 μm. Thus, for the visible diode used in this study, the webcam arm required an *f*/# of 4 for a speckle size of ~1.15 pixels, while the CCD arm required an *f*/# of 11 for a speckle size of ~1.20 pixels.

Each camera was controlled using a separate computer using custom software. The CCD camera was controlled using the Basler Pylon API (Basler AG), while the webcam was controlled using the NI IMAQdx library (National Instruments, Inc.). By

integrating the source code from freely available software from Logitech (bayer.exe) into the custom software, the webcam could be easily switched between color and Bayer modes. The custom software was modified to allow correct computation of the speckle contrast values for the webcam in both color mode (using the red color plane) and Bayer modes (using only the red filtered pixels) for live display during acquisition.

4.1.2 Image Display and Analysis

Raw images were converted to speckle contrast using Equation 1.1 with a 7×7 pixel window. By incorporating rapid processing techniques into the custom software [16], the speckle contrast images were computed and displayed in real-time during the procedure for both cameras. In this chapter, images are displayed as speckle contrast images, since these represent an instantaneous map of flow, and were averaged over 10 frames.

In post-processing after the completion of the experiments, speckle contrast images were converted to correlation time, τ_c, using Equation 1.4, where $T = 5$ ms exposure time and $\beta = 1$, which strictly allows computations of relative blood flow changes within patients. For this study, relative flow was calculated as the inverse correlation time relative to a baseline value, which is given by the ratio of an average baseline τ_c and the τ_c values at all remaining time points ($\text{flow} = \tau_{c,\,\text{baseline}} / \tau_{c,\,\text{current}}$) [17, 18]. For the microfluidic study, the baseline was defined as the average τ_c value for the ROI over time duration of one of the middle flow values investigated. For the *in vivo* study, the baseline was defined as the average τ_c over ~5 seconds at the start of acquisition for each individual ROIs analyzed. To visualize changes in blood flow, the deviation in CBF from a baseline value is used, $\%\Delta$, which allows easy visualization of flow changes relative to a baseline value.

4.1.3 Microfluidic Study

A microfluidic flow phantom was fabricated using the same general process described in Section 2.2.1 and Section 3.1 for *in vitro* validation, shown in Figure 4.2B. For this study, a patterned silicon wafer fabricated using photo-lithography techniques served as the mold for the channel [19, 20]. The cross-section of the silicon extrusion was ~200 × 200 μm, which became three walls of the smaller dimension microfluidic channel. Because of the smaller channel size, inlet and outlet holes were punched through bottom of the cured PDMS with a blunt tip needle before bonding to the glass slide to seal the channel. PTFE tubing was then inserted into the pre-punched holes and secured to the phantom using room temperature vulcanizing (RTV) silicone for inlet and outlet connections.

Because this camera comparison was performed before the microfluidic flow control assessment performed in Chapter 3, this microfluidic study was performed using the syringe pump. However, this study does not attempt to visualize small flow changes or transient flow dynamics, which means that the use of the syringe pump should not affect the accuracy of the results of this study. Thus, the microfluidic phantom was connected to the same syringe pump from Chapter 3 (74905-04, Cole-Parmer Instrument Company LLC) using the PTFE tubing secured to the phantom and a 1 mL plastic syringe (Becton, Dickinson and Company) held the same suspension of microspheres described in Section 3.1. The solution was pumped through the microfluidic channel at controlled rates from 1 – 10 mm/s in 1 mm/s increments using the syringe pump.

Images were recorded for 3 minutes, starting 30 seconds after starting each flow rate, and the average and standard deviation over this time period were used for assessment. Images were recorded sequentially using both color mode and Bayer mode for comparison. A neutral density filter was placed in front of one of the cameras to

match the raw image histogram peak within 10 intensity counts (histogram range = 255). The neutral density filter was placed in front of the webcam during color mode (optical density = 0.6, webcam peak = 125, CCD peak = 120) and in front of the CCD during Bayer mode (optical density = 0.3, webcam peak = 45, CCD peak = 50). Because the two camera sensors had different detection thresholds (CCD dark counts = 0, webcam dark counts = 15), the image averages (histogram peak) were matched so that the spread of the histogram was above the detection threshold.

Representative speckle contrast images from the microfluidic study are shown in Figure 4.3. The speckle contrast images serve as flow maps, where red regions correspond to faster flow (low K) and blue regions correspond to slower flow (high K). In these images, the red region corresponds to the location of the microfluidic channel within the phantom, and the surrounding area is static PDMS with scattering. The ROIs used for subsequent analysis are shown in black. The webcam images acquired in Color mode have a different visual appearance than those acquired in Bayer mode, which appears more similar to the images acquired from the CCD. Thus, the Color mode image is shown on a separate color bar, while both the Bayer mode and CCD images are shown on the same color bar. Image profiles are shown to allow quantitative comparisons between the cameras.

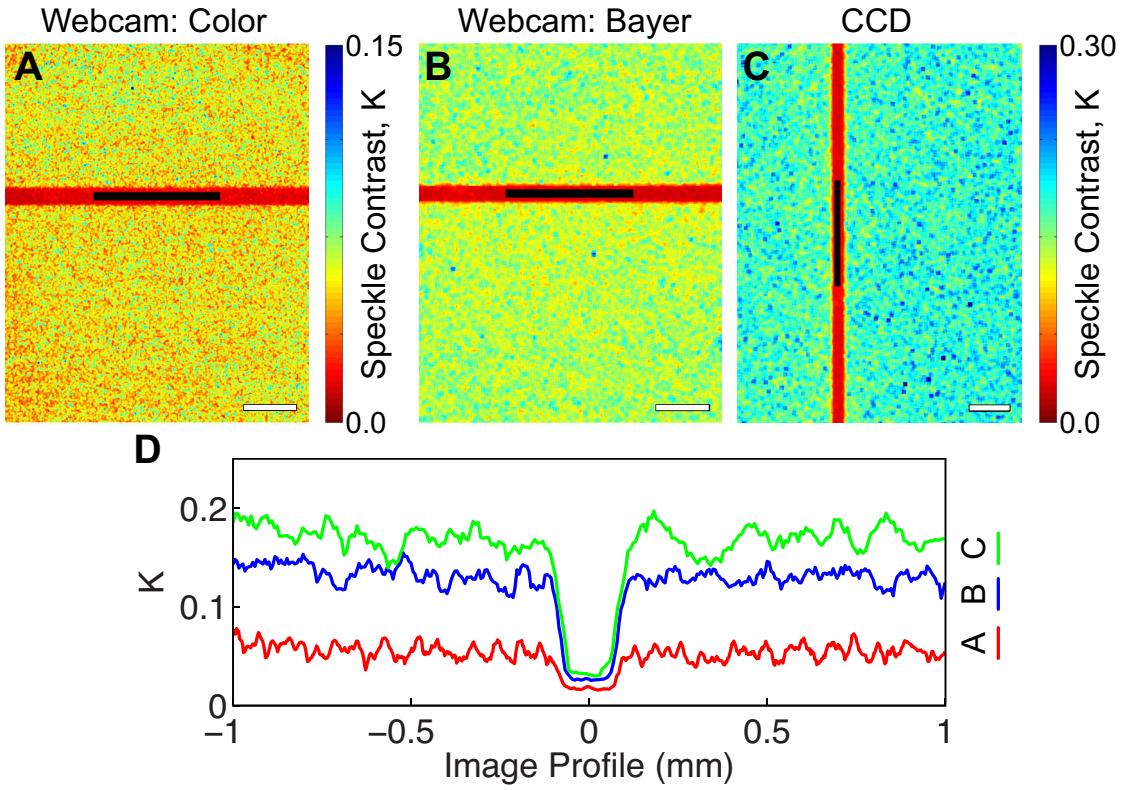

Figure 4.3: Representative speckle contrast images illustrating the location of the black ROIs used for analysis. Speckle contrast images are shown for (A) the webcam acquired in color mode (mean $K = 0.0536$), (B) the webcam acquired in Bayer mode (mean $K = 0.132$), and (C) the CCD acquired simultaneously with the webcam in Bayer mode (mean $K = 0.167$). The color bar for (B) is the same as (C). Scale bars (white) = 0.5 mm. (D) Cropped profiles are shown for images (A-C), where each profile is averaged over 20 pixels, and are plotted in physical space (mm) with the channels lined up for clarity. Adapted from [15].

The two cameras have different sensor sizes (4.8 × 3.6 mm for the CCD, 3.6 × 2.9 mm for the webcam) and pixel densities (648 × 488 pixels for the CCD, 1280 × 1024 pixels for the webcam). Since the imaging magnification is 1:1, the image field of view is approximately the same as the sensor size. The pixel resolution of the images in Figure 4.3 varies from 1274 × 1018 for (A), 634 × 506 for (B), and 642 × 482 for (C). The resolution is smaller than the sensor resolution because the edges of the

speckle contrast images are cropped to remove edge artifacts that occur during the speckle contrast calculation. The Bayer mode images are smaller than the color images because the red-filtered pixels have been extracted. To account for the differences in resolution and field of view, the ROIs were chosen so that they covered the same physical area (~0.09 mm^2) to ensure an equivalent sampling of photons in both cameras. This means that the number of pixels averaged for the ROIs in the CCD was fewer than that for the ROIs in the webcam. The webcam in color mode had 6.6× the spatial averaging of the CCD, and the webcam in Bayer mode had 1.7× the spatial averaging of the CCD.

Images were acquired over 3 minutes during each speed (1 – 10 mm/s in 1 mm/s increments), which was ~18000 images for the CCD and ~400 images for the webcam due to differences in frame rates. The CCD camera had a maximum effective frame rate of 150 fps and the webcam was operated at 5 fps at the native sensor resolution to allow proper use of the Bayer raw streaming feature. The average speckle contrast value was calculated within the ROI for each frame, and this was averaged over all frames and converted to correlation time τ_c. A single average τ_c was saved for each speed, and relative flow rates were calculated by assigning one of the speeds (2 mm/s) to be the baseline τ_c.

Relative flows for the CCD camera are plotted against relative flows for the webcam in Figure 4.4. The two axes are plotted on the same scale so that the diagonal line corresponds to a 1:1 correspondence between the two cameras. The red dots show the webcam in color mode, while the blue dots show the webcam in Bayer mode. Because these plots show the relative flow calculation, the axes do not match up with the speeds tested, but rather show how LSCI measures differences in the speeds. Thus, relative to 2 mm/s, the relative flow ranges from 0.67 – 1.57 in the Bayer mode plot and from 0.82 – 1.40 in the Color mode plot. The scatter plot indicates a very close linear

relationship between relative flows obtained from the CCD and the webcam in Bayer mode, whereas the webcam Color mode relative flows deviate from the CCD results. Poor sensitivity to the higher flow rates was observed, since the relative flows level off for speeds 7 – 10 mm/s. However, this reduced sensitivity was observed equally with both the CCD camera and the webcam in Bayer mode, as indicated by the excellent correspondence in Figure 4.4, and this sensitivity issue may be resolved by using a shorter camera exposure time.

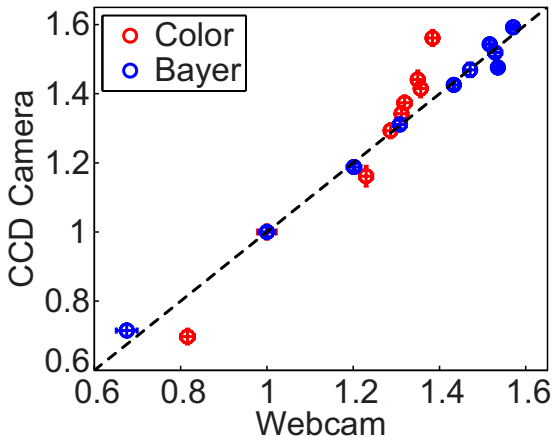

Figure 4.4: Scatter plot illustrating the relative flow changes between different speeds of the microfluidic experiment, with a direct comparison between the CCD and the webcam from simultaneous imaging with the two-camera system. 2 mm/s was used as the baseline flow (relative flow = 1). Each point is the average relative flow, with error bars in each direction depicting the standard deviations for each camera. Adapted from [15].

4.1.4 Animal Study

To assess the webcam in an *in vivo* setting, a single mouse with bilateral cranial windows was imaged in a photothrombotic stroke model. The mouse (CD-1, male, 25 – 30g, Charles River) was anesthetized with 80% N_2/O_2 vaporized isoflurane (2 – 3%) via nosecone. Temperature was maintained at 37°C with a feedback heating plate (World Precision Instruments Inc., Sarasota, FL). Before the surgery, the mouse was

administered carprofen (5 mg/kg, subcutaneous) for anti-inflammation and dexamethasone (2 mg/kg, intramuscular) for restriction of edema after skull removal. The mouse was placed in a supine position, and the head fixed to a stereotaxic frame (Narishige Scientific Instrument Lab, Tokyo, Japan). The scalp was shaved and resected to expose the skull between bregma and lambda skull sutures. A 3 – 4 mm diameter portion of the skull was removed from each hemisphere with a dental drill (Ideal Microdrill, 0.8 mm burr, Fine Science Tools, Foster City, CA) with frequent artificial cerebrospinal fluid (ACSF) perfusion. Cyanoacrylate (Vetbond, 3M, St. Paul, MN) was added to exposed skull areas to facilitate dental cement adhesion. A 5 – 8 mm round cover glass (#1.5) with a layer of ACSF was placed over the exposed brain on each hemisphere. A dental cement mixture was wicked around the perimeter of the cover glass and sealed to the surrounding skull. The mouse was allowed to recover from anesthesia and was monitored for cranial window integrity and behavior normality.

For the LSCI imaging study, the mouse was anesthetized with 1.5 – 2% vaporized isofluorane in N_2/O_2 (80%/20%) and remained under nosecone inhalation while in the stereotaxic frame. For *in vivo* imaging, only Bayer mode was examined based on the *in vitro* results from Section 4.1.3. A neutral density filter was placed in front of the CCD for histogram matching within 11 intensity counts (optical density = 0.3, CCD peak = 68, webcam peak = 57). The anesthetized mouse was placed under the two-camera setup and the right cranial window was aligned in the camera field of view. Baseline images were recorded for at least 5 minutes, then the mouse was administered Rose Bengal (0.15 mL, 15 mg/mL, intraperitoneal), which is a photothrombotic agent that produces vascular clots [21, 22]. After 2 minutes, green laser light illuminated the tissue surface to activate the Rose Bengal and initiate the clotting cascade. Although a red filter was used to block the green light from the cameras, the laser intensity was high

enough to bleed through the filter and accurate LSCI images could not be obtained during green laser irradiation. Therefore, the green laser was modulated using a function generator so that it was on for 15 seconds and off for 5 seconds in a repeating cycle to allow for imaging throughout the formation of the occlusion. The green laser was modulated for 19 minutes and then the function generator was turned off so that the laser was constantly illuminating the tissue. A second bolus of Rose Bengal (0.15 mL, 15 mg/mL, intraperitoneal), was administered 3 minutes after the modulation was turned off to help solidify clot formation. After the clot appeared stable in LSCI, the green laser was turned off and post-occlusion images were recorded for 15 minutes.

Images obtained from each camera were anatomically co-registered using an affine transform so that the images from both techniques could be easily compared. Because tissue deformation occurred following the ischemic event, the images acquired after the stroke were registered to the baseline images using a B-spline transform applied using *Elastix* [23], an open source software package for medical image registration described in detail in Chapter 5. This non-rigid registration allowed accurate tracking of the same tissue ROIs before and after the stroke occurred to allow visualization of the blood flow changes over time.

Baseline speckle contrast images are shown for the CCD and webcam in Figures 4.5A and 4.5B, respectively. The CCD images were registered to match the orientation of the webcam images and both images were cropped to remove regions that are not present in both cameras. Both images are shown with the same color bar for comparison, and the ROIs used for subsequent analysis are shown on both images. These two images demonstrate the similarity between the CCD and the webcam blood flow maps *in vivo*. The time courses of the relative flow is shown for vessel ROIs in Figure 4.5C and for parenchyma ROIs in Figure 4.5D. The relative flow time courses are

shown with solid lines for the CCD and with matched color dotted lines for the webcam. The average τ_c from the first 5 minutes of acquisition was used to set the baseline flow. The time course for the CCD was smoothed using a moving average filter with a window size that approximated the time it took to acquire each webcam image, so that the two cameras could be compared with the same temporal resolution. These plots clearly demonstrate the similarity in performance of the two cameras, as the solid and dotted lines are overlapping or very slightly offset throughout the time course.

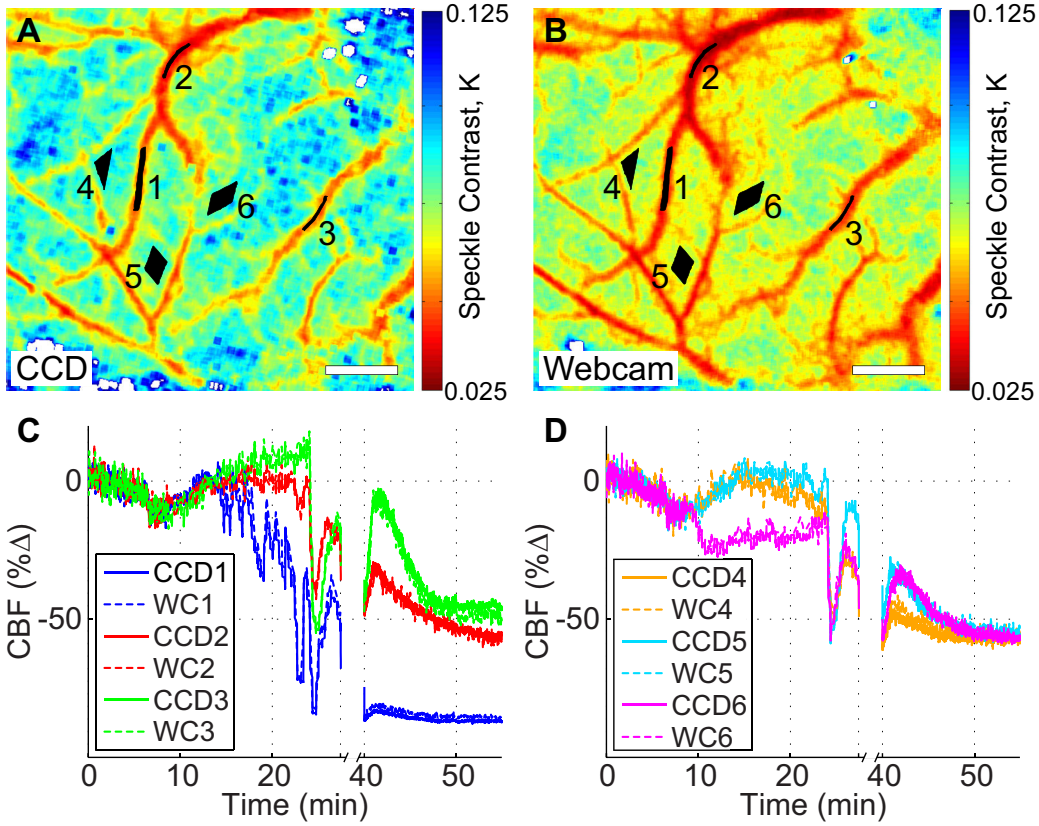

Figure 4.5: Results from the *in vivo* stroke study in a mouse, with a direct comparison between the CCD and the webcam from simultaneous imaging with the two-camera system. Registered baseline speckle contrast images for the CCD camera (A) and the webcam (B) with numbered black ROI locations used for analysis spanning both vessel and parenchyma regions. Scale bars (white) = 0.5 mm. The plots in (C) and (D) show the time courses for the vessel and parenchyma ROIs, respectively, and show the CCD and webcam (WC) relative flows for each ROI on the same plot for direct comparison. The break in the time course was when the green laser was left on continuously for clot formation. Adapted from [15].

For this experiment, dynamic flow changes are visible in both cameras during minutes 9 – 27 in the time course while the green light was modulated. Initially, the relative flow increased after the laser was turned on, but then the clot starts to form in the

central vein (ROI 1) and reduced flow significantly. The green light was left on continuously from 27 – 40 minutes, where there is a break in the time course (Figure 4.5), to solidify the vessel occlusion. Although ischemia was focused on ROI 1, all regions analyzed experienced a high reduction in flow after the stroke with flow rates <50% of baseline values in all cases.

To allow better visualization of the spatial extent of the occlusion, relative blood flow overlay images were generated that showed regions where relative blood flow was less than 35% of the baseline value overlaid on grayscale versions of the speckle contrast images (darker corresponds to faster flow). This is shown for both the CCD and webcam in Figure 4.6A and 4.6B, respectively, and highlights the spatial extent of the stroke in both cameras. The flow reduction visualized by both cameras was overall very similar. The CCD overlay shows slightly more regions colored red in the parenchyma, which indicates that the CCD measured a slightly higher reduction in flow than the webcam. The difference in maximum reduction of flow from baseline between the two overlay images is 3%. This is visible from the slight difference in the central vein (ROI 1) both in the overlay images and in the endpoint of the blue curves in Figure 4.5C. However, the overlay images are still exceedingly similar and indicate comparable performance of the webcam relative to the CCD during an *in vivo* change in blood flow.

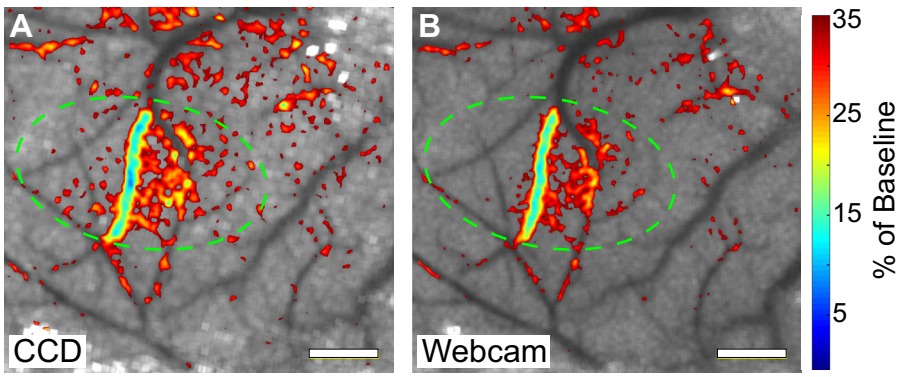

Figure 4.6: Relative blood flow overlay from the two-camera *in vivo* study depicting the reduction in flow for the CCD (A) and the webcam (B) after the stroke, overlaid over baseline speckle contrast values shown in grayscale (darker corresponds to faster flow). The overlay depicts spatial regions with 0 – 35% of baseline flow values, highlighting the spatial extent of the stroke. The targeted region for photothrombosis is marked with a green dashed circle in each image. Adapted from [15].

To further illustrate the utility of the webcam, images were recorded of the same cranial window using the two-camera setup 1-week after inducing the stroke. White light reflectance images were recorded with the webcam in Color mode to image the vascular anatomy (Figure 4.7A) along with speckle contrast images in Bayer mode (Figure 4.7B). The circled region centered over the location of the initial occlusion exhibited higher reflectance due to decreased absorption from blood in that region. The speckle contrast images also exhibited higher speckle contrast values in the same region, correlating with reduced blood flow. Both images indicated that vascular remodeling had taken place during the recovery period, as different vessel shapes were observed in the main vessels affected by the initial occlusion. Although quantitative comparisons cannot be made between two chronic measurements recorded with a single exposure time [24], these

images indicate that the webcam has the feasibility to be used as a tool for imaging both vascular anatomy and blood flow in acute and chronic settings.

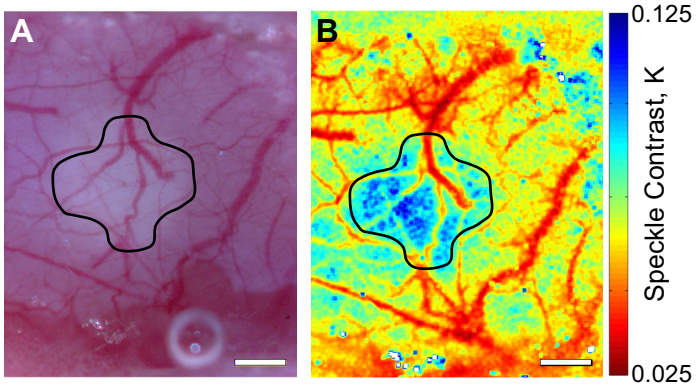

Figure 4.7: The webcam in the two-camera setup was used for chronic image acquisition from the right cranial window 1-week after the initial stroke. (A) Color mode white light reflectance image depicting vascular anatomy, and (B) speckle contrast image showing corresponding blood flow map. The black drawn-in region depicts the area with reduced blood flow 1-week post stroke. Scale bars (white) = 0.5 mm. Adapted from [15].

4.1.5 Discussion

The results from this study demonstrate that an expensive camera is not necessary for obtaining accurate relative blood flow measurements in a microcirculatory setting, both *in vitro* and *in vivo*. For this study, the values are considered accurate relative to the high performance CCD camera. The relative blood flow values calculated by the webcam had significant agreement with those measured by the CCD camera, as confirmed by the linear regression analysis in Table 4.1. The linear relationship between the relative flows measured by the two cameras was compared by calculating the R^2 value for a linear fit with a slope of 1 and intercept of 0 (perfect correspondence). The results indicate excellent correspondence between the two cameras, with an R^2 value of 0.991 *in vitro* with Bayer mode and R^2 values ranging from 0.958 – 0.994 for the

different ROIs analyzed *in vivo*. The relative flows were also compared statistically using Student's two-sample *t*-test. High *p*-values ($p > 0.3$) were calculated for all comparisons listed in Table 4.1, indicating that the difference between the two cameras was not statistically significant.

Table 4.1: Linear regression analysis between the relative flows measured from the webcam and CCD. R^2 values were calculated from a linear fit with slope = 1 and intercept = 0. Adapted from [15].

***In vitro* Results**		***In vivo* Results**	
Mode	**R^2**	**ROI**	**R^2**
Bayer	0.991	1, Blue	0.994
Color	0.767	2, Red	0.984
		3, Green	0.958
		4, Orange	0.983
		5, Cyan	0.984
		6, Magenta	0.984

One observation in this study was the slight difference in the speckle contrast images acquired from the webcam versus the CCD, even in Bayer mode. These differences were visible in both the *in vitro* and *in vivo* images, with a higher speckle contrast observed for the CCD camera relative to the webcam for both the static regions of the PDMS phantom (Figure 4.3C versus 4.3B) as well as the parenchyma regions in the mouse study (Figure 4.5A versus 4.5B). This may be due to the fact that every other pixel is used to calculate the speckle contrast image for the webcam in Bayer mode. This results in a reduction in the standard deviation of pixel intensities across the entire image, or effectively a narrower histogram. The image averages were approximately the same from matching the raw image histogram peak. However, the image standard deviations were lower for the webcam, which could explain the slightly lower speckle contrast

values. One possible improvement for the webcam-based LSCI would be to increase the speckle size by increasing the *f*/#. Because the speckle contrast calculation for Bayer mode uses every other pixel, a more accurate sampling of the speckle pattern would be achieved with a speckle size equal to twice the size of a pixel for speckle-pixel size matching, or at least four times the size of a pixel to satisfy the Nyquist criterion [25].

There are some the limitations associated with using a webcam as the camera sensor for LSCI imaging. The first major restriction is the maximum frame rate possible when using Bayer mode. For the Logitech webcams, Bayer mode is only accurate for certain camera resolutions. Almost all webcams have the ability to perform video rate imaging at ≥30 fps, since their main usage is live-streaming video. However, Bayer mode could only be used at the camera sensor's native resolution (1280 × 1024, 5 fps) for the webcam used in this study, meaning that the faster speed could not be utilized. Another limitation is that not all webcam models support Bayer mode. As of 2009, Logitech offered ~10 webcam models that support Bayer mode streaming, but other vendors that make USB video class (UVC) devices may also be compatible. Bayer mode support should be verified before purchase with any color camera used for LSCI. Because the bit depth of the webcam is limited to 8-bits, another potential limitation is that the sensitivity to small changes in flow may be reduced [26].

4.2 Complete Low-Cost, Compact LSCI System ($90, 5.6 cm length, 25 grams)

There is always interest in reducing the cost of imaging methods to improve ease of integration and increase adoption for both laboratory research and clinical applications. Other groups have begun examining the possibility of using low-cost devices (<$100) to perform LSCI for medical applications in tracking skin movement and movement of an artificial eye [27]. In addition, the low-cost devices have also been used to explore non-

medical applications such as monitoring wood deformation, paint drying, and membrane vibration [27, 28]. These studies were performed using low-cost camera sensors and low power 5 – 8 mW laser sources. One group demonstrated the use of a cell-phone camera to perform LSCI for assessing blood perfusion and pulsation in human skin; however, the optics and illumination used were not low-cost [29].

The objective of this study is to demonstrate that the entire LSCI system can be composed of very inexpensive instrumentation for accurate imaging of microcirculatory flows. This was investigated using low-cost components: a webcam for the camera, low-cost aspheric lenses as the imaging optics, and a laser pointer for the illumination. The feasibility of using a complete inexpensive LSCI system was assessed both *in vitro* and *in vivo*, and the performance of the low-cost system was compared to a traditional LSCI system.

4.2.1 Instrumentation

A schematic of the low-cost, compact setup is shown in Figure 4.8A, with a corresponding photograph in 4.8B. The webcam ($35) is imaged using two replicated aspheric lenses with 10 mm diameter and 40 mm effective focal lengths (68-118, Edmund Optics Inc., $25 each) to achieve 1:1 imaging. The lenses were mounted directly to the S-mount lens holder using S-mount components from Edmund Optics Inc. for simplicity. In the future, these mounting components could be customized to reduce cost, and thus the costs of the mounting components are not included in the overall system cost. A 650 nm laser pointer (AixiZ LLC, 5 mW, $5) was used for illumination, and the beam was expanded using an aspheric lens to evenly illuminate the sample. This laser was a lower power version of the low-cost model tested in Chapter 2. Similar to the setup in Figure 4.2A, a green laser was directed toward the sample for the *in vivo* study

only, and a red filter (0.5") was used to reduce the green light that reached the camera sensor. The *f*/# of this setup was not easily adjusted, but was calculated to be 4.44 (focal length = 40 mm, limiting aperture diameter = 9 mm). This gave a speckle size of approximately 1.28 pixels, which was sufficiently close to the speckle size in the two-camera system to allow cross-system comparisons.

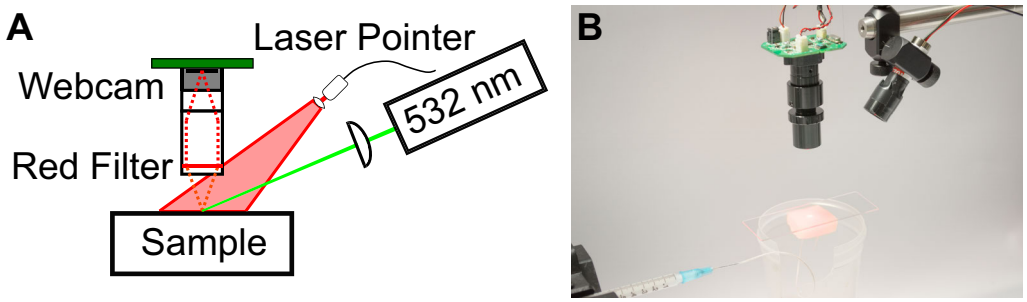

Figure 4.8: Schematic (A) and corresponding photograph (B) of the low-cost, compact LSCI system, where the lenses were inexpensive aspheres and the illumination was a laser pointer. The 532 nm laser was only used for the animal study. The sample corresponds to either a microfluidic flow phantom shown in (B), or a mouse prepared with bi-lateral cranial windows (Figure 4.2C). Adapted from [15].

The cost of all major components in the low-cost setup was $90, which was almost 40× less than the cost of the traditional LSCI components used in Figure 4.2A (~$3500 for the CCD camera, Nikon lenses, laser diode driver, mount, and laser diode). The length from the top of the webcam board to the bottom of the lens system was 5.6 cm, and the weight of the imaging system was 25 grams, which makes the system not only low-cost, but also compact and low weight.

4.2.2 Microfluidic Study

The same solution and syringe pump settings described in Section 4.1.3 were used to assess the complete low-cost setup. The illumination peak was adjusted to match the webcam raw images from the two-camera setup (color mode peak = 135, Bayer mode

peak = 40). Representative speckle contrast images from the microfluidic study with the low-cost setup are shown in Figure 4.9, with the ROI used for subsequent analysis shown in black. The general appearance of the webcam images for both acquisition modes is visually similar to those acquired using the two-camera setup from Figure 4.3. The images are shown on the same scale as the two-camera setup for comparison, which shows that the low-cost setup had higher speckle contrast values in both images (Color mode: low-cost mean $K = 0.0676$ versus two-camera mean $K = 0.0546$, Bayer mode: low-cost mean $K = 0.167$ versus two-camera mean $K = 0.132$). These differences could result from differences in laser illumination angle and slight differences in speckle size between the two setups. Overall, the trend is very similar to the two-camera setup, both qualitatively from visual inspection and quantitatively from the image profile.

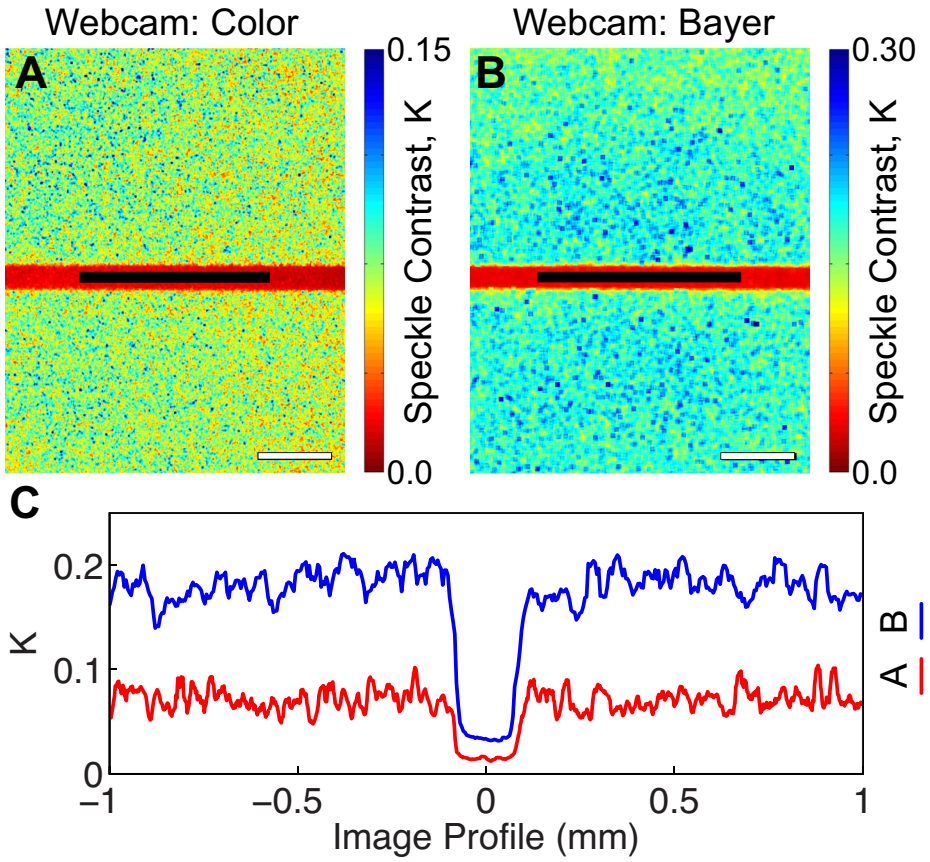

Figure 4.9: Representative speckle contrast images for the complete low-cost setup illustrating the location of the black ROIs used for analysis. Speckle contrast images are shown for (A) the webcam acquired in color mode (mean $K = 0.0676$) and (B) the webcam acquired in Bayer mode (mean $K = 0.167$). The color bar ranges are the same as Figure 4.3 for qualitative comparison. Scale bars (white) = 0.5 mm. (C) Cropped profiles are shown for images (A, B), where each profile is averaged over 20 pixels, and are plotted in physical space (mm) with the channels lined up for clarity. Adapted from [15].

Relative flows for the webcam in the low-cost setup are plotted against relative flows for the webcam in the two-camera setup in Figure 4.10. A single average τ_c was saved for each speed, and relative flow rates were calculated by assigning one of the speeds (3 mm/s) to be the baseline τ_c. Because a different speed was used as the baseline value for this plot, the axes do not match up with the plot in Figure 4.4; however,

the same τ_c data is used for both plots. Relative to 3 mm/s, the relative flow ranges from 0.56 – 1.31 in the Bayer mode plot, and from 0.66 – 1.14 in the Color mode plot. This scatter plot indicates that the inexpensive optics do not affect the relative flows measured for Bayer mode, at least for the slower speeds ($R^2 = 0.971$ for 1 – 7 mm/s, $R^2 = 0.765$ for 1 – 10 mm/s). The Bayer mode results for the inexpensive setup deviate from those acquired from the two-camera setup for the higher speeds, but the trend indicates improved sensitivity with the inexpensive setup. The relative flows from the low-cost setup continue to increase for higher speeds, while the relative flows for the two-camera setup level off for speeds 7 – 10 mm/s. These microfluidic experiments were performed sequentially using the syringe pump, meaning that poor repeatability across trials could be partially responsible for the variability between setups. The Color mode results ($R^2 = 0.937$) show excellent agreement between the two setups across all speeds, but there was very little differentiation in relative flows between speeds (poor sensitivity).

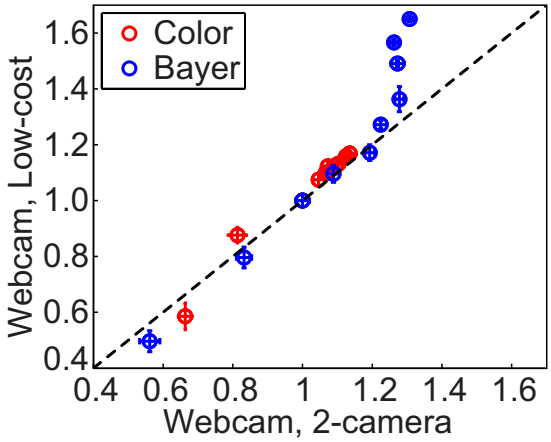

Figure 4.10: Scatter plot illustrating the relative flow changes between different speeds of the microfluidic experiment, with a direct comparison between the webcam in the low-cost system versus the two-camera system in Section 4.1. 3 mm/s was used as the baseline flow (relative flow = 1). Each point is the average relative flow, with error bars in each direction depicting the standard deviations for each setup. Adapted from [15].

4.2.3 Animal Study

For *in vivo* imaging, only Bayer mode was examined based on the *in vitro* results from Section 4.1.3. This imaging session was performed on the same mouse using the opposite cranial window, following the two-camera study in Section 4.1.4. The webcam was transferred to the inexpensive optics, and the anesthetized mouse was placed under the low-cost setup. The laser pointer was adjusted to illuminate the left cranial window, and the illumination peak was adjusted to within 11 intensity counts from the webcam raw images in the two-camera setup (webcam peak = 46). Approximately 1 hour elapsed between the first and second imaging sessions during the change in setup. Baseline images were acquired for at least 5 minutes, then a third bolus of Rose Bengal (0.15 mL, 15 mg/mL, intraperitoneal) was administered to initiate another stroke on the left hemisphere. The green laser modulation was started 2 minutes after the injection. For this setup, the green laser was less focused and spread out over a larger area on the tissue surface, which made clot formation difficult while modulating the laser. Thus, the green laser modulation was stopped after only 5 minutes and the laser was allowed to constantly illuminate the tissue for 33 minutes to form the occlusion. Then, the green laser was turned off after the clot appeared stable and post-occlusion images were recorded for 15 minutes.

The baseline speckle contrast image for the webcam in the low-cost setup is shown in Figure 4.11A, along with the numbered black ROIs used for subsequent analysis. Qualitatively, the speckle contrast image from the low-cost setup had similar quality to the webcam image obtained from the two-camera imaging system, despite the order of magnitude disparity in the component costs. Figure 4.11B shows the relative blood flow overlay, illustrating the spatial extent of the stroke with relative blood flow <35% of the baseline value overlaid on a grayscale version of the speckle contrast image.

This figure clearly shows that the spatial extent of the stroke was much larger for this setup compared to the two-camera setup (Figure 4.6), which was due to the larger size of the green laser spot for this setup. The time courses for the six ROIs were split into two plots, Figure 4.11C and 4.11D, for clarity. A similar shape is observed for the time courses before the occlusion (compared to Figure 4.5C and 4.5D), where the relative flow starts to increase when the green laser is turned on at 11 minutes. The green laser was left on continuously from 17 – 50 minutes, where there is a break in the time course (Figure 4.11), to allow stable clot formation. The time courses indicated that all regions experienced a high reduction in flow after the stroke with flow rates <50% of baseline values in all cases. As confirmed by the overlay image, vessel ROIs 2, 3, and 4 experienced the largest reduction in flow. The results from this experiment indicate that a $90 setup can be used to image dynamic changes in microcirculatory blood flow during an ischemic event.

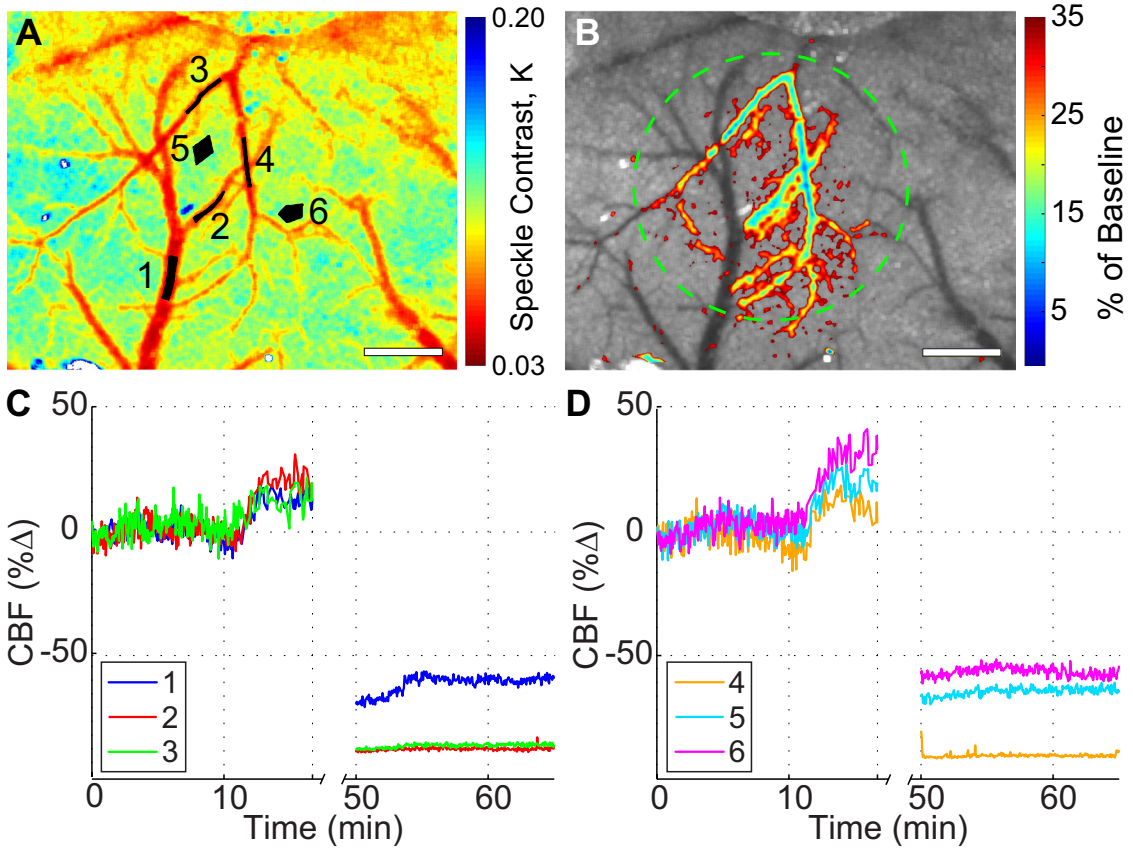

Figure 4.11: Results from the *in vivo* stroke study in a mouse with the webcam in the low-cost setup. (A) The baseline speckle contrast image with numbered black ROI locations used for analysis, spanning both vessel and parenchyma regions. Scale bars (white) = 0.5 mm. (B) Relative blood flow overlay depicting the reduction in flow after the stroke overlaid over the baseline speckle contrast images with a 35% reduction of baseline cutoff. The targeted region for photothrombosis is marked with a green dashed circle. The plots in (C) and (D) show the time courses for the vessel and parenchyma ROIs, respectively, and show the CCD and webcam (WC) relative flows for each ROI on the same plot for direct comparison. The break in the time course was when the green laser was left on continuously for clot formation. Adapted from [15].

4.2.4 Discussion

This study demonstrated the comparable performance of the low-cost imaging optics and illumination components relative to their expensive counterparts. The aspheric

lenses and low-power laser pointer provided images with similar quality to those obtained using the Nikon lenses and a single-mode laser diode. This implies that the differences in the imaging optics and illumination were not critical to the final results. This is a reasonable observation assuming the image aberrations are minimal and the coherence length of the source is sufficient in each case. For any LSCI system, chromatic aberrations are not an issue since it requires single-wavelength illumination. Spherical aberrations are minimized due to the large *f*/# settings primarily chosen to control the speckle size. Thus, any aberrations that were present were minimal enough so that the entire FOV was in good focus across both the low-cost and two-camera setups. The coherence length of both laser sources was acceptable for LSCI because de-correlation of the speckle pattern was consistently present under flow conditions. Overall, the comparable results observed between the traditional LSCI components and the low-cost counterparts indicate that the latter may be used with relative accuracy as long as minimum image quality is achieved.

One of the major advantages of the low-cost LSCI components is the compact size and weight of the overall setup. The total length of the LSCI instrumentation from the top of the camera to the edge of the lens system was 5.6 cm. Customizing the mounting components used for holding the lenses could reduce this length further, since the minimum focal length of the lenses was chosen based on the dimensions of the available mounting components. Having a compact setup could be useful for many reasons, including ease of integration with other techniques and portability. The weight of the LSCI instrumentation was 25 g, and could also be improved with further customization. A lightweight setup could make LSCI an even easier add-on feature where weight is a concern, such as integration with surgical microscopes and robotic

systems used in clinical medicine. A low-cost, compact setup that is easily portable could also increase access to the technology for global health care applications.

4.3 EM-CCD Study (16-bit, Cooled, 30 fps, $30K)

In opposition to the assessment performed with a very low-cost camera sensor, there is a need to determine whether expensive cooled CCDs that include higher bit depth, dynamic range, and sensitivity for low-light imaging are beneficial for LSCI imaging. Because higher bit depth cameras more precisely sample the image intensity (and thereby improve accuracy), it is commonly believed that these cameras are better for LSCI. This belief was supported by computational modeling and a single camera experimental study across multiple illumination levels used to simulate multiple bit depths [26]. This study suggested using the highest bit depth available, or correcting for contrast bias expected from lower bit depths. Although the bit depth will affect the actual value of the measured speckle contrast, the true question is whether it will affect the ability to visualize relative flow changes. Since higher bit depth should have higher precision in the measured speckle contrast, the question remains whether higher bit depth will provide improved sensitivity for visualizing small changes in flow magnitude. Because higher bit depth is traditionally associated with higher price, the results from this comparison will set the price range for high utility LSCI clinical systems.

To simulate the types of flow changes that could be encountered in a clinical setting, both small magnitude flow changes and temporally short flow dynamics must be investigated. To visualize transient flow dynamics, another question remains whether bit depth or frame rate matters more for accurate flow visualization, since a faster frame rate would allow for more temporal averaging. Because high bit depth and high frame rate are typically not available in the same camera models, the objective of this

comparison is to determine which specification is most important for high sensitivity to small transient flow changes similar to what is expected in a clinical setting, such as functional activation for mapping brain activity [30].

Because a frame transfer EM-CCD is used as the 16-bit camera sensor, an illustration of the general format of this sensor type is shown in Figure 4.12. A frame transfer sensor consists of two identical areas, one for imaging with light-sensitive pixels and one for storage with shielding to prevent light exposure [12]. After each camera exposure, charges are transferred from the light-sensitive region to the storage region. Frame transfer CCDs are susceptible to smearing artifacts, which occur when the camera exposes the light sensitive region and transfers to the storage region at the same time. An EM-CCD uses an extended multiplication register for on-chip multiplication of the charge (electrons) generated in pixels for low-light level imaging [12]. The readout register is composed of the traditional section with a fixed voltage as well as the multiplication section with a higher voltage to introduce gain.

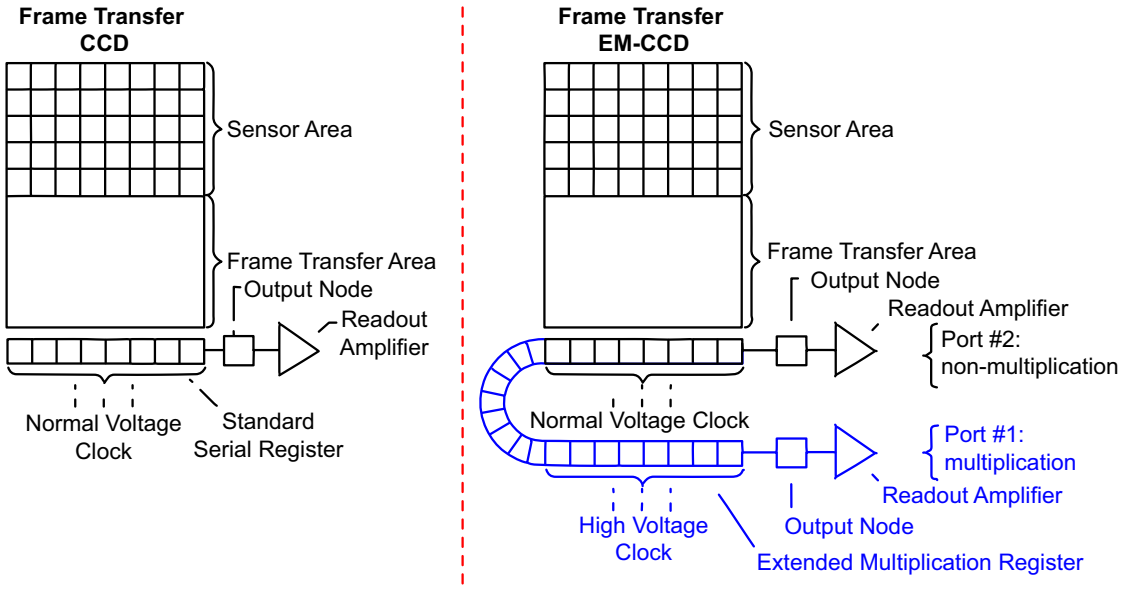

Figure 4.12: Schematic of a traditional frame transfer CCD (left) and an electron multiplying (EM) frame transfer CCD (right). The EM-CCD model used in this study allowed both traditional non-multiplication operation (port #2, same as left), as well as multiplication operation for low-light level imaging (port #1, shown in blue). Adapted from the Cascade™ User Manual (www.photometrics.com/support/pdfs/manuals/CascadeManual.pdf) provided by Photometrics® (www.photometrics.com/).

4.3.1 Instrumentation

To determine whether the 16-bit camera with video rate speed or the 8-bit camera with ~5× frame rate was preferable for LSCI, a two-camera setup was used to simultaneously image with both cameras, schematic shown in Figure 4.13. The imaging setup is the same as the two-camera setup used in Section 4.1. The 8-bit CCD camera used in this study was the same as the previous study as well (~150 fps effective, Basler Pilot piA640-210gm, Basler AG). The 16-bit EM-CCD camera (~30 fps effective, Cascade 512B, Photometrics®, Roper Scientific Inc.) was operated using the multiplication port (#1) to take advantage of the faster frame rate, but the multiplication gain was turned off for a fair comparison with the 8-bit camera. Because this was a

frame transfer CCD, the clear mode was set to clear the CCD before each exposure to achieve operation similar to a traditional CCD camera. This non-overlap operation included clearing the CCD, exposing the camera, shifting the image from the sensor to the frame transfer area, and then reading out the image. These settings were chosen to match operation settings between the two cameras as much as possible. The 660 nm, 120 mW laser diode (HL6545MG, Thorlabs Inc.) was mounted in a temperature-controlled housing (LDM21, Thorlabs Inc.) and expanded using an aspheric lens to evenly illuminate the sample. The laser was the same model studied in Chapter 2, and the parameters required for optimal performance were used in this study. This includes setting the diode to its operating current (170 mA) and using a temperature controller to regulate the temperature (10.5 kΩ, 23.9°C) for maximum stability. The laser was also run at operating levels for >1 hour to achieve a stable output before any images were recorded.

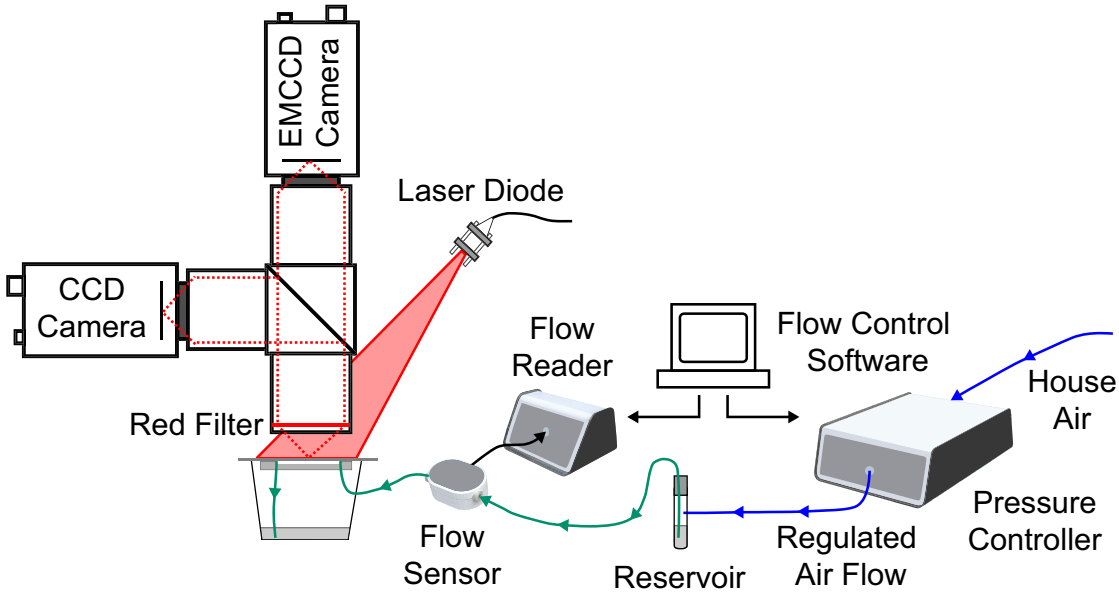

Figure 4.13: Schematic of the two-camera setup for simultaneous LSCI with an 8-bit CCD camera and a 16-bit EM-CCD camera, with the same design from Figure 4.2A. A 50-50 beamsplitter separated the light between the two imaging arms. The pressure regulated flow control system described in Chapter 3 was used for the microfluidic study. Blue lines represent air flow, green lines represent liquid flow, and black lines represent electronic connections.

Similar to Section 4.1, the *f*/# on the Nikon lenses was controlled using the lens closest to the camera to allow individual control for each camera, with the aperture on the common lens closest to the sample left all the way open (*f*/# = 1.8). The speckle size was matched as closely as possible between the two studies for a fair comparison. Again, a speckle size ≥1 pixel size was desired, in this case because it was the highest achievable given the maximum *f*/# of the camera lenses (*f*/22). The CCD camera had a pixel size of 7.4 μm and required an *f*/# of 11 for a speckle size of ~1.20 pixels, while the EM-CCD camera had a pixel size of 16 μm and required an *f*/# of 22 for a speckle size of ~1.11 pixels.

Each camera was controlled using a separate computer using custom software. The CCD camera was controlled using the Basler Pylon API (Basler AG), while the EM-CCD camera was controlled using the PVCAM software kit (Photometrics®, Roper Scientific Inc.). Because the two cameras have different sensor sizes (4.8 × 3.6 mm for the CCD, 8.2 × 8.2 mm for the EM-CCD) and pixel densities (648 × 488 for the CCD, 512 × 512 for the EM-CCD), the EM-CCD camera was acquired using an area of interest on the sensor defined to match the area visible on the CCD camera. This was simpler for matching illumination levels between the cameras, and increased the frame rate of the EM-CCD from approximately 20 fps to 30 fps. Thus, the EM-CCD raw images acquired had a resolution of 229 × 303, which was chosen to match the physical area of the CCD sensor. The speckle contrast images were cropped on the borders to remove edge artifacts that occur during speckle contrast calculation, giving a resolution of 642 × 482 for the CCD and a resolution of 223 × 297 for the EM-CCD (both 4.75 × 3.57 mm). The spatial location of the area of interest on the EM-CCD sensor was chosen to match the same region of the sample as closely as possible in both cameras. Image processing and display was the same as Section 4.1.2. The only differences were the camera exposure time used in this study (T = 1 ms), and the speckle contrast images displayed in this section were averaged over 15 frames.

4.3.2 Microfluidic Study – Linearity

A microfluidic flow phantom was fabricated using the same general process described in Section 2.2.1 and Section 3.1 for *in vitro* validation. For the phantom used in this study, a brass micro-machined metal mold (Potomac Photonics Inc., custom design) similar to the one pictured in Figure 3.2A was used to cast to microchannel within the PDMS-TiO_2 mixture. The cross-section of the extrusion was ~ 290 × 290 μm,

and the length was ~1 inch long. Similar to the phantom described in Section 4.1.3, the smaller channel size required that the inlet and outlet connections to the phantom come from the bottom of the cured PDMS. A blunt tip needle was used to punch the holes, and then the phantom was bonded to a glass slide to seal the channel. FEP tubing was inserted into the pre-punched holes and secured to the phantom using RTV silicone gasket maker (Permatex®, Illinois Tool Works Inc.) for inlet and outlet connections.

Based on the results from Chapter 3, this camera comparison was performed using the pressure regulated flow control system previously described, indicated in Figure 4.13. This was a critical choice for this particular study because the next section investigates small flow changes on a short time-scale, meaning that the highest stability and responsivity are needed to produce desired flow changes as accurately as possible. The experimental setup was almost identical to the setup described previously in Chapter 3, both in terms of the pressure system setup as well as the solution of microspheres. The only difference was that a different flow sensor was used to accommodate for the slower flows required by the smaller channel dimension (Flow Sensor M, 1 – 80 μL/min, FLU_M, Fluigent Inc.). Similar to the webcam study, the solution was flowed through the microfluidic channel at controlled rates from 1 – 10 mm/s (~5 – 50 μL/min). Since the pressure system had improved stability, the flow rates in this study were examined using 0.5 mm/s increments for 19 total flow rates. To examine the linearity of relative flow response between the two cameras, a stepped program was used similar to those shown in Figure 3.6C – 3.6F to visualize the flow range of interest, with a two-minute duration at each flow increment. The acquisition was split into two programs: 1 – 4.5 mm/s and 5 – 10 mm/s, both in 0.5 mm/s increments. Initial calibration experiments with this flow sensor and a precision scale demonstrated that correction factors were needed at different flow ranges to ensure

absolute accuracy in the flow sensor output. By splitting the acquisition up, the correct scale factor could be applied to each flow range individually to ensure the most accurate absolute flow rates were generated during the program. Similar to Chapter 3, the average and standard deviation of the relative flow from each individual step was extracted using standardized time ranges in the middle of the step. To visualize changes in flow, all plots are shown on a relative flow scale, where $\tau_{c,\,\text{baseline}}$ corresponds to the average τ_c for the 5 mm/s (~25 μL/min) flow rate in the middle of the range.

The raw image histograms were matched as closely as possible between the cameras during acquisition using a neutral density filter (optical density = 0.5) placed in front of the CCD camera. The histogram peaks were matched based on percentage, since the two cameras had a different histogram range. The CCD camera had a peak = 68 out of an intensity range of $2^8 - 1 = 255$ (26.7%), and the EM-CCD camera had a peak = 19492 out of an intensity range of $2^{16} - 1 = 65535$ (29.7%). Because the two camera sensors had different detection thresholds (CCD dark counts = 0, EM-CCD dark counts = ~1000), the image averages (histogram peak) were matched so that the spread of the histogram was above the detection threshold. To calculate the relative flow in the microfluidic channel, two ROI sizes were chosen: one with ROIs that covered the same physical area for each camera sensor, and one with ROIs that had equal pixel area across sensors for comparison. The EM-CCD ROI size was 8 × 139 pixels (~0.13 × 2.2 mm), with the CCD ROI size at 18 × 303 pixels for equal physical area and at matched pixel dimensions for equal pixel area. The equal physical area ROI corresponds to a pixel area ratio of ~4.9 for the CCD versus the EM-CCD, meaning that the CCD had ~5× improvement in both spatial averaging and frame rate compared to the EM-CCD.

Representative speckle contrast images from the microfluidic study are shown in Figure 4.14, along with a horizontal image profile across the channel to allow

quantitative comparisons between the cameras. In these images, the red region corresponds to the location of the microfluidic channel within the phantom and the surrounding area was the static PDMS with scattering. The ROIs used for subsequent analysis are shown in black. The 16-bit ROI had a physical area of 0.28 mm^2 and a pixel area of 1112 $pixels^2$ (Figure 4.14C). For the 8-bit camera, the matched pixel area ROI is shown in Figure 4.14A, and the matched physical area ROI is shown in Figure 4.14B. Equal physical area ROIs ensure equivalent sampling of photons in both cameras, while equal pixel area ROIs ensure equivalent spatial averaging. The equal physical area ROI results provide a more fair side-by-side comparison between the cameras and are displayed throughout this section. The equal pixel area ROI results are highlighted for a portion of the results to demonstrate the impact of spatial sampling. Each speckle contrast image was shown on its own colormap, since the average speckle contrast of the 16-bit image was much lower than the corresponding 8-bit image. The range was set using the maximum speckle contrast measured in each individual image. The image profile clearly highlights the absolute difference between the contrast levels measured between the two cameras, with much lower values visualized for the 16-bit camera. This trend is consistent with the theoretical relationship for a quantized speckle pattern, where the contrast is inversely related to the bit depth, and with simulation results from the same group [26]. The large discrepancy between the two cameras may be related to the fact that the raw image intensity was only ~30% of the maximum range for both cameras, since higher discrepancy between bit depths is expected for lower mean intensity levels [26]. However, the lower mean intensity was required for this study because the EM-CCD was a frame transfer CCD, and it was more susceptible to smearing artifacts at higher mean intensity.

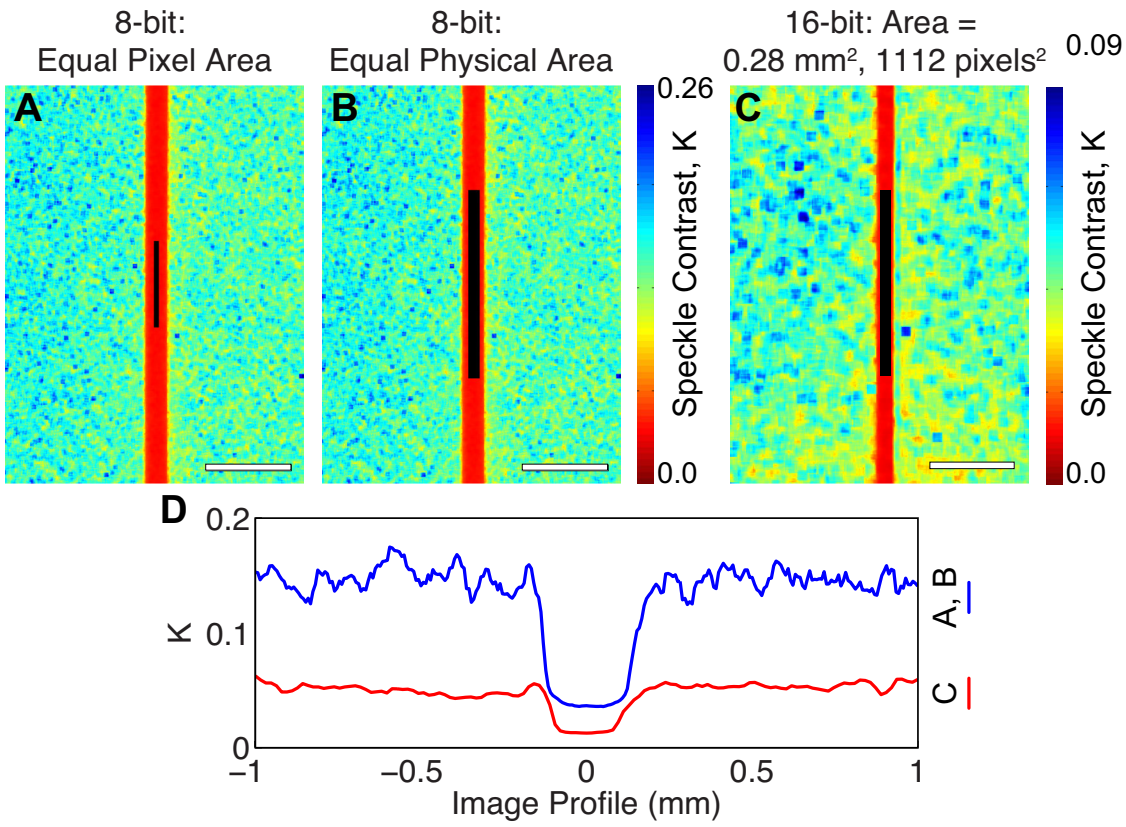

Figure 4.14: Representative speckle contrast images illustrating the location of the black ROIs used for analysis in both cameras. Speckle contrast images are shown for the 8-bit CCD camera (mean $K = 0.139$) with an equal pixel area ROI (A) and with an equal physical area ROI (B), as well as for the 16-bit EM-CCD camera (mean $K = 0.0481$) with the ROI physical and pixel area provided (C). The 8-bit and 16-bit images are shown using separate color bars, since the mean speckle contrast was much lower for the 16-bit camera. Scale bars (white) = 1 mm. (D) Cropped profiles are shown for the images (A, B *versus* C), where each profile is averaged over 20 pixels. Plots are shown in physical space (mm) with the channels lined up for clarity.

Relative flows for the CCD camera (8-bit) were plotted against relative flows for the EM-CCD camera (16-bit) in Figure 4.15, with the 8-bit results for the equal physical area ROI in Figure 4.15A and the equal pixel area ROI in Figure 4.15B. The two axes are shown on the same scale so that the diagonal line shows a 1:1 correspondence between the two cameras. The range of the plots indicate how LSCI measures

differences in speeds, where 5 mm/s was used as a baseline. The plot in Figure 4.15A shows excellent agreement between the two cameras, with an $R^2 = 0.9995$. This confirms that the bit depth difference between the two cameras does not affect the accuracy of the relative flow measurement. Regarding the magnitude of the relative flow changes measured, there is fairly good agreement between the relative flow measured by both cameras (0.24 – 1.6) and the actual relative flow requested (0.2 – 2.0), with a 20% reduction in the range on both ends. The endpoints started to deviate from expected values because a single exposure time was used to assess a fairly broad range of flow rates. Using multiple exposure times would give a more accurate representation of the relative flows against the requested values for the entire range [31]. One noticeable difference between the two cameras is the much larger noise measured from the EM-CCD (16-bit) camera in Figure 4.15A. The difference in noise is largely due to 5× less temporal averaging over the fixed acquisition time and 4.9× less spatial averaging in the ROI relative to the CCD (8-bit). The spatial averaging is equalized in Figure 4.15B, which shows more comparable noise levels between the two cameras. This demonstrates the importance of spatial averaging for reducing noise in the measured relative flow, and emphasizes the equivalent performance of the two cameras.

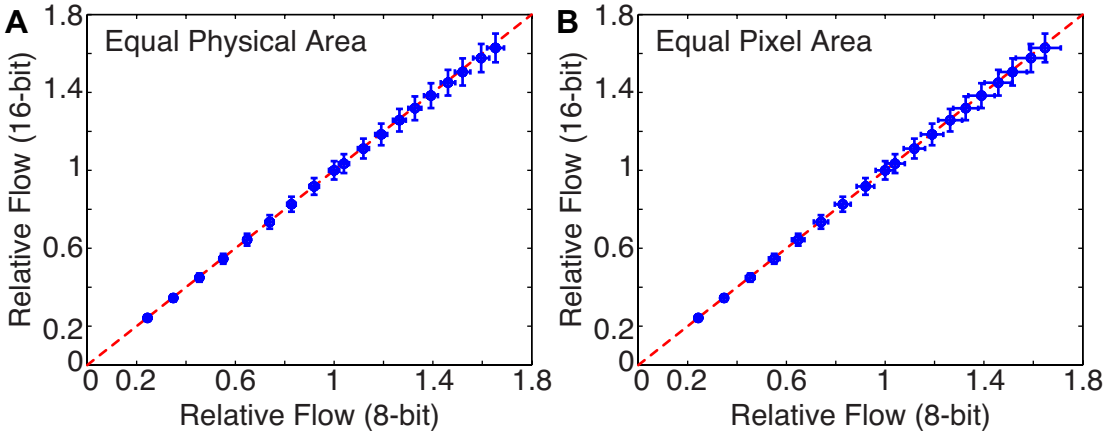

Figure 4.15: Scatter plots illustrating the relative flow changes between 1 – 10 mm/s, with a direct comparison between the CCD (8-bit) and EM-CCD (16-bit) from simultaneous imaging with the two-camera system. The 8-bit results for the equal physical area ROI are shown in (A), and results for the equal pixel area ROI are shown in (B). 5 mm/s was used as the baseline flow (relative flow = 1). Each point is the average relative flow, with error bars in each direction depicting relative standard deviations for each camera.

4.3.3 Microfluidic Study – Sensitivity

Immediately following the linearity study, a sensitivity study was performed using the same setup. This experiment was designed to produce small changes in flow, ranging from 1% to 20% of the baseline, and temporally short changes in flow that lasted only 2, 5, or 10 seconds before returning to baseline. To ensure good sensitivity to flow changes, a flow rate in the middle of the range (5 mm/s, ~25 μL/min) was used as the baseline value. The flow program design included baseline flow, an increase in flow for short duration, return to baseline flow, a decrease in flow for a short duration, and finished with return to baseline flow. A visual representation of the flow profile and corresponding time duration of each segment is shown in Figure 4.16, where the magnitude of the change is shown in blue and the time duration of the change is shown in red. The green region represents the zoomed view of the flow increase that will be shown in subsequent figures. All 15 combinations from the variables listed in the

schematic were tested during the experiment, and a reduced set will be shown for illustrative purposes (X = 1, 2, 5, 10 % change, Y = 2, 10 seconds).

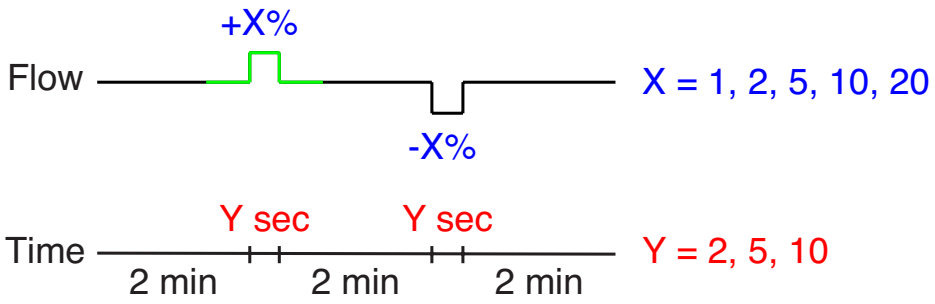

Figure 4.16: Schematic representation of the flow profile used to examine the sensitivity to a small, temporally short flow change. The top line shows the flow profile, with the change from baseline shown in blue, and the bottom line shows the time duration of each section of the profile, with the time duration of the change shown in red. The green portion represents the zoomed view of the flow increase that will be shown in subsequent figures.

To examine the effect of temporal averaging on visualizing the flow changes, the raw signal was temporally filtered with different time duration averaging windows for comparison. Time windows of 0.1, 0.25, 0.5, 0.75 and 1 second duration were examined. To perform the filtering, the raw signal was split into bins of the desired time length using the camera exposure signal recorded by both cameras. Then, the raw data in each bin was averaged together, and the bin start time was assigned as the time point for each bin. Because the cameras have different frame rates, the number of frames in each bin was different between the cameras. The number of frames in each bin for both cameras is shown in Table 4.2 (average and standard deviation).

Table 4.2: The number of frames in each time-duration filtering window assessed (average ± standard deviation). Because of the 5× faster frame rate of the 8-bit camera, this camera had much greater temporal averaging within any bin size relative to the 16-bit camera.

Camera	0.1 sec.	0.25 sec.	0.5 sec.	0.75 sec.	1 sec.
8-bit, 150 fps	14 ± 0.8	36 ± 2.9	72 ± 3.9	108 ± 7.3	143 ± 11
16-bit, 30 fps	3.1 ± 1.0	7.7 ± 1.4	15 ± 0.8	23 ± 1.9	31 ± 2.2

A zoomed view of 10 seconds before and after the 2-second flow increase duration is shown in Figure 4.17 for the subset of the magnitudes and filtering windows assessed. All plots in this section are shown using the 8-bit equal physical area ROI. Here, the requested flow program is shown in red and the actual relative flow profile measured by the flow sensor is shown in blue. The relative flows measured by both cameras are shown in green for the 8-bit CCD camera and in black for the 16-bit EM-CCD camera. The 0.1-second window has very minimal averaging for the 16-bit camera, which leaves the noise level at ~2.9% (standard deviation of the baseline flow region, converted to %). This is higher than both the 1% and 2% change in flow, making it impossible to visualize these smaller flow changes with this window size. On the other hand, the 8-bit camera has an average noise level of <0.7% for the 0.1-second window, and has a similar noise level and temporal accuracy relative to the flow sensor. Thus, it is possible to visualize even the smallest flow change with the smallest temporal filtering window with the faster 8-bit camera. With the larger time duration filtering windows, the 8-bit signal loses the temporal accuracy for resolving the flow change and temporal delays can start to be seen relative to the flow sensor curve, especially in the 1-second window. For the 16-bit camera, the larger filtering windows are essential for lowering the noise levels enough to make visualizing the magnitude of the flow change possible. Even with the 1-second filtering window, the 16-bit camera has an average noise level of 1.03%, which makes it impossible to visualize the 1% flow change. Although it should

be possible to visualize the 2% change with this window, the loss of temporal accuracy with increasing filter duration washes out the sharpness of the flow transition for this small magnitude change. The 16-bit camera does a better job visualizing the magnitude of the 5% and 10% flow changes with both the 0.5-second and 1-second filtering window. However, the loss in temporal accuracy for the 1-second window with both cameras is clearly an issue for accurately visualizing the temporal dynamics of this very short 2-second duration flow change.

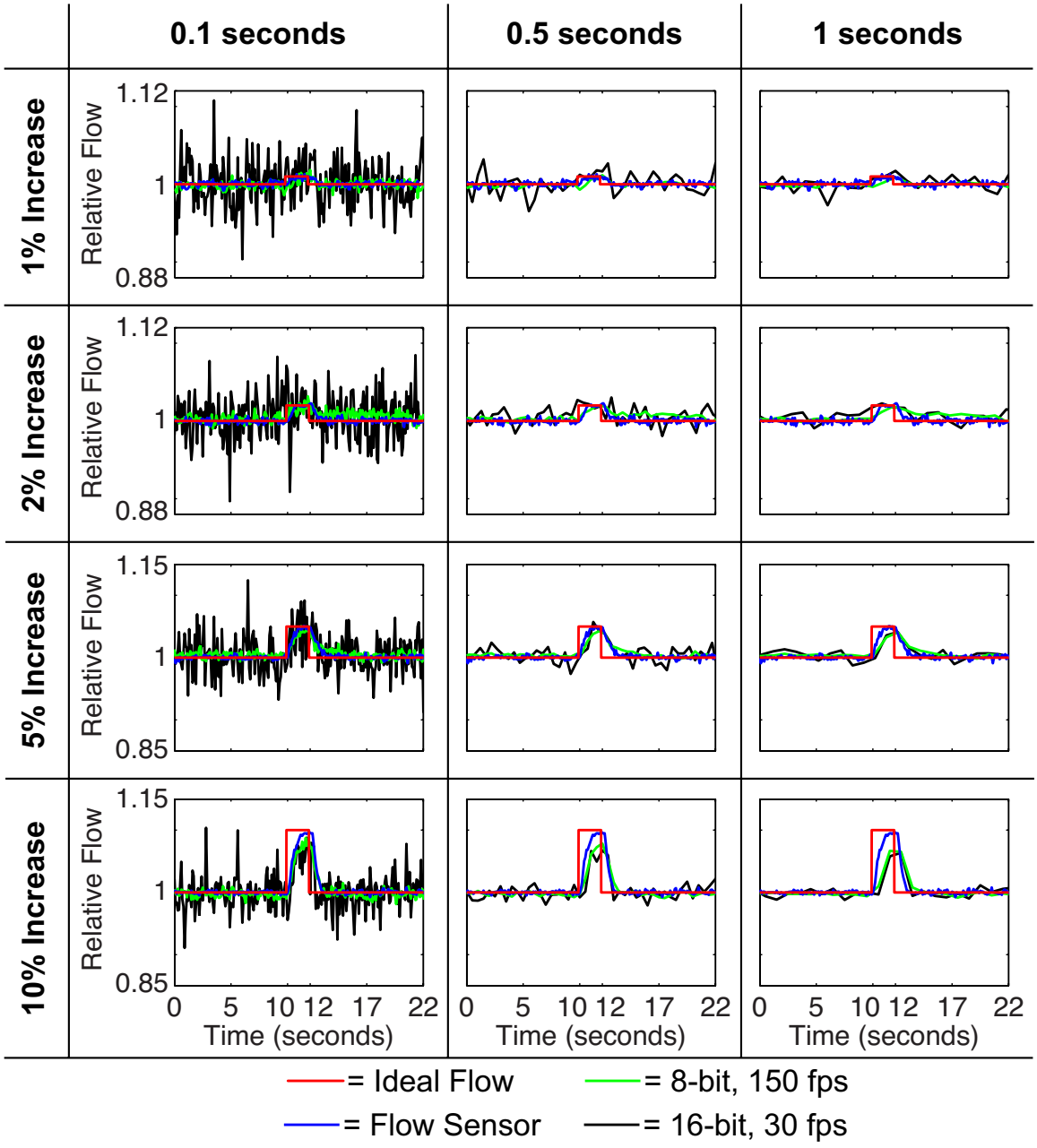

Figure 4.17: A zoomed view of 2-second length flow change with increasing magnitude shown by each row with three different temporal filtering windows applied shown by each column. The requested flow program is shown in red, the relative flow sensor recording is shown in blue, the 8-bit CCD is shown in green, and the 16-bit EM-CCD is shown in black. Each row has the same y-axis range shown on the left, and all plots have the same x-axis range shown on the bottom row.

It should be noted that this set of plots includes comparison of two variables, bit depth and frame rate. Although the linearity study revealed almost identical performance between the 8-bit and 16-bit cameras for sensing relative flow changes, the bit depth variable was isolated to allow a fair comparison. The 8-bit camera was down-sampled to include only frames that occurred at approximately the same time as the frames acquired from the 16-bit camera, producing a 30 fps version of the 8-bit recorded images. Then, the same filtering windows were applied for comparison, shown in Figure 4.18. Here, the noise level of the 8-bit camera is much greater in the 0.1-second filtering window at around 1.3%, making it difficult to visualize the 1% and 2% magnitude flow changes. The average noise level is reduced to <0.7% for both the 0.5-second and 1-second window, similar to performance with the 0.1-second window with the 150 fps results. However, the reduced temporal accuracy of the larger windows still makes it difficult to visualize the 1% change. The larger flow changes with ≥2% magnitude are clearly visible, with slightly improved performance relative to the 16-bit camera. It is important to note that the 8-bit camera has reduced noise relative to the 16-bit camera, even with equal levels of temporal averaging, across all filtering windows. This is most clearly visualized from the 0.1-second window, where the range of the 16-bit signal is much larger than the range of the down-sampled 8-bit signal. This is largely related to the fact that the 8-bit camera had 4.9× the spatial averaging of the 16-bit camera. This emphasizes that both temporal averaging and spatial averaging are critical for reducing noise in LSCI for accurately resolving dynamic relative flow changes.

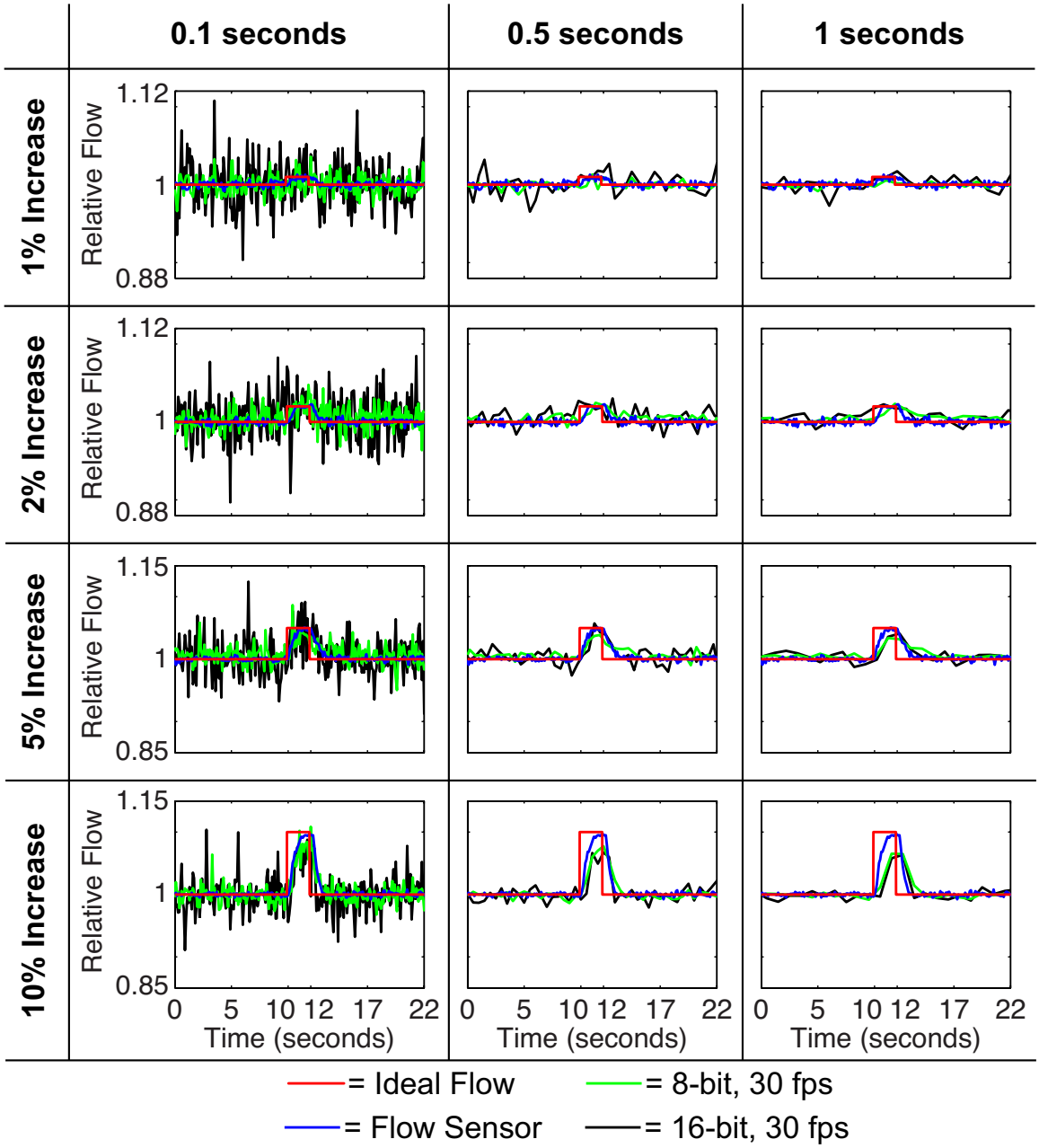

Figure 4.18: An identical set of plots from Figure 4.17 for the 2-second duration flow change, with the exception of the 8-bit camera signal in green, which has now been down-sampled to match the frame rate of the 16-bit camera signal.

Similar results are shown in Figure 4.19 and 4.20 for the 10-second duration flow change with the 8-bit camera sampled at 150 fps and 30 fps, respectively. Overall, these

plots show similar trends to the 2-second duration change in terms of noise levels as well as average noise reduction for each of the filtering windows. The faster sampling of the 8-bit camera can visualize all flow changes clearly with best agreement with the flow sensor at the smallest filtering window, which is consistent with the 2-second duration results. The main difference is that the loss in temporal accuracy for the longer duration filtering windows has a smaller impact on the ability to visualize a longer duration flow change. For the 10-second change, the 1-second window provides excellent visualization of the flow change ≥2% magnitude for both cameras, with less noticeable temporal delay between the relative flow measured by the cameras and the flow sensor. This is an improvement over the 16-bit performance for the 2-second duration change, where the ability to clearly visualize the 2% change was questionable. Thus, the longer filtering window with higher noise reduction makes it possible to visualize longer duration, smaller magnitude flow changes more clearly. When the 8-bit camera signal is down-sampled to match the frame rate of the 16-bit camera, similar levels of increased noise are visualized relative to the 2-second duration results. However, the 8-bit signal still has reduced noise relative to the 16-bit signal, again as a result of increased spatial averaging related to the difference in pixel area between the camera ROIs. Here, the 0.5-second window shows excellent agreement between the 8-bit down-sampled signal and the flow sensor, and shows improved noise levels relative to the 16-bit camera. Again, this highlights the importance of spatial averaging and shows that excellent agreement can be observed with relative flow changes of slower dynamics, even with slower frame rate signal, using sufficient temporal averaging.

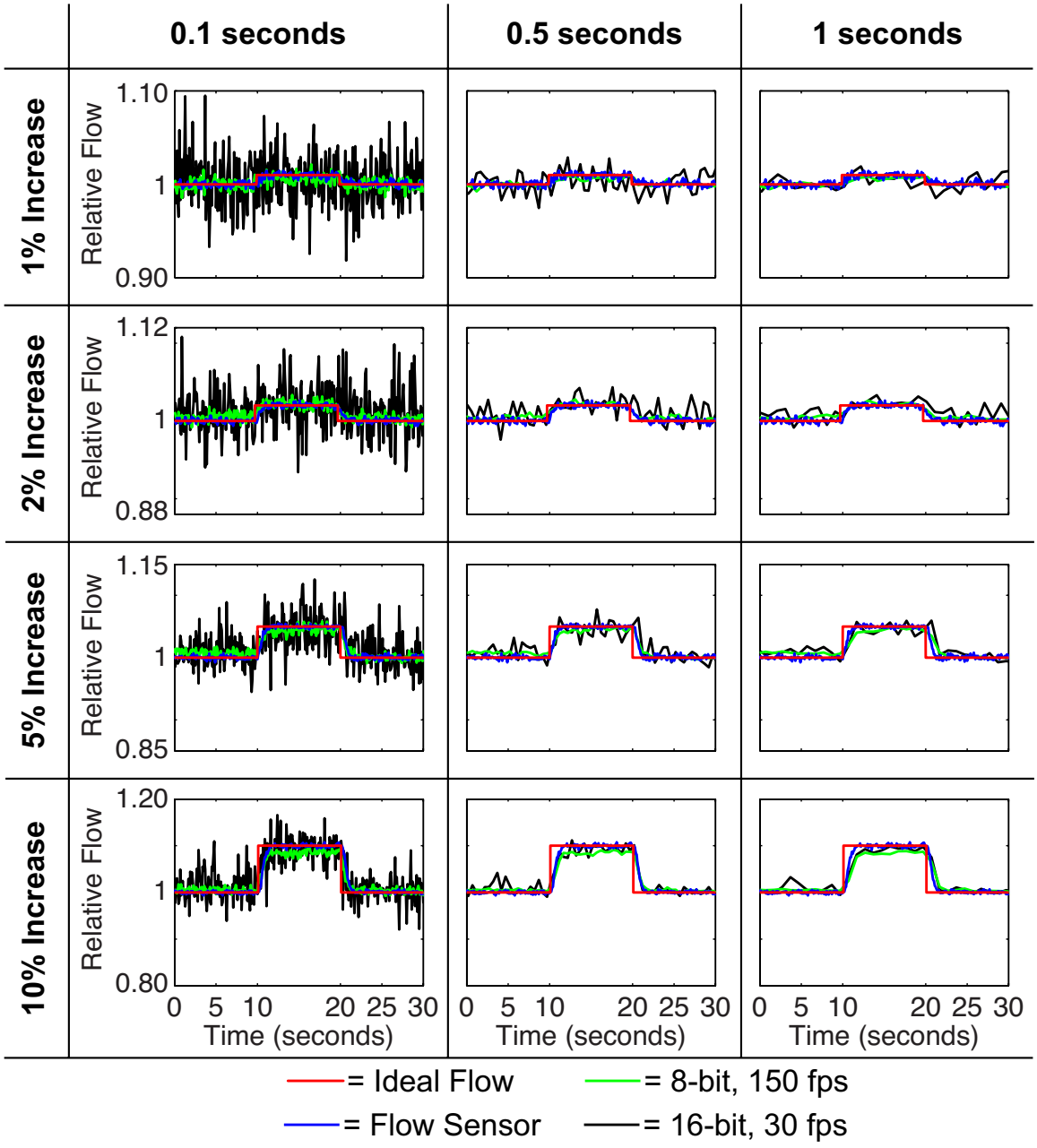

Figure 4.19: A zoomed view of 10-second length flow change with increasing magnitude shown by each row with three different temporal filtering windows applied shown by each column. The requested flow program is shown in red, the relative flow sensor recording is shown in blue, the 8-bit CCD is shown in green, and the 16-bit EM-CCD is shown in black. Each row has the same y-axis range shown on the left, and all plots have the same x-axis range shown on the bottom row.

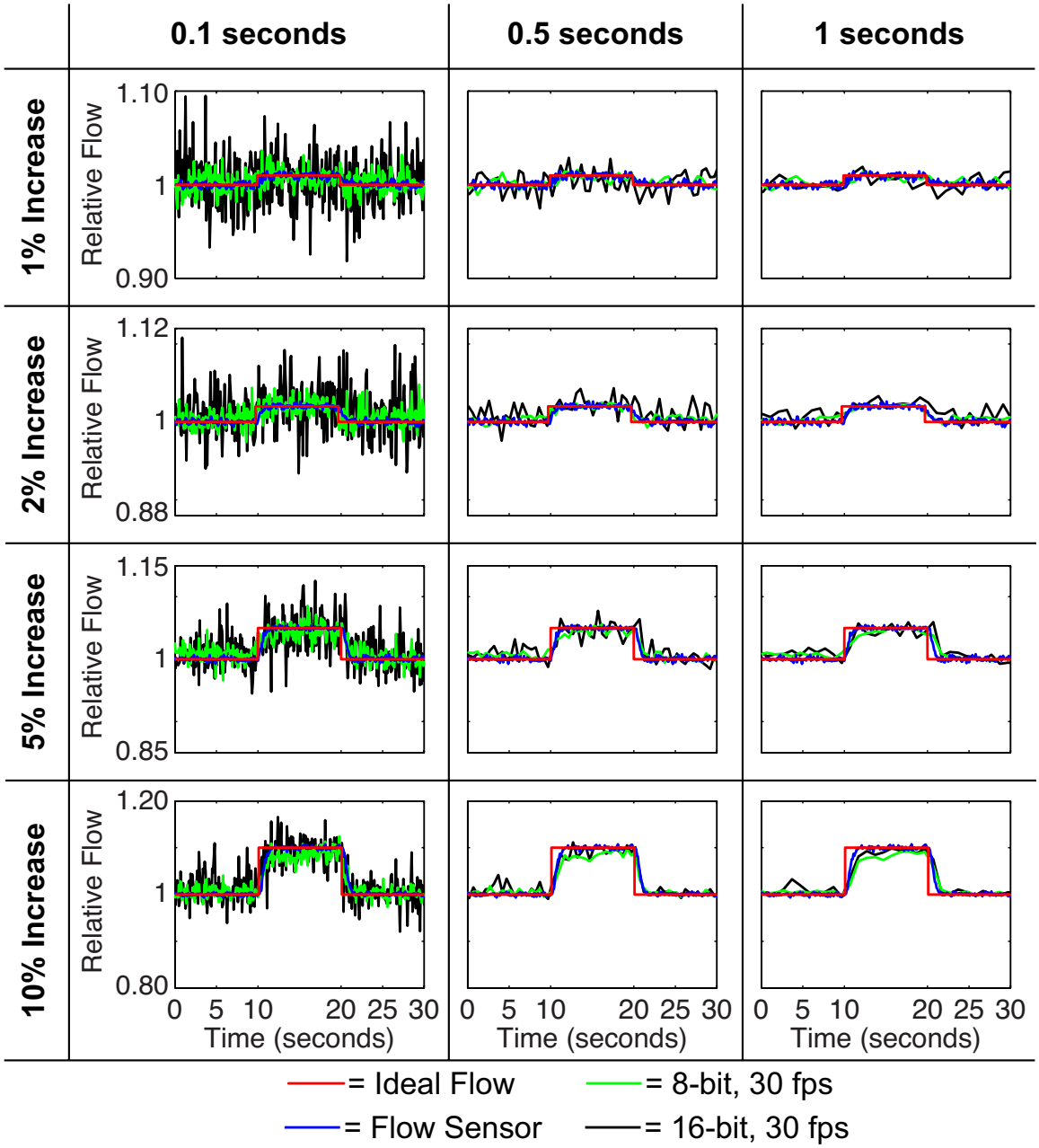

Figure 4.20: An identical set of plots from Figure 4.19 for the 10-second duration flow change, with the exception of the 8-bit camera signal in green, which has now been down-sampled to match the frame rate of the 16-bit camera signal.

4.3.4 Discussion

The results from the camera comparison clearly indicate that equivalent relative flows can be measured with both 8-bit and 16-bit cameras, and that both spatial and temporal averaging are critical for accurately visualizing small, transient flow changes. The linearity study shows very promising results, indicating excellent agreement between the relative flows measured across both bit depths ($R^2 = 0.9995$). This is exciting from a cost standpoint, since the 8-bit camera used in this study was more than an order of magnitude (15×) less expensive than the 16-bit camera. A clear difference in noise levels was visible in the equal physical area scatter plot, which shows the impact of reduced spatial and temporal filtering on the noise in the measured signal. The importance of both spatial and temporal averaging for noise reduction of LSCI relative flow rates has been previously demonstrated [32], and is consistent with the trends observed in this camera comparison. In the sensitivity study, spatial and temporal averaging play an even larger role for accurate visualization of a small magnitude, temporally short flow change. The noise level improves for increasing duration filtering windows, as shown in Figure 4.21. Overall, the lowest noise was seen in the 8-bit, 150 fps signal with equal physical area ROI, which had 4.9× higher spatial averaging compared to the equal pixel area ROI. Reducing the spatial averaging by 4.9× (8-bit, 150 fps, equal pixel area) or the temporal averaging by 5× (8-bit, 30 fps, equal physical area) produced higher noise levels, both with similar magnitudes. The average noise of the 16-bit camera was comparable to noise levels of the 8-bit, 30 fps with equal pixel area, which had equivalent spatial and temporal averaging. This emphasizes that both spatial and temporal averaging are important for reducing noise in measured flows. This plot clearly shows the filtering thresholds that are required to visualize flow changes of varying magnitudes. For the 8-bit, 150 fps signal with equal physical area, flow changes

as small as 1% could be visualized even with the smallest filtering window. For the 8-bit camera with ~5× reduction in spatial or temporal averaging, a filtering window ≥0.5-second duration was required for similar noise levels, and flow changes ≥2% magnitude could be visualized. Finally, for the 16-bit, 30 fps signal and the 8-bit with equivalent spatial and temporal averaging, a filtering window ≥0.5-second duration was required for visualization of the 5% and 10% flow changes, with the smaller changes lost in the noise. The 2% magnitude change was more easily visualized with the 1-second filtering window for a longer duration flow change, where the accuracy of the flow transition was less critical. Overall, the 8-bit, 150 fps signal with 0.1-second filtering provided optimal performance for both the 2-second and 10-second duration changes, and had the best agreement with the relative flow measured by the flow sensor. The results from this study confirm that lower bit depth cameras provide equivalent relative flow measurements compared to the more accurate quantization provided by the high bit depth cameras, and that both spatial and temporal averaging are critical for accurate visualization of dynamic flow changes.

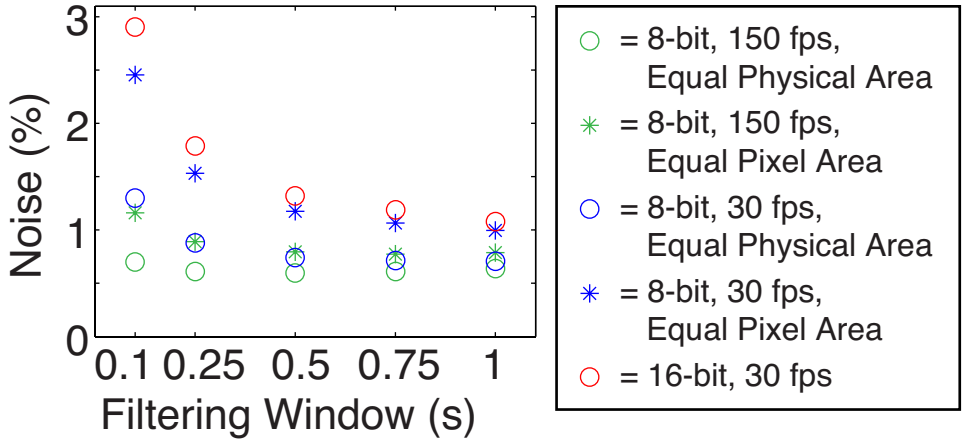

Figure 4.21: Average and standard deviation of the noise levels in the baseline flow regions across all 15 measured trials for five different filtering window durations. The noise results are shown from the 8-bit camera at 150 fps and 30 fps with both the equal physical area ROI and the equal pixel area ROI, along with the 16-bit results at 30 fps. Noise is given by the standard deviation of the relative flow, converted to %.

4.4 Conclusions

The results from this camera comparison study show definitive trends that can be used as a starting point to guide optimal camera choice for LSCI instrumentation. The two cameras assessed sample a broad range of specifications, including bit depth, frame rate, color versus monochrome, and cost. The 8-bit and 16-bit cameras produced equivalent magnitudes of relative flow predictions across a broad flow range. Larger pixel size in the 16-bit camera led to lower spatial averaging, and resulted in higher noise levels across all flow trials. Higher frame rates (150 fps versus 30 fps) enabled more temporal averaging, which produced better agreement with true flow dynamics for visualizing a small, transient change in flow. The color sensor in Bayer mode produced highly equivalent relative flow measurements compared to a monochrome sensor for both *in vitro* and *in vivo* settings. The slow frame rate of the color camera (5 fps) did not hinder visualization of a slow, large magnitude blood flow change produced by a focal

ischemic stroke. The performance of the color sensor confirmed that LSCI could be performed at a very low cost, given that the camera was an inexpensive webcam ($35). A complete low-cost and compact LSCI setup also had comparable performance if a very inexpensive system is required (<$100). The bit depth result also confirms that expensive, cooled 16-bit cameras are not required for accuracy in relative flow measurements, and that lower cost 8-bit cameras are sufficient. Overall, these studies show that frame rate is more important than bit depth, color cameras in Bayer mode can be used with high accuracy, and low-cost systems can provide excellent performance.

4.5 REFERENCES

[1] B. Choi, N. M. Kang, and J. S. Nelson, "Laser speckle imaging for monitoring blood flow dynamics in the in vivo rodent dorsal skin fold model," *Microvascular Research,* **68**(2), pp. 143-146 (2004).

[2] P. Miao, H. Lu, Q. Liu, Y. Li, and S. Tong, "Laser speckle contrast imaging of cerebral blood flow in freely moving animals," *Journal of Biomedical Optics,* **16**(9), pp. 090502 (2011).

[3] M. Wang, Y. Zeng, X. Liang, G. Feng, X. Lu, J. Chen, D. Han, and G. Yang, "In vivo label-free microangiography by laser speckle imaging with intensity fluctuation modulation," *Journal of Biomedical Optics,* **18**(12), pp. 126001 (2013).

[4] T. Durduran, M. G. Burnett, G. Yu, C. Zhou, D. Furuya, A. G. Yodh, J. A. Detre, and J. H. Greenberg, "Spatiotemporal quantification of cerebral blood flow during functional activation in rat somatosensory cortex using laser-speckle flowmetry," *Journal of Cerebral Blood Flow & Metabolism,* **24**(5), pp. 518-525 (2004).

[5] K. Murari, N. Li, A. Rege, X. Jia, A. All, and N. Thakor, "Contrast-enhanced imaging of cerebral vasculature with laser speckle," *Applied Optics,* **46**(22), pp. 5340-5346 (2007).

[6] O. Yang, D. Cuccia, and B. Choi, "Real-time blood flow visualization using the graphics processing unit," *Journal of Biomedical Optics,* **16**(1), pp. 016009 (2011).

[7] B. Kruijt, H. S. de Bruijn, A. van der Ploeg-van den Heuvel, H. J. Sterenborg, and D. J. Robinson, "Laser speckle imaging of dynamic changes in flow during photodynamic therapy," *Lasers in Medical Science,* **21**(4), pp. 208-212 (2006).

[8] Z. Wang, S. Hughes, S. Dayasundara, and R. S. Menon, "Theoretical and experimental optimization of laser speckle contrast imaging for high specificity to brain microcirculation," *Journal of Cerebral Blood Flow & Metabolism,* **27**(2), pp. 258-269 (2007).

[9] A. Rege, J. Senarathna, N. Li, and N. V. Thakor, "Anisotropic processing of laser speckle images improves spatiotemporal resolution," *IEEE Transactions on Biomedical Engineering,* **59**(5), pp. 1272-1280 (2012).

[10] I. Sigal, R. Gad, A. M. Caravaca-Aguirre, Y. Atchia, D. B. Conkey, R. Piestun, and O. Levi, "Laser speckle contrast imaging with extended depth of field for in-vivo tissue imaging," *Biomedical Optics Express,* **5**(1), pp. 123-135 (2013).

[11] S. Dufour, Y. Atchia, R. Gad, D. Ringuette, I. Sigal, and O. Levi, "Evaluation of laser speckle contrast imaging as an intrinsic method to monitor blood brain barrier integrity," *Biomedical Optics Express,* **4**(10), pp. 1856-1875 (2013).

[12] Gerald C. Holst and Terrence S. Lomheim, *CMOS/CCD sensors and camera systems*, 2nd ed. Winter Park, FL; Bellingham, WA: JCD Publishing; SPIE, 2011.

[13] O. Yang and B. Choi, "Laser speckle imaging using a consumer-grade color camera," *Optics Letters,* **37**(19), pp. 3957-3959 (2012).

[14] E. H. Ratzlaff and A. Grinvald, "A tandem-lens epifluorescence macroscope: hundred-fold brightness advantage for wide-field imaging," *Journal of Neuroscience Methods,* **36**(2-3), pp. 127-137 (1991).

[15] L. M. Richards, S. M. S. Kazmi, J. L. Davis, K. E. Olin, and A. K. Dunn, "Low-cost laser speckle contrast imaging of blood flow using a webcam," *Biomedical Optics Express,* **4**(10), pp. 2269-2283 (2013).

[16] W. J. Tom, A. Ponticorvo, and A. K. Dunn, "Efficient processing of laser speckle contrast images," *IEEE Transactions on Medical Imaging,* **27**(12), pp. 1728-1738 (2008).

[17] A. K. Dunn, H. Bolay, M. A. Moskowitz, and D. A. Boas, "Dynamic imaging of cerebral blood flow using laser speckle," *Journal of Cerebral Blood Flow & Metabolism,* **21**(3), pp. 195-201 (2001).

[18] C. Ayata, A. K. Dunn, Y. Gursoy-Özdemir, Z. Huang, D. A. Boas, and M. A. Moskowitz, "Laser speckle flowmetry for the study of cerebrovascular physiology in normal and ischemic mouse cortex," *Journal of Cerebral Blood Flow & Metabolism,* **24**(7), pp. 744-755 (2004).

[19] J. R. Anderson, D. T. Chiu, R. J. Jackman, O. Cherniavskaya, J. C. McDonald, H. Wu, S. H. Whitesides, and G. M. Whitesides, "Fabrication of Topologically Complex Three-Dimensional Microfluidic Systems in PDMS by Rapid Prototyping," *Analytical Chemistry,* **72**(14), pp. 3158-3164 (2000).

[20] S. M. S. Kazmi, E. Faraji, M. A. Davis, Y. Y. Huang, X. J. Zhang, and A. K. Dunn, "Flux or speed? Examining speckle contrast imaging of vascular flows," *Biomedical Optics Express,* **6**(7), pp. 2588-2608 (2015).

[21] B. D. Watson, W. D. Dietrich, R. Busto, M. S. Wachtel, and M. D. Ginsberg, "Induction of reproducible brain infarction by photochemically initiated thrombosis," *Annals of Neurology,* **17**(5), pp. 497-504 (1985).

[22] S. Zhang and T. H. Murphy, "Imaging the impact of cortical microcirculation on synaptic structure and sensory-evoked hemodynamic responses in vivo," *PLoS Biology,* **5**(5), pp. e119 (2007).
[23] S. Klein, M. Staring, K. Murphy, M. A. Viergever, and J. P. Pluim, "elastix: a toolbox for intensity-based medical image registration," *IEEE Transactions on Medical Imaging,* **29**(1), pp. 196-205 (2010).
[24] S. M. S. Kazmi, A. B. Parthasarathy, N. E. Song, T. A. Jones, and A. K. Dunn, "Chronic imaging of cortical blood flow using Multi-Exposure Speckle Imaging," *Journal of Cerebral Blood Flow & Metabolism,* **33**(6), pp. 798-808 (2013).
[25] S. J. Kirkpatrick, D. D. Duncan, and E. M. Wells-Gray, "Detrimental effects of speckle-pixel size matching in laser speckle contrast imaging," *Optics Letters,* **33**(24), pp. 2886-2888 (2008).
[26] L. Song and D. S. Elson, "Effect of signal intensity and camera quantization on laser speckle contrast analysis," *Biomedical Optics Express,* **4**(1), pp. 89-104 (2013).
[27] M. M. da Silva, J. R. D. A. Nozela, M. J. Chaves, R. Alves Braga Jr., and H. J. Rabal, "Optical mouse acting as biospeckle sensor," *Optics Communications,* **284**(7), pp. 1798-1802 (2011).
[28] M. Vannoni, M. Trivi, R. Arizaga, H. Rabal, and G. Molesini, "Dynamic speckle imaging with low-cost devices," *European Journal of Physics,* **29**(5), pp. 967-975 (2008).
[29] I. Remer and A. Bilenca, "Laser speckle spatiotemporal variance analysis for noninvasive widefield measurements of blood pulsation and pulse rate on a camera-phone," *Journal of Biophotonics,* **8**(11-12), pp. 902-907 (2015).
[30] A. Raabe, D. Van De Ville, M. Leutenegger, A. Szelenyi, E. Hattingen, R. Gerlach, V. Seifert, C. Hauger, A. Lopez, R. Leitgeb, M. Unser, E. J. Martin-Williams, and T. Lasser, "Laser Doppler imaging for intraoperative human brain mapping," *NeuroImage,* **44**(4), pp. 1284-1289 (2009).
[31] A. B. Parthasarathy, W. J. Tom, A. Gopal, X. J. Zhang, and A. K. Dunn, "Robust flow measurement with multi-exposure speckle imaging," *Optics Express,* **16**(3), pp. 1975-1989 (2008).
[32] P. Rousseau, G. Mahe, F. Haj-Yassin, S. Durand, A. Humeau, G. Leftheriotis, and P. Abraham, "Increasing the "region of interest" and "time of interest", both reduce the variability of blood flow measurements using laser speckle contrast imaging," *Microvascular Research,* **82**(1), pp. 88-91 (2011).

Chapter 5: Pilot Clinical Study – Feasibility and Developing Motion Compensation Techniques[2]

The first demonstration of LSCI during neurosurgery was in 2009 by a group of neurosurgeons using a commercial LSCI system [1]. This initial study (N = 3) showed the use of LSCI during cerebral revascularization procedures (extracranial-intracranial bypass) with both before and after CBF "flux" maps as well as visualization of a transient CBF decrease during a test occlusion of an arterial graft. Overall, the study showed general feasibility of using LSCI as a potential tool for intraoperative blood flow monitoring during neurosurgery. Since this initial demonstration of its potential clinical utility, multiple clinical studies have examined LSCI during a broad range of neurosurgical procedures including: flow interruption during direct surgical revascularization [2, 3], awake functional mapping of the motor cortex [4], and visualizing cortical spreading depression after decompressive hemicraniectomy for malignant stroke [5]. All of these studies corroborate the initial demonstration of feasibility and clinical value of LSCI for monitoring changes in CBF intraoperatively, now evidenced for a broader range of neurosurgical applications.

Despite the promising results in these studies, each had associated limitations related to the instrument design, image acquisition speed, and image analysis. Most of the aforementioned studies used a stand-alone commercial LSCI instrument [1, 2, 4, 5], which had multiple associated disadvantages. First and foremost, the instrument was not

[2] Portions of this chapter were adapted from: L. M. Richards, E. L. Towle, D. J. Fox, Jr., and A. K. Dunn, "Intraoperative laser speckle contrast imaging with retrospective motion correction for quantitative assessment of cerebral blood flow," *Neurophotonics,* **1**(1), pp. 015006 (2014). L. M. R. built the clinical imaging system, acquired the clinical data, analyzed the results, and wrote the manuscript. E. L. T. built the clinical imaging system and acquired the clinical data. D. J. F., Jr. conceived the project and acquired the clinical data. A. K. D. conceived and supervised the project. All authors contributed to manuscript revisions.

integrated into the surgical workflow and required interruption of the procedure for imaging. Furthermore, the speed of image acquisition and processing was slow. The raw image acquisition speed was considered video-rate (25 fps), but 25 – 100 frame averaging resulted in a much slower effective frame rate (0.25 – 1 fps). These two factors actually reduce patient safety because of additional time under anesthesia, which increases the risk of post-operative complications. In addition to the limitations related to the instrument, none of these studies addressed correction for physiological motion artifacts as part of their image analysis procedure. Given that LSCI is a highly motion-sensitive technique, unavoidable pulsatile and respiration artifacts encountered in a clinical setting would have a large impact on the measured images.

This chapter details the assessment of LSCI for intraoperative CBF monitoring during brain tumor resection procedures in a pilot clinical study (N = 10). The overall goal of the clinical study was to demonstrate feasibility and performance of LSCI in a neurosurgical setting. To address the limitations from previous studies, the LSCI hardware was integrated into the surgical workflow, fast image acquisition speeds and processing allowed real-time visualization, and retrospective motion correction techniques were developed for noise reduction. LSCI hardware was added-on to an existing neurosurgical microscope to reduce interruption to the surgical procedure. In addition, a fast camera with 100 fps acquisition speed and rapid processing allowed real-time display of CBF maps during imaging. Finally, the impact of physiological motion artifacts on recorded blood flow maps was examined, and methods of retrospectively compensating for both pulsatile CBF changes during the cardiac cycle and tissue motion artifacts were developed [6-10].

5.1 INSTRUMENTATION

LSCI instrumentation was adapted for clinical use during neurosurgery by integrating the hardware components into the standard neurosurgical microscope already present in the operating room. This particular design was advantageous because the microscope was already being used during the procedure and the surgeons were familiar with the functionality of the microscope, both of which reduced setup time. The LSCI hardware was adapted into the Zeiss OPMI CS microscope on the NC31 floor stand for patients 1 – 5 for initial feasibility testing [6], and later into the newer model Zeiss OPMI Pentero microscope for patients 6 – 10 to improve ease-of-use for the surgeon [9]. The following instrument description focuses on the newer microscope model; however, the overall design was the same for both systems, and the information is applicable to the entire patient set (1 – 10). A schematic of the LSCI adapted microscope (Zeiss OPMI Pentero, Carl Zeiss Meditec Inc.) is shown in Figure 5.1A, with a corresponding photograph shown in Figure 5.1B. The added hardware components were attached to the microscope prior to the start of the surgery, and did not interfere with the sterile draping or with the normal use of the microscope. This meant that the surgeon could still use the microscope to assist with the tumor resection as needed, as shown in Figure 5.1C.

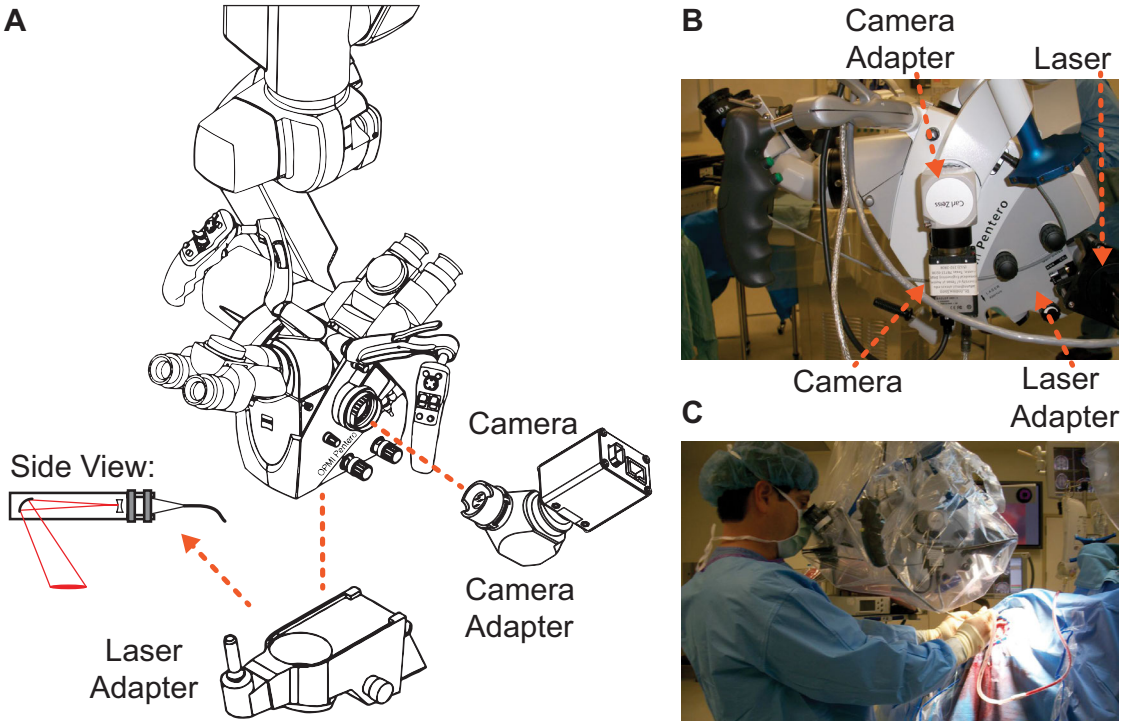

Figure 5.1: Zeiss OPMI Pentero neurosurgical microscope adapted to measure cerebral blood flow intraoperatively using LSCI. (A) Schematic of the intraoperative instrumentation, showing the add-on hardware attachments for LSCI. The camera is attached to a side viewing port on the microscope, and the laser diode is attached to a laser adapter that attaches to the bottom of the microscope head. Drawings were adapted from the Zeiss OPMI Pentero Manual Issue 9.3. (B) Photograph of the intraoperative instrumentation with add-on components labeled. (C) The LSCI adapted microscope is covered in a sterile drape and used to assist with the surgical procedure without any interference from the additional hardware. Adapted from [10] with permission from Springer Science and Business Media.

A 660 nm, 120 mW laser diode (ML101J27, Thorlabs Inc.) was incorporated into an add-on laser adapter (MM6 Micromanipulator, Carl Zeiss Meditec Inc.), which was attached to the bottom of the microscope head. This laser diode model was the older version of the traditional diode HL6545MG studied in Chapter 2, and had the same specifications. A wavelength in the visible range was chosen due to the visible

wavelength pass filters (400 – 700 nm) built-into the microscope. The laser beam traveled linearly through the adapter until it encountered a curved mirror, which directed the beam towards the cortex, shown in the side view of Figure 5.1A. The laser light delivery was co-located with the built-in xenon lamp illumination of the microscope, making it possible to visualize the same tissue area under both illumination sources. The steering toggle on the laser adapter controlled the angle of the mirror, which allowed positioning of the beam on the tissue surface. This was critical because the size of the laser beam (~2 cm beam diameter) was smaller than the size of the built-in illumination spot. Thus, the steering toggle provided the flexibility required to center the laser beam over the tissue area of interest visualized by the camera. The laser power was adjusted using a laser diode controller and was measured to be 28 mW/cm^2 for a 2 cm beam size, which was far below the ANSI standard of 200 mW/cm^2 for maximum permissible exposure (MPE) to a visible laser beam [11]. Although the ANSI standard only lists the MPE for skin exposure, no standards exist for direct exposure of laser light to the cortex. However, the MPE of cortical tissue is expected to be higher than that of skin since cortical tissue has a greater perfusion than skin, and therefore, a greater capacity to dissipate heat. Therefore, the potential risk of exposure to the laser light used in this study was minimal, and no adverse effects were reported.

The camera (Basler A602f, Basler AG) was connected to a side viewing port on the microscope using a C-mount camera adapter (f = 60 mm video lens with C-mount, Carl Zeiss Meditec Inc.). This 8-bit camera had a sensor size of 656 × 491 pixels, a pixel size of 9.9 μm, and a frame rate of 100 fps. Because the camera also had C-mount threading, the camera was simply screwed onto the adapter with no other modifications required. This makes it very easy to swap out the camera with a different model if desired. The side viewing port used for connecting the camera adapter is typically used

for an additional eyepiece for an assisting surgeon, and receives 17.5% of the total light split within the microscope. The camera adapter used in this study limited attachment to the right viewing port, shown in the schematic, due to the position of the locking ring for these side ports. This was a drawback of the instrument design, since it prevented the surgeon from using an assisting eyepiece on the right side during the procedure. The need for an assisting eyepiece in this position depends on the craniotomy position and whether an assisting surgeon or surgical technician would require visualization of the operating field. This limitation was resolved in the modified design discussed in Chapter 6.

The built-in imaging optics from the surgical microscope were used for LSCI imaging. Thus, the automatic zoom and focus controls on the handgrip were used to zoom into an area of interest on the tissue surface and to focus the light onto the camera sensor. Because the microscope manufacturer also makes the camera adapter, the focal plane of the added camera for LSCI was the same as the focal plane of the built-in color camera. This made it easy to obtain both anatomic photographs under the xenon lamp illumination with the built-in camera and LSCI flow maps of the same tissue region without adjusting the microscope. Because the laser beam had a maximum size of ~2 cm diameter, the microscope was set to maximum zoom, which corresponded to a camera field of view of ~2 × 1.5 cm. This corresponds to ~3× demagnification relative to the camera sensor. For the settings used for image acquisition in this study, the microscope's depth of field was measured to be 5.7 ± 0.6 mm. This large depth of field kept the image in focus during normal pulsatile cortical tissue motion. Because the camera already only receives a small percentage of the total light split within the microscope, an additional aperture was not used to control the speckle size. However, the fairly large depth of field implies that the microscope has a small aperture, or a large effective *f*/#, which in turn

produces larger speckles. Since a speckle pattern was clearly visible on the camera sensor in the raw images, the speckle size was large enough to visualize without too much averaging. The speckle size to pixel size ratio would normally factor into the β term in Equation 1.4, which would require measuring the exact speckle size. Because the speckle size also varies with magnification, this would be impractical to measure for the intraoperative system, since the magnification varies slightly even at maximum zoom depending on the working distance of the microscope. This means that the speckle size may be slightly different for every positioning of the microscope, both within and between patients. To eliminate this uncertainty, only intra-patient comparisons were performed and β was set to 1 for relative flow calculations.

5.2 Image Display and Analysis

Raw images were converted into speckle contrast images using Equation 1.1 with a 7×7 pixel window. The custom software used for image acquisition incorporated rapid processing techniques [12] for real-time computation and display of the speckle contrast images. This allowed live visualization of CBF during the procedure, which helped ensure the highest quality images were acquired during each case. In this chapter, images are displayed as speckle contrast images, since these represent an instantaneous map of blood flow, and were averaged over 30 frames after the image registration procedure described in Section 5.5.2.

In post-processing after the completion of each case, speckle contrast images were converted to correlation time, τ_c, using Equation 1.4, where $T = 5$ ms exposure time and $\beta = 1$, which strictly allowed computations of relative blood flow changes within patients. For this study, CBF was calculated as the flow relative to a baseline value, which is the ratio of an average baseline τ_c and the τ_c values at all remaining time points

[13, 14]. The baseline was defined as the average τ_c over ~5 seconds at the start of acquisition for each individual region of interest (ROI) analyzed. To visualize changes in blood flow, the deviation in CBF from a baseline value is used, $\%\Delta$, which allowed easy visualization of flow changes relative to a baseline value.

5.3 INTRAOPERATIVE PROCEDURE

All experiments were performed during brain tumor resection procedures at the NeuroTexas Institute at St. David's Medical Center in Austin, TX. The clinical study was approved by the Institutional Review Boards of the University of Texas at Austin and St. David's Medical Center (Austin Multi-Institutional Review Board), and written informed consent was obtained from all patients. A summary of the patient details for the pilot clinical study is shown in Table 5.1. All hardware attachments were added to the microscope before the start of the surgery and the microscope was re-balanced using the auto-balance feature from the Zeiss control station. Then, a sterile surgical staff member covered the adapted microscope in a standard size sterile drape from the microscope manufacturer to allow normal use of the microscope during the procedure. LSCI imaging was performed after the craniotomy and dura opening at the discretion of the surgeon, either before or after the tumor resection. Immediately prior to LSCI imaging, the surgeon positioned the adapted microscope over the cortical tissue area of interest. The surgeon could easily adjust the location and angle of the microscope head, which provided the flexibility needed to accommodate for variability in the craniotomy location between patients. Once positioned, the surgeon adjusted the focus and zoom as needed, and then sterile warmed saline was flushed over the cortical surface to reduce specular reflections. Setup time was <5 minutes, and then LSCI images were recorded for ~10 – 15 minutes. For this pilot study, a camera exposure time of 5.0 ms was used based

on previous studies in rodents [15]; however, the optimal exposure time for clinical size vasculature is explored in Chapter 6. The camera exposure signal and the patient's electrocardiogram (ECG) waveform were recorded simultaneously during image acquisition for retrospective cardiac cycle motion compensation described in the next section.

Baseline blood flow images were recorded in all patients, and in three cases, images were acquired before and after cortical stimulation with either bipolar cautery or the Ojemann cortical stimulator. Bipolar electrocautery passes high frequency electrical current through the tissue from one forcep tip to the other and is commonly used for surgical hemostasis, since it allows precise control of coagulation and limits thermal injury to surrounding tissue. The Ojemann cortical stimulator is a bipolar electrode with two ball tips separated by 5 – 10 mm used to electrically stimulate the cortex to help identify eloquent areas of the brain (motor, speech) prior to the resection of pathologic tissue, either from a tumor or epilepsy. Both bipolar cautery and the Ojemann stimulator induce a local change in blood flow in the cortical tissue surrounding the stimulation site, and the goal was to determine whether or not this change was visible on recorded LSCI images. At the end of the surgery, the LSCI hardware add-ons were removed from the microscope, leaving it exactly as it was prior to the procedure. Because the LSCI hardware was truly an add-on to an existing instrument, the system was easily portable to different operating rooms, as long as the surgical microscope was available.

Table 5.1: Clinical patient overview for the pilot study. All patients were undergoing brain tumor resection procedures and were imaged either before or after the resection at the discretion of the surgeon.* Adapted from [7, 9].

Patient	Gender	Age	1st Brain Surgery?	Previous Treatment?	Craniotomy Position	LSCI vs. Resection?	Baseline vs. Stimulation?
1	M	52	Y	N/A	R Temporal	Before	Baseline
2	M	33	N	Chemo	R Frontal	After	Baseline
3	F	25	N	XRT, Chemo	R Fronto-temporal	Before	Baseline
4	F	57	Y	N/A	L Sphenoid wing	After	Bipolar Cautery
5	F	62	Y	N/A	L Frontal above orbit	After	Baseline
6	M	64	Y	N/A	L Posterior Frontal	After	Ojemann Cortical Stimulator
7	M	57	Y	N/A	R Frontal	After	Baseline
8	M	70	N	N/A	R Parietal	After	Baseline
9	F	75	Y	N/A	L Occipital	After	Baseline
10	F	42	Y	XRT	Bifrontal, falcine based	After	Bipolar Cautery

*M = male, F = female, Age given in years, Y = yes, N = no, N/A = not applicable, XRT = Cranial radiation therapy, Chemo = chemotherapy

5.4 Clinical Study Overview

The results from the pilot clinical study are promising and demonstrate the instrument's ability to visualize blood flow in a real-time, minimally intrusive manner. For a subset of patients (7 – 10), images were acquired with the microscope's built-in color camera for comparison with the speckle contrast images. Figure 5.2 shows the camera field of view (FOV) recorded by the Zeiss built-in color camera under xenon lamp illumination along with corresponding representative speckle contrast images recorded from the same areas. The speckle contrast images serve as blood flow maps, where red regions correspond to faster flow (low K), blue regions correspond to slower flow (high K), and white regions correspond to specular reflections or other imaging artifacts. The color images were registered to match the orientation of the speckle contrast images for ease of comparison. These image sets show excellent alignment of the anatomical vasculature in the color images and the blood flow maps in the LSCI images. The overlay images showing the fastest flows from larger vessels on top of the color images truly highlights the agreement between the two image sets, which implies that all of these vessels were unobstructed during image acquisition. Some of the larger diameter vasculature indicated by the yellow stars was not clearly visualized in the LSCI images, such as Case 8 (Figure 5.2D – 5.2F) with a thick vessel wall seen by the white appearance on the surface and Case 10 (Figure 5.2J – 5.2L) with specular reflections along the vessel midline, both of which prevented proper flow sampling. The larger vessel in Case 9 (Figure 5.2G – 5.2I) was clearly visualized with LSCI, but appears to be flowing slower than the smaller vessel to its left. This implies that the larger vessel was likely a slow-flowing draining vein, while the smaller vessel to the left was a faster flowing arteriole. The color images from Cases 8 and 9 show blood pools present in the

surgical field indicated by the black dotted lines that obscure the view of the local vasculature underneath. As seen in the LSCI images and corresponding overlays, the blood pools do not interfere with visibility in the LSCI images, and flow is still clearly observed in these regions. This is most obvious in Figure 5.2F, where flow from vessels underneath the blood pool are clearly visualized within the black dotted line. The ability to distinguish between varying magnitudes of flow across the surgical field as well as the ability to "see through" blood vessels are two examples of the improved visualization possible with LSCI. Overall, all image sets demonstrate that the microscope-integrated LSCI system can provide blood flow maps for the microscope's FOV with the spatial resolution of the microscope, which serves as both a confirmation of the microscope-integrated system performance as well as a major benefit of this instrument design.

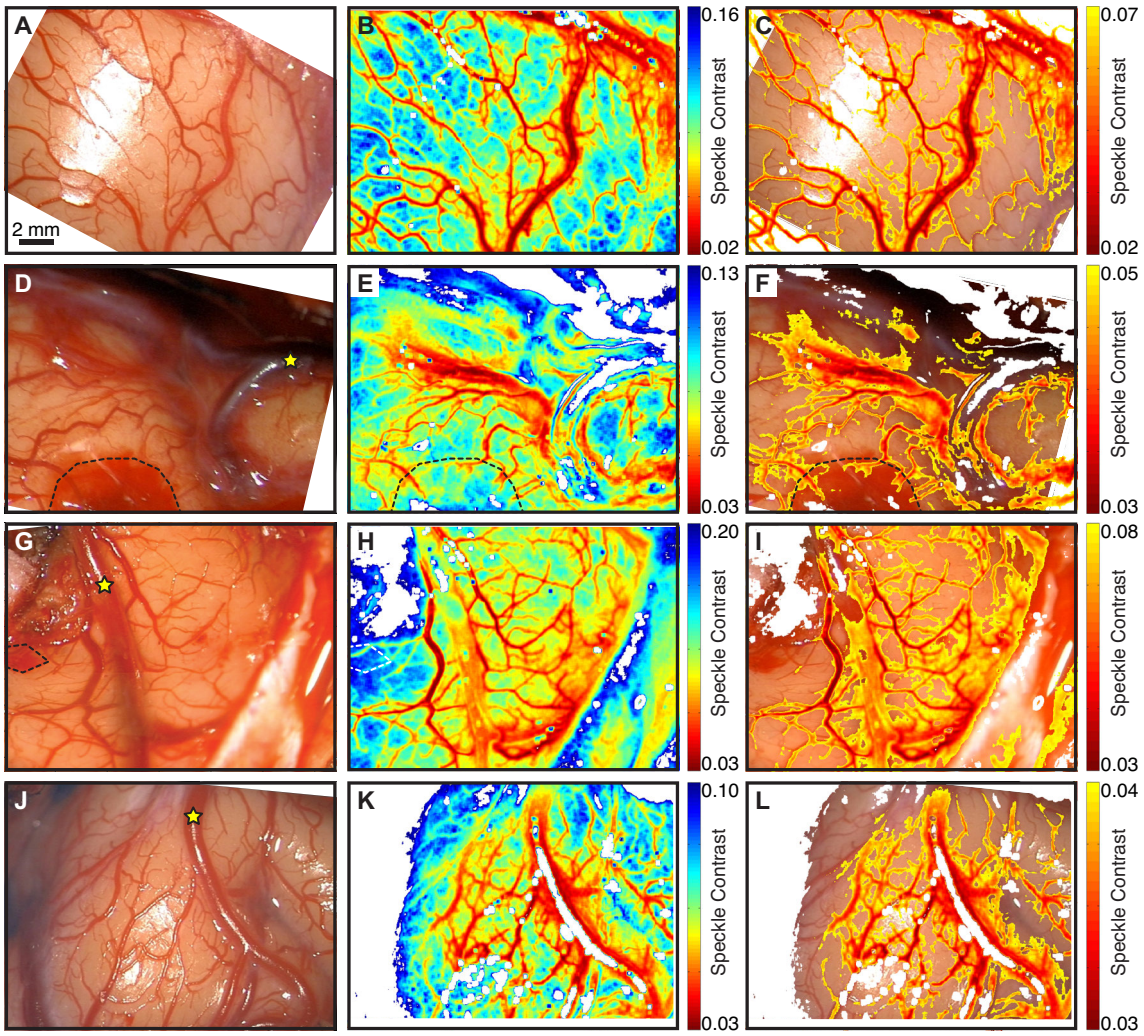

Figure 5.2: Comparison between color photographs taken under xenon illumination using the built-in Zeiss color camera (A, D, G, J) and corresponding speckle contrast images (B, E, H, K) for patients 7 – 10, respectively. The dotted lines correspond to blood pools on the cortical surface, and the yellow stars correspond to the largest vessel in the FOV. At maximum zoom, the FOV is ~1.5 × 2 cm and the scale bar in (A) applies to all images. The right column (C, F, I, L) shows thresholded LSCI images displaying <40% of the maximum K overlaid on top of the color photographs. Adapted from [9].

5.5 Dealing with Motion Artifacts

One of the major challenges involved in using an imaging technique that is highly sensitive to motion is dealing with physiological motion, both due to the pulsatile nature

of blood flow during the cardiac cycle and the physical motion of the brain after the skull has been removed. The unavoidable pulsatile variation in CBF present in any *in vivo* measurement can be tolerated for qualititative visualization of CBF and for imaging large blood flow changes, such as during aneurysm or vessel bypass procedures. However, these cardiac fluctuations could mask small changes in flow, such as the 5 – 10% change in blood flow expected from functional activation procedures such as awake cranial mapping [16]. Thus, ECG filtering is a crucial step for increasing applicability of intraoperative LSCI to a wide range of neurosurgical procedures. Using the recorded ECG signal for each patient, an *ad hoc* cardiac filter can be generated to reduce the fluctuations within each heartbeat, which results in improved visualization of actual functional blood flow changes. Because the brain tissue is able to deform after a portion of the skull is removed during the craniotomy, there are also motion artifacts due to pulsation of the brain tissue as a whole as well as respiration. This tissue deformation results in a constantly changing camera field of view, which makes it difficult to track a specific tissue region over time. Image registration can be used to match the spatial location between images taken at a different time point for a complete image set. This helps account for the physical motion of the brain visible in the original image sets and allows more accurate tracking of tissue ROIs over time.

5.5.1 Cardiac Filtering

To account for blood flow changes synchronized with the cardiac cycle, an *ad hoc* ECG filter was implemented to reduce beat-to-beat fluctuations in recorded τ_c values. The filter design is similar to an adaptive filter technique used for MRI data developed by Deckers *et al* [17], and was first described by Parthasarathy *et al* [6]. The basic design of the ECG filter identifies the time of the camera exposure relative to the ECG cycle to

account for the shape of the signal at that relative time. Both the camera exposure signal and the ECG waveform were recorded during image acquisition, meaning that the actual time of each speckle image and the actual time of each surrounding heartbeat were both known. Thus, each speckle image was assigned a "normalized time", which was defined as the time relative to the nearest heartbeat. For the purposes of cardiac filtering, the *R*-peak of the ECG waveform was defined as the time of each heartbeat, and the duration of the heartbeat was defined as the time between adjacent *R*-peaks in the waveform. The normalized time, $t_{normalized}$, is given by,

$$t_{normalized} = \frac{t_{frame} - t_{beat}}{t_{RR}} \quad , \tag{5.1}$$

where t_{frame} is the time of the camera exposure, t_{beat} is the time of the nearest previous heartbeat, and t_{RR} is the duration of the heartbeat. Images from the first 25 heartbeats in the acquired set were used to generate the *ad hoc* filter function by plotting either the average correlation time τ_c, or CBF ($\%\Delta$), against the normalized time. For ease of interpretation, the plots in this chapter are shown using CBF. The filter is defined as the average shape of the measured blood flow signal versus normalized time within the ECG cycle, calculated using a large window moving average filter (width = 100 data points). To apply the filter to the data, the normalized time of each image in the acquired set was calculated. Then, the corresponding filter value for each normalized time was subtracted from the CBF value, and the median CBF was added back. To further reduce noise in the filtered measurements, a small window moving average filter (width = 0.15 seconds) was applied to the ECG filtered result.

The result of applying the ECG filtering procedure on a selected tissue ROI is shown for a representative example in Figure 5.3. Figure 5.3A shows the location of the ROI in the parenchyma near two surrounding vessels and Figure 5.3B shows the

synchronization of the CBF fluctuations with the heartbeat, where the minimum CBF is consistently aligned with the ECG *R*-peak. Using image data accumulated from 25 heartbeats, the ECG filter shape for the original dataset is shown in Figure 5.3C, where the blue dots represent actual image data points and the red line represents the average shape calculated from the large window moving average filter. The result of applying this filter to the raw recorded data is shown in Figure 5.3D, where the ECG filtered result is shown in red and the result after applying a small window moving average filter is shown in black. Because tissue motion can influence the accuracy of the CBF data points and therefore the shape of the cardiac filtering function, both the ECG filter shape and the filtered results are shown after image registration is performed on the same data set, with the procedure details described in the next Section 5.5.2. The filter shape after image registration is clearly altered, as shown in Figure 5.3E. This is expected since tissue movement artifacts can result in sampling different tissue areas, which in turn can manifest as CBF changes. The registration effect on the filtered result is shown in Figure 5.3F, where now the blue data points follow a more stable flow pattern, with minimal deviation from the baseline. This implies that the increase in CBF visualized in Figure 5.3D from the original data set was simply from the ROI spatially sampling the neighboring vasculature as a result of tissue motion. These results demonstrate that ECG filtering greatly reduces the variability within the cardiac cycle and gives a relatively smooth curve for baseline flow (Figure 5.3F), while preserving inherent physiological flow changes. The filtered output reduces the beat-to-beat variability from 12% to 3.0% (blue versus black curves in Figure 5.3F) over 15 seconds, which is consistent with previously published results [6] and allows the possibility of visualizing small changes in CBF.

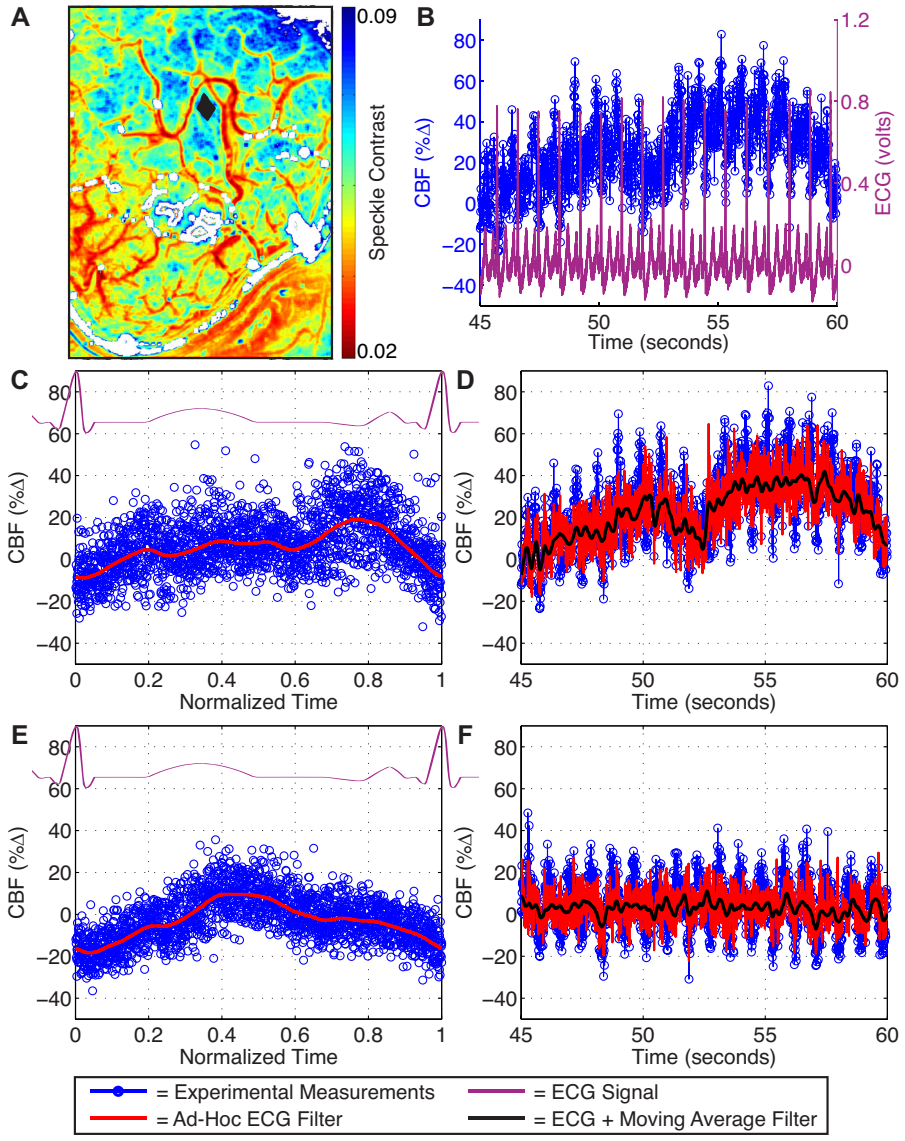

Figure 5.3: Demonstration of the ECG filtering process used to remove pulsatile CBF artifacts, both before and after image registration, shown for patient 4. (A) The speckle contrast image shows the location of the parenchymal ROI in black. (B) The average CBF percent change (%Δ) computed from the ROI is co-localized in time with the ECG waveform recorded from the patient, shown for 15 seconds of recorded data. (C) The *ad hoc* ECG filter shape is generated from 25 heartbeats from the original dataset. (D) The ECG filtered output is shown in red, and the result after applying a small window moving average filter is shown in black for the original dataset. (E) and (F) are the filter shape and filtered results, respectively, for the translation-based registered dataset. Adapted from [9].

One important detail to point out is that the ECG filter shape varies greatly between different tissue regions and between patients, meaning that a general ECG filter cannot be used. A sample of this variability in ECG filter shape is shown in Figure 5.4 for patients 1, 6, and 10. For patient 1, there is a clear difference between filter shapes for the vessel and parenchyma regions, with the vessel showing much larger change in CBF during each heartbeat. For patient 6, there is again a clear difference in shape between the vessel and parenchyma regions, but the magnitude of CBF change during the heartbeat is much smaller for the vessel region compared to patient 1. For patient 10, two parenchyma regions are shown, with similar shapes but higher magnitude CBF change for Figure 5.4I. The CBF changes are expected to follow the shape of the mean arterial pressure changes that occur within the cardiac cycle [18], meaning that the general ECG filter shape observed (increase in CBF followed by a gradual return to baseline) is expected physiologically. However, the time where the peak CBF occurs varies depending on the individual region selected. Figure 5.4B, 5.4E, 5.4H, and 5.4I have a peak CBF between 0.2 – 0.4 seconds of normalized time in the ECG cycle, while Figure 5.4C and 5.4F have a peak between 0 – 0.2 seconds of normalized time. This spatially varying phase shift in the peak CBF is likely due to variations in pulsatile transmission through diverse regions of brain tissue resulting from differences in blood vessel impedance. Because the ECG filter shape is so variable from region-to-region, each ROI analyzed within each patient must have its own filter shape to correct for beta-to-beat fluctuations in measured CBF.

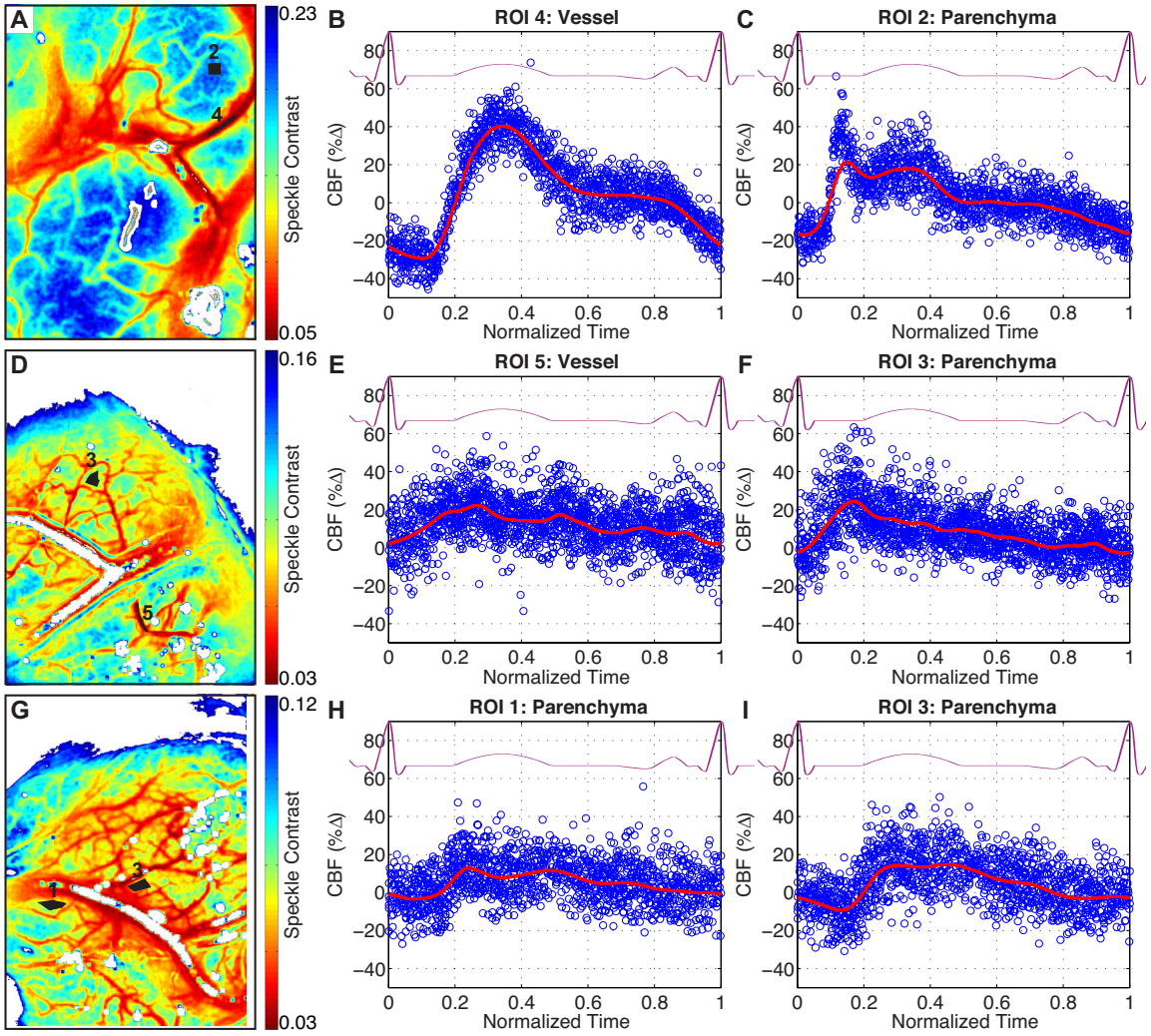

Figure 5.4: Demonstration of variability in the *ad hoc* ECG filter shape across different ROIs both within and between patients. (A-C) are from patient 1, (D-F) are from patient 6, and (G-I) are from patient 10. (A, D, G) The speckle contrast images with two ROIs selected, where the ROI numbering matches Figures 5.6 and 5.9 with analysis using the same regions. The ECG filter shape generated from 25 heartbeats is shown for two ROIs from each patient in the plots on the same row (B, C), (E, F), and (H, I), with the titles indicating which ROI number the plot applies to from its corresponding speckle contrast image.

Although other techniques could be used for cardiac filtering, there are disadvantages associated with each. A large-window moving average filter alone

(width = 0.5 seconds) can also be used to reduce the beat-to-beat variability from 12% to 2.8%, as shown by the green curve in Figure 5.5. This is a similar reduction to the ECG filtering method shown in the black curve (12% to 3.0% reduction), which is expected since a large window moving average filter acts as a low pass filter. The moving average filter alone (green curve) follows the same general shape as the ECG filtered result (black curve), but retains the sinusoidal shape of the cardiac fluctuations at a smaller magnitude and ends up washing out the finer features of measured blood flow variation. Thus, the large window moving average filter reduces variability in CBF both due to cardiac fluctuations as well as due to inherent variability resulting from physiology. On the other hand, the ECG filtering method retains inherent physiological variability by removing variations due to cardiac fluctuations alone, with similar noise reduction to the large window moving average filter [6]. Another alternative technique for cardiac filtering is synchronizing the image acquisition with the cardiac cycle. By recording from the same portion of the cardiac cycle at every beat, the observed cardiac shift would be minimized assuming stable physiology, which would reduce the CBF measurement error and eliminate the need for cardiac filtering. However, gating the signal acquisition would reduce the effective frame rate by 24% to retain data ±10% from baseline, and by 63% to retain data ±5% from baseline. This would reduce both the continuity of the data, as well as the ability to perform frame averaging. Inter-pulse averaging in post-processing would be a better approach for synchronized imaging, which filters out the rise in flow during each heartbeat with a standard Butterworth filter and averages the remaining signal [19]. This approach is fairly smilar to the ECG filtering method already described, and would be a good approach if a simplified filter design was required. However, the customization of the ECG filter for each ROI reduces generalization and improves sensitivity to the unique physiological dynamics for that tissue region. Thus, all future

time courses shown in this section have been ECG filtered, and are equivalent to the black curves from Figure 5.3D and 5.3F (or Figure 5.5A and 5.5B).

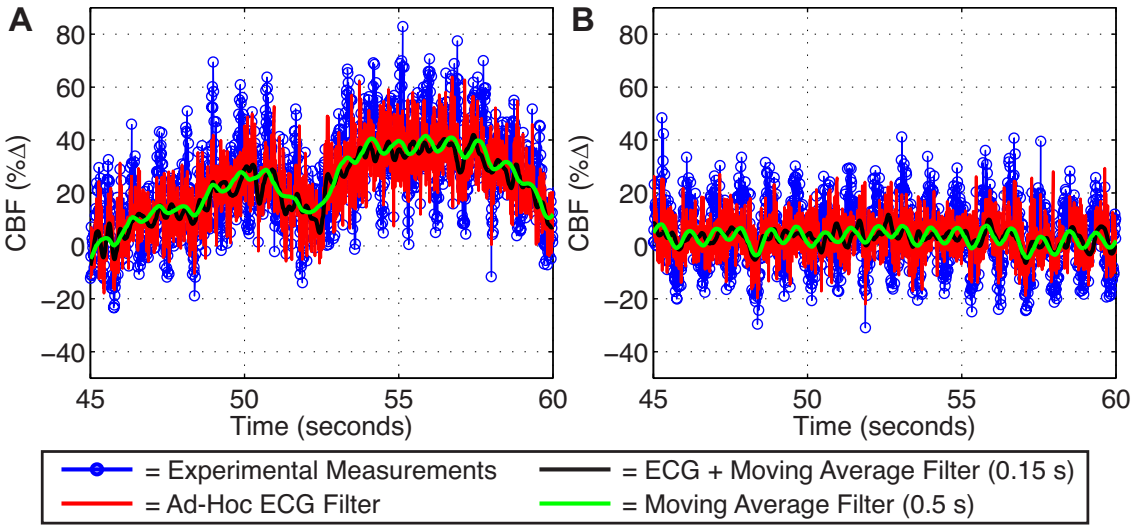

Figure 5.5: Comparison of the ECG filtered results shown in Figure 5.3D and 5.3F with the result from a large window moving average filter alone (width = 0.5 seconds). The filtered results from the original dataset are shown in (A), and the results from the translation-registered dataset are shown in (B).

5.5.2 Image Registration

To account for large-scale tissue motion due to pulsation and respiration, image registration was performed on the speckle contrast images to align the camera FOV for each acquired image set. Registration was performed using *Elastix*, an open-source software package for medical image registration based on the Insight Segmentation and Registration Toolkit (ITK) [20]. This program performs automatic intensity-based image registration by finding a coordinate transformation $T_{\mu}(x)$ to spatially align a moving image to match a fixed image. For this study, the fixed image was the first image of each acquired set, and the moving images were all subsequent images in the set.

The basic registration components involve sampling the fixed image and interpolating the moving image for sampling non-pixel positions to compute the similarity measure, or the cost function. The similarity measure defines the quality of alignment between the fixed and moving images using an intensity-based metric, such as the sum of squared differences, the correlation ratio, or mutual information. An optimizer routine then iteratively tries to find the optimal registration solution given by the minimum of the cost function by determining the search direction and the step size (gain) required to approach the solution. The seach is limited by the degrees-of-freedom (DOF) set by the transformation type, which determines allowed deformation for creating the mapping between the fixed image and the moving image. This process is iteratively repeated until either the global minimum is found, or until the maxiumum number of iterations is reached.

For this study, the similarity measure was set to mutual information (MI), which is a measure of the amount of information one random variable contains about the other. For image registration, the random variable is the intensity distribution of the image. It can also be described as the reduction in uncertainty of one image due to knowledge of the other, which is a special case of relative entropy [21]. Given the definition for marginal entropies of the fixed image $H(I_f)$ and moving image $H(I_m)$ as well as their jointy entropy $H(I_f, I_m)$ [21], MI and closely related normalized mutual information (NMI) [22] is given by,

$$MI(I_f, I_m) = H(I_f) + H(I_m) - H(I_f, I_m)$$
$$NMI(I_f, I_m) = \frac{H(I_f) + H(I_m)}{H(I_f, I_m)} \quad . \tag{5.2}$$

MI was used for registration for this pilot study, and NMI is introduced here because it is used in the phase II study in Chapter 6. The main difference between the techniques is

that NMI is not sensitive to the overlap region between the two images, which makes it more robust to large-scale misalignment [22]. MI assumes a relationship between the probability distribution of the intensities of the fixed and moving images, but doesn't require equivalent distributions. This makes MI suitable for both mono- and multi-modal image pairs, making it a good starting metric for any type of image registration. The number of histogram bins used for computing the joint histogram was usually left at the default value of 32. The random image sampler refreshed with new spatial samples for every iteration, and used both pixel and non-pixel positions across the entire image to compute the similarity metric. Linear interpolation was used to estimate the intensity for non-pixel positions during registration and optimization steps. The optimization procedure was set to adaptive stochastic gradient descent, which uses an adaptive step size for stochastic approximations of the cost function [23]. The image can deform beyond recognition if the step size is too high or can get stuck in a nearby local optimum and never reach the true solution if the step size is too low. This is where the adaptive step size estimation becomes very helpful, since it eliminates the need to tune this parameter. A hierarchical multi-resolution registration strategy was used on both the fixed and moving images, which included Gaussian smoothing and downsampling of the image at lower resolutions to help with coarse alignment of larger structures. These parameters are the recommended starting point for *Elastix*, and were selected for this study because they provided good registration performance for the speckle contrast image sets.

The transformation type used during registration is one of the most important parameters and must be chosen carefully to ensure the deformation is both accurate as a spatial mapping and realistic given the input image modality. For a rigid transform, the

image integrity is maintained and the image can only be translated, rotated, scaled, and sheared uniformly. The translation transform is simply given by,

$$T_{\mu}(x) = x + t \ , \tag{5.3}$$

where x represents the fixed image, t represents the translation vector (x- and y-offset), and $T_{\mu}(x)$ represents the mapped position of the moving image to the fixed image. Here, μ represents the parameter vector containing the elements required to describe the transform. For translation in 2D, $\mu = (t_x, t_y)$, and these two parameters are the only two DOF allowed during computation of the transformation. For a nonrigid transform, different regions of the image can deform independently along a regular grid of control points defined on the fixed image. The B-spline transform is most common for nonrigid registration, where the B stands for either basis or basic [24]. The B-spline transform is given by a linear combination of a third order (cubic) B-spline functions shifted by the control points,

$$T_{\mu}(x) = x + \sum_{x_k \in N_x} p_k \beta^3 \left(\frac{x - x_k}{\sigma} \right) \ , \tag{5.4}$$

where $\beta^3(x)$ is the cubic B-spline piecewise polynomial, p_k are the B-spline coefficients (scaling factors), x_k are the control points, σ is the control point spacing, and N_x are the set of all control points within the compact support of the B-spline at x [25]. Compact support refers to the fact that the B-spline is locally controlled by the close neighborhood of the control point, which allows nonlinear local transformations throughout the control point grid [26]. The spacing of the control points throughout the fixed input image affects the size of μ, which means that the B-spline transform can have varying DOF depending on the grid spacing. A large spacing will model global nonrigid deformations, while a dense spacing will model highly localized nonrigid deformations. Thus, the spacing of the control point grid is a critical parameter, since very large spacing

may not model small structures accurately and very small spacing may produce unrealistic transforms from too many DOF.

Because the brain tissue is able to deform after removal of the skull, a nonrigid transform would be required for an exact mapping of the images to account for tissue distortion. However, LSCI records a 2D view of the 3D deformation and the surgical microscope has a large enough depth of field to keep the image in focus during tissue motion. This limits the majority of tissue deformation in the recorded images to the *x* and *y* directions. Thus, the rigid translation transform was performed on all cases to preserve image integrity and decrease the complexity of the registration, and the nonrigid B-spline transform was performed on a subset of cases for comparison. For the translation transform, the *x*- and *y*-offsets needed for mapping each moving image back to the fixed image are output from *Elastix* in the generated transform parameter file. This allowed calculation of an overall total displacement for each registered image, which was used to assess the spatial shift between the original and registered images. Contrast-adjusted speckle contrast images were provided to *Elastix* for registration, since the blood flow maps provide clear image features to improve registration performance. After registration, the transform was applied to the un-adjusted speckle contrast images using *Transformix* [20] to allow proper calculation of the correlation time and CBF.

A comparison between the original and translation-registered image sets is shown for three baseline patients 1, 7, and 9, in Figure 5.6. Four ROIs are selected for each patient including both vessel and parenchyma regions, and the recorded time course from those regions are shown for both the original and registered data sets. The plots show greater stability and reduced fluctuations in the ROI time courses after registration, especially for the vessel ROIs. Stable CBF levels are expected for baseline recording, assuming stable physiology for the duration of the recording (~60 seconds), which means

that the registered result matches the expected dynamics. This confirms that the large-scale CBF changes observed in the original time courses were solely due to tissue motion, causing vessel ROIs to sample the parenchyma, and vice versa. Compared to the dramatic improvement for vessel ROIs, the registered parenchyma ROIs are visually similar to their original curves, especially those placed farther away from nearby vessels. Overall, the registered flow dynamics are easier to interpret and quantify compared to the dynamics in the original time courses.

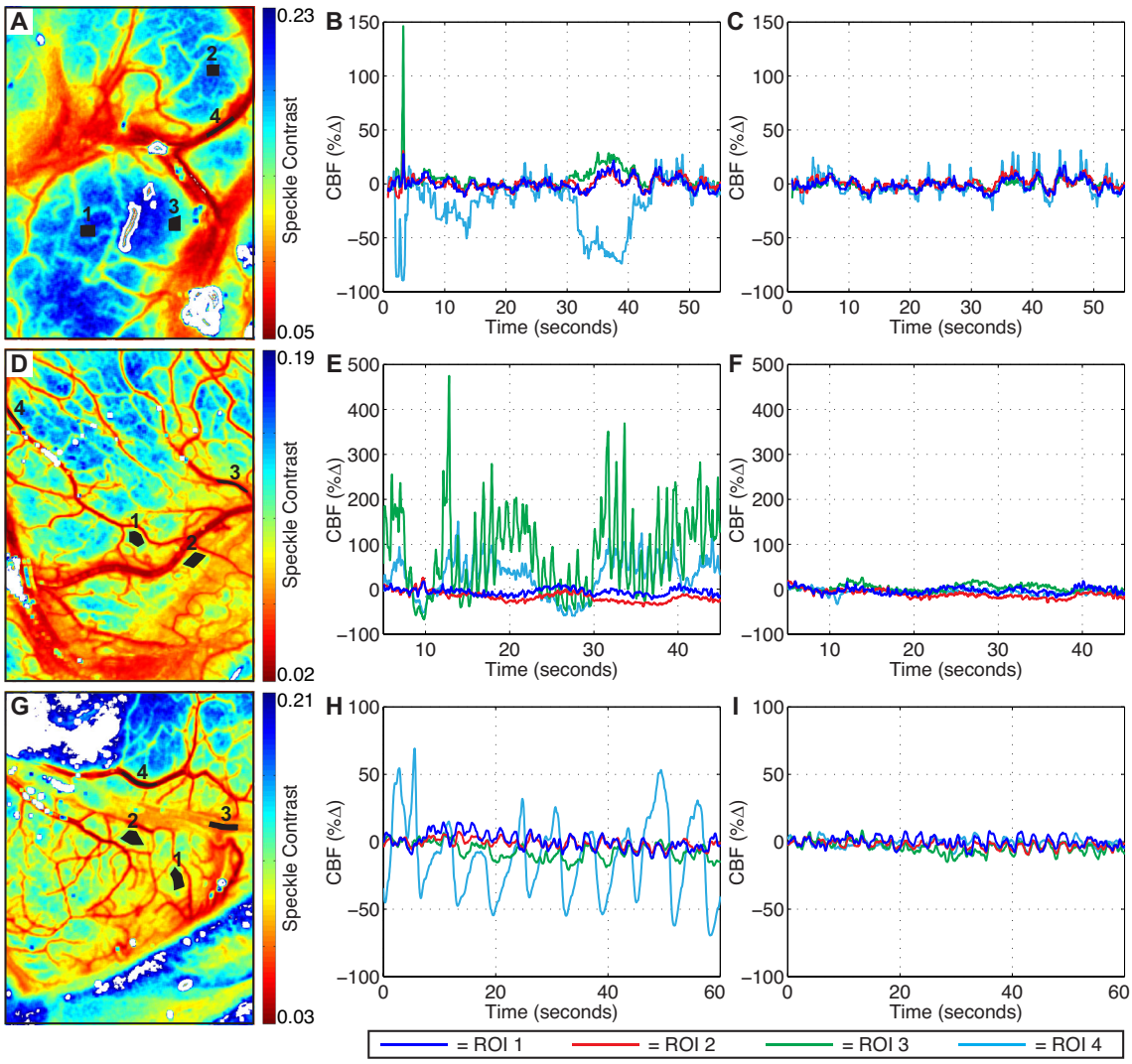

Figure 5.6: A comparison between the time courses of ROIs before and after translation-based image registration for baseline patients 1, 7, and 9 in parts (A-C), (D-F), and (G-I), respectively. (A, D, G) The speckle contrast image at the start of acquisition shows four numbered ROIs overlaid in black where analysis is taking place. The middle column of plots (B, E, H) displays the time course of the original recorded CBF %Δ during intraoperative acquisition. The right column of plots (C, F, I) displays the time course of the CBF %Δ after translation-based image registration. Plots from the same patient are shown with the same axes for comparing ROI curves before and after registration. Adapted from [9].

Because lateral displacement due to tissue motion is a significant source of noise in the ROI analysis, this displacement was quantified as the total spatial shift of each registered image relative to the fixed image at the start of image acquisition. Across seven cases, the mean lateral displacement ranged from 0.12 ± 0.078 to 0.64 ± 0.15 mm, and the maximum lateral displacement ranged from 0.41 – 1.9 mm. To illustrate how tissue motion affects the measured CBF changes, the relationship between the change in change in τ_c and displacement is shown in Figure 5.7 for two cases corresponding to Figure 5.6B and 5.6E. The displacement is co-localized in time with the change in τ_c, showing excellent correspondence between the magnitude of the spatial shift and the change in flow measured by LSCI. Pearson's correlation coefficient indicates a positive correlation between the displacement and the change in flow, with $r \geq 0.9$ for two of the ROIs.

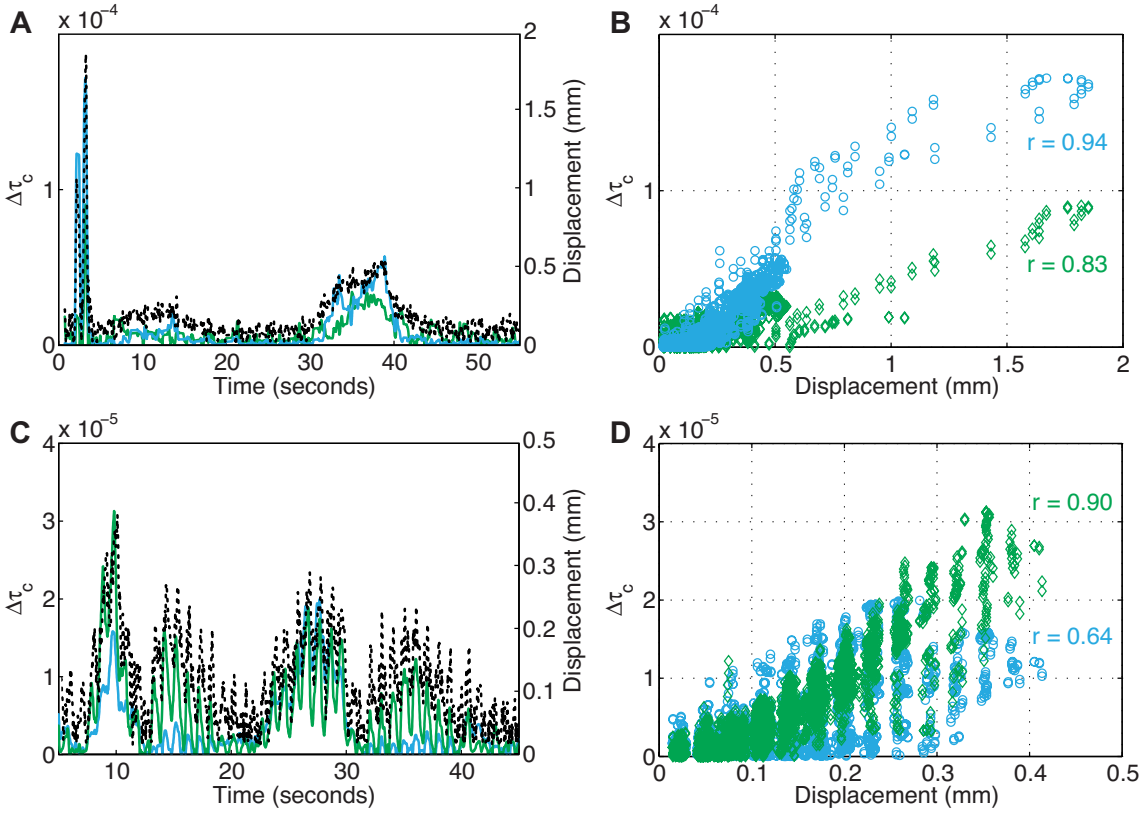

Figure 5.7: (A, C) The displacement is co-localized in time with the change in correlation time ($\Delta\tau_c$) for two ROIs from Figure 5.6B and 5.6E, respectively. Two ROIs are shown for each case to improve visibility on the plots, with colors corresponding to those in Figure 5.6. The black dashed line corresponds to the displacement. (B, D) Correlation between the displacement and $\Delta\tau_c$ for (A, C), respectively, with the Pearson's correlation coefficient listed for each ROI. Adapted from [9].

Quantitative analysis confirmed that both vessel and parenchyma regions had statistically significant noise reduction after ECG filtering plus registration, as shown in Figure 5.8. Noise was quantified as the standard deviation of the CBF % over the recorded time course for each ROI analyzed. Noise levels were compared for the original recorded images versus ECG filtering alone, image registration alone, and ECG filtering plus image registration. The scenarios highlighted in the plots from Figure 5.6 are ECG

filtering alone and ECG filtering plus image registration. As shown in Figure 5.8, ECG filtering alone causes a statistically significant noise reduction in the parenchyma regions ($15\% \pm 3\%$ to $8.3\% \pm 2.7\%$, $p \leq 10^{-5}$). Registration alone causes a statistically significant noise reduction in the vessel regions relative to ECG filtering alone ($38\% \pm 25\%$ to $16\% \pm 5.8\%$, $p \leq 0.05$), as well as a large reduction relative to the vessel noise in the original set. These motion correction techniques could be used individually if the image application focused on only certain tissue types. However, the most dramatic noise reduction is seen after combining both ECG filtering and image registration, which had a statistically significant noise reduction for all tissue regions. Combined ECG filtering and image registration significantly reduced the noise across all ROIs to $6.2\% \pm 2.6\%$. This was statistically significant compared to the original set ($25\% \pm 27\%$, $p \leq 0.05$), ECG filtering alone ($20\% \pm 21\%$, $p \leq 0.05$), and image registration alone ($15\% \pm 4\%$, $p \leq 10^{-5}$). This significant noise reduction is consistent with the significant spatial de-noising observed in a rodent study using a similar image registration procedure [27]. Although the noise quantification in this study assesses the temporal noise over the duration of the time course, it confirms spatial de-noising as well since the temporal noise arises from spatial sampling of different tissue regions during motion. Overall, this noise reduction makes it possible to visualize small changes in flow from any tissue region.

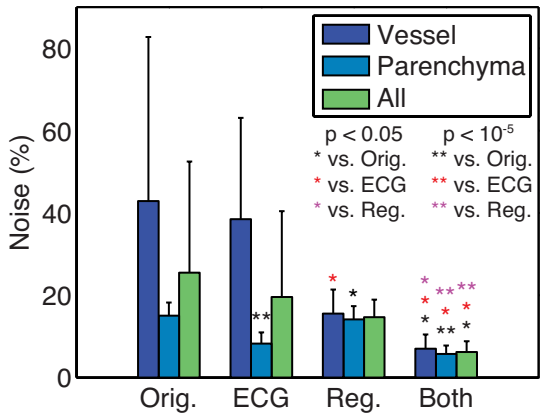

Figure 5.8: Quantification of noise (standard deviation of CBF %) before and after ECG filtering and translation-based image registration across ROI groups from baseline cases 1, 5, 7, and 9. Statistical significance is calculated using a right-tailed t-test. Sample sizes are $N = 6$ for vessel ROIs, $N = 10$ for parenchyma ROIs, and $N = 16$ for all ROIs. Orig. = original data set; ECG = ECG filtering only; Reg. = image registration only; and Both = ECG filtering plus image registration. Adapted from [9].

A comparison between the original and registered images is also shown for the three cortical stimulation patients 4, 6, and 10 in Figure 5.9. Similar to the baseline cases, large-scale fluctuations resulting from tissue motion make it difficult to accurately quantify and interpret the flow dynamics from the original time courses, especially in Figure 5.9B and 5.9E. After registration, the noise is largely suppressed and clear trends in CBF change are easily visualized in each case. Given the significant noise reduction of ECG filtering plus image registration from Figure 5.8, as well as the relatively flat blood flow profiles in the baseline cases from Figure 5.6, the change in blood flow visualized in the registered time courses of Figure 5.9 are true physiological changes occuring in those tissue regions. Quantification of the flow change confirms that region 5 experienced the smallest change from baseline in all cases with a flow reduction of 24%, flow increase of 31%, and flow decrease of 46% for Figures 5.9C, 5.9F, and 5.9I, respectively. This improved sensitivity to small changes in flow increases LSCI's

applicability and utility as a neurosurgical monitoring tool. Although LSCI can only provide relative flow information, the ability to identify changes in blood flow before and after surgical manipulation is clinically most important. LSCI provides both the relative magnitude and the temporal dynamics of the blood flow change with the help of motion correction, which is the information the surgeon needs for clinical decision making. Removing tissue motion artifacts also increases the accuracy of the results and patient safety, as the original region 5 time courses misleadingly suggested larger flow reductions in Figures 5.9B and 5.9E that may have prompted unnecessary surgical action. Although translation-based image registration is computationally intensive, combined ECG filtering and image registration provides the highest level of noise reduction, allowing visualization of blood flow changes. These results suggest that intraoperative implementation of real-time motion compensation techniques will increase the value and efficacy of LSCI as a CBF monitoring tool.

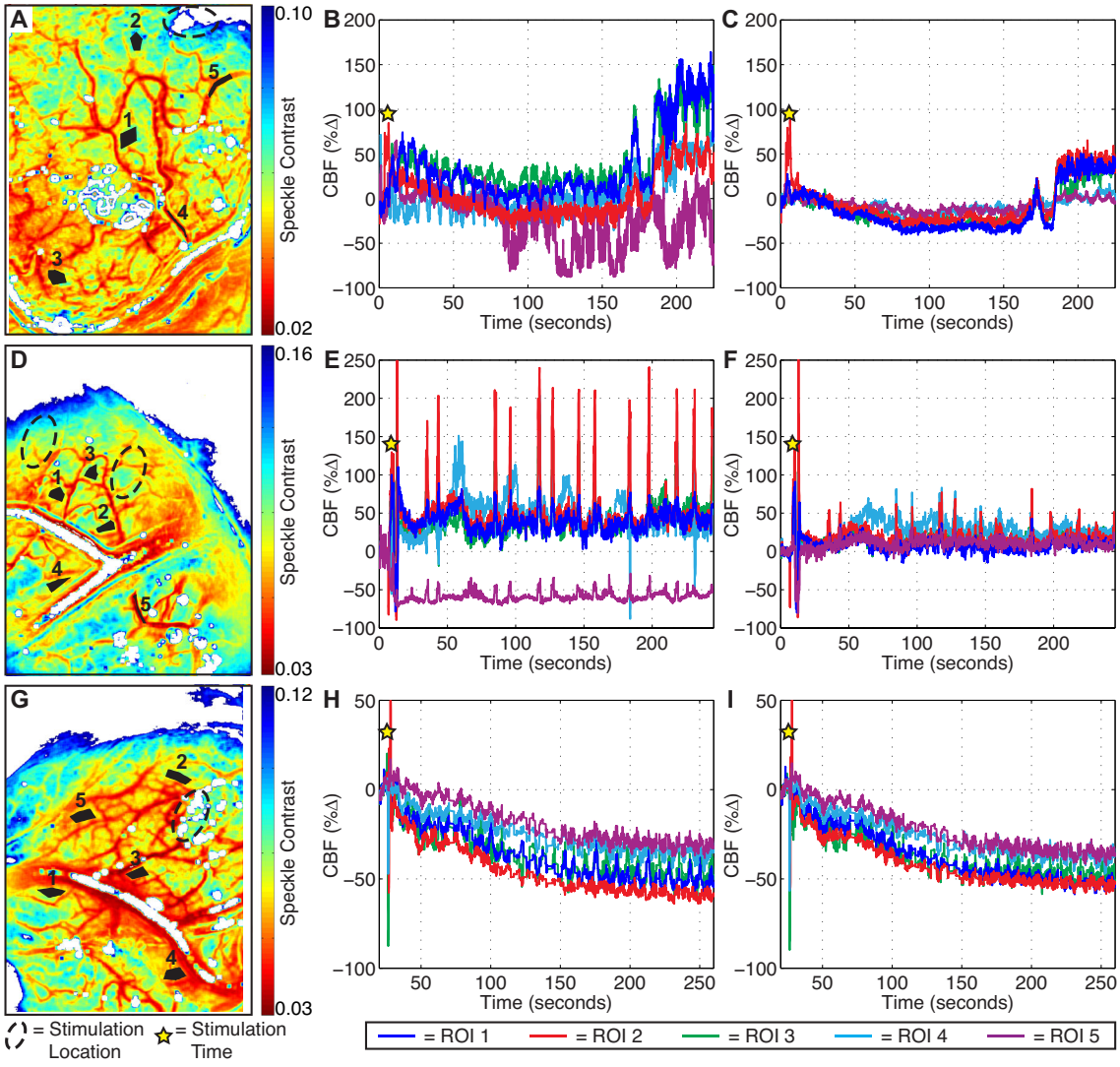

Figure 5.9: A comparison between the time courses of ROIs before and after translation-based image registration for cortical stimulation patients 4, 6, and 10 in parts (A-C), (D-F), and (G-I), respectively. (A, D, G) The speckle contrast image at the start of acquisition shows five numbered ROIs overlaid in black where analysis is taking place. The dashed black oval indicates the location of stimulation in the camera FOV. The middle column of plots (B, E, H) displays the time course of the original recorded CBF %Δ during intraoperative acquisition, where the yellow star indicates the time that stimulation occurred. The right column of plots (C, F, I) displays the time course of the CBF %Δ after translation-based image registration. Plots from the same patient are shown with the same axes for comparing ROI curves before and after registration. Adapted from [9].

Since brain tissue may deform after skull removal, a nonrigid transform may be required to account for axial tissue deformation. Because of increased computational costs, B-spline nonrigid registration was performed on a subset of the pilot study data from four baseline patients for comparison to the translation transform. Representative results are shown for a single patient in Figure 5.10. Similar to the results from the baseline patients in Figure 5.6, both registration methods greatly reduce fluctuations and improve stability, with the most significant impact on the vessel ROI and visible improvement on the parenchyma regions placed near vessels. When Figures 5.10C and 5.10D are directly compared, the time courses are visually similar between the two methods, despite the additional correction for axial tissue deformation artifacts from B-spline registration. Quantitatively, the average percent difference between rigid and nonrigid registration methods is displayed in Table 5.2 for the ROIs shown in Figures 5.6A, 5.6D, 5.6G, and 5.10A. Although B-spline registration is effective for removing residual nonrigid tissue deformation artifacts that occur in the axial direction, the difference compared to translation registration was minimal, with <1% difference for 11/16 ROIs and <3% difference for 15/16 ROIs. Region 4 in Figure 5.10A had the largest discrepancy with a 7% difference. However, the improvement of the B-spline registration was only moderate relative to translation registration when viewing region 4 over time with a low impact on overall visualization. On the whole, the lower complexity translation registration had excellent agreement with B-spline registration. The improved motion correction indicated by the small percent differences would not change the course of treatment in an intraoperative monitoring setting, confirming that translation registration is sufficient to reduce computational costs.

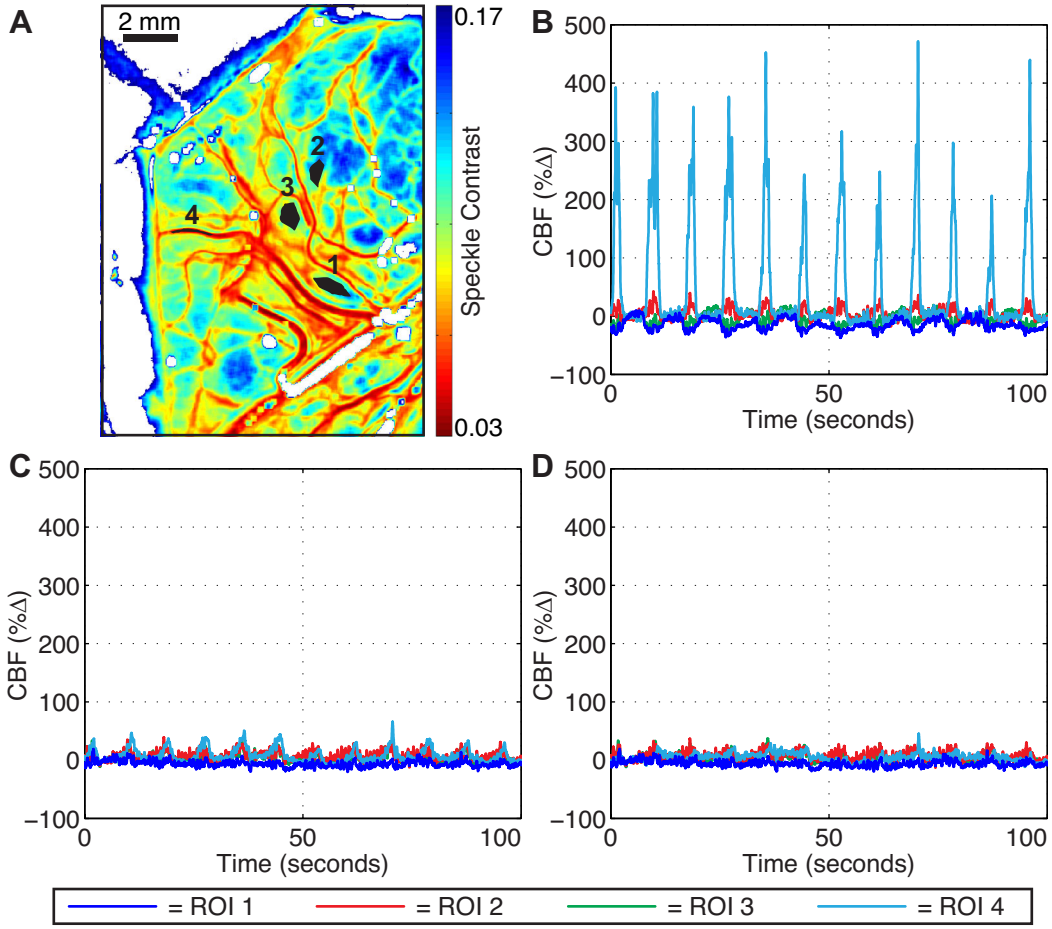

Figure 5.10: A comparison between translation-based rigid registration and B-spline-based nonrigid registration illustrated with the time courses of ROIs for a single baseline patient 5. (A) The speckle contrast image at the start of acquisition shows four numbered ROIs overlaid in black where analysis is taking place. (B) The original recorded CBF %Δ during course of intraoperative acquisition. (C) The time course of the CBF %Δ after translation-based image registration. (D) The time course of the CBF %Δ after B-spline-based image registration. All plots are shown with the same axes for comparing ROI curves before and after registration, as well as between registration methods. Adapted from [9].

Table 5.2: Average and standard deviation of the percent difference between translation and B-spline registration over the time course of image acquisition. The regions correspond to the four numbered ROIs in Figures 5.6A, 5.6D, 5.6G, and 5.10A. Adapted from [9].

Region	5.6A	5.6D	5.6G	5.10A
1	0.58 ± 0.44	0.19 ± 0.14	0.59 ± 0.42	0.61 ± 0.48
2	0.35 ± 0.28	0.76 ± 0.51	0.21 ± 0.17	0.66 ± 0.48
3	1.6 ± 1.2	1.5 ± 1.3	0.32 ± 0.29	0.33 ± 0.23
4	0.39 ± 0.29	2.9 ± 2.6	1.1 ± 0.87	7.0 ± 5.1

5.6 DISCUSSION

The results from this study demonstrate that retrospective motion correction techniques can dramatically improve the accuracy for quantitatively monitoring relative blood flow over time. However, other groups who have tested LSCI intraoperatively have not investigated the impact of motion compensation [1-5], which may be due to inherent differences in the instrumentation. Compared to the commercial LSCI system used in the majority of those studies, the LSCI hardware was integrated into the neurosurgical microscope for this study. This had many benefits, including improving the surgical workflow, reducing setup time for imaging, and increasing the surgeon's familiarity with the instrument. However, the magnified imaging through the microscope in this study led to a relatively small FOV (~1.5 × 2 cm compared to 5 × 5 cm [2] up to 18 × 24 cm [5]). This made tissue motion compensation more critical, since smaller pixel resolution results in a larger relative tissue displacement in the images. A recent study also adapted the Zeiss neurosurgical microscope for performing LSCI [3], placing a camera on the rear assistant port using a beamsplitter and illuminating with a separately mounted 780 nm laser diode. The rear assistant port was used because both the main and assistant ports on the microscope pass NIR light, in contrast to the side viewing ports which have internal NIR blocking filters. Despite the fact that this group also used the

neurosurgical micrscope, their magnification was much less and the FOV appears to be several centimeters, as evidenced by their surgical photographs. Although not as sensitive to motion, large FOV images can still benefit from motion correction. This is evident from a CBF time course shown from the same group, where large scale periodic fluctuations are visible from tissue parenchyma ROIs before and after flow interruption during a bypass procedure [3].

Another difference was the 4× faster frame rate of the camera used in this study [5]. At rapid image acquisition, the camera more accurately captures the inherent physiological motion, which was why both cardiac and tissue motion correction significantly reduced CBF fluctuations in this study. The faster frame rate was beneficial because it allowed more averaging of the acquired images, which improved the SNR in the image and ROI analysis. In this section, averaging was performed using a moving average filter in post-processing as part of the ECG filtering step. For real-time display, five-frame averaging could be performed to improve the SNR, resulting in an effective frame rate of 20 fps. As magnified LSCI becomes more widely investigated and as camera frame rates continue to increase, motion compensation will only become more important.

5.7 CONCLUSIONS

The results from this 10-patient pilot study are promising, and demonstrate the feasibility of using LSCI to monitor blood flow changes during neurosurgery. This general feasibility has also been confirmed from intraoperative LSCI assessments performed by other groups. This pilot study also demonstrated the ability to perform LSCI in real-time with high spatiotemporal resolution and with minimal interruption to the surgical procedure using a microscope-integrated LSCI system. Excellent

correspondense between the anatomical vasculature and LSCI blood flow maps was observed in four cases, even with the presence of blood pools in the FOV. The *ad hoc* ECG filtering method consistently reduced the beat-to-beat blood flow fluctuations, and using a custom filter for each ROI eliminated issues with cardiac variability across spatial regions. Image registration had a dramatic impact on the time course of the recorded CBF signal, and significantly reduced noise caused by the ROI spatially sampling surrounding tissue regions. This noise reduction allowed detection of blood flow changes after cortical stimulation, which increases the applicability of LSCI in a neurosurgical setting. LSCI has the potential to be a valuable intraoperative monitoring tool for a variety of neurosurgical procedures, and should be studied further for possible addition to the current collection of available monitoring options. Future work should include development of real-time motion correction techniques to allow intraoperative feedback with improved sensitivity to blood flow changes.

5.8 REFERENCES

[1] N. Hecht, J. Woitzik, J. P. Dreier, and P. Vajkoczy, "Intraoperative monitoring of cerebral blood flow by laser speckle contrast analysis," *Neurosurgical Focus,* **27**(4), pp. E11 (2009).

[2] N. Hecht, J. Woitzik, S. Konig, P. Horn, and P. Vajkoczy, "Laser speckle imaging allows real-time intraoperative blood flow assessment during neurosurgical procedures," *Journal of Cerebral Blood Flow & Metabolism,* **33**(7), pp. 1000-1007 (2013).

[3] S. Nomura, T. Inoue, H. Ishihara, H. Koizumi, E. Suehiro, F. Oka, and M. Suzuki, "Reliability of laser speckle flow imaging for intraoperative monitoring of cerebral blood flow during cerebrovascular surgery: comparison with cerebral blood flow measurement by single photon emission computed tomography," *World Neurosurgery,* **82**(6), pp. e753-757 (2014).

[4] E. Klijn, H. C. Hulscher, R. K. Balvers, W. P. Holland, J. Bakker, A. J. Vincent, C. M. Dirven, and C. Ince, "Laser speckle imaging identification of increases in cortical microcirculatory blood flow induced by motor activity during awake craniotomy," *Journal of Neurosurgery,* **118**(2), pp. 280-286 (2013).

[5] J. Woitzik, N. Hecht, A. Pinczolits, N. Sandow, S. Major, M. K. Winkler, S. Weber-Carstens, C. Dohmen, R. Graf, A. J. Strong, J. P. Dreier, and P. Vajkoczy, "Propagation of cortical spreading depolarization in the human cortex after malignant stroke," *Neurology,* **80**(12), pp. 1095-1102 (2013).
[6] A. B. Parthasarathy, E. L. Weber, L. M. Richards, D. J. Fox, and A. K. Dunn, "Laser speckle contrast imaging of cerebral blood flow in humans during neurosurgery: a pilot clinical study," *Journal of Biomedical Optics,* **15**(6), pp. 066030 (2010).
[7] L. M. Richards, E. L. Weber, A. B. Parthasarathy, K. L. Kappeler, D. J. Fox, and A. K. Dunn, "Intraoperative laser speckle contrast imaging for monitoring cerebral blood flow: results from a 10-patient pilot study," *Proceedings of SPIE, Photonic Therapeutics and Diagnostics VIII,* **8207**(82074L), pp. 1-12 (2012).
[8] L. M. Richards, E. L. Towle, D. J. Fox, and A. K. Dunn, "Laser Speckle Imaging of Cerebral Blood Flow," in *Optical Methods and Instrumentation in Brain Imaging and Therapy*, S.J. Madsen, Ed.: Springer New York, 2013, pp. 117-136.
[9] L. M. Richards, E. L. Towle, D. J. Fox, Jr., and A. K. Dunn, "Intraoperative laser speckle contrast imaging with retrospective motion correction for quantitative assessment of cerebral blood flow," *Neurophotonics,* **1**(1), pp. 015006 (2014).
[10] S. M. S. Kazmi, L. M. Richards, and A. K. Dunn, "Cerebral Blood Flow Imaging with Laser Speckle Contrast Imaging," in *Neurovascular Coupling Methods*, M. Zhao, H. Ma, and T. H. Schwartz, Eds., New York: Springer Science+Business Media, 2014, pp. 287-305.
[11] "American National Standard for the Safe Use of Lasers," in *ANSI Z136.1-2007*: Laser Institute of America, 2007.
[12] W. J. Tom, A. Ponticorvo, and A. K. Dunn, "Efficient processing of laser speckle contrast images," *IEEE Transactions on Medical Imaging,* **27**(12), pp. 1728-1738 (2008).
[13] A. K. Dunn, H. Bolay, M. A. Moskowitz, and D. A. Boas, "Dynamic imaging of cerebral blood flow using laser speckle," *Journal of Cerebral Blood Flow & Metabolism,* **21**(3), pp. 195-201 (2001).
[14] C. Ayata, A. K. Dunn, Y. Gursoy-Özdemir, Z. Huang, D. A. Boas, and M. A. Moskowitz, "Laser speckle flowmetry for the study of cerebrovascular physiology in normal and ischemic mouse cortex," *Journal of Cerebral Blood Flow & Metabolism,* **24**(7), pp. 744-755 (2004).
[15] S. Yuan, A. Devor, D. A. Boas, and A. K. Dunn, "Determination of optimal exposure time for imaging of blood flow changes with laser speckle contrast imaging," *Applied Optics,* **44**(10), pp. 1823-1830 (2005).
[16] A. Raabe, D. Van De Ville, M. Leutenegger, A. Szelenyi, E. Hattingen, R. Gerlach, V. Seifert, C. Hauger, A. Lopez, R. Leitgeb, M. Unser, E. J. Martin-Williams, and T. Lasser, "Laser Doppler imaging for intraoperative human brain mapping," *NeuroImage,* **44**(4), pp. 1284-1289 (2009).
[17] R. H. Deckers, P. van Gelderen, M. Ries, O. Barret, J. H. Duyn, V. N. Ikonomidou, M. Fukunaga, G. H. Glover, and J. A. de Zwart, "An adaptive filter

for suppression of cardiac and respiratory noise in MRI time series data," *NeuroImage,* **33**(4), pp. 1072-1081 (2006).
[18] D. Dan, J. B. Hoag, K. A. Ellenbogen, M. A. Wood, D. L. Eckberg, and D. M. Gilligan, "Cerebral blood flow velocity declines before arterial pressure in patients with orthostatic vasovagal presyncope," *Journal of the American College of Cardiology,* **39**(6), pp. 1039-1045 (2002).
[19] P. Zakharov, F. Scheffold, and B. Weber, "Laser Speckle Analysis Synchronized with Cardiac Cycle," *Proceedings of SPIE, Novel Biophotonics Techniques and Applications III,* **9540**(954008), pp. 1-9 (2015).
[20] S. Klein, M. Staring, K. Murphy, M. A. Viergever, and J. P. Pluim, "elastix: a toolbox for intensity-based medical image registration," *IEEE Transactions on Medical Imaging,* **29**(1), pp. 196-205 (2010).
[21] T. M. Cover and J. A. Thomas, *Elements of Information Theory*, 2nd ed.: John Wiley & Sons, Inc., 2006.
[22] C. Studholme, D. L. G. Hill, and D. J. Hawkes, "An overlap invariant entropy measure of 3D medical image alignment," *Pattern Recognition,* **32**(1), pp. 71-86 (1999).
[23] S. Klein, J. P. Pluim, M. Staring, and M. A. Viergever, "Adaptive Stochastic Gradient Descent Optimisation for Image Registration," *International Journal of Computer Vision,* **81**(3), pp. 227-239 (2009).
[24] Michael Unser. (1999) Splines: A Perfect Fit for Signal and Image Processing. *IEEE Signal Processing Magazine*, pp. 22-38.
[25] S. Klein and M. Staring, "Elastix: the manual," http://elastix.isi.uu.nl, 2014.
[26] D. Rueckert, L. I. Sonoda, C. Hayes, D. L. Hill, M. O. Leach, and D. J. Hawkes, "Nonrigid registration using free-form deformations: application to breast MR images," *IEEE Transactions on Medical Imaging,* **18**(8), pp. 712-721 (1999).
[27] P. Miao, A. Rege, N. Li, N. V. Thakor, and S. Tong, "High resolution cerebral blood flow imaging by registered laser speckle contrast analysis," *IEEE Transactions on Biomedical Engineering,* **57**(5), pp. 1152-1157 (2010).

Chapter 6: Phase II Clinical Study – Instrument Optimization and Multi-Exposure Speckle Imaging

For the phase II clinical study described in this chapter, the first objective was to build upon the results from the pilot study by optimizing the instrument design for improved image quality. The primary goal arises from the presence of imaging artifacts in almost all acquired images from the pilot study, shown by white regions of specular reflections scattered throughout the images. Some examples where this was especially prominent are Case 1 (Figure 5.6A), Case 4 (Figure 5.9A), Case 5 (Figure 5.10A), Case 6 (Figure 5.9D), and Case 10 (Figure 5.9G). The specular reflection blocks out a big area of the tissue parenchyma in some cases, while others show that the specular reflection follows the centerline of the larger vessels due to the vessel wall thickness. These artifacts make it impossible to accurately measure blood flow in those tissue regions, and effectively reduce the area of usable blood flow information. To reduce the impact of these specular reflections, it is imperative to implement a polarizer before the camera. Because light reflecting off the cortical surface is partially polarized, a polarizer can be used to block the polarization plane of the reflections to greatly reduce glare in the recorded image. This was not implemented earlier in the pilot study because it requires customization of the hardware attachments for LSCI, since extra space is required between the camera adapter and the camera for the polarizer. Another imaging artifact present in the pilot study was the high absorption of 660 nm light by hemoglobin, which led to a much lower mean intensity value inside vessels and produced an edge artifact around larger size vasculature. This is most obviously seen in Case 6 (Figure 5.9D), where the large Y-shaped vessel in the middle of the imaging field has a rim of high speckle contrast values surrounding it. To reduce the impact of total hemoglobin

absorption, the wavelength of light needs to be shifted farther into the NIR range, as shown by Figure 6.1. Although 660 nm is already in a region of low hemoglobin absorption often called the "optical window" as shown in the full spectra, the zoomed inset shows that >2× reduction in total hemoglobin absorption can be achieved by shifting the wavelength to 785 nm. This wavelength choice is also optimal because it can also be used to simultaneously excite ICG fluorescence [1], which would be useful for a future side-by-side clinical comparison. This wavelength switch was not implemented earlier in the pilot study because it required an extra adapter to connect to a different eyepiece port, since the side port had NIR blocking filters.

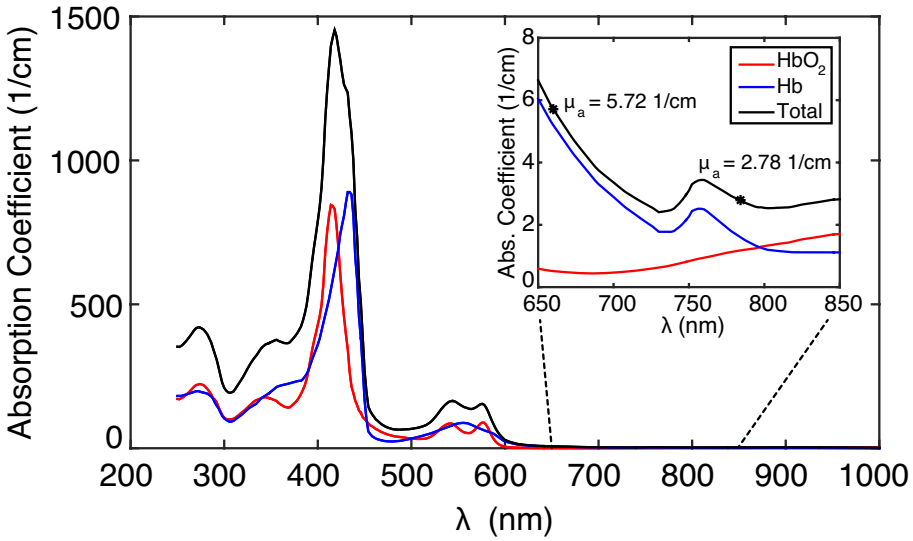

Figure 6.1: Absorption spectra of hemoglobin, assuming a concentration of 150 g/L [2]. Oxygenated hemoglobin (HbO_2) is shown in red, deoxygenated hemoglobin (Hb) is shown in blue, and the total hemoglobin from the addition of both HbO_2 and Hb is shown in black. In the zoomed inset, the total absorption coefficient μ_a is shown for both 660 nm and 785 nm (locations indicated by the black stars), with >2× reduction in absorption.

The second objective was to maximize sensitivity to blood flow in clinical size vasculature, which was performed by changing image acquisition parameters. The first

primary question is what camera exposure time has the best sensitivity to the faster flows present in the larger vessels seen on the human cortical surface. Previous studies have shown that 5 ms exposure time had the best sensitivity for visualizing blood flow changes in the rodent somatosensory cortex [3]. However, the caliber of clinical size vessels is much larger and their associated flow rates are much faster. To visualize faster flow rates with better sensitivity, a shorter exposure time is required. Despite this known trend, most of the clinical studies that assess LSCI during neurosurgery use camera exposure times that are on the same order or longer than this 5 ms exposure time benchmark. The pilot clinical study in Chapter 5 used an exposure time of 5 ms to match the rodent study. Other published studies have used an exposure time of 4 ms [4, 5], 8.4 ms [4, 6], 16 ms [7], and 20 ms [8]. Some of these studies focus on blood flow in parenchyma tissue regions, which may explain the longer exposure time choice, while others may have been simply light limited [7]. No studies have shown the difference in flow sensitivity visualized in the human cortex with an exposure time <4 ms. Because optimizing sensitivity to flow change is critical for clinical adoption of LSCI, one of the main objectives of this chapter is to determine what exposure time provides the best sensitivity to flows across the imaging field.

To explore the relationship between the exposure time and measured speckle contrast in a clinical setting, multiple camera exposure times were recorded from patients 15 – 24 with the same camera FOV. In addition to visualizing each exposure time independently, the images from each exposure were analyzed together using the Multi-Exposure Speckle Imaging (MESI) model [9]. This model maps the speckle contrast using a range of camera exposure times and is able to achieve higher quantitative accuracy in the computed correlation times [9-11]. MESI-computed inverse correlation times are highly correlated with absolute velocities measured by red blood cell (RBC)

tracking *in vivo* [11], and have high agreement with direct temporal autocorrelation measurements both *in vitro* and *in vivo* [12]. In comparison to single exposure LSCI at 5 ms, the relationship with absolute velocities measured using RBC tracking showed higher deviation and weaker correlation *in vivo* [11]. By sampling only a single exposure time, LSCI is only sensitive to a small portion of the flow range within the camera FOV. The accuracy of LSCI is also affected by instrumentation factors, including illumination variations and noise across imaging sessions, as well as the proportion of dynamic versus static scattering contribution in the recorded light. The MESI model attempts to account for all of these variables by mapping the speckle contrast to the correlation time utilizing the dependence on camera exposure. The model also accounts for mixing of statically and dynamically scattered light as well as exposure-independent noise and the non-ergodic variance associated with spatial analysis of a temporal phenomenon [9, 11]. Thus, utilizing the MESI model provides a more quantitatively accurate view of the true CBF dynamics, and is examined intraoperatively here for the first time.

6.1 INSTRUMENTATION

To optimize performance of the LSCI adapted surgical microscope, two of the primary design changes were to integrate a polarizer in front of the camera to reduce the impact of specular reflections and to switch to a NIR laser diode to reduce the effects of hemoglobin absorption. A schematic and photograph of the modified instrument design is shown in Figure 6.2. Similar to the previous study, all hardware components were attached prior to the start of the surgery, and did not interfere with normal use of the microscope during the procedure. Because the modified design required extra attachments, the adapted LSCI hardware added ~3 kg weight to the microscope. The

microscope only allows a total of 6 kg added weight, which means that only one assistant eyepiece (side or rear) could be attached with our LSCI hardware. This is a limitation of the design that could be improved by further customizing the add-ons to reduce the weight of the hardware attachments. However, this was not an issue for the procedures in this extended study, since all procedures only required a side assistant eyepiece.

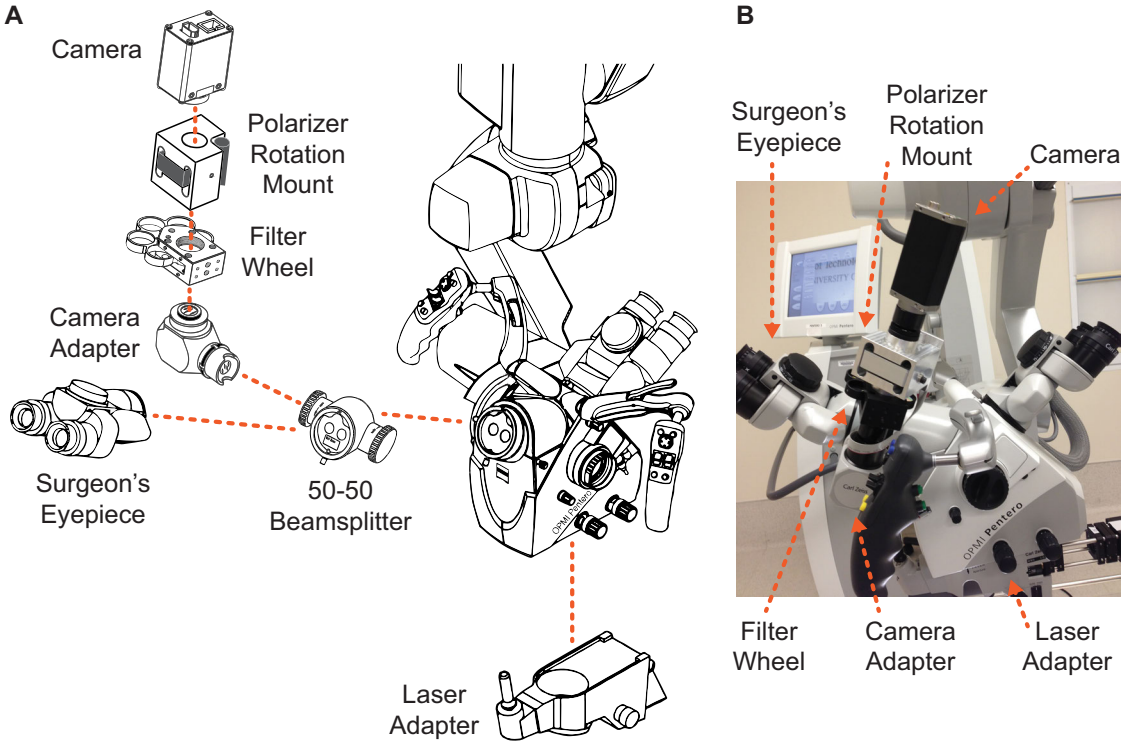

Figure 6.2: Optimized Zeiss OPMI neurosurgical microscope adapted to measure cerebral blood flow intraoperatively using LSCI. (A) Schematic of the intraoperative instrumentation, showing the hardware attachments for LSCI and how they fit into the existing microscope system. Drawings were adapted from the Zeiss OPMI Pentero Manual Issue 9.3. Filter wheel drawing adapted from Thorlabs Inc. (B) Photograph of the modified intraoperative instrumentation with add-on components labels.

The 785 nm, 300 mW laser diode used in this study (LD785-SH300, Thorlabs Inc.) was incorporated into the add-on laser adapter similar to the previous study for

attachment to the bottom of the microscope head. The coherence length of this laser diode model was tested in Chapter 2 and is >10 m. A set of lenses was used to re-shape the highly elliptical beam from the diode using a cage system that attached to the back of the laser adapter. The beam travels linearly through the adapter, and a 1" diameter convex mirror directed the beam towards the cortex and expanded the beam size. Because the beam expands along the path, the beam size varies depending on the working distance of the microscope relative to the surface of the cortex. The beam size was optimized for ~2 × 1.5 cm size at a working distance of 12", but the working distance of each case varied depending on how the surgeon positioned the microscope. Similar to the previous study, the surgeon used the steering toggle to position the beam on the tissue surface to the area of interest. The laser power was adjusted using a laser diode controller, and a temperature controller was used to ensure maximum stability (10.5 kΩ, 23.9°C). The laser power was measured to be 0.12 W/cm^2 at the maximum operating current used in the study for a 2 cm beam size. Although this is higher than the power used in the pilot study, it is still well below the ANSI standard of 0.3 W/cm^2 for MPE to a near infrared light source at 785 nm [13]. Therefore, the potential risks associated with the laser level were minimal, and no adverse effects were reported.

Because the laser wavelength is now NIR, the LSCI camera had to be moved to either the main surgeon's eyepiece or the rear assistant eyepiece, since both allowed passage of NIR light. A 50-50 beamsplitter (Carl Zeiss Meditec Inc.) was used to attach the camera adapter to the main surgeon's eyepiece, since it receives the highest percentage of light across all eyepiece ports. Due to the beamsplitter configuration, the LSCI camera receives 12.5% of the total light split within the microscope. After the camera adapter, the design integrates relay lenses to extend the imaging arm for placement of both a filter wheel and polarizer rotation mount before the camera. The

relay lenses used were $f = 60$ mm achromatic doublets (AC254-060-B, Thorlabs Inc.), and were placed inside the threaded holes on the custom machined aluminum adapter for the polarizer rotation mount. C-mount fine focus tubes (58-736, Edmund Optics Inc.) were used on either side of the filter wheel and rotation mount to allow precise control of the relay lens position for optimal focus at the conjugate imaging plane and the camera sensor. The filter wheel (CFW6, Thorlabs Inc.) was used for swapping between various neutral density filters for the latter patients in the study. A polarizer (LPNIR100, Thorlabs Inc.) was secured inside a motorized rotation mount (RSC-100, Pacific Laser Equipment Inc.). A rotation mount is required to allow orientation of the transmission axis of the polarizer perpendicular to the polarization plane of the undesirable specular reflections present in the imaging field. Because the polarization angle of the reflections may vary depending on the microscope positioning, the polarizer must be able rotate for custom alignment during each case. Since the microscope must be under a sterile drape during operation, it would be difficult to finely control the rotation manually. Thus, a motorized mount that could be controlled remotely with higher precision was used, which simplified setup for the neurosurgeon controlling the microscope. Since an invisible NIR wavelength was used in this study, the laser illumination doesn't interfere with traditional color visualization using the built-in xenon lamp illumination. Thus, an NIR long pass filter (715 nm blocking edge, FF01-715/LP-25, Semrock Inc.) was added next to the polarizer to allow simultaneous imaging with LSCI during normal operation of the microscope under white light illumination. The camera followed the rotation mount, and the entire attachment above the camera adapter could be rotated to match the orientation of the Zeiss built-in color camera for comparison.

Two different cameras were used in this study: 1) the fast 8-bit CCD camera used in Chapters 2 – 4 (Basler Pilot piA640-210gm, Basler AG) was used for patients 11 – 14,

and 2) a NIR-enhanced CMOS camera sensor (Basler Ace acA1300-60gm-NIR, Basler AG) was used for patients 15 – 24. The first camera was an 8-bit camera with 150 fps effective frame rate with continuous data writing. The sensor size was 648 × 488 pixels and the pixel size was 7.4 μm. The second camera was an 8-bit, NIR-enhanced sensor with ~5× improvement in quantum efficiency at 785 nm, with a sensor size of 1280 × 1024 pixels and a pixel size of 5.3 μm. To improve camera frame rate and provide equivalent imaging area to the first camera, the second camera was recorded using a 905 × 681 pixel area of interest, which gave an effective frame rate of 75 fps. Although the frame rate was reduced in half with the second camera, the 5× improvement in light sensitivity was more critical for this study.

The automatic zoom and focus controls on the microscope were used to zoom into a tissue area of interest and focus the light onto the camera sensor. The relative position of the relay lens pair was adjusted such that the focus at the LSCI camera matched the focus of the built-in color camera to allow simultaneous recording with both cameras. Because the laser beam size was similar to the pilot study, the microscope was set for maximum zoom, providing ~3× demagnification relative to the camera sensor. Because the system was already light limited, an additional aperture was not used to control the speckle size. Since a longer wavelength was used in this study, the speckle size should be larger than the pilot study. The cameras used in this study also had smaller pixels, which means that the speckle sampling should be sufficient. The speckle size to pixel size ratio factors into the β term in Equation 1.4. For single-exposure speckle imaging in patients 11 – 14, the absolute value of β was not required, since relative flow visualization alone was used and β was set to 1. For multi-exposure speckle imaging in patients 15 – 24, an absolute value for β was calculated using an extra calibration step.

6.2 IMAGE DISPLAY AND ANALYSIS

Raw images were converted to speckle contrast images using Equation 1.1 with a 7×7 pixel window. Single exposure LSCI images were displayed as speckle contrast images, since they represent an instantaneous qualitative map of blood flow. In post-processing after each case, the image analysis procedure described in Chapter 5 was used, including image registration and cardiac filtering for ROI analysis. Because higher image registration accuracy was required to match multiple image sets across various exposure times, translation-based rigid registration was followed by B-spline based nonrigid registration to account for both lateral and axial movement artifacts, both using the NMI similarity metric. For this study, images across multiple exposure times were all registered to a single frame from a single exposure time. This provided spatial alignment across all recorded images, which was critical for combining multiple exposure times using the MESI model. Images were averaged over 50 frames after image registration for display and computation of MESI inverse correlation time (ICT) maps, which represent a quantitative map proportional to the instantaneous blood flow.

For single exposure LSCI analysis, speckle contrast images were converted to correlation time, τ_c, using Equation 1.4, where T was set to the exposure time used for data acquisition. For MESI analysis, the speckle visibility expression is given by,

$$K(T,\tau_c) = \left(\beta\rho^2 \frac{e^{-2x} - 1 + 2x}{2x^2} + 4\beta\rho(1-\rho)\frac{e^{-x} - 1 + x}{x^2} + \beta(1-\rho)^2 + v_{noise} \right)^{1/2} \quad (6.1)$$

where $x = T/\tau_c$, β represents the same instrumentation factor discussed previously, ρ represents the fraction of dynamically scattered light, and v_{noise} represents a constant noise term to account for shot noise and readout noise from the camera [9, 14]. Similar to Equation 1.4, this expression applies to the single scattering regime where photons are scattered from particles undergoing Brownian motion, and to the multiple scattering

regime where photons are scattered from particles undergoing bulk flow [15]. However, a scaling term that represents the average number dynamic scattering events must be included in the *x* term for the latter assumption [16]. This speckle visibility expression is a more robust model that applies to a wider range of imaging scenarios by accounting for the presence of static scattering as well as non-ergodic and camera-related noise. If there are no static scatterers, then $\rho \to 1$ and Equation 6.1 simplifies to Equation 1.4, with the exception of the v_{noise} term. If there are only static scatterers, then $\rho \to 0$ and the speckle contrast reduces to a constant value $\beta(1-\rho)^2 + v_{noise}$ independent of exposure time. This term represents the upper limit of the speckle variance K^2 as the exposure time T approaches infinity. The lower limit of K^2 as the exposure time T approaches 0 is given by $\beta + v_{noise}$. This can be approximated by β, since v_{noise} will be a small percentage of the total lower bound.

The minimum number of exposure times required to solve the MESI fitting is 4, since there are 4 unknowns (τ_c, β, ρ, v_{noise}). The MESI model was fit using nonlinear least-squares with the least absolute residual method. Because the speckle variance is dependent on the camera exposure time, the speckle variance K^2 is commonly plotted against the exposure time T on a semi-logarithmic scale since the first demonstration of MESI [9] to visualize how well the model fits the experimental results. These curves will be shown for the MESI analysis both to assess the goodness of fit, and to view the shape of the curve for each ROI. When a large enough exposure time range is used to assess the flows within a sample, a sigmoidal curve will be seen that starts at $\beta + v_{noise}$ at the smallest exposure and decays down to $\beta(1-\rho)^2 + v_{noise}$ at the longest exposure. The rate of the decay is inversely related to τ_c within the ROI, and thus proportional to the flow (faster decay corresponds to faster flow, and vice versa). This relationship is visualized

for six selected ROIs spanning both vessel and parenchyma regions across six patients to assess whether the data follows the expected physiological trend in Section 6.5.2.

For image display in this chapter, all single exposure images are displayed with individual color bars that have been scaled to span the full range of the speckle contrast histogram. White regions correspond to areas outside this range, and usually indicate specular reflections, image saturation, or poor illumination. The MESI ICT images displayed are also individually scaled so that the color bar spans the full range of the ICT histogram. These images are displayed on a logarithmic scale due to the large range of the image data.

6.3 Intraoperative Procedure

All experiments were performed during neurosurgeries at the NeuroTexas Institute at St. David's Medical Center in Austin, TX. The clinical study extension was approved by the Institutional Review Boards of the University of Texas at Austin and St. David's Medical Center (Austin Multi-Institutional Review Board), and written informed consent was obtained from all patients. A summary of the patient details for the phase II clinical study is shown in Table 6.1. Patients 11 – 21 were brain tumor resection procedures and will be presented in this chapter. Recently, a few neurovascular procedures were imaged with patients 22 – 24, including aneurysm clipping and arteriovenous malformation resection, but more clinical cases are required before conclusions can be drawn from these types of procedures. Similar to the previous study, all hardware attachments were attached to the microscope before the procedure, and the microscope was re-balanced and checked by the main surgeon before use. The microscope was then covered in a sterile drape so that it could be used as part of the procedure. LSCI imaging was performed at the discretion of the surgeon, with imaging

time relative to the main surgical intervention in Table 6.1. Prior to LSCI imaging, the surgeon positioned the microscope over the cortical area of interest and adjusted the focus and zoom as needed. Saline was flushed over the cortical surface to reduce specular reflections, and the polarizer was rotated until specular reflections were maximally eliminated in the camera FOV.

For patients 11 – 13, a single exposure time (5 ms) was recorded with camera #1 (150 fps), mostly to assess the performance of the modified instrument design. Light limitations also did not allow using a shorter exposure time with this camera. For patients 15 – 21, multiple exposure times were recorded using camera #2, which was integrated to allow imaging with shorter exposure times. To combine images acquired across multiple exposure times using the MESI model, it is important to maintain equivalent light levels to minimize the variations in shot noise. Thus, the illumination intensity was matched as closely as possible using the raw image histogram peak displayed live in the custom image acquisition software. For patients 15 – 19, the laser intensity was adjusted by lowering the drive current on the laser diode controller. The shortest exposure was acquired at the operating current (425 mA), and longer exposures were acquired at reduced current levels down to 110 mA. For patients 20 – 21, the laser intensity was adjusted using various neutral density filters (Edmund Optics Inc.) placed inside the 6-slot filter wheel. The first slot had an optical window to allow full transmission of light with no attenuation at the operating current. The five subsequent slots had different optical density (OD) filters placed inside to control the laser power. Because it was difficult to predict exactly what OD would be required for each exposure time, small variations in laser current were still required. For patient 21, all recorded images maintained a laser current >260 mA and 5 of the 8 exposures were recorded at the operating current (425 mA). To swap to a different OD filter, the surgeon was asked to

manually rotate the filter wheel in the desired direction, which was demonstrated before the start of the procedure.

During the imaging session, the camera exposure signal as well as the patient's ECG and blood pressure signal were recorded simultaneously (ME590257P, Maguire Enterprises Inc.). Either the ECG or BP signal were used in post-processing for retrospective cardiac cycle motion compensation for ROI analysis, and for selection of images from the same region of the cardiac cycle for MESI ICT image generation. Baseline blood flow images were recorded in all cases. For the cases that indicate imaging before and after the surgical intervention in Table 6.1, this simply indicates multiple imaging sessions of different cortical tissue regions recorded at different time points during the procedure. Imaging following an induced change in flow was not performed in this study. For all cases, imaging time was limited to a total of 15 minutes to minimize additional risks for extended time under anesthesia. At the end of the procedure, the LSCI hardware was removed from the microscope and it was re-balanced for normal use. Even with the modified LSCI instrument design presented in this study, the microscope could still be used to assist with the procedure and did not interfere with normal use of the microscope, including ICG fluorescence using IR 800 mode. This fact is an important point, since LSCI is designed as a useful add-on to the current surgical microscope, and the instrument design should not detract from built-in functionality.

Table 6.1: Clinical patient overview for the Phase II clinical study. Patients 11 – 21 were undergoing brain tumor resection procedures. Patients 22 and 24 were undergoing an aneurysm clipping. Patient 23 was undergoing a right arteriovenous malformation (AVM) resection after rupture. All patients were imaged at the discretion of the surgeon, with imaging time relative to the tumor/ AVM resection or clipping procedure listed below.*

Patient	Gender	Age	1st Brain Surgery?	Previous Treatment?	Craniotomy Position	LSCI vs. Resection?	Camera	Exposure Time (ms)
11	F	42	Y	N/A	L Frontal	Before	150 Hz	5
12	F	70	Y	XRT, Chemo	R Parietal, R Posterior Fossa	After	150 Hz	5
13	F	67	Y	N/A	IH fissure	Both	150 Hz	5
14	M	65	Y	N/A	L Frontal	Before	150 Hz	5 – 25
15	M	28	Y	N/A	R Frontal	After	75 Hz NIR-E	1 – 5
16	M	56	Y	N/A	L Temporal	After	75 Hz NIR-E	0.5 – 5
17	M	85	Y	N/A	Bifrontal	Before	75 Hz NIR-E	0.5 – 5
18	F	31	Y	N/A	R Frontal	After	75 Hz NIR-E	0.5 – 5
19	M	60	Y	N/A	R Frontal	After	75 Hz NIR-E	1 – 5
20	M	66	Y	N/A	R Temporal	Before	75 Hz NIR-E	0.5 – 20
21	F	53	Y	N/A	L Frontal	After	75 Hz NIR-E	0.5 – 20
22	F	46	Y	N/A	L OZ	After	75 Hz NIR-E	0.5 – 5
23	M	58	Y	N/A	R Cerebellar	After	75 Hz NIR-E	0.5 – 5
24	F	68	Y	N/A	R OZ	Both	75 Hz NIR-E	0.5 – 10

* M = male, F = female, Age given in years, Y = yes, N/A = not applicable, XRT = Cranial radiation therapy, Chemo = chemotherapy, IH = Interhemispheric, OZ = Orbitozygomatic (skull base approach), NIR-E = Near-infrared enhanced sensor

6.4 IMAGE QUALITY ASSESSMENT: PATIENTS 11 – 13

For the first few patients in the phase II clinical study, the primary goal was to validate the performance of the modified instrument design and demonstrate that improved image quality could be achieved compared to the pilot study. To demonstrate the effect of rotating the polarizer on the recorded images, Figure 6.3 shows the raw speckle images and corresponding speckle contrast images with the polarizer oriented both parallel and perpendicular to the specular reflections for patient 12. Figure 6.3C shows the raw speckle image with the polarizer in the parallel orientation, which allows specular reflections to pass through the polarizer to the camera sensor and results in high image saturation in the raw image (intensity = 255). This is shown by the blue curve in the histogram in Figure 6.3A, with >1300 pixels saturated. In the corresponding speckle contrast image in Figure 6.3D, image artifacts shown in white and dark blue are visible throughout the FOV and mostly correspond with the saturated regions of the raw image. This image is comparable to some of the images from the pilot study without a polarizer, and shows that these artifacts greatly hinder blood flow visibility. The polarizer was then rotated to the position that minimized these image artifacts, which corresponds to an orientation perpendicular to the specular reflections. The bottom row (Figure 6.3E and 6.3F) shows the raw image and speckle contrast image at this perpendicular orientation, and show greatly reduced saturation in the raw image and much improved image quality in the speckle contrast image. The green curve in Figure 6.3A shows the raw histogram at this orientation, and indicates ~6× reduction in saturation. With the polarizer correctly aligned, a much higher percentage of the image can provide usable blood flow information. Thus, the polarizer provides the flexibility to minimize these artifacts as

much as possible, which is an advantage in a clinical setting and increases the usefulness of intraoperative LSCI.

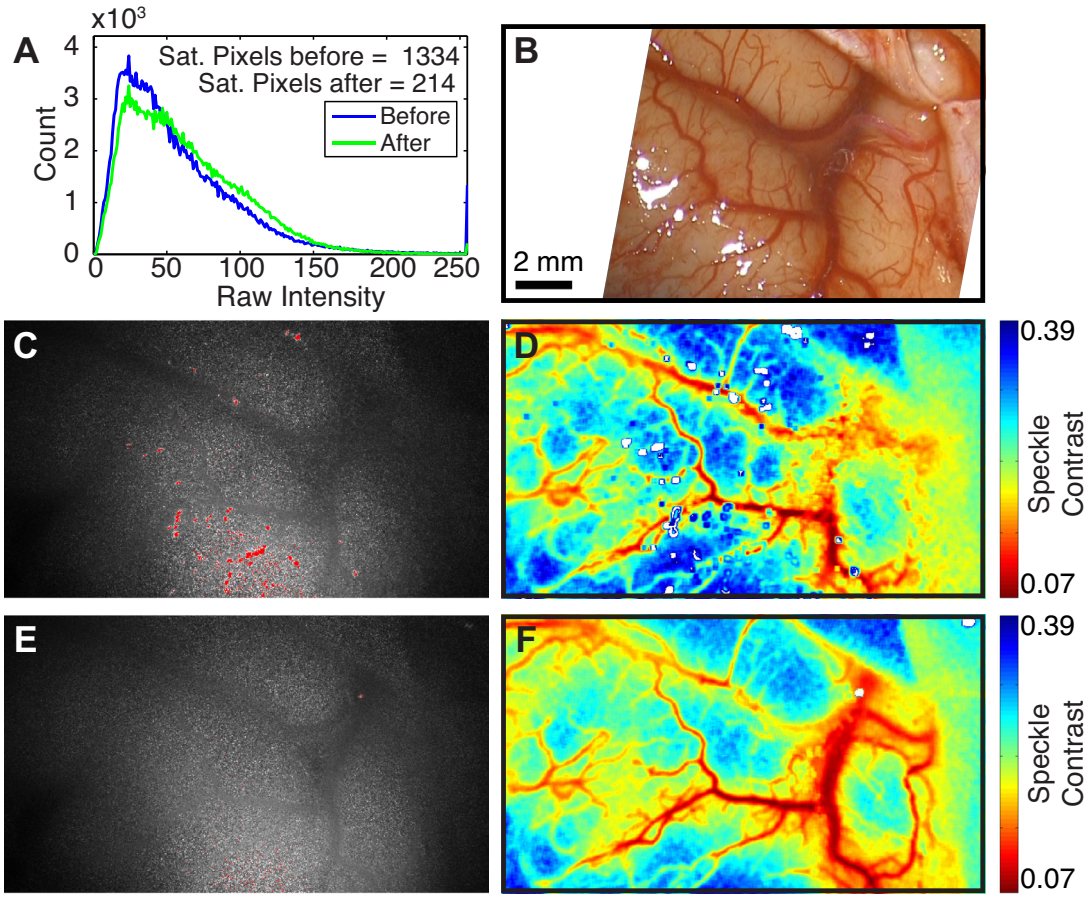

Figure 6.3: The impact of the polarizer on the recorded images, with representative raw and speckle contrast (SC) images shown at orthogonal orientations for patient 12. (A) Image histograms corresponding to the raw images shown in (C) and (E), showing reduced image saturation after proper alignment of the polarizer. (B) Color photograph of the cortical tissue, registered to match the orientation of the SC images. Scale bar corresponds to all images. (C) Raw speckle image with saturated pixels shown in red, and (D) corresponding SC image when the polarizer is oriented *parallel* to specular reflections, allowing them to pass through to the camera sensor and produce artifacts on the SC image (shown in white). (E) Raw speckle image and (F) corresponding SC image when the polarizer is oriented *perpendicular* to specular reflections, blocking most reflections and reducing raw image saturation resulting in improved image quality.

A demonstration of the overall image quality improvement with the modified instrument design in the phase II study is shown in Figure 6.4, as an analog to Figure 5.2 from the pilot study. For these images, the polarizer position was adjusted to the optimal orientation for blocking specular reflections prior to recording. Here, two cortical views recorded from patient 11 and patient 13 are shown for qualitative assessment. Looking at the speckle contrast images in the middle column, minimal image artifacts from specular reflections are visible, demonstrating the excellent performance of the polarizer for reducing these artifacts. There are only a few small regions of specular reflections visible in each image, marking a dramatic improvement over the previous study. There are also very few artifacts along the centerline of the larger vessels. There are a few artifacts along the edge of the vessel in the second row, where a thicker scattering region can be seen in the color photograph. There are also a few spots along the centerline of the larger artery in the third row, which seem to line up with artifacts seen in the photograph as well. This indicates that some reflection artifacts were bright enough that the polarizer could not completely eliminate them. For the largest vessel imaged in the last row, no artifacts are observed at all, and the white region at the bottom corresponded to an area of higher speckle contrast likely due to the high curvature of the cortical surface in that portion of the image. There are also no edge effects observed around the larger diameter vessels, indicating that the 785 nm wavelength does in fact minimize the hemoglobin absorption artifacts. This results in a more even average intensity distribution across the image, even in the presence of larger vessels. The 785 nm laser also contributes to a higher maximum speckle contrast value in the first two rows, relative to the speckle contrast images from the pilot study. The longer wavelength produces larger speckles relative to the pixel size, which likely produced better speckle sampling in this study. This laser also has a much longer coherence length than the 660 nm laser used in the pilot

study, as demonstrated in Chapter 2, which also likely contributed to higher maximum values in the speckle contrast. This demonstrates improved performance, since it corresponds to an increase in the dynamic range of the qualitative flow maps.

The speckle contrast images displayed also exhibit good correspondence with expected clinical flows. The first row shows a cortical tissue region highlighted by the dotted black line that was cauterized prior to imaging as part of the procedure. This region showed reduced blood flow in the speckle contrast image as expected, and showed an even larger reduction in flow than what was visible by eye. This is accentuated in the overlay of the faster flows from the speckle image on top of the color photograph, where the overlay shows exactly where the flow stops *en route* to the cautery location. The last row shows a cortical tissue region after the resection where the large vein in the middle of the FOV was sacrificed as part of the procedure. Thus, low flow is expected in this vessel, and is visualized clearly in both the speckle contrast image and the overlay image. The flow visualized in this vessel is lower than surrounding parenchyma tissue to the left, which is truly low flow for a vessel of this caliber (>3 mm diameter). Keep in mind that these images are only snapshots from several minutes of recorded images, and a video would show pulsatile variations across the field of view within each heartbeat. Reduced levels of pulsatile flow were visible even in the sacrificed vein from the last row, meaning that flow was not completely stopped. Overall, these images demonstrate the improved visualization with the modified instrument design and confirm that the hardware changes are performing as expected.

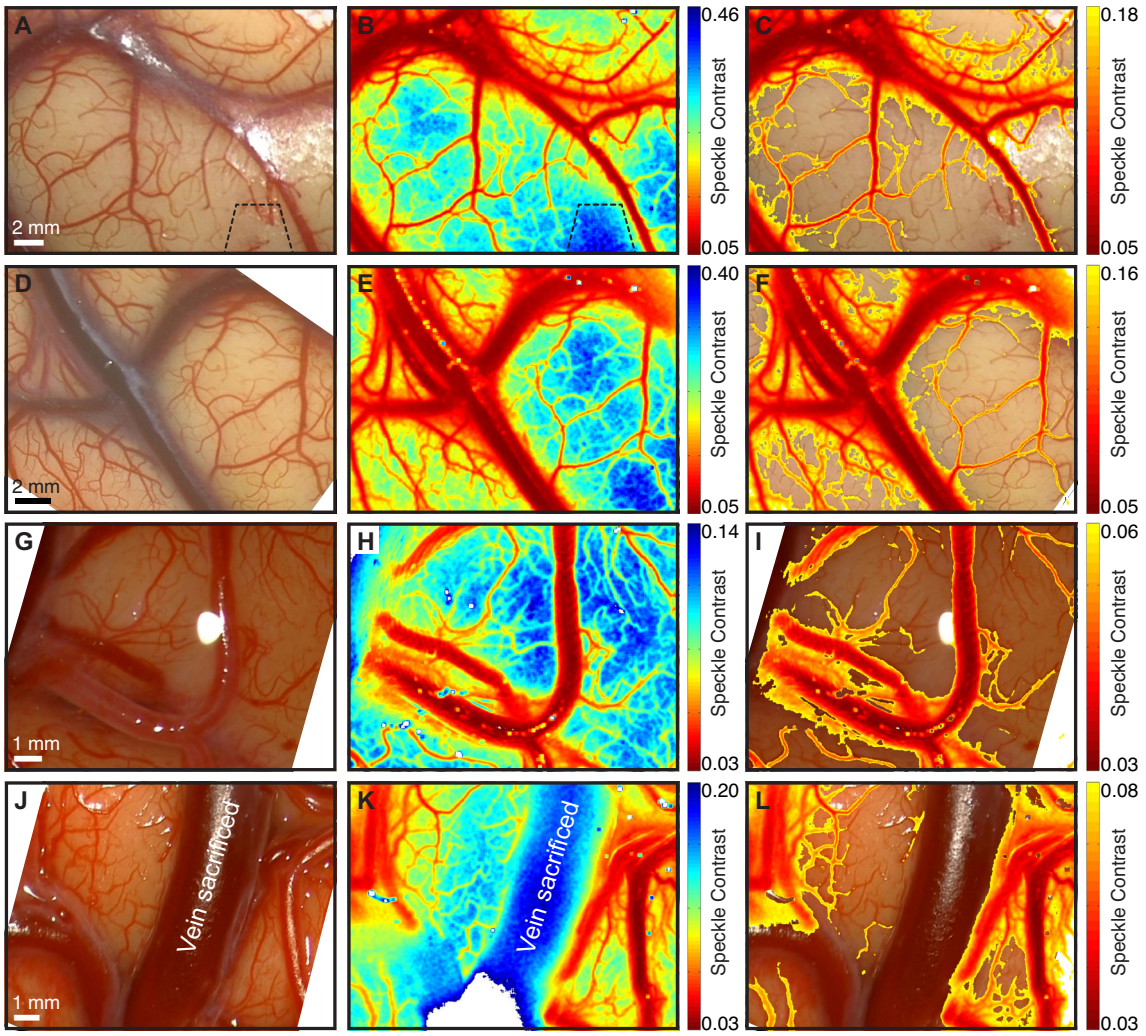

Figure 6.4: Comparison between color photographs taken under xenon lamp illumination using the built-in color camera (A, D, G, J) and the corresponding speckle contrast images (B, E, H, K) for two patients in the phase II study. The right column (C, F, I, L) shows the thresholded LSCI images displaying <40% of the maximum K overlaid on top of the color photographs. The first two rows (A – F) correspond to two different cortical views from patient 11 (both before the resection), and the second two rows (G – L) correspond to two cortical views of patient 13 (before and after the resection). The scale bar shown in the color photograph applies to the entire row. The first row shows a region of bipolar cautery on the tissue surface within the black dotted lines performed before imaging, and the last row shows a >3 mm diameter vein that was sacrificed as part of the resection procedure (low flow is expected).

6.5 Clinical Multi-Exposure Speckle Imaging (MESI): Patients 15 – 21

For the next set of patients in the phase II clinical study, the main goal was to modify image acquisition parameters to maximize the sensitivity to blood flow in clinical size vasculature. For LSCI, sensitivity to blood flow is inherently related to the exposure time used to image the sample. Thus, the first objective was to determine the optimal exposure time to provide the best sensitivity to the range of flows visualized in a clinical setting. The second objective was to combine images across multiple exposures using the MESI model to produce a more quantitatively accurate map of blood flow based on a wider sampling of the flow distribution.

6.5.1 Optimizing Single Exposure LSCI – Which Exposure Time is Best?

To allow imaging with a shorter exposure time, a NIR-enhanced camera sensor was used for the remainder of the study with a ~5× improvement in quantum efficiency. This was the best solution for increasing light levels to the camera without altering the internal light split within the surgical microscope. Images were recorded using 5 exposure times for 3 cases, 6 for 2 cases, and 8 for 1 case. Usually 7 to 15 exposure times are recorded to improve fitting accuracy, and at least 6 exposure times spread across multiple decades (50 μs – 100 ms) are required to maintain accuracy for microcirculatory flows in the rodent brain [17]. In this study, the lower limit for the minimum exposure time was determined by the light levels reaching the LSCI camera (0.5 ms at maximum laser operating current), and higher light throughput would be required to image with shorter exposure times in the same range as previous animal studies (tens of μs). For the first five patients highlighted, the upper limit for the exposure time was the lowest laser power that could be achieved while still above the lasing threshold (5 ms at slightly above threshold ~110 mA). For the last patient, the lower limit was the same, but the upper limit was increased using neutral density filters to

further lower the laser power for imaging at longer exposure times. The goals are to compare images acquired across multiple exposure times and assess which provides highest sensitivity to the range of flows visualized in each FOV.

To compare single exposure LSCI frames and subsequently to generate MESI ICT maps, registered images were selected from the same time region of the cardiac cycle across exposure times to minimize pulsatile variation. For maximum visibility across the images, the cardiac region with the lowest blood flow was selected. For most cases, the lowest region of the blood pressure (BP) signal corresponded with the lowest flow levels within the cardiac cycle. The normalized time of the BP signal was calculated using an analog of Equation 5.1, and the BP signal was split into regions of 0.2-second duration normalized time, i.e. $0 \le t_{normalized} \le 0.2$, $0.2 \le t_{normalized} \le 0.4$, etc. For all cases with a recorded BP signal, each region of normalized time was overlaid on the original signal to display the portion of the BP curve selected. The section that matched up with the lowest magnitude BP signal was selected. For patients 16, 17, 18, and 21, the BP region selected was $0.6 \le t_{normalized} \le 0.8$. For patient 15, the BP region selected was $0.4 \le t_{normalized} \le 0.6$. For patient 19, the BP signal was not recorded, meaning that the signal was missing from the recorded anesthesia output. For this case, the region with the lowest flow was selected empirically from normalized sections of the ECG signal ($0.6 \le t_{normalized} \le 0.8$). A representative view of the cardiac region selected for each of the six cases presented in this section is shown in Figure 6.5, where 3 heartbeats are shown. The portion of the cardiac cycle used for subsequent analysis is highlighted in red for the BP signal and in green for the ECG signal. Because 50 frames were desired for averaging, images selected spanned multiple cardiac heartbeats and were not completely continuous in time. The image registration process ensured that all images were spatially aligned, which means that non-continuous image averaging did not introduce image

artifacts. This procedure assumes that no physiological changes have occurred to alter the blood flow across the time duration between the averaged frames. Similarly, using images from multiple exposure times to generate a MESI ICT frame in the next sub-section also assumes that the images from each individual exposure time were acquired under the same physiological conditions. The instrument design required exposure times to be acquired in sequence, rather than interleaved as is common in laboratory MESI systems [9, 11]. Thus, the time span between the first and last recorded image in a given set was typically >10 minutes. Physiological uniformity may not be a valid assumption, and could explain some unexpected trends in recorded images.

Assuming that physiology remains constant during image acquisition, the expected trend should exhibit decreasing maximum speckle contrast as the exposure time increases. This is because flow causes a greater de-correlation of the speckles with longer exposure times, leading to a lower speckle contrast value and the overall appearance of faster flows across the image. If the speckle contrast value increases or stays the same as exposure time increases, this would suggest that flow levels have changed between the recording times of different exposures. This is why image selection was restricted to the same region of the cardiac cycle for cross-comparison, since viewing a different region of the cardiac cycle could sample higher or lower relative flow values and make it difficult to visualize expected trends. Next, examples from six cases will be presented, demonstrating the differences in flow visualization across exposures and highlighting that proper exposure time selection matters.

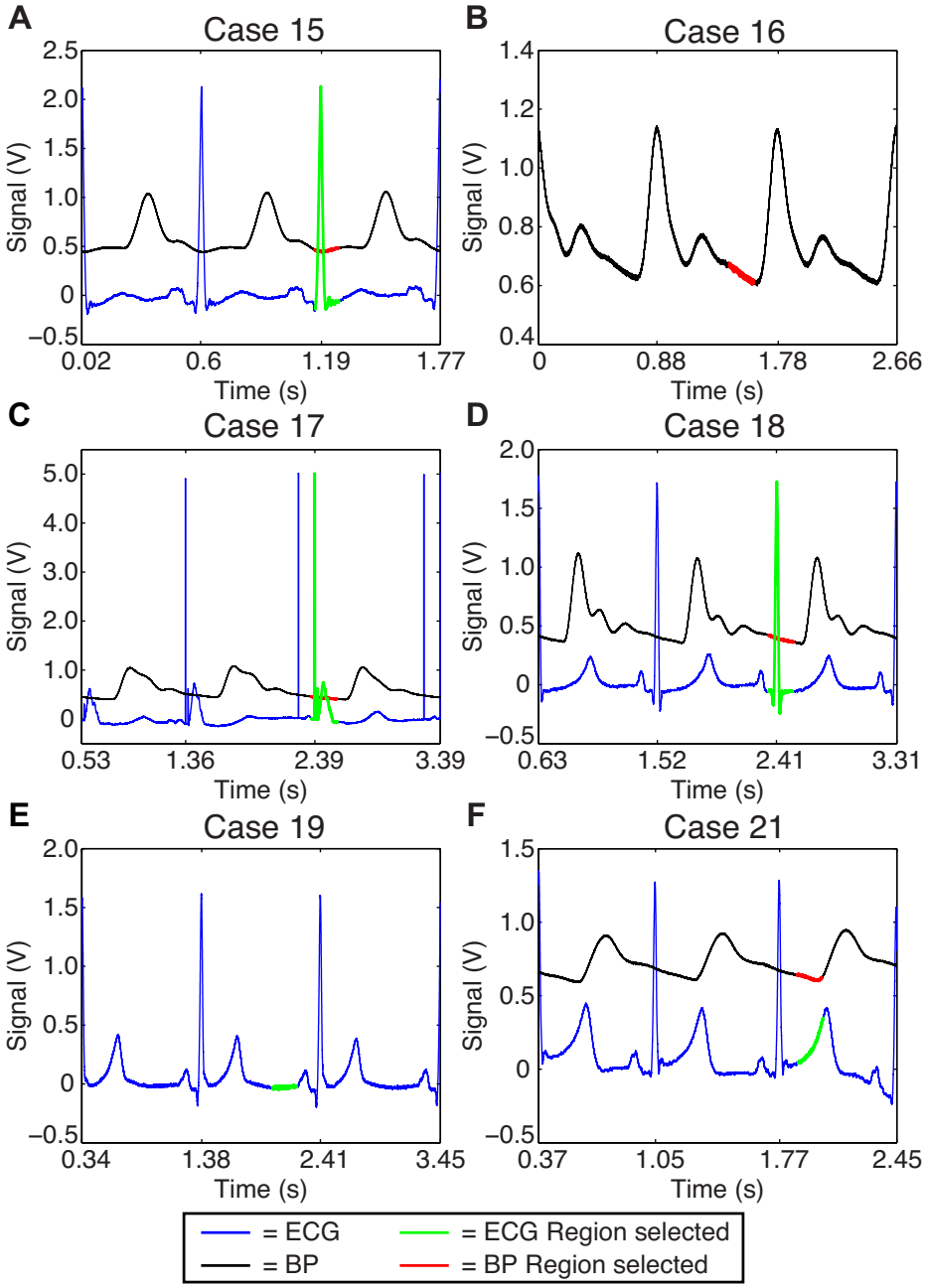

Figure 6.5: Representative recorded cardiac signals from the first three heartbeats for each patient highlighted in Section 6.5. The region of the signal used for selecting single exposure LSCI frames for averaging as well as subsequent MESI ICT computation is shown in green (ECG), red (BP), or both. Cases 15 – 19 are shown in (A) – (E), and Case 21 is shown in (F).

The first three examples are from cases where 5 exposure times were recorded. The individual exposure times from Case 15 are shown in Figure 6.6, with the exposure time of each image provided. All images are displayed with the same color bar, with limits that span the full range of the speckle contrast histogram across all exposures. This example follows the expected trend, since the maximum speckle contrast decreases as the exposure time increases. This indicates that the LSCI image is estimating faster flow levels across the FOV as the exposure time increases. As seen from these images, the best visibility of flows across the image is seen from the shorter exposure times at 1 ms and 1.5 ms. Here, flow levels are easily differentiated among vessels of various sizes as well as among different regions of the tissue parenchyma. As exposure time increases, the variability in measured speckle contrast goes down and similar flow estimates are obtained from a larger portion of the image. This indicates that the sensitivity to flow differences within the image is decreasing as exposure time increases.

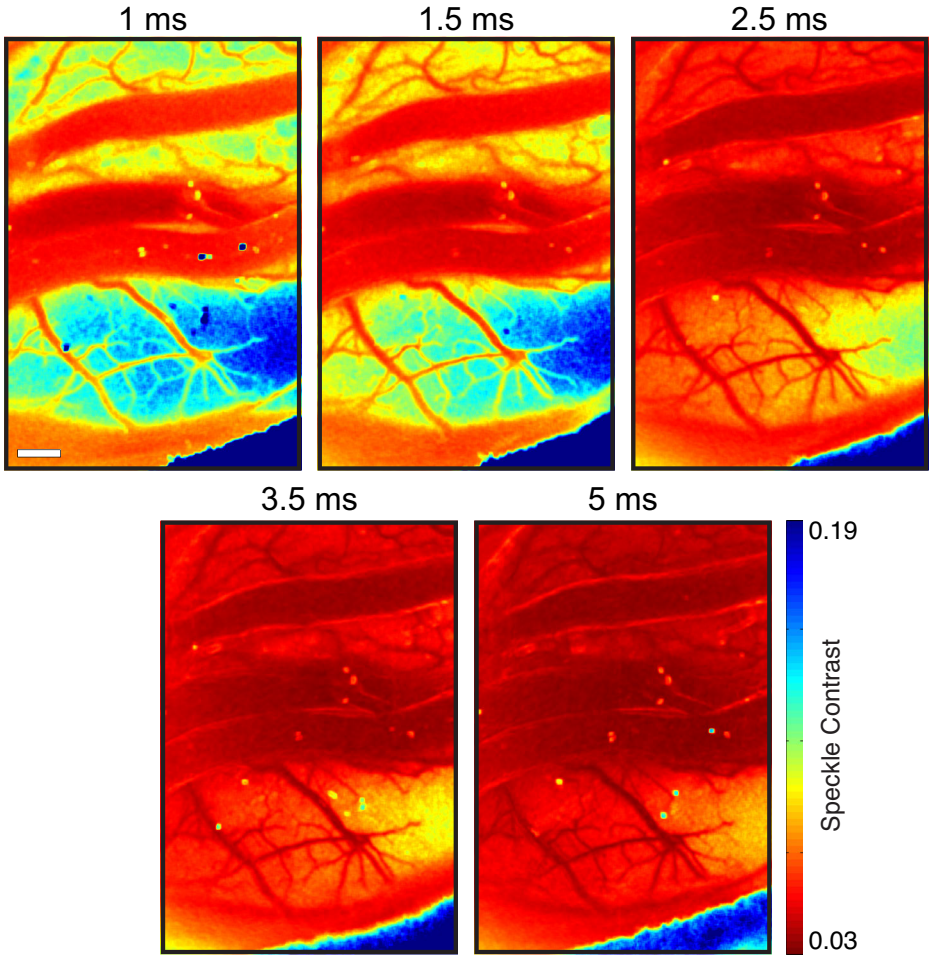

Figure 6.6: Single exposure LSCI frames from patient 15 spanning 1 – 5 ms exposure time. The color bar applies to all five images. The speckle contrast decreases incrementally as exposure time increases, which indicates increasing measured flows as expected. Scale bar (white) = 1 mm.

The individual exposure times from Case 16 are shown in Figure 6.7, with the exposure time of each image provided. Here, very similar trends of reducing flow visibility are observed as exposure time increases. The shortest exposure time (1 ms) provides the optimal sensitivity to a wide range of flows in this cortical region. Here, flow levels can be easily differentiated between vessels of various sizes. The horizontal draining vein in the middle of the FOV is clearly the fastest, followed by vessel branches

coming off of it, and then subsequently followed by the smaller diameter vasculature on both sides. For the middle exposure times (2 – 4 ms), the draining vein still appears the fastest in the FOV, but sensitivity to differences between flows in surrounding smaller diameter vasculature starts to get lost. For the longest exposure time (5 ms), the draining vein has similar speckle contrast to its main vertical branch in the middle of the image as well as smaller diameter vasculature. Visualizing this longer exposure time alone would lead to flow estimates that inaccurately model the true CBF dynamics of the cortex.

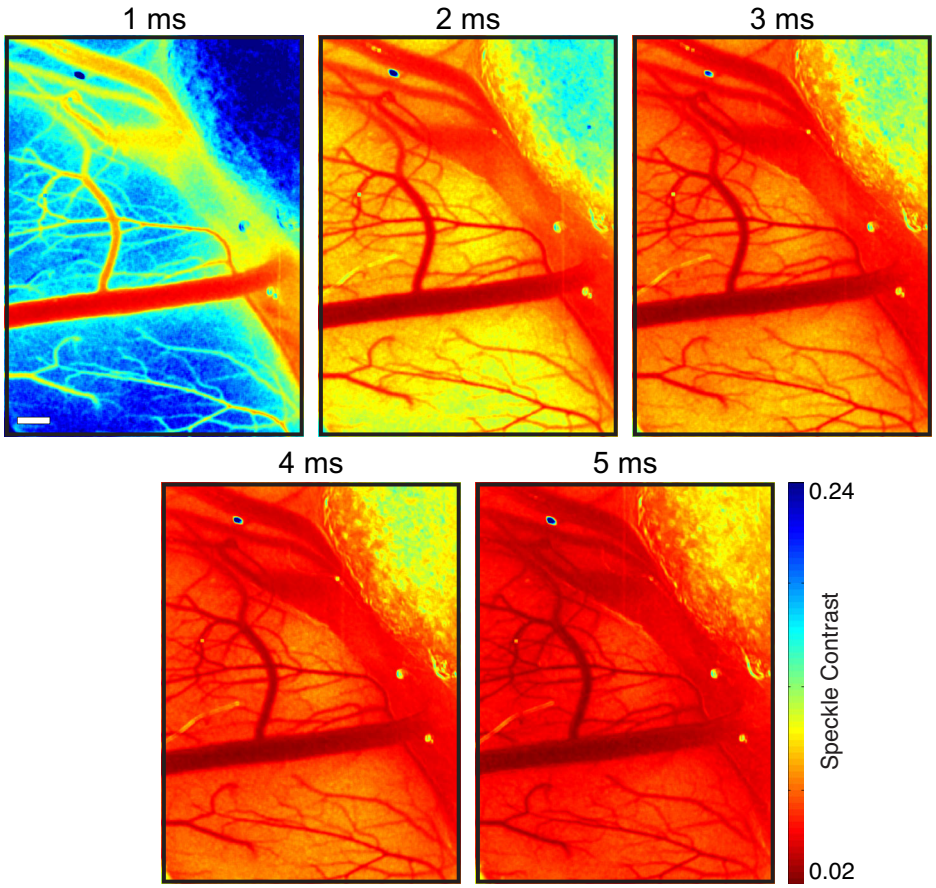

Figure 6.7: Single exposure LSCI frames from patient 16 spanning 1 – 5 ms exposure time. The color bar applies to all five images. The speckle contrast decreases incrementally as exposure time increases, which indicates increasing measured flows as expected. Scale bar (white) = 1 mm.

The individual exposure times from Case 19 are shown in Figure 6.8, with the exposure time of each image provided. Here, the central region of decreased flow in the center of the cortical FOV was a result of tissue cautery performed as part of the resection procedure before imaging started. This is a unique example because there is a region of known reduced flow that can be used as a benchmark for assessing the individually recorded exposure times. Overall, similar trends are observed, with decreasing speckle contrast as exposure time increased. However, a very minor decrease was observed between 4 and 5 ms, seen mostly within the central region of reduced flow. These images are striking because only the shortest exposure times (1 ms, 2 ms) clearly visualize the expected clinical trend. The reduced flow in the center of the image is less obvious with the longer exposure times due to the reduced dynamic range. The image edge is still slightly darker red for 3 – 5 ms, meaning that the flow reduction is still visible, but it is harder to see with this color bar range. Differences in flow among the smaller vasculature around the edge of the cautery can also be seen across different exposure times. The most prominent example is in the top portion of the image. Flow levels are easily differentiated among the smaller diameter vasculature at the 1 ms exposure time and slight differences are even observed at 2 ms. However, measured flows become very similar for ≥3 ms. This trend is consistent with previous examples, and demonstrates reduced sensitivity to flow differences with longer exposure times.

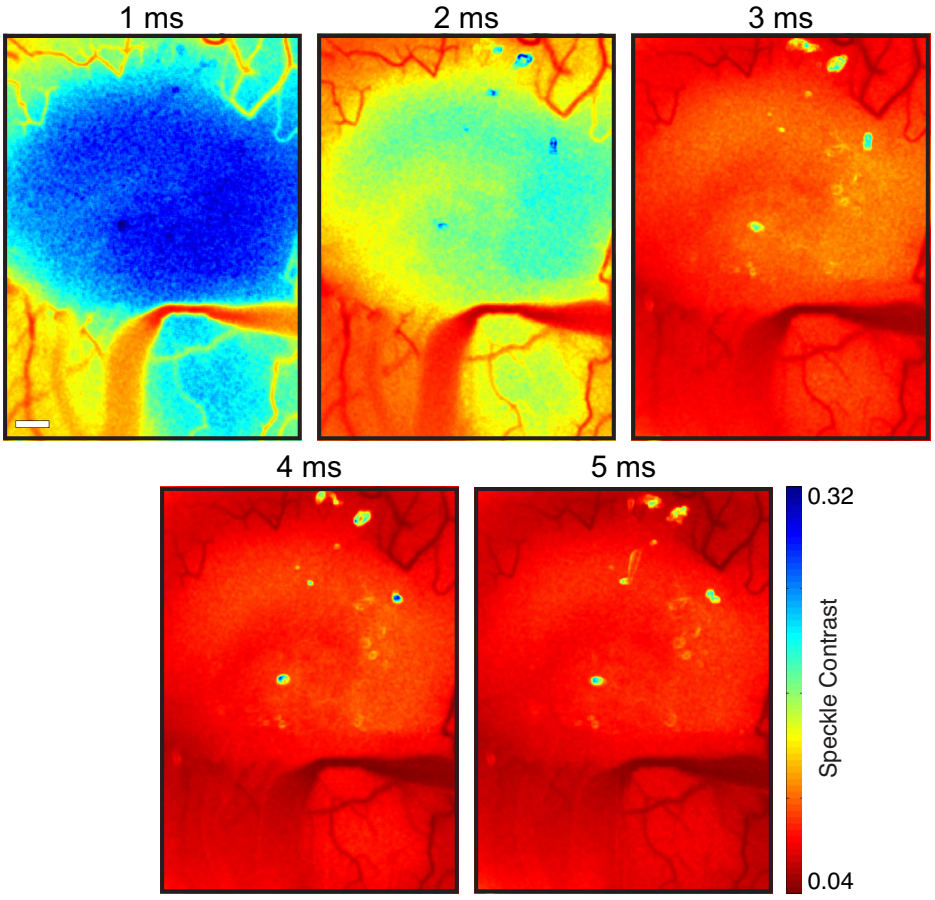

Figure 6.8: Single exposure LSCI frames from patient 19 spanning 1 – 5 ms exposure time. The color bar applies to all five images. The speckle contrast decreases incrementally as exposure time increases, with a very minor decrease between 4 and 5 ms. The central region of decreased flow is from an area of tissue cautery performed as part of the resection procedure before imaging. Scale bar (white) = 1 mm.

The next two examples are from cases where 6 exposure times were recorded, and a sterile ruler was placed on the cortical tissue within the camera FOV as a static reference. This will be used in the next section to estimate the instrumentation factor, β. Because of the orientation of the craniotomy for both of these cases, the operating surgeon physically held the ruler in place during the imaging session. Thus, the ruler is not in the same physical location within a single exposure time or across exposure times.

The individual exposure times from Case 17 are shown in Figure 6.9, with the exposure time of each image provided. The static ruler is the slowest flow measured across all exposure times, which is expected for normal physiology. The ruler moves between exposure times, and the range in speckle contrast levels visualized in the ruler region for the 5 ms exposure are a result of the ruler moving between averaged frames. This cortical tissue region is different from previous examples in that there is relative uniformity among the vasculature size in the FOV. Case 15 and 16 both had large diameter vessels in the FOV that required the lowest available exposure time to provide visibility among the smaller vessels in the FOV. With all vessels at a smaller size, the flow distribution of this cortical region is expected to be slower than previously imaged cases. The shortest exposure time from this set (0.5 ms) provides a slow estimate of flows throughout the FOV, given by the high speckle contrast in the tissue parenchyma. The larger vessels in this FOV do not appear red until the 1 ms exposure time, which also shows a large shift in the flow levels measured from the tissue parenchyma. The smaller cortical vasculature is more easily visualized in the 1 ms exposure time image, which provides a better sampling of slower flows. A large reduction in tissue parenchyma flows is also observed with the jump to 2 ms exposure time, and better visualization of small vessels is possible. Another clear reduction is seen with the 3 ms exposure, followed by more minor decreases between 4 and 5 ms images. It should be noted that larger shifts in the speckle contrast values are observed when the exposure time approximately doubles in length (i.e. 0.5 $\rightarrow$ 1 $\rightarrow$ 2 $\rightarrow$ 5 ms), and smaller changes are observed for smaller magnitude increases (i.e. 2 $\rightarrow$ 3 ms, and 3 $\rightarrow$ 4 ms). This makes sense because a larger difference in exposure time corresponds to a larger disparity in the range of flows with maximal sensitivity for each exposure time. This trend is clearly seen here since there are three images with doubled exposure time relative to the shortest exposure time, but is

also visible looking back at previously shown cases (1 → ~2 → 5 ms). Given the range of flows present in this set, either 1 or 2 ms provides the best overall view of the full range of flows present in the image, while better differentiability among the larger diameter vasculature is more clearly visualized with the 0.5 ms image.

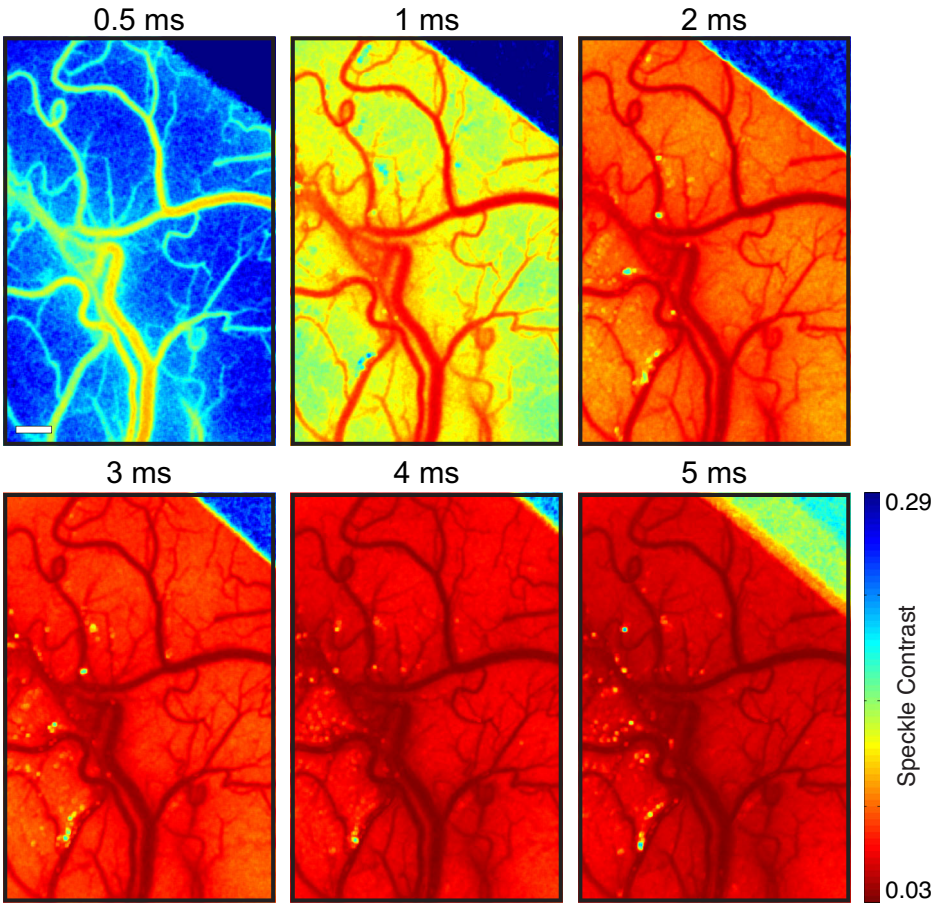

Figure 6.9: Single exposure LSCI frames from patient 17 spanning 0.5 – 5 ms exposure time. The color bar applies to all six images. The speckle contrast decreases incrementally as exposure time increases, with a minor but visible decrease between 4 and 5 ms. A sterile ruler was placed on the upper right corner of the camera FOV to provide a static reference. Scale bar (white) = 1 mm.

The individual exposure times from Case 18 are shown in Figure 6.10, with the exposure time of each image provided. Here, the ruler was not added to the surgical field until the 1 ms exposure time, and clearly moves around between exposure times. Similar to Case 17, the ruler always has the slowest flow, or highest speckle contrast in the camera FOV, as expected physiologically. This cortical view does have some slightly larger vessels towards the upper portion of the FOV compared to Case 17, and thus has more variation in vessel sizes. This case does follow a similar trend with the largest changes in speckle contrast observed as the exposure time is doubled (i.e. 0.5 $\rightarrow$ 1 $\rightarrow$ 2 $\rightarrow$ 5 ms). Very minor differences are visualized between 3 $\rightarrow$ 4 $\rightarrow$ 5 ms. Smaller differences within this range are expected because of overlapping flow sensitivity ranges. However, the differences are so small that they are only visualized by very close inspection. Some of the smaller diameter vasculature in the lower left portion of the image do appear darker and more prominent between 3 $\rightarrow$ 4 $\rightarrow$ 5 ms, but the tissue parenchyma exhibits very little change. This could be attributed to a change in physiology between these recordings; however, the average heart rate had <6% variation across trials. This could also be attributed to a high degree of tissue motion during acquisition. Although the images are spatially aligned after image registration, the tissue motion contributes to faster decorrelation in the image. This has a larger effect on longer exposure times, since more of this motion is integrated during the exposure duration. Finally, it could be related to the fact that the laser drive current was used to control the laser power. As shown in Chapter 2, the coherence of this particular laser model decreases as the drive current is reduced. The laser current was reduced to <200 mA for 3 – 5 ms exposure times to match intensity levels with the shorter exposure times. A reduced coherence length at these longer exposure times could also contribute to decreased visibility in the speckle pattern compared to shorter exposure times. Despite

this uncertainty in the trend for the longer exposure times, the overall trend across all exposures is consistent with previous cases.

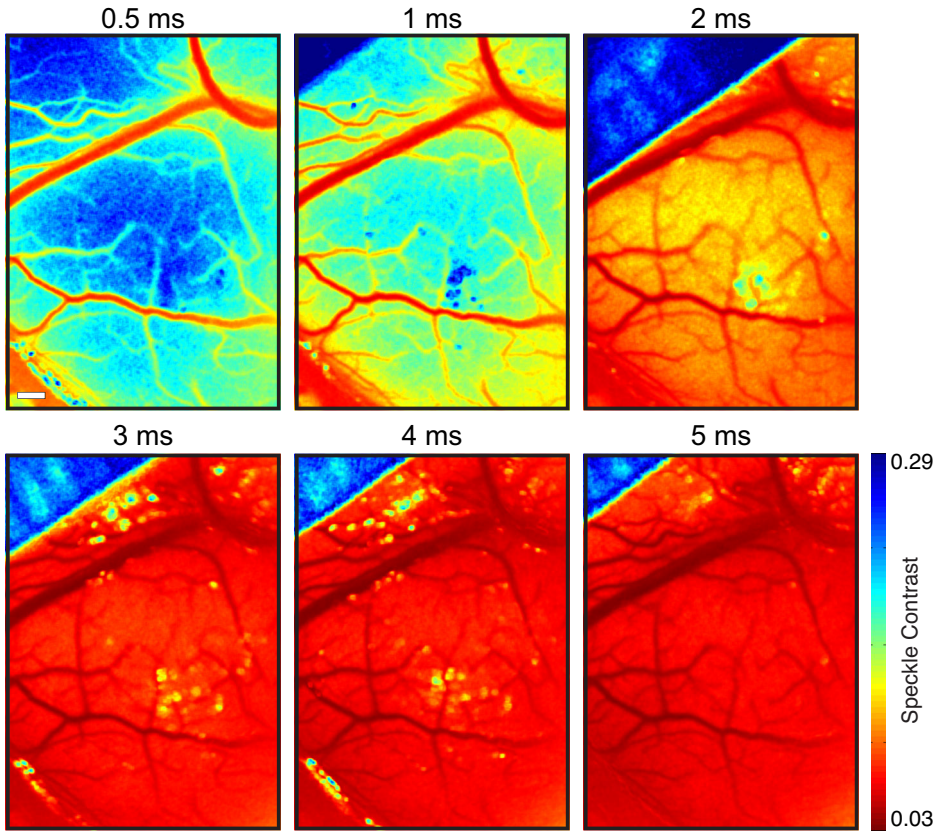

Figure 6.10: Single exposure LSCI frames from patient 18 spanning 0.5 – 5 ms exposure time. The color bar applies to all six images. The speckle contrast decreases incrementally as exposure time increases, here with very minor changes between 3 – 5 ms. A sterile ruler was placed on the upper left corner of the camera FOV to provide a static reference. Scale bar (white) = 1 mm.

The last example is from Case 21 where 8 exposure times were recorded, using neutral density filters to assist both with keeping the laser current within a smaller range of values and to allow imaging at longer exposure times up to 20 ms. Although the MESI approach factors the finite coherence of the laser into the instrumentation factor, this term

assumes that the coherence is not changing across exposures. Because it is known that the coherence of the laser changes with the drive current, a better approach for decreasing the laser power would be to use neutral density filters and keep the laser current constant. The filter wheel used in this study had discrete slots for single optical density filters rather than a continuously variable filter, which was simpler for the surgeon to control under the sterile drape. This meant that some of the exposure times still required slight adjustment of the current to match illumination levels. As mentioned in Section 6.3, all exposures were recorded with a current >260 mA and 5 of the 8 exposures were recorded at the operating current (425 mA). This is a large improvement relative to previous cases where the current was as low as 110 mA for the longest exposure time. The individual exposure times from Case 21 are shown in Figure 6.11, with the exposure time of each image provided. A sterile ruler was placed on the cortical tissue within the camera FOV as a static reference, similar to Cases 17 and 18. This cortical region had multiple branches of large diameter vessels in the center of the FOV, with what appears to be a 4-way intersection towards the right side. The presence of large diameter vasculature suggests that one of the shortest exposure times will likely provide the best sensitivity to the full range of flows in the image. The shortest exposure time (0.5 ms) provides high differentiation between the flows within the large vessel branch as well as larger diameter vasculature, with the vessel branch going to the left of the intersection point appearing much slower than the other 3 branches. This exposure also shows that a smaller diameter descending arteriole has the fastest flow in the entire imaging field. This would not be expected from the vessel diameter alone, but is clinically feasible if the larger vessel branch is a slow flowing draining vein segment. With the 1 ms exposure time, differentiation between the flows in these same vessels is still visible, and a shift in the tissue parenchyma is seen as expected. For the 2 and 3 ms images, this trend is still

present, but slightly harder to visualize. For images ≥4 ms, the vessel branch going to the left of the intersection point is no longer clearly slower than the other branches. For the 10 and 20 ms images, all 4 branches as well as the descending arteriole appear to have similar flow levels, which indicated poor sensitivity to the flow range in the FOV. For the 20 ms image, the dynamic range of the speckle contrast image is very low, with poor differentiation between the large vessels and neighboring tissue parenchyma. This is partly due to improper matching of the exposure time with the flows sampled and partly due to increasing integration of tissue motion artifacts within the camera exposure time, which increases decorrelation within the exposure time. The 20 ms exposure was the longest measured in this case because images from longer exposures were blurred from tissue motion. Because this image set goes up to 20 ms, there are five exposure doubles included in this range ($0.5 \rightarrow 1 \rightarrow 2 \rightarrow 5 \rightarrow 10 \rightarrow 20$ ms). A clear decrease in speckle contrast is observed for the first 3 doubles up to 5 ms exposure. The difference between 5 and 10 ms is subtle, while the jump from 10 to 20 ms shows a larger change.

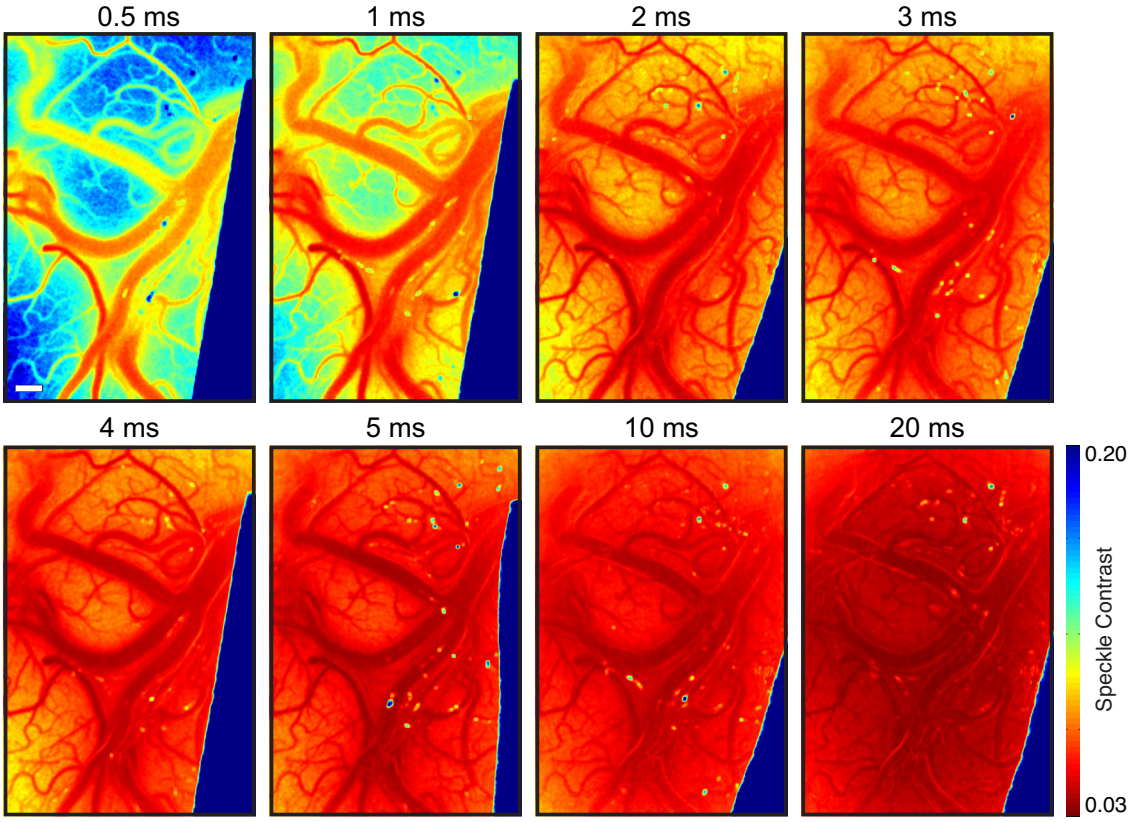

Figure 6.11: Single exposure LSCI frames from patient 21 spanning 0.5 – 20 ms exposure time, where neutral density filters were used to match average intensities across frames. The color bar applies to all eight images. The speckle contrast decreases incrementally as exposure time increases, consistent with expected trends. Poor image quality is observed for the longer exposure times, with edge artifacts present for the larger vasculature. A sterile ruler was placed on the lower right side of the camera FOV to provide a static reference. Scale bar (white) = 1 mm.

These six examples consistently demonstrate that shorter exposure times provide better flow sampling for the clinical size vasculature seen in the human cortex. The shorter exposure times provide the highest dynamic range of the speckle contrast images, and have the broadest sensitivity to a wide range of flows in each patient. The difference in dynamic range across exposure times can be easily visualized by the histograms of the speckle contrast images, which are displayed for all six cases in Figure 6.12. The curves

in these plots correspond to the histogram of each individual exposure time image displayed in Figures 6.6 – 6.11. As seen from these plots, the shortest exposure time always has the widest distribution, and the width decreases incrementally as exposure time increases with larger disparity between the shorter exposures. Case 16 and 17 show a clear reduction in the speckle contrast peak with each exposure time, while Case 18 and 19 show partially overlapping curves for the longer exposure times. Case 15 has a low speckle contrast peak for all exposure times given the 3 large diameter vessels in the FOV, but the width does follow the expected trend. Case 21 shows partially overlapping curves for 2 – 4 ms and for 5 and 10 ms, with other exposure times showing a clearly progressing decrease in magnitude and width. These histograms show the difference in dynamic range between exposure times and emphasize that each exposure time is sensitive to a different range in flow. These cases demonstrate that exposure time selection matters and that shorter tends to provide better sensitivity in a clinical setting.

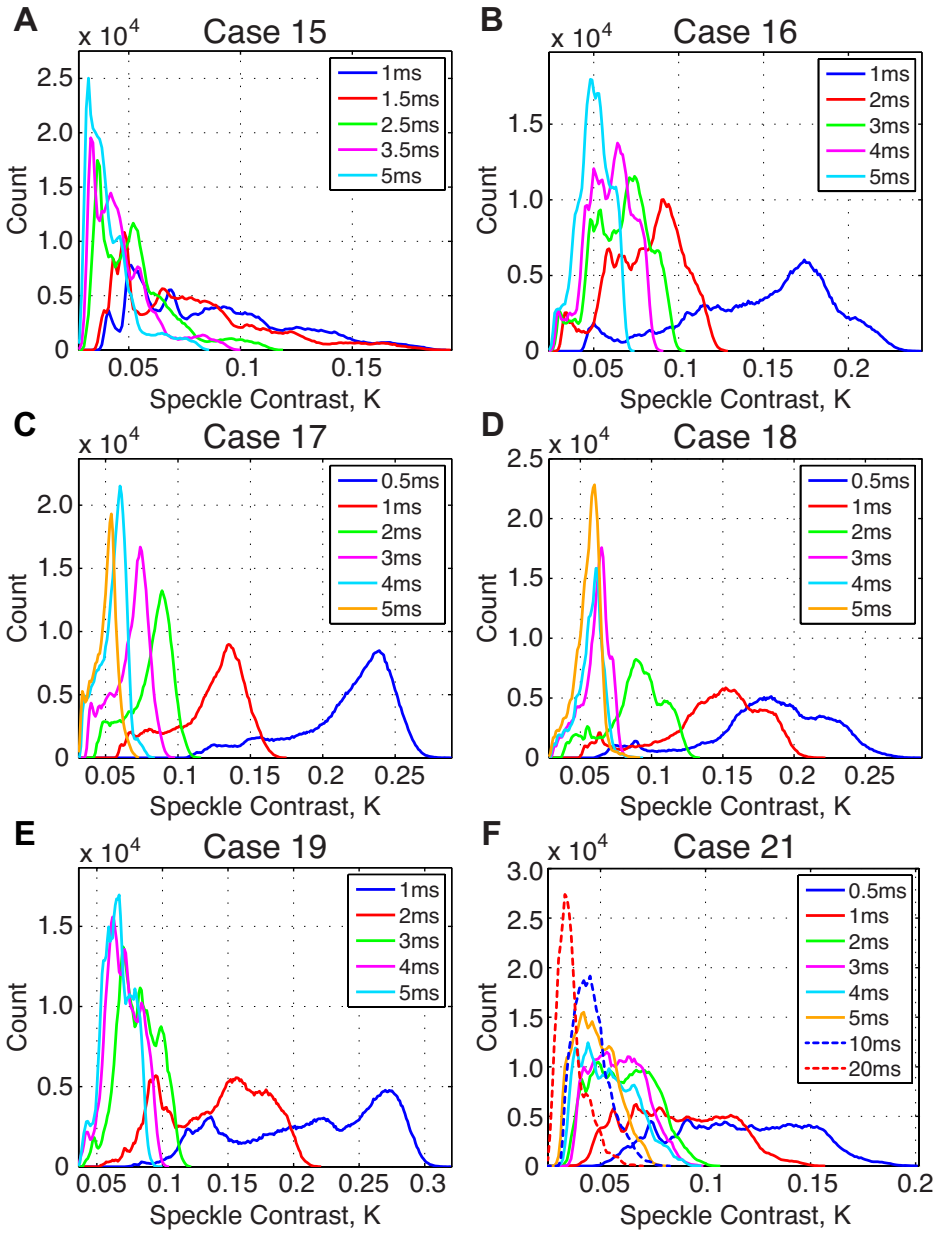

Figure 6.12: Histograms of the speckle contrast images within the range of the color bar are shown for Cases 15 – 19 in (A) – (E) and for Case 21 in (F). Each plot has its own legend showing the representation of each exposure time recorded for that case. Overall, the histogram width decreases as exposure time increases.

6.5.2 Quantitative CBF Assessment using the MESI Model

In this section, the individual images from each exposure time are combined using the MESI model and a blood flow map that has higher quantitative accuracy was computed for each case. Then, select ROIs were chosen within each FOV for processing with both the single exposure and MESI models. The relationship between the speckle variance and the exposure time is shown for these ROIs to assess the goodness of fits for the MESI model.

To improve accuracy of both the single exposure LSCI analysis as well as the MESI processing, the instrumentation factor β was set experimentally using a calibration procedure involving imaging a static sample at the shortest exposure time possible. A static sample was used because β inherently represents the value of the speckle variance when there is no flow. The lowest exposure time was used because it gives the highest β value that approaches the theoretical maximum measurable speckle variance for that particular imaging configuration (recall that the limit of K^2 as $T \rightarrow 0$ can be approximated by β). The static sample was a static tissue region, surgical gauze or foam, or a sterile ruler depending on the patient, shown in Figure 6.13. The cases that used a ruler are expected to have the most accurate estimate of β, since the other sources may not have been truly static. However, even the ruler is not a fully static sample due to unavoidable tissue motion. The average speckle contrast was extracted from the static region in the image, and then squared to give the speckle variance of the region. This value was then used as an estimate for β in that imaging session, and was calculated on a case-by-case basis to account for differences in illumination angle, magnification, and speckle sampling effects. This fixed estimate for β was then plugged into Equation 1.4 for more quantitatively accurate single exposure estimates of correlation time, as well as into Equation 6.1 for MESI estimates of correlation time. This reduced the number of

variables in the MESI expression, which helped improve fitting accuracy and produced correlation times that made sense physiologically. The process of fitting the MESI expression using a fixed β was originally suggested in the first MESI publication [9] to reduce the search space of the nonlinear fit within a reasonable range that produces physically realistic results. The results presented below follow expected trends very well, which helps validate this calibration process for the instrumentation parameter.

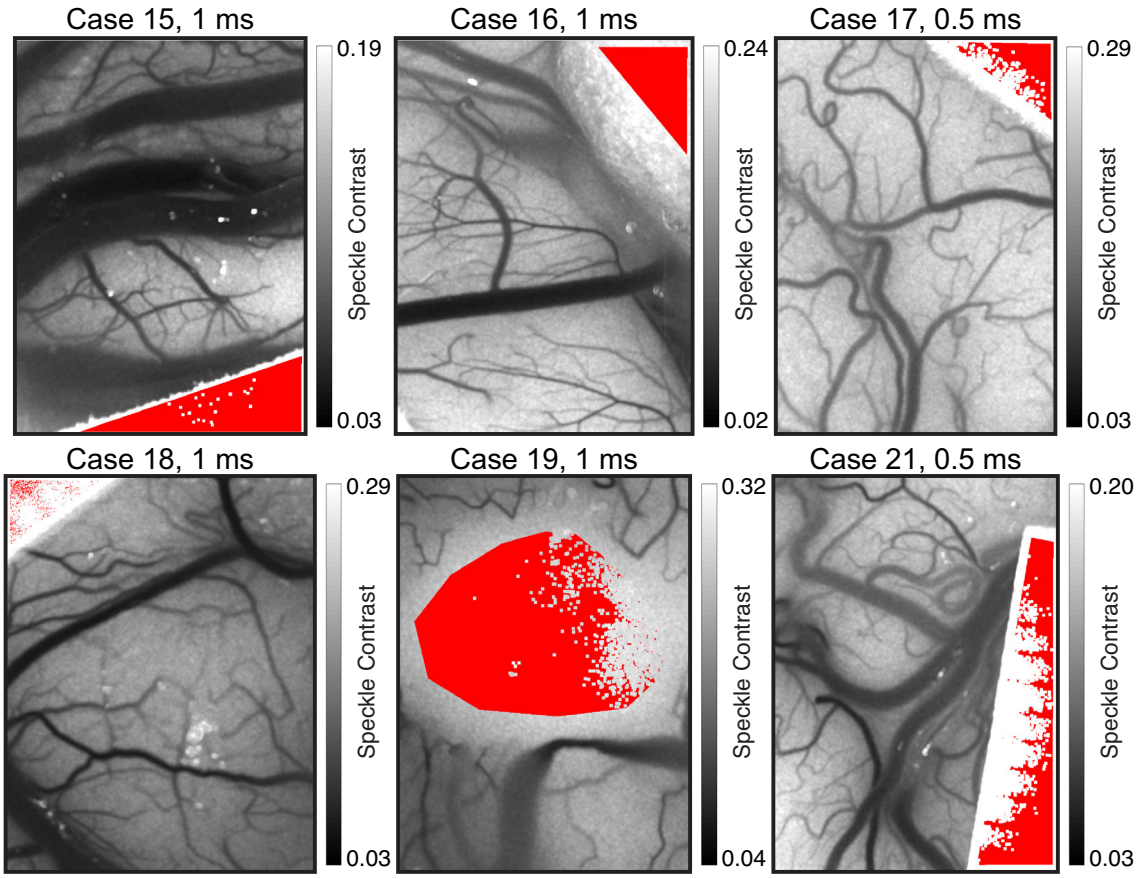

Figure 6.13: The region selected for calculation of β is shown in red for each case, with each grayscale speckle contrast image titled for reference. This was computed from the shortest exposure time image from each case with a static region present. Cases 17, 18, and 21 had a true static reference from a sterile ruler. Case 15 used surgical gauze, Case 16 used surgical foam, and Case 19 used the tissue cautery region as a "static" reference.

The individual exposure images presented earlier, averaged over 50 frames and selected from the same region of the cardiac cycle, were used as inputs for the MESI model along with the fixed β value. The model generates the τ_c, ρ, and v_{noise} for every pixel of image. The ICT, or $1/\tau_c$, will be highlighted here, since it represents a quantitative map of blood flow. Along with a full-field map of blood flow, individual ROIs were also analyzed using the same general process for quantitative assessment. The only difference was that all available data was used for each ROI within each exposure time, which was usually 20 – 30 seconds worth of data (1400 – 2000 frames). The entire set was input to the model for fitting, and then summary statistics are displayed of the computed fits. Thus, a time course is not presented, but rather a representative summary of the results over the brief imaging time. The median fits for each exposure are displayed for the speckle variance versus the exposure time plots for assessment of the goodness of fit. This is the first time this model has been applied to clinical data, so the goal was to assess how well the model matches the measured results. For comparison of the blood flow information measured by the ROIs, the ROI with the slowest flow from the tissue parenchyma was used as the baseline, and the relative ICT was computed for all five remaining regions. This spatial normalization was used to highlight the sensitivity differences between the MESI model and the individual exposure times, meaning how well each method is able to differentiate flow levels between different tissue regions. This also shows the vastly different flow distribution estimated for those five ROIs for each individual exposure time compared to the MESI model. The average and standard deviation are displayed for computation of relative ICT values in each ROI.

The first example is shown for patient 15 in Figure 6.14, which includes the photograph recorded by the built-in color camera under xenon lamp illumination as well as the single exposure images for reference. The MESI computed ICT map is shown on

the right side on a logarithmic scale, which is able to visualize greater flow differences across the FOV than any of the individual exposure times alone. Three vessel ROIs and three parenchyma ROIs were selected, spanning various vessel sizes and spatially sampling different regions of the tissue. The model fits for the speckle variance against the exposure time are shown in Figure 6.14B, which are known as the speckle visibility curves. The first point to notice from these curves is that this range of exposure times is only sampling the tail end towards the upper limit of the full sigmoidal shaped speckle visibility relationship with exposure time. This indicates much shorter exposure times are needed to capture the full visibility range for human cortical tissues. Nevertheless, these curves show the expected trend physiologically between the different ROI regions selected. For the 3 vessel regions selected, the decays proceed in the expected order by vessel size, with the largest vessel on the bottom (fastest decay) and the smallest vessel on the top (slowest decay). All the parenchyma regions have slower decays than the vessel regions, which is expected, and the flow order visualized by the speckle visibility curve follows the color map seen in both the single exposure and MESI frames. From these curves, the vessel regions have high agreement between the measured data and the MESI fitted results. The parenchyma regions only have agreement for the shortest exposure time, and essentially fit the average with higher deviation for the longer exposure times. For the spatial relative ICT comparison, the estimated flow distributions from the MESI and single exposure highlight that each model provides a different estimate of the relative flows across the FOV. Here, the MESI relative ICT computations are assumed to be the most accurate based on previous studies in animal models, with comparisons to absolute speeds and correlation time measurements [11, 12, 16]. The MESI model provides similar results to 1 and 1.5 ms, depending on the ROI, and shows a much broader relative flow distribution compared to the longer exposure times.

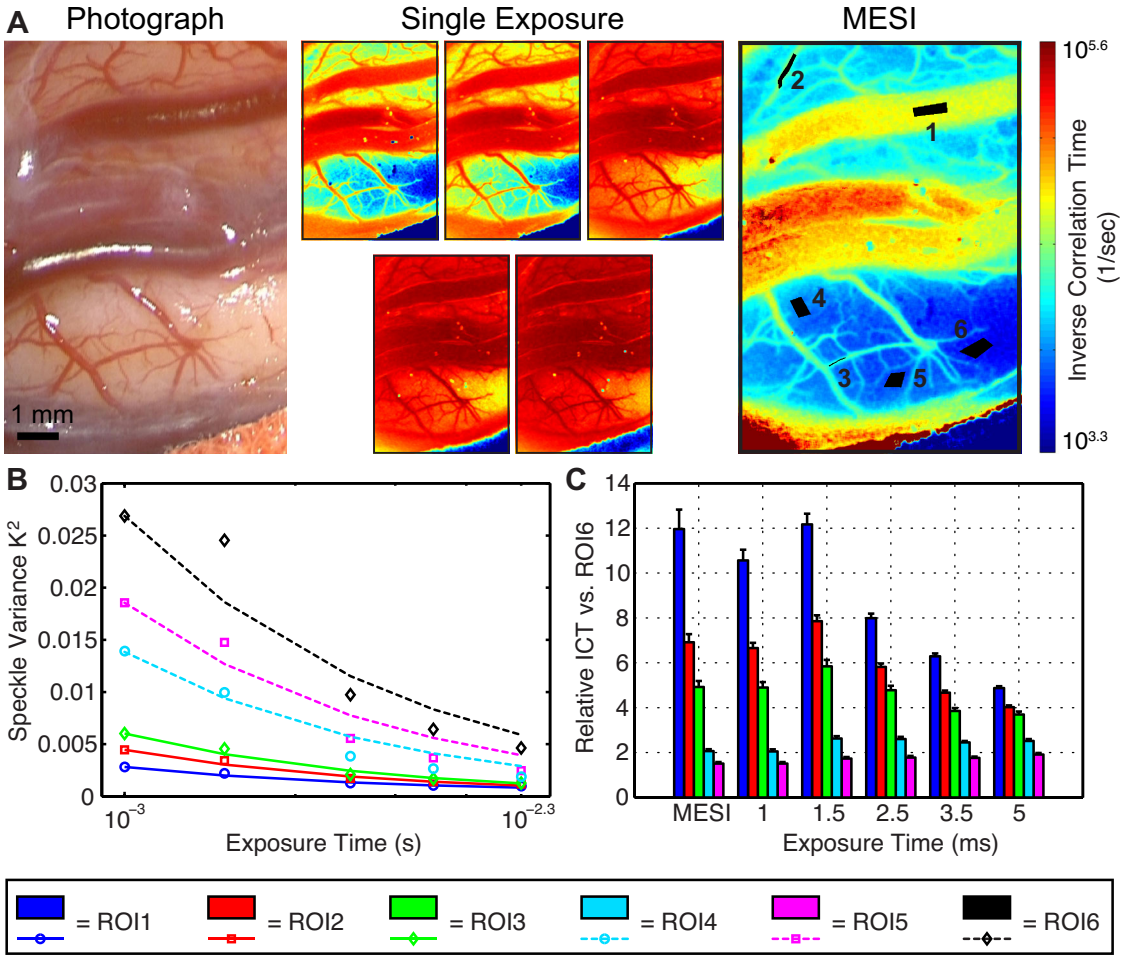

Figure 6.14: MESI model results for patient 15, with comparison to single exposure imaging. (A) Color photograph (left) and corresponding MESI ICT map (right) computed from five single exposure LSCI frames (middle), included here for reference. The color bar only applies to the MESI frame, and higher ICT values (red) indicate faster flow. The numbered ROIs used for analysis are shown in black in the MESI ICT frame. (B) MESI-computed speckle visibility curves for each of the six ROIs shown on a semi-logarithmic scale. The fits are given by the solid or dotted lines, and the points show the measured data. (C) Relative ICT comparison across ROIs, using ROI 6 as a baseline (slowest flow), for the MESI model as well as each of the individual exposure times measured.

The second example is shown for patient 16 in Figure 6.15 with the same layout. Here, the MESI computed ICT map on the right side has very similar overall appearance to the shortest single exposure time image. The branching vessels from the central horizontal vein do appear slower in the MESI ICT frame, which highlights the fact that the MESI frame is displaying a wider range of measured flows. A similar span of ROIs was selected for this case, and similar agreement with expected physiology is observed for the speckle visibility curve. The vessel ROIs have the fastest decay and proceed in the expected order based on the vessel size, and the parenchyma ROIs follow the flow order visualized in both the single exposure and MESI frames. The fits have higher deviation across all ROIs for the shortest exposure time, but good agreement for the longer exposure times across both tissue regions. For the relative ICT comparison, the 1 ms exposure time estimates the widest distribution of flows among the ROIs, but the MESI computation is expected to be more accurate since it accounts for a wider sampling of flows overall. For the single exposure times, the span of the measured flow distribution decreases incrementally as exposure time increases. Here, it is interesting to point out that the 5 ms exposure estimates that vessel ROI 1 and its vessel branch ROI 2 have the same relative flow. This is not physiologically realistic, since blood flow must follow conservation of mass. This means that the total flow in a vessel approaching an intersection must be equal to the sum of flows in each of the daughter vessels after that junction. Since ROI 2 is a daughter branch of ROI 1, it is not possible for these flows to be exactly the same. This highlights the fact that improper exposure time selection can lead to clinically incorrect flow estimates, which could provide misleading information to the surgeon. Overall, the MESI model provides flow estimates in between the 1 and 2 ms single exposure times, all of which provide improved sensitivity relative to the longer exposure times.

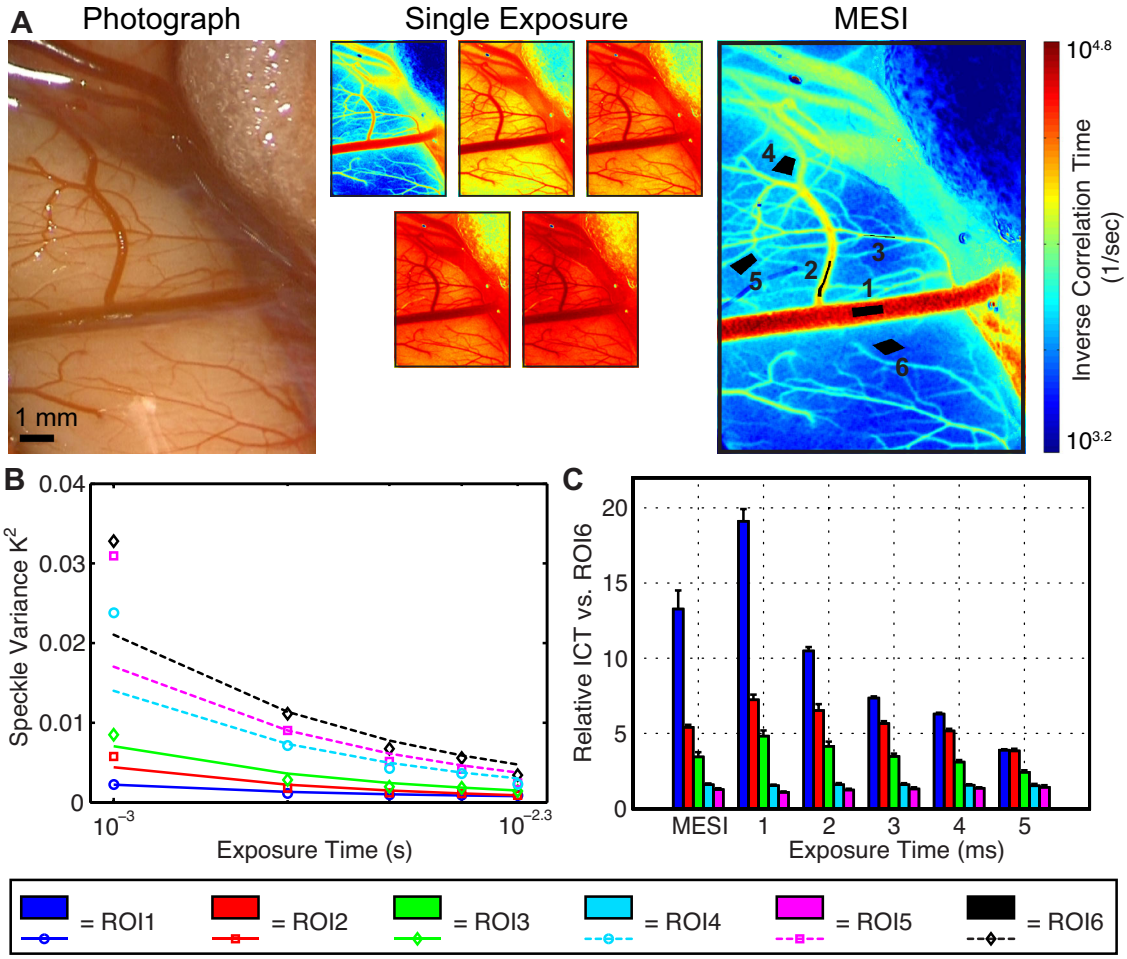

Figure 6.15: MESI model results for patient 16, with comparison to single exposure imaging. (A) Color photograph (left) and corresponding MESI ICT map (right) computed from five single exposure LSCI frames (middle), included here for reference. The color bar only applies to the MESI frame, and higher ICT values (red) indicate faster flow. The numbered ROIs used for analysis are shown in black in the MESI ICT frame. (B) MESI-computed speckle visibility curves for each of the six ROIs shown on a semi-logarithmic scale. The fits are given by the solid or dotted lines, and the points show the measured data. (C) Relative ICT comparison across ROIs, using ROI 6 as a baseline (slowest flow), for the MESI model as well as each of the individual exposure times measured.

The third example is shown for patient 19 in Figure 6.16 with the same layout. Similar to patient 16, the MESI computed ICT map on the right has a very similar appearance to the shortest single exposure time image. A similar span of ROIs was selected for this case, and similar trends are observed in the speckle visibility curve. This is a special case with the region of tissue cautery in the middle of the camera FOV, as evidenced by the color photograph. Physiological expectations are not as obvious, especially regarding the extent of the flow reduction caused by the cautery. ROI 1 in the narrowed vessel immediately next to the cautery has the fastest measured flow, which is not easily discernible from the photograph. The decays of the smaller vessel ROIs follow in the expected order given their size, with the parenchyma ROI outside the cautery tissue region next as expected. The two parenchyma ROIs selected on the edge of the tissue cautery follow the order suggested by the single exposure and MESI frames, although it is difficult to tell if this is clinically expected. This case also has relatively high deviation for the fits at both the shortest exposure time and the longer exposure time, with better overall fits for the vessel regions. The parenchyma regions only have agreement for the 2 ms exposure time, and essentially fit the average with high deviation for all other exposure times. As discussed more in more qualitative terms in Section 6.5.1, exposure times 3 – 5 ms show a large jump in decorrelation relative to shorter exposures, and then have very small differences between them. This is clearly evident with the parenchyma ROIs, which creates some uncertainty for the accuracy of these longer exposure images. It is possible that physiology may have changed during the recording. The degree of tissue motion or the laser coherence reduction may have also accelerated decorrelation for these longer exposures. For the relative ICT comparison, the 1 ms exposure time estimates the widest distribution of flows among the ROIs. The MESI computation has better agreement with the 2 ms exposure, which is reasonable given the model fits. It is

interesting to point out vessel ROIs 2 and 3 switch flow orders as exposure time increases, with the flow in ROI 2 > ROI3 for MESI, 1 ms, and 2 ms, ROI 2 ≅ ROI 3 for 3 ms, and then ROI 2 < ROI3 for 4 and 5 ms. The swap in flow estimates depending on the exposure time further supports the improved accuracy gained by sampling flows across multiple exposure times.

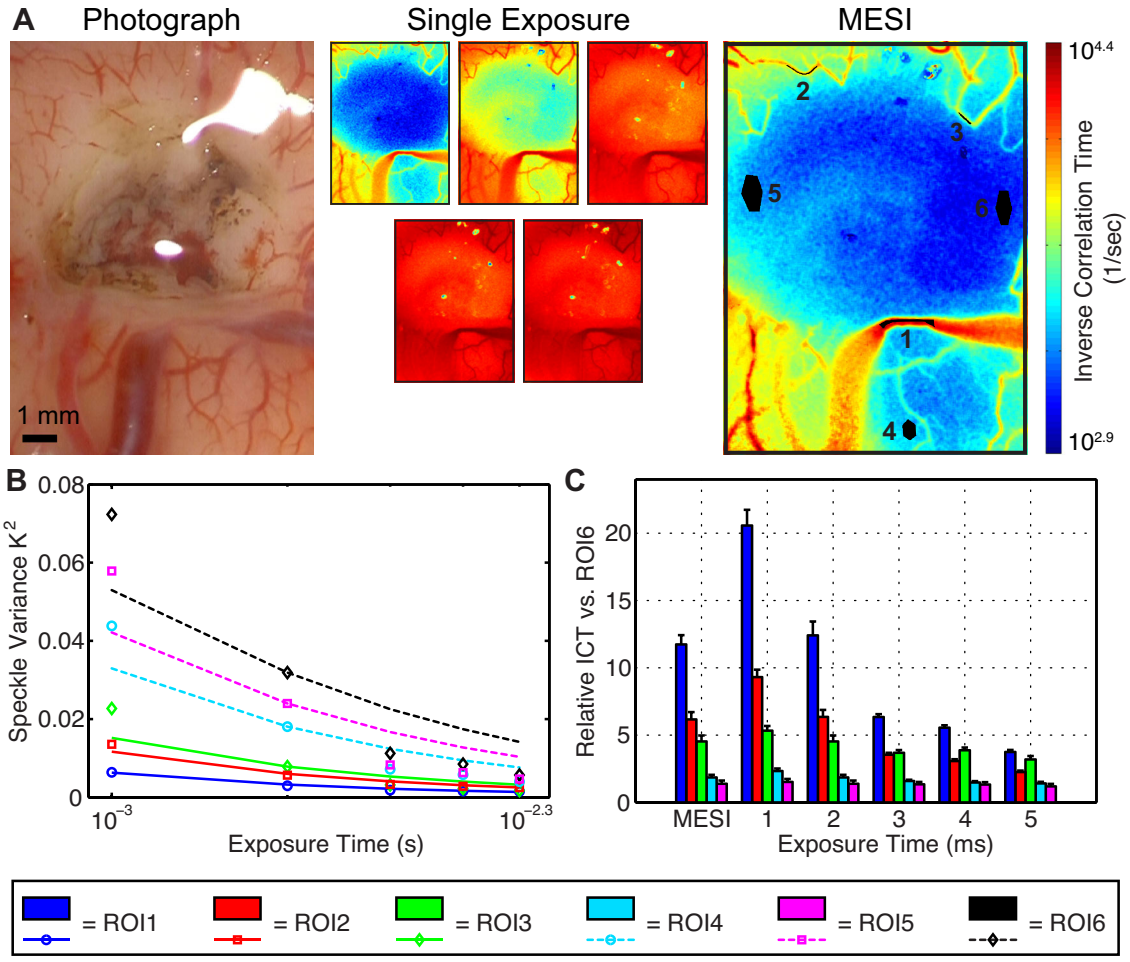

Figure 6.16: MESI model results for patient 19, with comparison to single exposure imaging. (A) Color photograph (left) and corresponding MESI ICT map (right) computed from five single exposure LSCI frames (middle), included here for reference. The color bar only applies to the MESI frame, and higher ICT values (red) indicate faster flow. The numbered ROIs used for analysis are shown in black in the MESI ICT frame. (B) MESI-computed speckle visibility curves for each of the six ROIs shown on a semi-logarithmic scale. The fits are given by the solid or dotted lines, and the points show the measured data. (C) Relative ICT comparison across ROIs, using ROI 6 as a baseline (slowest flow), for the MESI model as well as each of the individual exposure times measured.

The fourth example is shown for patient 17 in Figure 6.17 with the same layout. Here, the MESI computed ICT map on the right visualizes a larger range of flow differences relative to each individual exposure, and visually looks like a composite of the information from the first three single exposure images. A similar span of ROIs was selected for this case, and similar agreement with expected physiology is observed for the speckle visibility curve. Because of the smaller diameter vasculature in this case, the largest vessel ROI 1 has slower decays relative to previously displayed examples, but still has the fastest decay for this set of ROIs. The decays of the smaller vessel ROIs follow in the expected order given their size, though the difference in decay rates is very small. This may be clinically expected, given the relative uniformity of vasculature size distribution across the cortical region. The parenchyma ROIs are all slower than the vessels as expected, but the decays are all very similar, indicating a small distribution of flows across the tissue. All of the ROIs have high deviation in the fits at the shortest exposure time (0.5 ms), with best agreement throughout at the second exposure time (1 ms). Similar to cases 15 and 19, the fits for the longer exposure times have lower deviation for the vessel ROIs compared to the parenchyma regions. For the relative ICT comparison, there is similar performance across all ROIs for the MESI, 0.5 ms, 1 ms, 2 ms, and even 3 ms exposure times, as all produce similar flow distributions. The exposure time with the best agreement with the MESI estimate is a close call between either 1 or 2 ms, depending on the ROI. Both 1 and 2 ms produce equivalent estimates with MESI except ROI 1, which is closer in the 2 ms exposure, and ROI 3, which is closer in the 1 ms exposure. The 3 ms exposure provides a good sensitivity to flow differences among the ROIs, with different magnitude estimates than MESI for the shorter exposure times. The sensitivity drops for the 4 and 5 ms exposure times, where

the width of the flow distribution decreases and vessel ROIs 2 and 3 start to appear more similar.

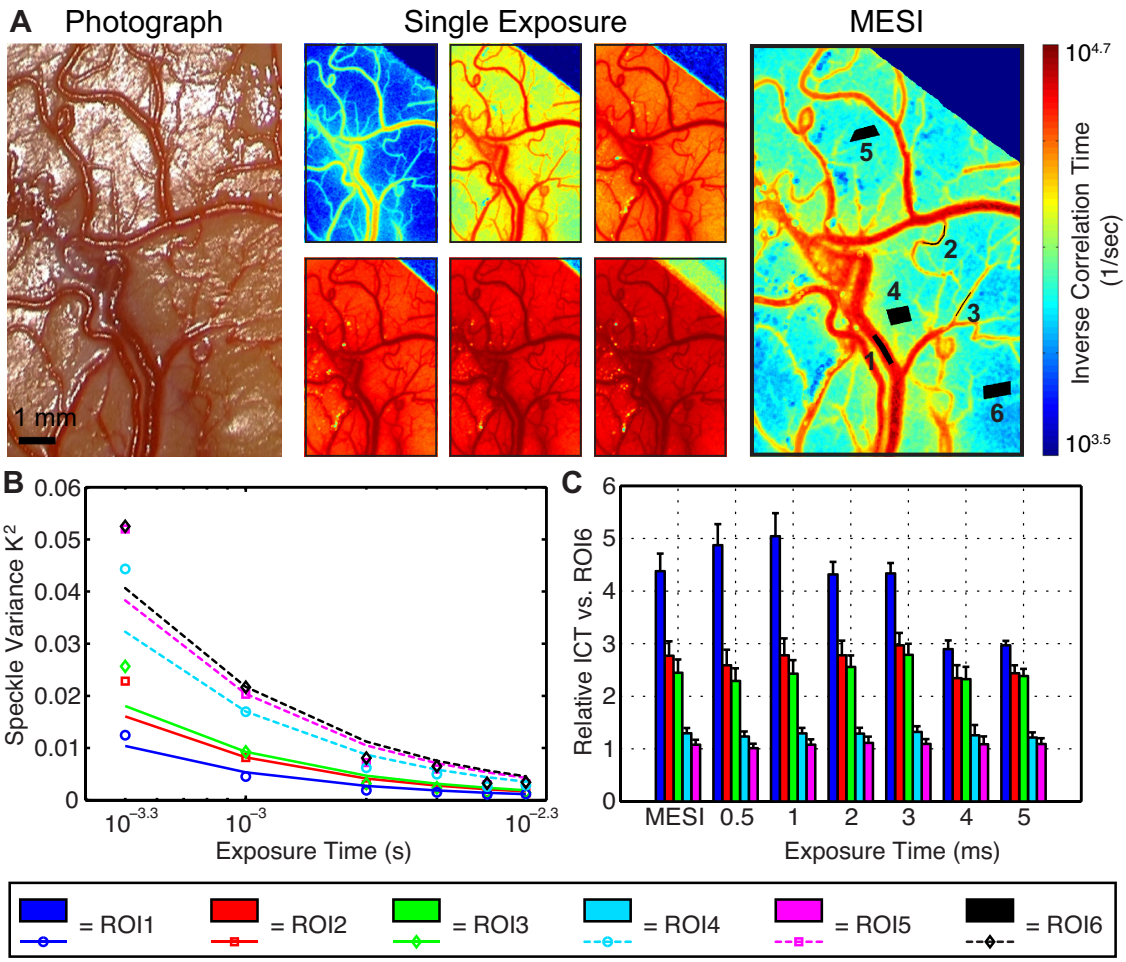

Figure 6.17: MESI model results for patient 17, with comparison to single exposure imaging. (A) Color photograph (left) and corresponding MESI ICT map (right) computed from six single exposure LSCI frames (middle), included here for reference. The color bar only applies to the MESI frame, and higher ICT values (red) indicate faster flow. The numbered ROIs used for analysis are shown in black in the MESI ICT frame. (B) MESI-computed speckle visibility curves for each of the six ROIs shown on a semi-logarithmic scale. The fits are given by the solid or dotted lines, and the points show the measured data. (C) Relative ICT comparison across ROIs, using ROI 6 as a baseline (slowest flow), for the MESI model as well as each of the individual exposure times measured.

The fifth example is shown for patient 18 in Figure 6.18 with the same layout. Here, the MESI computed ICT map on the right has overall very similar appearance to the shortest single exposure time image with a larger range of flows visualized, similar to Case 16 and 19. A similar span of ROIs was selected for this case, and similar agreement with expected physiology is observed for the speckle visibility curve. The vessel ROIs have the fastest decay and proceed in the expected order based on the vessel size. The parenchyma ROIs follow with slower decays and low spread in the speckle visibility curve. The vessel ROIs 1 and 2 have the best fits, with good agreement across all exposure times, with slightly higher deviation in the smallest vessel ROI 3 for the longer exposures. The parenchyma ROIs had good agreement at 0.5 ms and 2 ms with higher deviation at the remaining exposure times, showing that fits are following the average across the exposure range. Similar to Case 19, the longer exposure times 3 – 5 ms show a large jump in decorrelation relative to shorter exposures, which may point to some uncertainty in these measurements as discussed previously. For the relative ICT comparison, the MESI computed relative flows have the best agreement with the shortest exposure time, 0.5 ms, with only a small difference in predicted value for the largest vessel ROI 1. The 1 and 2 ms exposures provide good sensitivity to flow differences among the ROIs, with different magnitude estimates than MESI. The sensitivity drops for the 3 – 5 ms exposure times, as expected from the individual exposure images, where the width of the flow distribution decreases dramatically. Similar to Case 19, it is interesting to point out that vessel ROIs 2 and 3 switch flow orders as exposure time increases, with the flow in ROI 2 > ROI 3 for MESI, 0.5 ms, 1 ms, and 2 ms, ROI 2 ≅ ROI 3 for 3 ms, and then ROI 2 < ROI 3 for 4 and 5 ms. This is another example that confirms higher accuracy with shorter exposure times, which have

improved sensitivity to flow differences and prevent computation of misleading flow relationships.

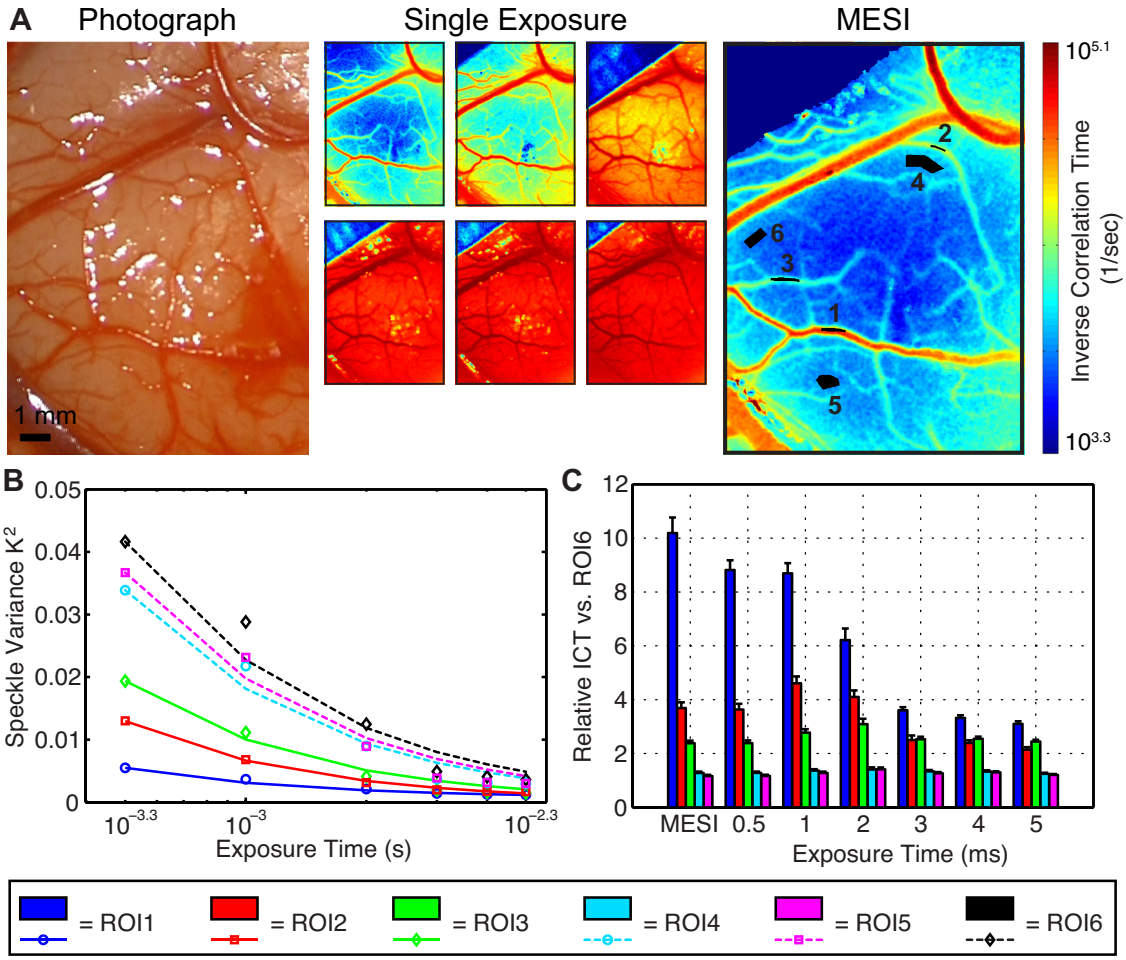

Figure 6.18: MESI model results for patient 18, with comparison to single exposure imaging. (A) Color photograph (left) and corresponding MESI ICT map (right) computed from six single exposure LSCI frames (middle), included here for reference. The color bar only applies to the MESI frame, and higher ICT values (red) indicate faster flow. The numbered ROIs used for analysis are shown in black in the MESI ICT frame. (B) MESI-computed speckle visibility curves for each of the six ROIs shown on a semi-logarithmic scale. The fits are given by the solid or dotted lines, and the points show the measured data. (C) Relative ICT comparison across ROIs, using ROI 6 as a baseline (slowest flow), for the MESI model as well as each of the individual exposure times measured.

The sixth and final example is shown for patient 21 in Figure 6.19 with the same layout. Here, the MESI computed ICT map on the right has very similar overall appearance to the shortest single exposure time image with a larger range of flows visualized, similar to Cases 16, 18, and 19. A similar span of ROIs was selected for this case, here with four vessels to span the broader range of vessel sizes present in the FOV. For the first time, the speckle visibility curve shows excellent fits across almost all exposure times and all ROIs, spanning both vessel and parenchyma regions. As a reminder, this case used neutral density filters to control the laser power and to record up to 20 ms exposure time. These results are promising, and show that this revised acquisition method provides improved quality in the single exposure images, and in turn leads to a better fit for the MESI model. The acquisition of the longer exposure times also helped improve fitting accuracy by providing data points at the tail end of the curve. For the vessel ROIs selected, the decay order is not based on vessel size, but is still clinically feasible. The small diameter descending arteriole ROI 1 has the fastest decay, followed by the large vessel ROI 2, followed by its branch ROI 3, and finally a small cortical vessel ROI 4. The parenchyma ROIs follow with slower decays in the order expected from both the MESI and single exposure images. For the relative ICT comparison, the MESI computed relative flows have the widest flow distribution and are expected to be the most accurate, given the excellent fits in the speckle visibility curve. Both the 0.5 and 1 ms exposure times have similar flow sensitivities, and show close agreement the MESI predicted flows. The main discrepancy is the flow prediction for the descending arteriole ROI 1, which is a smaller magnitude for the single exposure frames. For longer exposure times between 2 and 5 ms, the flow distribution is much smaller, but still follows the expected trend overall. The 4 ms exposure time shows that ROIs 2 and 3 have equivalent flow, which again is unexpected clinically since ROI 3 is a daughter

branch of ROI 2. The 10 ms exposure shows a very small distribution, with magnitudes around half that seen from the 5 ms exposure, but continues to follow expected trends. The 20 ms exposure shows very little differentiation among vastly different tissue ROIs, and even shows that the very small cortical vessel ROI 4 has faster flow than larger vessel ROI 3, and almost equivalent flow to the largest vessel ROI 2. This is clearly not clinically feasible, and demonstrates that individual exposure times cannot provide accurate flow estimates when sampled alone. This is the best example of the MESI performance relative to the single exposure LSCI images, showing excellent fits. The results show higher accuracy and improved sensitivity to flow differences with the MESI model and comparable performance with the shortest available exposure time.

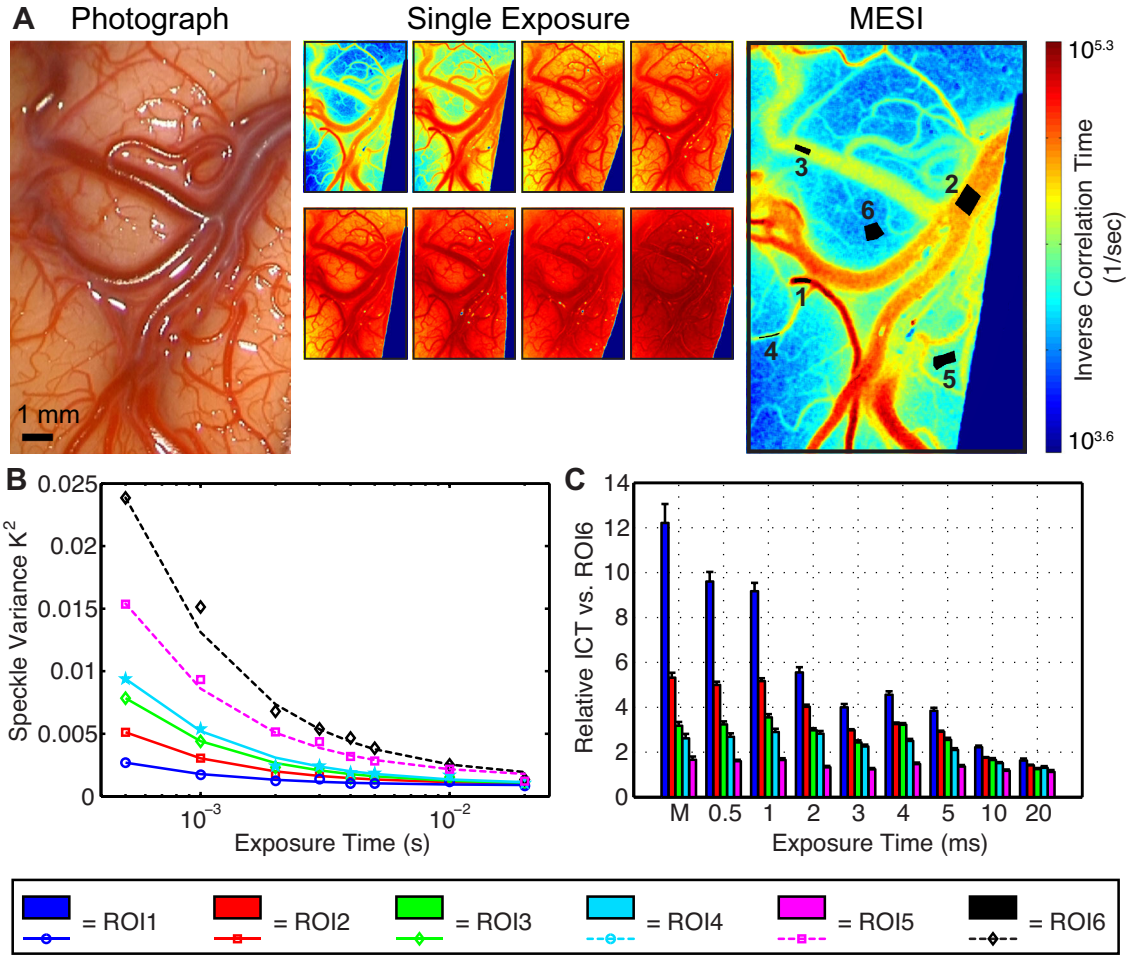

Figure 6.19: MESI model results for patient 21, with comparison to single exposure imaging. (A) Color photograph (left) and corresponding MESI ICT map (right) computed from eight single exposure LSCI frames (middle), included here for reference. The color bar only applies to the MESI frame, and higher ICT values (red) indicate faster flow. The numbered ROIs used for analysis are shown in black in the MESI ICT frame. (B) MESI-computed speckle visibility curves for each of the six ROIs shown on a semi-logarithmic scale. The fits are given by the solid or dotted lines, and the points show the measured data. (C) Relative ICT comparison across ROIs, using ROI 6 as a baseline (slowest flow), for the MESI model as well as each of the individual exposure times measured.

6.6 CLINICAL MESI DISCUSSION

The results from this study demonstrate that exposure time selection matters, and that multiple exposure speckle imaging can be performed in the clinic with excellent performance with proper image acquisition. Both the qualitative assessment from single exposure frames and the quantitative comparison across ROIs demonstrates that each individual exposure time predicts a different range of flows across the cortical FOV. For all of the cases, the shorter exposure times provided the best overall sensitivity. The optimal agreement with the MESI predictions spanned between 0.5 – 2 ms exposure times, depending on the case. This is significant because the shortest exposure time previously measured with intraoperative LSCI was 4 ms [4, 5]. The other frequently used exposure times, 8.4 ms [4, 6], 16 ms [7], and 20 ms [8], are closer to the longer exposure times measured in Case 21, 10 and 20 ms. These exposure times had poor sensitivity among different tissue regions, with a span of ≤2.5× in relative flow distributions across the ROIs sampled. As mentioned previously, the size of the camera FOV was much smaller in this study compared to other groups (several centimeters). Thus, the magnitude of the tissue motion may have been higher in this study, which could have resulted in faster decorrelation of the speckles at longer exposure times. Also, the cutoff where the tissue motion is high enough to result in image blurring will vary depending on the magnification of the image. Nevertheless, the optimal exposure time is more closely related to the range of blood flows within the tissue sample, which is expected to be similar between various groups regardless of the camera FOV. This implies that sensitivity should still be higher at shorter exposures given the range of clinical flows expected. Any future clinical studies involving intraoperative examination of LSCI should choose their exposure time carefully to maximize their sensitivity.

The implementation of the MESI model in the clinic demonstrates that proper image acquisition and processing of clinical MESI images can result in excellent performance (Case 21) with clinically valid flow estimates. The first component that led to high goodness of fit was modifying the laser power using neutral density filters, which stabilized laser coherence across exposures, and acquisition of longer exposure times, which helped improve fitting accuracy approaching the upper exposure time limit. The second component that led to clinically feasible flow rates was the calibration procedure used to set the instrumentation factor, β. By fixing β using a static reference within the imaging field, reliable fitting of the MESI model was achieved and every case demonstrated realistic flow trends across ROIs. This suggests that this calibration procedure was a valid method of accounting for instrument variations from case-to-case. Because β is an estimate for the lower limit of the speckle variance at very short exposure times, this calibration also helped the MESI model fit the measured data from a very small range of the entire speckle visibility curve. An illustration of the full theoretical speckle visibility curve speckle in relation to the measured data is shown for Case 21 in Figure 6.20. Here, the theoretical estimates shown with the thicker solid lines were computed by estimating the speckle variance using Equation 6.1 across a broader exposure time range in both directions. The β for this case and the MESI model outputs (τ_c, ρ, and v_{noise}) were fixed for each ROI to ensure the fits for the measured data were correctly extrapolated. This theoretical plot shows the full sigmoidal shape of the speckle visibility curve, which approaches the β estimate of 0.153 for this case as $T \rightarrow 1$ μs for most ROIs and as $T \rightarrow 0.1$ μs for the fastest vessel ROI. These exposure times are 3 – 4 orders of magnitude shorter than what was measured in this study, which is not feasible to measure without a re-design of the intraoperative instrument to significantly increase light throughput. Also, many currently available cameras have a lower exposure time

limit of tens of μs, meaning that recording at these values could be limited by the camera hardware. Estimating this lower bound experimentally helped the MESI model fit the full visibility curves from the small range of measurable exposure times. This calibration practice was also applied to the single exposure time images, and high accuracy in the relative flow estimates relative to the MESI model was measured from many of the shorter exposure times across cases. This suggests that this simple calibration procedure during image acquisition can improve performance for single exposure LSCI analysis as well. This is significant because single exposure LSCI may be the best option for some surgeries, where time limitations prevent the measurement of multiple exposure times. In these critical monitoring situations, high sensitivity is required with real-time feedback, and single exposure LSCI with a short exposure time may be a suitable alternative to the MESI estimates.

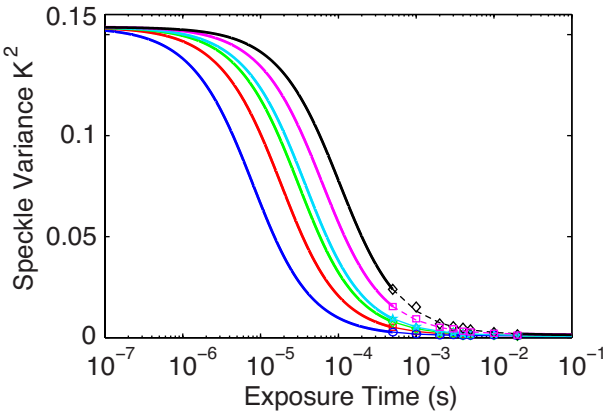

Figure 6.20: Theoretical estimation of the full speckle visibility curve from Case 21, showing the original measured data and fits along with theoretical estimates of the speckle variance for each ROI shown with thicker line width. This plot demonstrates the lower limit of exposure times that are theoretically required for measuring the full visibility curve in a clinical setting.

6.7 CONCLUSIONS

The results from this phase II clinical study are promising, and demonstrate specific hardware, image acquisition, and image processing optimizations for improving the accuracy and sensitivity of LSCI recordings for monitoring blood flow during neurosurgery. The hardware design changes in this study, including the addition of the polarizer to reduce specular reflections and the shift to a NIR wavelength to reduce hemoglobin absorption, significantly improved image quality and reduced the presence of image artifacts that reduce the area of usable blood flow information. Recording multiple camera exposure times from the same cortical tissue area demonstrated the importance of proper exposure time selection for sampling the flow magnitude in the human brain. Across all cases, shorter exposure times had higher dynamic range and improved sensitivity for spatial differentiation of flows within the FOV. A calibration procedure estimated the instrumentation parameter β experimentally using a static sample at the shortest available exposure time. The addition of neutral density filters to the instrumentation improved the quality of the single exposure images, and enabled imaging at longer exposure times. All of these image acquisition optimizations improved the quantitative and physiological accuracy in both the MESI and single exposure flow estimates. Overall, this study showed that clinical MESI is possible to perform intraoperatively to maximize flow sensitivity and accuracy, and that single exposure LSCI at the proper exposure selection using the estimate for β can provide very similar performance.

6.8 REFERENCES

[1] E. L. Towle, L. M. Richards, S. M. S. Kazmi, D. J. Fox, and A. K. Dunn, "Comparison of indocyanine green angiography and laser speckle contrast

imaging for the assessment of vasculature perfusion," *Neurosurgery,* **71**(5), pp. 1023-1030; discussion 1030-1031 (2012).
[2] S. A. Prahl. (1999). *Optical Absorption of Hemoglobin*. Available: http://omlc.ogi.edu/spectra/hemoglobin/index.html
[3] S. Yuan, A. Devor, D. A. Boas, and A. K. Dunn, "Determination of optimal exposure time for imaging of blood flow changes with laser speckle contrast imaging," *Applied Optics,* **44**(10), pp. 1823-1830 (2005).
[4] N. Hecht, J. Woitzik, S. Konig, P. Horn, and P. Vajkoczy, "Laser speckle imaging allows real-time intraoperative blood flow assessment during neurosurgical procedures," *Journal of Cerebral Blood Flow & Metabolism,* **33**(7), pp. 1000-1007 (2013).
[5] J. Woitzik, N. Hecht, A. Pinczolits, N. Sandow, S. Major, M. K. Winkler, S. Weber-Carstens, C. Dohmen, R. Graf, A. J. Strong, J. P. Dreier, and P. Vajkoczy, "Propagation of cortical spreading depolarization in the human cortex after malignant stroke," *Neurology,* **80**(12), pp. 1095-1102 (2013).
[6] N. Hecht, M-M. Müller, N. Sandow, A. Pinczolits, P. Vajkoczy, and J. Woitzik, "Infarct prediction by intraoperative laser speckle imaging in patients with malignant hemispheric stroke," *Journal of Cerebral Blood Flow & Metabolism,* pp. 1-11 (Published online before print, Oct 23, 2015).
[7] S. Nomura, T. Inoue, H. Ishihara, H. Koizumi, E. Suehiro, F. Oka, and M. Suzuki, "Reliability of laser speckle flow imaging for intraoperative monitoring of cerebral blood flow during cerebrovascular surgery: comparison with cerebral blood flow measurement by single photon emission computed tomography," *World Neurosurgery,* **82**(6), pp. e753-757 (2014).
[8] E. Klijn, H. C. Hulscher, R. K. Balvers, W. P. Holland, J. Bakker, A. J. Vincent, C. M. Dirven, and C. Ince, "Laser speckle imaging identification of increases in cortical microcirculatory blood flow induced by motor activity during awake craniotomy," *Journal of Neurosurgery,* **118**(2), pp. 280-286 (2013).
[9] A. B. Parthasarathy, W. J. Tom, A. Gopal, X. J. Zhang, and A. K. Dunn, "Robust flow measurement with multi-exposure speckle imaging," *Optics Express,* **16**(3), pp. 1975-1989 (2008).
[10] A. B. Parthasarathy, S. M. S. Kazmi, and A. K. Dunn, "Quantitative imaging of ischemic stroke through thinned skull in mice with Multi Exposure Speckle Imaging," *Biomedical Optics Express,* **1**(1), pp. 246-259 (2010).
[11] S. M. S. Kazmi, A. B. Parthasarathy, N. E. Song, T. A. Jones, and A. K. Dunn, "Chronic imaging of cortical blood flow using Multi-Exposure Speckle Imaging," *Journal of Cerebral Blood Flow & Metabolism,* **33**(6), pp. 798-808 (2013).
[12] S. M. S. Kazmi, R. K. Wu, and A. K. Dunn, "Evaluating multi-exposure speckle imaging estimates of absolute autocorrelation times," *Optics Letters,* **40**(15), pp. 3643-3646 (2015).
[13] "American National Standard for the Safe Use of Lasers," in *ANSI Z136.1-2007*: Laser Institute of America, 2007.

[14] D. A. Boas and A. K. Dunn, "Laser speckle contrast imaging in biomedical optics," *Journal of Biomedical Optics,* **15**(1), pp. 011109 (2010).
[15] R. Bandyopadhyay, A. S. Gittings, S. S. Suh, P. K. Dixon, and D. J. Durian, "Speckle-visibility spectroscopy: A tool to study time-varying dynamics," *Review of Scientific Instruments,* **76**(9), pp. 093110 (2005).
[16] S. M. S. Kazmi, E. Faraji, M. A. Davis, Y. Y. Huang, X. J. Zhang, and A. K. Dunn, "Flux or speed? Examining speckle contrast imaging of vascular flows," *Biomedical Optics Express,* **6**(7), pp. 2588-2608 (2015).
[17] S. M. S. Kazmi, S. Balial, and A. K. Dunn, "Optimization of camera exposure durations for multi-exposure speckle imaging of the microcirculation," *Biomedical Optics Express,* **5**(7), pp. 2157-2171 (2014).

Chapter 7: Conclusions and Future Work

7.1 SUMMARY

Laser speckle contrast imaging (LSCI) is a very useful tool for monitoring blood flow in exposed tissues, and can be adapted for clinical use during surgeries. This dissertation characterizes the main hardware components in an LSCI imaging system, the laser and the camera, and adapts the instrumentation for intraoperative use during neurosurgery. The hardware and image acquisition parameters required for the highest accuracy and sensitivity to relative flow changes were determined for optimized LSCI performance, both in a laboratory and clinical setting.

7.1.1 LSCI Hardware Assessment

For the LSCI laser diode assessment, both the coherence length and the stability of the diode output were examined across a wide range of lasers spanning 635 – 850 nm, including both traditional and low-cost options. All near infrared (NIR) laser diodes had more than sufficient coherence length for LSCI (>10 m), while only one visible laser diode model had a coherence length >2 mm. For traditional diode options, the laser diode drive current affected the measured coherence length, and should be kept constant within and across experiments. Also, the traditional diode stability in an imaging setting was improved with the use of a temperature controller. The NIR low-cost diodes provided equivalent coherence length and stability relative to traditional counterparts, and serve as an excellent low-cost option if needed.

For the LSCI camera assessment, both the accuracy of relative flows and the sensitivity to a small change in flow was measured to assess the most clinically relevant performance metrics. Microfluidics were used to assess these parameters in a controlled setting, and a thorough assessment of two available flow control systems was performed.

The pressure regulated flow system was superior to the syringe pump in terms of stability, repeatability, and responsivity, and provides the best flow control option for cross-camera comparisons. The camera specifications compared included bit depth, frame rate, color versus monochrome, and cost. Bit depth studies demonstrated nearly perfect 1:1 correspondence in relative flow estimates from both 8-bit and 16-bit cameras. Frame rate was more critical than bit depth for sensitivity to small flow changes, and superior performance was observed with the faster, 8-bit camera. Increasing both spatial and temporal averaging decreased noise levels as expected, and improved visualization of small, transient flow changes. A color camera sensor provided highly equivalent relative flow estimates compared to an 8-bit monochrome sensor when operated in the correct video output mode. The color camera examined was a webcam, which demonstrated that low-cost cameras could provide excellent LSCI performance. A complete compact, lightweight LSCI setup was also built to demonstrate that relative blood flow could be measured very inexpensively, and that costly components are not required.

7.1.2 Intraoperative LSCI during Neurosurgery

The 10-patient pilot clinical study demonstrated that LSCI could be adapted for intraoperative use, and that the microscope-integrated instrument design provided excellent performance with minimal interference to the brain tumor resection procedure. Methods for accounting for cardiac and tissue motion artifacts were designed, and significantly reduced noise in the measured relative blood flow recordings. These motion correction techniques enabled detection of both the relative magnitude and temporal dynamics of blood flow changes after cortical stimulation, which is clinically useful to surgeons.

The ongoing phase II clinical study (14-patients to date) demonstrated hardware as well as image acquisition and processing optimizations for improving clinical performance. The modified instrument design improved image quality by greatly reducing the presence of undesirable image artifacts that reduce the area of usable blood flow information. The image acquisition procedure was altered to record multiple camera exposure times from the same tissue region to determine which exposure time was best suited for clinical use. The shorter exposure times had higher dynamic range and improved sensitivity for differentiating blood flows within the tissue region. The multi-exposure speckle imaging (MESI) model was then used to compute more accurate estimates of relative blood flow levels, using a calibration procedure to set the instrumentation factor in the model. The results demonstrated MESI-estimated relative flows were realistic physiologically, and that single exposure LSCI at the proper exposure time could provide similar performance. MESI and single exposure LSCI relative blood flow estimates (0.5 – 2 ms) provided the highest accuracy and sensitivity to differences in flows, which are critical performance metrics for clinical decision making.

7.2 Future Directions

This dissertation focuses on the optimization and improvement of LSCI hardware, image acquisition, and image analysis methods for translation of LSCI to a clinical setting during neurosurgery. The best possible instrument performance is required before surgeons can adopt LSCI as a tool for monitoring blood flow, and this work represents the first steps towards this ultimate goal. A discussion of next steps for hardware design as well as clinical data interpretation and application that are required to make LSCI truly clinic-ready are included below.

7.2.1 Laser Diode Selection

The laser diode models examined in this work represent a very small percentage of commercially available diodes, and there are many other wavelengths and powers available in the 600 – 850 nm range most commonly used for LSCI. The coherence length and stability of the diode varies from the semiconductor material, drive current, temperature control, and likely from many other factors (environmental, lifetime hours, model-to-model variations). Only a small sampling of these variables was tested in this study, and a more in-depth review is still needed. Although it is almost impossible to test diodes from every manufacturer, more studies can be used to confirm general trends in laser diode performance with a broader sampling. For example, it would be useful for LSCI users to know the optimal laser diode current and temperature settings for best performance. This work showed that the current level affected the coherence, and that the temperature improved stability, but broader studies are still required to confirm this trend is true across diode models. It is also expected that there are more visible laser diode models available that provide >2 mm coherence length, and more options should be identified for applications that require a visible wavelength.

The performance of these laser diodes in a LSCI imaging setting was studied with a static sample in this work, to ensure all measured noise was a result of the diode rather than the sample. However, further studies should be performed to assess stability levels *in vitro* using microfluidic studies, since this is a better representation of the end use of LSCI in a clinical setting. It is difficult to predict how much the differences in coherence length and the stability of the diode will affect measured relative flow from LSCI. This is ultimately the question that needs to be answered, and will help solidify design specifications for LSCI systems. Because each laser diode has to be examined sequentially, any microfluidic studies should be performed using the pressure regulated

flow control system to enable cross-diode comparisons. This will provide the stability and repeatability required to properly assess the diodes in a controlled flow setting.

7.2.2 Camera Selection

Similarly, the camera models examined in this work are a very small percentage of commercially available cameras, both in terms of specifications and manufacturers. Although a broad range of camera specifications were studied in this work, more studies are required to confirm the trends observed across a broader range of cameras. Future studies are planned to expand the camera comparison to include more bit depths (12-bit), a low-cost monochrome sensor, a traditional color sensor, and a camera with a high pixel density. Expanding the bit depth study to include at least one more example will strengthen the results found in this study. Monochrome cameras are easier to work with for LSCI, making investigation of a low-cost option of high interest for researchers. Color cameras are commonly used in clinical instruments, such as the built-in Zeiss color camera. Thus, demonstrating equivalent performance in a higher-grade color camera sensor could lead to faster integration of LSCI into currently available clinical systems. A camera with a high pixel density is also of interest because this work demonstrated the importance of spatial averaging for reducing noise in measured relative flow. Higher pixel density would allow more spatial averaging for the same physical area, which could lead to higher noise reduction and will also lead to better image quality (spatial resolution).

Other camera specifications that could be added to the comparison for completeness are CCD vs. CMOS, full well capacity, and quantum efficiency of the camera sensor. CMOS sensors have non-rectangular shaped active areas, which could lead to irregular sampling of the speckle pattern. This comparison would require two

cameras with the exact same specifications except sensor type, to ensure that results could be attributed to CCD versus CMOS differences. Alternatively, pixel fill factor could be compared, since this would likely produce similar results, although the manufacturer does not always report this specification. The full well capacity and quantum efficiency (QE) of cameras could the affect visualization of the speckle pattern, since camera pixels could prematurely saturate due to full well capacity and since a high percentage of light is usually lost due to QE. Ideally, this comparison would also be performed using cameras with similar specifications excluding either full well capacity or QE to draw valid conclusions.

Future studies should also include a multi-camera comparison *in vivo* to assess the sensitivity to a small, transient change in flow. This work presented results in a controlled microfluidic study for a single camera pair, and extension to an *in vivo* setting in the presence of physiological noise and other artifacts would be better representative of clinical applications. This could be performed in rodent models where small flow changes are expected, such as functional activation using forepaw stimulation. Flow changes as small as $5 - 10\%$ lasting <10 seconds are commonly visualized with functional activation in both animal [1-3] and clinical studies [4], making this a good model to examine optimal sensitivity to small flow changes. Examination of the cameras in an *in vivo* setting will improve translatability of the sensitivity results to a clinical setting.

7.2.3 Clinical Instrumentation

The modified clinical instrument design in the phase II study had significant improvements over the direct attachments used in the pilot study. However, improvements are still required to optimize clinical performance, mainly relating to

instrument light levels and MESI acquisition speed. Light levels reaching the camera sensor limited the minimum exposure time used in the phase II clinical study. Since the results demonstrated that even shorter exposure times are required to better sample the clinical flow distribution, higher light throughput is required. Most of the light limitations come from integrating the LSCI hardware into the neurosurgical microscope, since the light split between the different ports immediately limits light levels to ~12.5% of the total light collected. Further light loss is expected due to the coatings of the optics within the microscope, which may not be optimized for NIR light transmission along the camera path. Light levels were improved in the phase II study by using a NIR-enhanced camera sensor with ~5× improvement in QE. To further improve light levels, it may be required to use a different surgical microscope model with higher light throughput or to build a stand-alone system, both simply for validation purposes rather than a final clinical design. Eventually, the LSCI hardware could be properly integrated into neurosurgical microscopes by collaborating with the microscope manufacturer to maximize light throughput to the LSCI camera during use.

Another major improvement would be adapting the clinical MESI acquisition to perform automated, interleaved image acquisition similar to laboratory setups [5, 6]. This would increase acquisition speed by reducing downtime during intensity adjustment for each exposure time. It would also increase confidence in physiological uniformity among each exposure time since, since each MESI set would be acquired in <1 second rather than over the course of several minutes. Laboratory setups use an acousto-optic modulator (AOM) in a free-space setup to modulate the laser intensity across exposure times after an initial calibration procedure. Because AOMs produce a deflected beam, integration into the laser adapter for the surgical microscope could be more difficult. An electro-optic modulator (EOM) could also be used, which produces an on-axis beam with

modulated laser intensity. Both free-space and fiber-based EOMs are available, and integration in the laser adapter is more easily feasible. Because single-mode fibers are typically required for illumination with LSCI, fiber-based EOMs could limit the maximum laser power output. Integration of either modulator would require higher light throughput for proper evaluation.

7.2.4 Clinical Data Processing

In these clinical studies, real-time display of the speckle contrast images was available intraoperatively, but all other processing was performed offline after the procedure. Thus, all of the ROI-based results relating to noise reduction for detecting relative blood flow changes as well as MESI analysis techniques to improve quantitative accuracy are not clinically useful until real-time, intraoperative processing is available. Thus, efforts to speed up motion correction techniques are needed, such as faster implementation of image registration using parallel processing or a customized field programmable gate array (FPGA). A real-time feedback loop using the simultaneously recorded cardiac signals is also required to integrate pulsatile flow correction. Finally, real-time fitting to the MESI model will ultimately be required for clinical application. This is almost impossible with current data acquisition methods, since a calibration image must be acquired first with a static sample to compute β followed by exposure time images recorded sequentially over several minutes before the MESI analysis can be performed. However, if motion correction techniques were implemented in real-time and MESI acquisition was interleaved, it could be possible to perform processing within several minutes on selected ROIs of interest, again using parallel processing methods.

7.2.5 Clinical Data Interpretation

In this work, the relative inverse correlation time (ICT) was used as a metric for blood flow, using both single exposure and MESI computed values. However, a recent study demonstrated that this metric must be linearly scaled to account for the vessel size, which is proportional to the number of dynamic scattering events [7]. This scaling accounts for more rapid de-correlation of speckles within larger vessels by using the vessel diameter (D) as an estimate for the degree of multiple scattering. This accounts for the differences in tissue volume sampling over vessels with various calibers. The results from this study demonstrate that the volumetric flux (flow) is most accurately predicted by the ICT*D product for vascular perfusion [7]. This scaling factor does not apply to parenchymal perfusion with unresolvable vasculature, since tissue volume sampling and number of scattering events should be similar across different parenchymal regions. This implies that the quantitative relative blood flows estimated by the MESI ICT values are off by a scaling factor that depends on the vascular size for vessel ROIs. This affects the ratio of relative flow computations, meaning that the accuracy of the spatial comparisons between vessel regions (bar plots in Chapter 6) have a higher deviation from actual blood flow dynamics.

To improve the accuracy of quantitative relative flow predictions, the diameter of the vessel must be estimated for proper scaling. The diameter can be computed in pixels or physical units, as long as the same unit is used for all vessels in the same tissue region (will cancel out for relative comparisons). Ideally, the diameter should be computed from an anatomic photograph, since LSCI computed diameters using flow-based contrast might not be a good representation of the true vessel diameter. Since specular reflections can be a significant source of artifacts even in color photographs recorded

intraoperatively, it may be necessary to use either the single exposure or MESI ICT frames for estimation.

To assess how well the corrected flow metric (ICT*D) performs in a clinical setting, ROIs from vessel branches can be used to assess how well the metric predicts conservation of flow between parent and daughter branches. Physiologically, the flow from two daughter branches should add up to the total flow in the parent branch with normal, unoccluded vasculature. Thus, examining how well the MESI flow term, ICT*D, predicts this flow conservation provides a quantitative estimate of the accuracy of measured flows. One of the major drawbacks of the relative flows measured intraoperatively is that validation from a second flow measurement technique is unavailable. This conservation of flow assessment provides a useful alternative method for validating the accuracy of the measured flows.

This image analysis method and its implications are currently being explored for the MESI data from the phase II study. Preliminary results from Case 17 are shown as an example in Figure 7.1, demonstrating how to apply this conservation of flow analysis along with computed performance. The ROIs used to compute the MESI ICT values are shown in different colors for each branch, and diameters were estimating using an average metric over the same portion of each vessel segment. Within each branch, the vessel with the largest computed diameter was assumed to be the parent vessel (p), and the two remaining branches were assumed to be the daughter vessels ($d1$, $d2$). Then, the percent difference was calculated assuming conservation of flow, given by

$$\%\ \text{Difference} = \frac{abs(ICT_{d1} * D_{d1} + ICT_{d2} * D_{d2} - ICT_p * D_p)}{ICT_p * D_p} * 100\ , \qquad (7.1)$$

where the subscripts indicate values computed from either the daughter or parent vessel(s). Since the percent difference includes a normalization term, these ICT values

refer to absolute ICT in units of 1/second, rather than relative ICTs. Physiologically, the percent difference should be zero, so lower values indicate higher agreement with true clinical flows. Here, three of the Y-branches have a percent difference <10%, which is encouraging. The largest vessel branch has a higher error of 20.8%. This could possibly be related to errors in diameter computation accuracy, or from placement of the ROIs too far away from the intersection. It could also indicate that the conservation of flow analysis starts to break down in larger diameter vasculature. LSCI imaging of a vessel region samples dynamically scattered light that is spatially localized to the vascular region [8]. As the vessel size increases, LSCI will only sample the flows in the top fraction of the full cross-sectional area. The diameter scaling may then overestimate the number of dynamic scattering events for that vessel, and increase errors in computed conservation of flow. Overall, the diameter scaling represents a possible correction for properly estimating the relative blood flow values using MESI computed ICT values, and conservation of flow analysis can be used to assess agreement with expected physiology. This analysis serves as a useful accuracy check in the absence of an absolute flow measure.

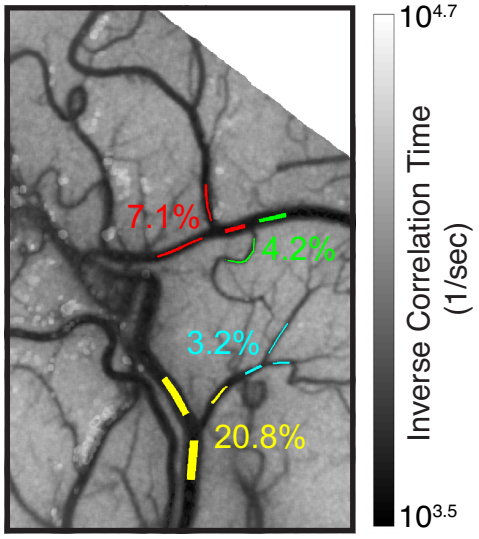

Figure 7.1: Example of conservation of flow analysis in four vessel branches from Case 17 overlaid on the grayscale MESI ICT map, with each branch highlighted in a different color. The percent difference between the addition of flows from the two daughter vessels and the flow from the parent vessel is shown for each branch in its associated color.

7.2.6 Future Clinical Studies

The clinical studies presented in this work are at the very initial steps of instrument validation, and further studies that quantify LSCI's ability to detect a clinical flow change with agreement to a second metric is required. Secondary metrics could be any of the currently available clinical monitoring tools for blood flow. An agreement between LSCI and a current tool would help validate its performance and demonstrate what information LSCI can add to the intraoperative setting. One particularly useful study would be a direct comparison with indocyanine green (ICG) angiography, which is currently the most widely used intraoperative monitoring tool. Demonstrating that LSCI can provide complementary information in general agreement with ICG, similar to a previous rodent study [9], would be a significant advance toward clinical adoption. ICG angiography is more commonly used to assess blood flow during neurovascular

procedures, where the surgeon is operating on the blood vessels themselves. The phase II study currently underway has only recently started accrual of patients undergoing aneurysm clipping or arteriovenous malformation resection, and further assessment is required to determine the full utility for these types of procedures. Other groups have demonstrated LSCI assessment during neurovascular procedures [10-12], and have shown potentially useful visualization of blood flow changes before and after vessel bypass or flow interruption. Further study is required both for a side-by-side comparison with ICG angiography, and to determine the neurovascular applications where LSCI is the most clinically useful.

Other potential clinical applications include procedures that require localization of eloquent areas of the brain to aid in the resection of diseased tissue. This could include awake functional mapping procedures usually performed for brain tumor resection or epilepsy. Another group has previously demonstrated LSCI use during awake craniotomy and found a correlation between cortical microcirculatory flow increases and measured electrocortical stimulation maps of functional areas [13]. This study highlights a potentially useful clinical application of LSCI for noninvasive functional brain mapping based on blood flow response, and warrants further clinical studies for thorough evaluation.

7.3 Conclusions

Several contributions to the field of laser speckle contrast imaging have been demonstrated in this work, and bring this technology one step closer to clinical adoption. A hardware comparison identified trends for proper laser diode and camera selection to maximize accuracy and sensitivity to flow changes. Most notably, laser diodes should be run at a constant current using temperature control to ensure maximum stability and

uniformity in coherence between trials. Cameras with a higher frame rate are preferable over higher bit depths, and temporal averaging with appropriate window size can be used to reduce noise while maintaining high temporal resolution. Low-cost cameras can provide equivalent performance to more expensive models, and color cameras can also be used if the sensor data is properly extracted and analyzed. Pressure regulated flow control systems are the preferred choice for controlled microfluidic studies for characterizing hardware performance. Real-time, simultaneous validation with an absolute flow sensor revealed for the first time how accurately LSCI predicts relative flow dynamics with the proper exposure time selection.

The clinical studies described in this dissertation demonstrated the feasibility and utility of LSCI in an intraoperative setting, and identified hardware design choices, image acquisition procedures, and post-processing methods to refine LSCI as a clinically worthwhile tool. This study was the first to adapt an existing neurosurgical microscope for intraoperative LSCI, and the phase II study identified further design modifications for improved performance. The rotatable polarizer and the shift to a near infrared wavelength were critical for maximizing image quality. Consistent with the hardware assessment, the use of neutral density filters to control the laser power rather than the drive current greatly improved comparability across acquired images. Multiple exposure speckle imaging was performed for the first time in a clinical setting, and trends showed that shorter exposure times were preferable for proper sampling of the distribution of flow rates in the human cortex. In post-processing, motion correction techniques to account for tissue motion and pulsatile flow were developed and significantly reduced measured noise for identifying relative blood flow changes. Applying the MESI model to the image sets demonstrated that proper calibration of the imaging setup using a static reference could be used to measure physiologically appropriate relative flows. In

combination, these image analysis methods can provide quantitative flow information to the surgeon. Future work of real-time implementation of the aforementioned image analysis methods is required before true utility can be achieved in an intraoperative setting. The work presented in this dissertation demonstrates the incredible potential of laser speckle contrast imaging as a tool for neurosurgical blood flow visualization, and marks a significant leap forward towards safer intraoperative guidance.

7.4 REFERENCES

[1] T. Durduran, M. G. Burnett, G. Yu, C. Zhou, D. Furuya, A. G. Yodh, J. A. Detre, and J. H. Greenberg, "Spatiotemporal quantification of cerebral blood flow during functional activation in rat somatosensory cortex using laser-speckle flowmetry," *Journal of Cerebral Blood Flow & Metabolism,* **24**(5), pp. 518-525 (2004).

[2] A. K. Dunn, A. Devor, H. Bolay, M. L. Andermann, M. A. Moskowitz, A. M. Dale, and D. A. Boas, "Simultaneous imaging of total cerebral hemoglobin concentration, oxygenation, and blood flow during functional activation," *Optics Letters,* **28**(1), pp. 28-30 (2003).

[3] A. K. Dunn, A. Devor, A. M. Dale, and D. A. Boas, "Spatial extent of oxygen metabolism and hemodynamic changes during functional activation of the rat somatosensory cortex," *NeuroImage,* **27**(2), pp. 279-290 (2005).

[4] A. Raabe, D. Van De Ville, M. Leutenegger, A. Szelenyi, E. Hattingen, R. Gerlach, V. Seifert, C. Hauger, A. Lopez, R. Leitgeb, M. Unser, E. J. Martin-Williams, and T. Lasser, "Laser Doppler imaging for intraoperative human brain mapping," *NeuroImage,* **44**(4), pp. 1284-1289 (2009).

[5] A. B. Parthasarathy, W. J. Tom, A. Gopal, X. J. Zhang, and A. K. Dunn, "Robust flow measurement with multi-exposure speckle imaging," *Optics Express,* **16**(3), pp. 1975-1989 (2008).

[6] S. M. S. Kazmi, A. B. Parthasarathy, N. E. Song, T. A. Jones, and A. K. Dunn, "Chronic imaging of cortical blood flow using Multi-Exposure Speckle Imaging," *Journal of Cerebral Blood Flow & Metabolism,* **33**(6), pp. 798-808 (2013).

[7] S. M. S. Kazmi, E. Faraji, M. A. Davis, Y. Y. Huang, X. J. Zhang, and A. K. Dunn, "Flux or speed? Examining speckle contrast imaging of vascular flows," *Biomedical Optics Express,* **6**(7), pp. 2588-2608 (2015).

[8] M. A. Davis, S. M. S. Kazmi, and A. K. Dunn, "Imaging depth and multiple scattering in laser speckle contrast imaging," *Journal of Biomedical Optics,* **19**(8), pp. 086001 (2014).

[9] E. L. Towle, L. M. Richards, S. M. S. Kazmi, D. J. Fox, and A. K. Dunn, "Comparison of indocyanine green angiography and laser speckle contrast imaging for the assessment of vasculature perfusion," *Neurosurgery,* **71**(5), pp. 1023-1030; discussion 1030-1031 (2012).

[10] N. Hecht, J. Woitzik, J. P. Dreier, and P. Vajkoczy, "Intraoperative monitoring of cerebral blood flow by laser speckle contrast analysis," *Neurosurgical Focus,* **27**(4), pp. E11 (2009).

[11] N. Hecht, J. Woitzik, S. Konig, P. Horn, and P. Vajkoczy, "Laser speckle imaging allows real-time intraoperative blood flow assessment during neurosurgical procedures," *Journal of Cerebral Blood Flow & Metabolism,* **33**(7), pp. 1000-1007 (2013).

[12] S. Nomura, T. Inoue, H. Ishihara, H. Koizumi, E. Suehiro, F. Oka, and M. Suzuki, "Reliability of laser speckle flow imaging for intraoperative monitoring of cerebral blood flow during cerebrovascular surgery: comparison with cerebral blood flow measurement by single photon emission computed tomography," *World Neurosurgery,* **82**(6), pp. e753-757 (2014).

[13] E. Klijn, H. C. Hulscher, R. K. Balvers, W. P. Holland, J. Bakker, A. J. Vincent, C. M. Dirven, and C. Ince, "Laser speckle imaging identification of increases in cortical microcirculatory blood flow induced by motor activity during awake craniotomy," *Journal of Neurosurgery,* **118**(2), pp. 280-286 (2013).

Appendix I: Laser Speckle Imaging Theory

A derivation of the speckle models relating the speckle contrast to the correlation time are included for reference, since these models are used throughout this dissertation to relate speckle images to relative blood flow. Speckle is a random phenomenon, and its underlying physics is rooted in statistical optics theory. The intensity of a polarized speckle pattern follows negative exponential statistics, while the phase follows uniform statistics [1, 2]. This implies that the intensity I has a probability density function (PDF) of the form,

$$p(I) = \frac{1}{\langle I \rangle} \exp^{\left(-I/\langle I \rangle\right)} \ , \ I \geq 0 \, , \tag{I.1}$$

where $\langle I \rangle$ is the mean intensity [2, 3]. The first-order statistical properties of the intensity are used to define the speckle contrast. For a negative exponential PDF, the standard deviation of the intensity is equal to the mean intensity $\sigma_s = \langle I \rangle$ [1-3], which leads to the expression for the speckle contrast,

$$K = \frac{\sigma_s}{\langle I \rangle} \ . \tag{I.2}$$

This is the origin of the theoretical maximum speckle contrast value (K = 1) for polarized speckle patterns following a negative exponential PDF. In this expression, $\langle I \rangle$ refers to the spatial intensity average. Since speckle varies in time, the time-averaged intensity, $\langle I \rangle_t$, is given by,

$$\langle I \rangle_t = \lim_{T \to \infty} \frac{1}{T} \int_0^T I(t) \, dt \ , \tag{I.3}$$

where $I(t)$ is the intensity at time t. In this expression, the average is independent of time t, and assumes stationarity [2, 4].

To relate the measured speckle contrast with underlying flow, autocorrelation functions are used to quantify the temporal dynamics of the speckle pattern. The autocorrelation function quantifies the similarity of a signal with a time-shifted version of itself [4, 5]. The probability that the signal at the shifted time will be similar to the value recorded at an earlier time decreases as the time interval increases. The probability of similarity also decreases the more rapidly the signal changes, which results in a shorter correlation time. The temporal fluctuations of speckles can be quantified using the normalized electric field autocorrelation function $g_1(\tau)$ and the normalized intensity autocorrelation function $g_2(\tau)$. The temporal intensity autocorrelation function is given by,

$$\tilde{R}_I(\tau) = \left\langle I(t)I(t+\tau)\right\rangle_t \ , \tag{I.4}$$

where τ is the time lag between the two intensity signals [2, 4]. For $t = 0$, this gives $\tilde{R}_I = \left\langle I(0)I(\tau)\right\rangle$. Since this is a time-averaged quantity, Equation I.4 can also be expressed as,

$$\tilde{R}_I(\tau) = \lim_{T\to\infty} \frac{1}{T}\int_0^T I(t)I(t+\tau)\,dt \ . \tag{I.5}$$

The normalized intensity autocorrelation function, $g_2(\tau)$, is given by

$$\begin{aligned} g_2(\tau) &= \frac{\tilde{R}_I(\tau)}{\left\langle I(t)\right\rangle_t^2} \\ &= \frac{\left\langle I(t)I(t+\tau)\right\rangle_t}{\left\langle I(t)\right\rangle_t^2} \ , \end{aligned} \tag{I.6}$$

which is normalized by $\left\langle I(t)\right\rangle_t^2$ because the $\lim_{t\to\infty} \tilde{R}_I(\tau) = \left\langle I(t)\right\rangle_t^2$ [4]. A closely related function is the statistical autocorrelation function that describes the ensemble average of the entire random process, given by

$$R_I(t_2,t_1) = \overline{I(t_2)I(t_1)} \ , \tag{I.7}$$

where the bar represents the ensemble average [2]. Physically, the temporal autocorrelation function $\tilde{R}_I(\tau)$ measures the similarity between $I(t)$ and $I(t+\tau)$ averaged over all time, while the statistical autocorrelation function $R_I(t_2,t_1)$ measures the statistical similarity of $I(t_1)$ and $I(t_2)$ over the ensemble, where $\tau = t_2 - t_1$ [2]. Assuming ergodicity, time-averaged and ensemble-averaged correlation functions are equal, giving $\tilde{R}_I(\tau) = R_I(t_2,t_1)$. The statistics of ergodic systems are independent of the choice of time origin, meaning that the system has the same behavior when it is averaged over time or over all possible arrangements over time [2]. This is a common assumption for speckle systems, since the intensity variations are expected to be stationary (non-changing) over time. The temporal intensity autocovariance function $C_t(t_2,t_1)$ is defined as the intensity autocorrelation function minus the mean intensity squared [2],

$$\begin{aligned} C_t(t_2,t_1) &= \overline{\left[I(t_2) - \bar{I}(t_2) \right]\left[I(t_1) - \bar{I}(t_1) \right]} \\ &= \overline{I(t_2)I(t_1)} - \bar{I}(t_2)\bar{I}(t_1) \\ &= R_I(t_2,t_1) - \bar{I}(t_2)\bar{I}(t_1) \ . \end{aligned} \tag{I.8}$$

Assuming ergodicity, the autocovariance can also be expressed as a time-averaged quantity using the single time lag τ, given by,

$$\begin{aligned} C_t(\tau) &= \left\langle \left[I(t) - \left\langle I(t) \right\rangle_t \right]\left[I(t+\tau) - \left\langle I(t) \right\rangle_t \right] \right\rangle_t \\ &= \left\langle I(t)I(t+\tau) \right\rangle_t - \left\langle I(t) \right\rangle_t^2 \\ &= \tilde{R}_I(\tau) - \left\langle I(t) \right\rangle_t^2 \ . \end{aligned} \tag{I.9}$$

This expression is included in the original Fercher and Briers paper (first publication on LSCI, originally called single-exposure speckle photography) [6].

The normalized autocovariance is also standardized by $\langle I(t)\rangle_t^2$, given by,

$$\begin{aligned} c_t(\tau) &= \frac{C_t(\tau)}{\langle I(t)\rangle_t^2} \\ &= \frac{\tilde{R}_I(\tau) - \langle I(t)\rangle_t^2}{\langle I(t)\rangle_t^2} \\ &= \frac{\tilde{R}_I(\tau)}{\langle I(t)\rangle_t^2} - \frac{\langle I(t)\rangle_t^2}{\langle I(t)\rangle_t^2} \\ &= \frac{\tilde{R}_I(\tau)}{\langle I(t)\rangle_t^2} - 1 \\ &= g_2(\tau) - 1 \,. \end{aligned} \tag{I.10}$$

The expression for the normalized intensity autocorrelation $g_2(\tau)$ can be written in terms of the autocovariance, given by,

$$\begin{aligned} g_2(\tau) &= c_t(\tau) + 1 \\ &= \frac{C_t(\tau)}{\langle I(t)\rangle_t^2} + 1 \,. \end{aligned} \tag{I.11}$$

To calculate the correlation time τ_c, or the decay time of the autocorrelation function, the autocorrelation of the electric field is required, rather than the intensity. The normalized electric field autocorrelation function, $g_1(\tau)$, is given by

$$g_1(\tau) = \frac{\langle E(t)E^*(t+\tau)\rangle}{\langle E(t)E^*(t)\rangle}, \tag{I.12}$$

where $E(t)E^*(t) = I(t)$ [6]. For $t = 0$, this gives

$$g_1(\tau) = \frac{\langle E(0)E^*(\tau)\rangle}{\langle |E(0)|^2 \rangle} \,. \tag{I.13}$$

Since the electric field is difficult to measure directly, the Siegert relationship is used to relate the electric field and intensity autocorrelation functions, which is valid for Gaussian statistics [6],

$$g_2(\tau) = 1 + \beta\left|g_1(\tau)\right|^2 \ . \tag{I.14}$$

Here, β is a normalization term that accounts for speckle averaging due to mismatch between speckle size and pixel size, polarization of the light source versus the detector, and the finite coherence of the light source [7, 8]. Now, Equation I.11 can be plugged into Equation I.14, giving

$$\begin{aligned} \frac{C_t(\tau)}{\left\langle I(t)\right\rangle_t^2} + 1 &= 1 + \beta\left|g_1(\tau)\right|^2 \\ \frac{C_t(\tau)}{\left\langle I(t)\right\rangle_t^2} &= \beta\left|g_1(\tau)\right|^2 \\ C_t(\tau) &= \beta\left\langle I(t)\right\rangle_t^2\left|g_1(\tau)\right|^2 \ . \end{aligned} \tag{I.15}$$

To quantify the correlation time from the speckle contrast (K), the autocovariance must be related to the spatial variance (K^2) of the speckle pattern.

I.1 Original Fercher and Briers Derivation

In the original Fercher and Briers paper [6], the following relationship was used to define the variance of the speckle pattern,

$$\sigma_s^2(T) = \frac{1}{T}\int_0^T C_t(\tau)\,d\tau \ . \tag{I.16}$$

where T is the camera exposure time. A closely related term, the speckle variance, defined as K^2, is given by,

$$K^2(T) = \frac{\sigma_s^2(T)}{\left\langle I\right\rangle^2} = \frac{1}{T\left\langle I\right\rangle^2}\int_0^T C_t(\tau)\,d\tau \ . \tag{I.17}$$

Plugging the expression for the autocovariance in Equation I.15 into Equation I.17 gives

$$\begin{aligned} K^2(T) &= \frac{1}{T\left\langle I\right\rangle^2}\int_0^T \beta\left\langle I(t)\right\rangle_t^2 \left|g_1(\tau)\right|^2 d\tau \\ &= \beta\frac{\left\langle I(t)\right\rangle_t^2}{\left\langle I\right\rangle^2}\frac{1}{T}\int_0^T \left|g_1(\tau)\right|^2 d\tau \ . \end{aligned} \tag{I.18}$$

Assuming ergodicity, the time-averaged intensity $\left\langle I(t)\right\rangle_t^2$ can be replaced with the ensemble average $\left\langle I\right\rangle^2$, giving

$$\begin{aligned} K^2(T) &= \beta\frac{\left\langle I\right\rangle^2}{\left\langle I\right\rangle^2}\frac{1}{T}\int_0^T \left|g_1(\tau)\right|^2 d\tau \\ &= \beta\frac{1}{T}\int_0^T \left|g_1(\tau)\right|^2 d\tau \ . \end{aligned} \tag{I.19}$$

To solve this expression, a form for $g_1(\tau)$ must be assumed. Using the original assumptions from Fercher and Briers, $g_1(\tau)$ is approximated as a negative exponential function with a Lorentzian velocity distribution, given by

$$g_1(\tau) = e^{-\tau/\tau_c} \ . \tag{I.20}$$

Here, τ_c is the correlation time required for quantifying relative flow from LSCI. Now, plugging Equation I.20 back into Equation I.19 gives

$$\begin{aligned} K^2(T) &= \beta\frac{1}{T}\int_0^T \left|e^{-\tau/\tau_c}\right|^2 d\tau \\ &= \beta\frac{1}{T}\int_0^T e^{-2\tau/\tau_c} d\tau \ . \end{aligned} \tag{I.21}$$

Evaluating the integral gives,

$$\begin{aligned} K^2(T) &= \beta\left(\frac{1}{T}\right)\frac{e^{-2\tau/\tau_c}}{-2/\tau_c}\Bigg|_0^T \\ &= \beta\left[-\frac{e^{-2T/\tau_c}}{2T/\tau_c} - \left(\frac{-1}{2T/\tau_c}\right)\right] \\ &= \beta\left(\frac{1-e^{-2T/\tau_c}}{2T/\tau_c}\right) \\ &= \beta\left(\frac{1-e^{-2x}}{2x}\right),\ x = T/\tau_c\ . \end{aligned} \tag{I.22}$$

Taking the square root of the speckle variance K^2 gives the speckle contrast K, given by

$$K(T,\tau_c) = \frac{\sigma_s(T)}{\langle I\rangle} = \left(\beta\frac{1-e^{-2x}}{2x}\right)^{1/2},\ x = T/\tau_c\ . \tag{I.23}$$

This is the original relationship between the speckle contrast and the correlation time from Fercher and Briers [6], with the addition of the β term which was originally assumed to equal 1.

I.2 Bandyopadhyay Derivation

More recently, a modification to the original expression defining the variance of the speckle pattern was proposed by Dixon and Durian [9], and fully derived by Bandyopadhyay *et al* from the same group [10]. They define the speckle variance as

$$\begin{aligned} K^2(T) &= \frac{1}{T^2\langle I\rangle^2}\int_0^T\int_0^T C_t(\tau-\tau')\,d\tau\,d\tau' \\ &= \frac{2}{T\langle I\rangle^2}\int_0^T\left(1-\frac{\tau}{T}\right)C_t(\tau)\,d\tau\ . \end{aligned} \tag{I.24}$$

This expression calculates the variance as a double integral over all possible time differences ($\tau = t_2 - t_1$) in the window, which is the correct calculation of the second moment [10]. The simplification in the second line can be made since $g_1(\tau)$ is an even

function, i.e. $g_1(\tau) = g_1(-\tau)$ [9], which accordingly applies to the autocovariance given by the definition in Equation I.15. Plugging in Equation I.15 into Equation I.24 gives,

$$\begin{aligned} K^2(T) &= \frac{2}{T\left\langle I\right\rangle^2}\int_0^T\left(1-\frac{\tau}{T}\right)\beta\left\langle I(t)\right\rangle_t^2\left|g_1(\tau)\right|^2 d\tau \\ &= \frac{2\beta\left\langle I(t)\right\rangle_t^2}{T\left\langle I\right\rangle^2}\int_0^T\left(1-\frac{\tau}{T}\right)\left|g_1(\tau)\right|^2 d\tau \ . \end{aligned} \tag{I.25}$$

Assuming ergodicity, the time-averaged intensity $\left\langle I(t)\right\rangle_t^2$ is replaced with the ensemble average $\left\langle I\right\rangle^2$, giving

$$\begin{aligned} K^2(T) &= \frac{2\beta\left\langle I\right\rangle^2}{T\left\langle I\right\rangle^2}\int_0^T\left(1-\frac{\tau}{T}\right)\left|g_1(\tau)\right|^2 d\tau \\ &= \frac{2\beta}{T}\int_0^T\left(1-\frac{\tau}{T}\right)\left|g_1(\tau)\right|^2 d\tau \ . \end{aligned} \tag{I.26}$$

Again, assuming that $g_1(\tau) = e^{-\tau/\tau_c}$, this expression is plugged into Equation I.26, giving,

$$\begin{aligned} K^2(T) &= \frac{2\beta}{T}\int_0^T\left(1-\frac{\tau}{T}\right)\left|e^{-\tau/\tau_c}\right|^2 d\tau \\ &= \frac{2\beta}{T}\int_0^T\left(1-\frac{\tau}{T}\right)e^{-2\tau/\tau_c}\, d\tau \ . \end{aligned} \tag{I.27}$$

Using integration by parts for definite integrals:

$$\begin{aligned} &\int_a^b u\, dv = uv\Big|_a^b - \int_a^b v\, du \\ &u = 1-\frac{\tau}{T}, \qquad dv = e^{-2\tau/\tau_c}d\tau \\ &du = -\frac{1}{T}d\tau, \qquad v = -\frac{\tau_c}{2}e^{-2\tau/\tau_c} \ . \end{aligned} \tag{I.28}$$

Using these definitions for integration by parts gives:

$$
\begin{aligned}
K^2(T) &= \frac{2\beta}{T}\left[\left(1-\frac{\tau}{T}\right)\left(-\frac{\tau_c}{2}e^{-2\tau/\tau_c}\right)\Bigg|_0^T - \int_0^T\left(-\frac{\tau_c}{2}e^{-2\tau/\tau_c}\right)\left(-\frac{1}{T}\right)d\tau\right] \\
&= \frac{2\beta}{T}\left[\cancel{\left(1-\frac{T}{T}\right)\left(-\frac{\tau_c}{2}e^{-2T/\tau_c}\right)} - \left(1-\frac{0}{T}\right)\left(-\frac{\tau_c}{2}e^{0}\right)\right] - \ldots \\
&\quad \frac{2\beta}{T}\left[\left(\frac{\tau_c}{2T}\right)\left(\frac{-\tau_c}{2}e^{-2\tau/\tau_c}\right)\Bigg|_0^T\right] \\
&= \frac{2\beta}{T}\left[-(1)\left(-\frac{\tau_c}{2}\right) - \left[\left(\frac{\tau_c}{2T}\right)\left(\frac{-\tau_c}{2}e^{-2T/\tau_c}\right) - \left(\frac{\tau_c}{2T}\right)\left(\frac{-\tau_c}{2}e^{0}\right)\right]\right] \\
&= \frac{2\beta}{T}\left[\frac{\tau_c}{2} + \left(\frac{{\tau_c}^2}{4T}e^{-2T/\tau_c}\right) + \left(\frac{-{\tau_c}^2}{4T}\right)\right].
\end{aligned}
\tag{I.29}
$$

Now, simplify, distribute the constant term ($2/T$), and rearrange, giving

$$
\begin{aligned}
K^2(T) &= \beta\left[\frac{2\tau_c}{2T} + \frac{2{\tau_c}^2}{4T^2}e^{-2T/\tau_c} - \frac{2{\tau_c}^2}{4T^2}\right] \\
&= \beta\left[\frac{\tau_c}{T} + \frac{{\tau_c}^2}{2T^2}e^{-2T/\tau_c} - \frac{{\tau_c}^2}{2T^2}\right] \\
&= \beta\left[\frac{1}{x} + \frac{1}{2x^2}e^{-2x} - \frac{1}{2x^2}\right],\ x = T/\tau_c \\
&= \beta\left[\frac{e^{-2x}-1+2x}{2x^2}\right],\ x = T/\tau_c\ .
\end{aligned}
\tag{I.30}
$$

Taking the square root of the speckle variance K^2 gives the speckle contrast K, given by

$$
K(T,\tau_c) = \frac{\sigma_s(T)}{\langle I\rangle} = \left(\beta\frac{e^{-2x}-1+2x}{2x^2}\right)^{1/2},\ x = T/\tau_c\ . \tag{I.31}
$$

This is the modified relationship between the speckle contrast and the correlation time from Bandyopadhyay *et al* [10], and has been adopted in most recent LSCI studies as the correct formulation [11, 12]. In this model, $\beta \neq 1$ and instead accounts for effects of

speckle averaging within a pixel, polarization, and finite coherence effects. However, for relative flow comparisons ($\tau_{c,\,baseline} / \tau_{c,\,current}$), β can be set to 1 since it will cancel out. This leaves a single unknown, τ_c, which allows use for single-exposure LSCI.

I.3 Parthasarathy Derivation – Multi-Exposure Speckle Imaging Model

The model in Equation I.31 has been shown to be fairly accurate for estimating relative flow changes for completely dynamically scattered light (homodyne detection, ergodic), but breaks down in the presence of statically scattered light from static tissue elements (heterodyne detection, non-ergodic). For neuroscience applications, this could arise from a thinned skull rather than a complete craniotomy in rodent models, or from the dura or arachnoid mater after craniotomy in humans. Light that scatters from a static region will produce the same speckle contrast value regardless of exposure time [11], which causes a deviation from assumed Gaussian statistics and requires the use of a modified form of the Siegert relationship.

The heterodyne electric field, $E_h(t)$, with contributions from both dynamic (fluctuating) and static (non-moving) scatterers can be expressed as,

$$E_h(t) = E_f(t) + E_s \ . \tag{I.32}$$

where $E_f(t)$ is the fluctuating electric field from dynamically scattered light (Gaussian) and E_s is the static electric field amplitude from non-moving scatterers [7, 8]. From this expression, the modified Siegert relationship is given by,

$$g_2^h(\tau) = 1 + \beta\left(\frac{\langle I_s\rangle\left|g_{1,s}(\tau)\right| + \langle I_f\rangle\left|g_{1,f}(\tau)\right|}{\langle I_s\rangle + \langle I_f\rangle}\right)^2 \ . \tag{I.33}$$

where $g_2^h(\tau)$ represents the normalized intensity autocorrelation function with a heterodyne component, $g_{1,s}(\tau)$ represents the normalized electric field autocorrelation function from the static component, and $g_{1,f}(\tau)$ represents the normalized electric field

autocorrelation function from the fluctuating component and is equivalent to the previously defined $g_1(\tau)$ [8]. Here, $I_f = E_f(t)E_f^*(t)$ is the intensity from dynamically scattered light, and $I_s = E_s E_s^*$ is the intensity from statically scattered light that is constant over time. Although the static component is constant over time, temporal variations between different regions of the imaging field are possible, i.e. from speckle to speckle [8]. Thus, the intensities are ensemble averaged to account for these spatial variations. Assuming the decay time of $g_{1,s}(\tau)$ is much greater than $g_{1,f}(\tau)$, $g_{1,s}(\tau) \approx 1$ for short time scales, where the decay corresponds to fluctuating dynamics [8]. Using this assumption and replacing $g_{1,f}(\tau)$ with $g_1(\tau)$, Equation I.33 can be simplified:

$$\begin{aligned} g_2^h(\tau) &= 1+\beta\left(\frac{\langle I_s\rangle+\langle I_f\rangle|g_1(\tau)|}{\langle I_s\rangle+\langle I_f\rangle}\right)^2 \\ &= 1+\beta\left(\frac{\langle I_s\rangle+\langle I_f\rangle|g_1(\tau)|}{\langle I_s\rangle+\langle I_f\rangle}\right)\left(\frac{\langle I_s\rangle+\langle I_f\rangle|g_1(\tau)|}{\langle I_s\rangle+\langle I_f\rangle}\right) \\ &= 1+\beta\left(\frac{\langle I_s\rangle^2+2\langle I_f\rangle\langle I_s\rangle|g_1(\tau)|+\langle I_f\rangle^2|g_1(\tau)|^2}{\left(\langle I_s\rangle+\langle I_f\rangle\right)^2}\right) \\ &= 1+\beta\left(\frac{\langle I_s\rangle^2}{\left(\langle I_s\rangle+\langle I_f\rangle\right)^2}+\frac{2\langle I_f\rangle\langle I_s\rangle|g_1(\tau)|}{\left(\langle I_s\rangle+\langle I_f\rangle\right)^2}+\frac{\langle I_f\rangle^2|g_1(\tau)|^2}{\left(\langle I_s\rangle+\langle I_f\rangle\right)^2}\right). \end{aligned} \tag{I.34}$$

To simplify even further, ρ is defined as the fraction of dynamically scattered light, given by $\frac{\langle I_f\rangle}{\langle I_f\rangle+\langle I_s\rangle}$ [13]. The fraction of statically scattered light is given by $(1-\rho)=\frac{\langle I_s\rangle}{\langle I_f\rangle+\langle I_s\rangle}$. Equation I.34 can now be simplified further,

$$g_2^h(\tau) = 1+\beta\left((1-\rho)^2+2\rho(1-\rho)|g_1(\tau)|+\rho^2|g_1(\tau)|^2\right). \tag{I.35}$$

Rearranging and distributing β gives,

$$g_2^h(\tau) = 1 + \beta\rho^2\left|g_1(\tau)\right|^2 + 2\beta\rho(1-\rho)\left|g_1(\tau)\right| + \beta(1-\rho)^2 \ . \tag{I.36}$$

which is the version of the modified Siegert relationship used to derive a new speckle visibility expression relating speckle contrast *K* and correlation time τ_c for heterodyne imaging of both static and dynamic scatterers [13, 14].

Using the definition of the speckle variance from Bandyopadhyay *et al* [10], Equation I.24 is re-stated here for reference:

$$\begin{aligned} K^2(T) &= \frac{1}{T^2\left\langle I\right\rangle^2}\int_0^T\int_0^T C_t(\tau-\tau')\,d\tau\,d\tau' \\ &= \frac{2}{T\left\langle I\right\rangle^2}\int_0^T\left(1-\frac{\tau}{T}\right)C_t(\tau)\,d\tau \ . \end{aligned} \tag{I.24}$$

Re-iterating Equation I.11 assuming ergodicity with the heterodyne version of the normalized intensity autocorrelation provides a new definition for the autocovariance, given by

$$g_2^h(\tau) = \frac{C_t(\tau)}{\left\langle I\right\rangle^2} + 1 \ . \tag{I.37}$$

Plugging Equation I.37 into the updated Siegert relation in Equation I.36 provides the heterodyne definition of the autocovariance, given by

$$\begin{aligned} 1 + \beta\rho^2\left|g_1(\tau)\right|^2 + 2\beta\rho(1-\rho)\left|g_1(\tau)\right| + \beta(1-\rho)^2 &= \frac{C_t(\tau)}{\left\langle I\right\rangle^2} + 1 \\ \left\langle I\right\rangle^2\left(\beta\rho^2\left|g_1(\tau)\right|^2 + 2\beta\rho(1-\rho)\left|g_1(\tau)\right| + \beta(1-\rho)^2\right) &= C_t(\tau) \ . \end{aligned} \tag{I.38}$$

Plugging the autocovariance definition in Equation I.38 into Equation I.24 gives,

$$\begin{aligned} K^2(T) &= \frac{2}{T\left\langle I\right\rangle^2}\int_0^T\left(1-\frac{\tau}{T}\right)\left\langle I\right\rangle^2\left(\beta\rho^2\left|g_1(\tau)\right|^2 + 2\beta\rho(1-\rho)\left|g_1(\tau)\right| + \beta(1-\rho)^2\right)d\tau \\ &= \frac{2\beta}{T}\int_0^T\left(1-\frac{\tau}{T}\right)\left(\rho^2\left|g_1(\tau)\right|^2 + 2\rho(1-\rho)\left|g_1(\tau)\right| + (1-\rho)^2\right)d\tau \ . \end{aligned} \tag{I.39}$$

Here, the coefficients are temporarily replaced with $A=\rho^2$, $B=2\rho(1-\rho)$, and $C=(1-\rho)^2$ to simplify the equation, giving

$$\begin{aligned} K^2(T) &= \frac{2\beta}{T}\int_0^T\left(1-\frac{\tau}{T}\right)\left(A\left|g_1(\tau)\right|^2+B\left|g_1(\tau)\right|+C\right)d\tau \\ &= \frac{2\beta}{T}\left[A\int_0^T\left(1-\frac{\tau}{T}\right)\left|g_1(\tau)\right|^2 d\tau + B\int_0^T\left(1-\frac{\tau}{T}\right)\left|g_1(\tau)\right| d\tau + C\int_0^T\left(1-\frac{\tau}{T}\right)d\tau\right]. \end{aligned} \tag{I.40}$$

Again, assuming that $g_1(\tau)=e^{-\tau/\tau_c}$, this expression is plugged into Equation I.40, giving,

$$K^2(T)=\frac{2\beta}{T}\left[A\int_0^T\left(1-\frac{\tau}{T}\right)e^{-2\tau/\tau_c}\,d\tau + B\int_0^T\left(1-\frac{\tau}{T}\right)e^{-\tau/\tau_c}\,d\tau + C\int_0^T\left(1-\frac{\tau}{T}\right)d\tau\right]. \tag{I.41}$$

Here, the first term is the same as Equation I.27 with the addition of the coefficient A. Thus, the first term can be replaced with the result from the integral given in Equation I.30:

$$\begin{aligned} K^2(T) &= A\beta\left[\frac{e^{-2x}-1+2x}{2x^2}\right]+\frac{2\beta}{T}\left[B\int_0^T\left(1-\frac{\tau}{T}\right)e^{-\tau/\tau_c}d\tau + C\int_0^T\left(1-\frac{\tau}{T}\right)d\tau\right] \\ x &= T/\tau_c\ . \end{aligned} \tag{I.42}$$

Similar to the derivation in Section I.2, integration by parts is used to solve the integral in the second term, given by

$$\begin{aligned} &\int_a^b u\,dv = uv\Big|_a^b - \int_a^b v\,du \\ &u=1-\frac{\tau}{T}, \qquad dv=e^{-\tau/\tau_c}d\tau \\ &du=-\frac{1}{T}d\tau, \qquad v=-\tau_c e^{-\tau/\tau_c}\ . \end{aligned} \tag{I.43}$$

Using these definitions and plugging back into Equation I.42 gives,

$$\begin{aligned} K^2(T) = A\beta\left[\frac{e^{-2x}-1+2x}{2x^2}\right] &+ C\frac{2\beta}{T}\left[\tau-\frac{\tau^2}{2T}\right]_0^T + \ldots \\ B\frac{2\beta}{T}&\left[\left(1-\frac{\tau}{T}\right)\left(-\tau_c e^{-\tau/\tau_c}\right)\Big|_0^T - \int_0^T\left(-\tau_c e^{-\tau/\tau_c}\right)\left(-\frac{1}{T}\right)d\tau\right]. \end{aligned} \tag{I.44}$$

First, solving the second term with the C coefficient,

$$\begin{aligned}
&\rightarrow C\frac{2\beta}{T}\left[\left(T-\frac{T^2}{2T}\right)-\left(0-\cancel{\frac{0^2}{2T}}\right)\right] \\
&= C\frac{2\beta}{T}\left(T-\frac{T}{2}\right) \\
&= C\frac{2\beta}{T}\left(\frac{T}{2}\right) \\
&= C\beta\ .
\end{aligned} \tag{I.45}$$

Now, solving the last term with the B coefficient,

$$\begin{aligned}
&\rightarrow B\frac{2\beta}{T}\left[\cancel{\left(1-\frac{T}{T}\right)\left(-\tau_c e^{-T/\tau_c}\right)}-\left(1-\frac{0}{T}\right)\left(-\tau_c e^{0}\right)-\left[\left(\frac{\tau_c}{T}\right)\left(-\tau_c e^{-\tau/\tau_c}\right)\Big|_0^T\right]\right] \\
&= B\frac{2\beta}{T}\left[-(1)(-\tau_c)-\left[\left(\frac{\tau_c}{T}\right)\left(-\tau_c e^{-T/\tau_c}\right)-\left(\frac{\tau_c}{T}\right)\left(-\tau_c e^{0}\right)\right]\right] \\
&= B\frac{2\beta}{T}\left[\tau_c+\left(\frac{{\tau_c}^2}{T}e^{-T/\tau_c}\right)+\left(\frac{-{\tau_c}^2}{T}\right)\right].
\end{aligned} \tag{I.46}$$

Now, simplify, distribute the constant term ($2/T$), and rearrange, giving

$$\begin{aligned}
&\rightarrow B\beta\left[\frac{2\tau_c}{T}+\left(\frac{2{\tau_c}^2}{T^2}e^{-T/\tau_c}\right)+\left(\frac{-2{\tau_c}^2}{T^2}\right)\right] \\
&= B\beta\left[\frac{2}{x}+\left(\frac{2}{x^2}e^{-x}\right)+\left(\frac{-2}{x^2}\right)\right],\ x=T/\tau_c \\
&= 2B\beta\left[\frac{e^{-x}-1+x}{x^2}\right],\ x=T/\tau_c\ .
\end{aligned} \tag{I.47}$$

Now, plugging Equations I.45 and I.47 back into Equation I.44 gives:

$$K^2(T)=A\beta\left[\frac{e^{-2x}-1+2x}{2x^2}\right]+2B\beta\left[\frac{e^{-x}-1+x}{x^2}\right]+C\beta\ . \tag{I.48}$$

Replacing the definitions for the coefficients into Equation I.48 gives,

$$\begin{aligned} K^2(T) &= \rho^2\beta\left[\frac{e^{-2x}-1+2x}{2x^2}\right]+2(2\rho(1-\rho))\beta\left[\frac{e^{-x}-1+x}{x^2}\right]+(1-\rho)^2\beta \\ &= \beta\rho^2\left[\frac{e^{-2x}-1+2x}{2x^2}\right]+4\beta\rho(1-\rho)\left[\frac{e^{-x}-1+x}{x^2}\right]+\beta(1-\rho)^2 \ . \end{aligned} \tag{I.49}$$

Before finalizing this expression, an additional constant term is added to account for experimental noise that can affect the speckle contrast, mostly arising from the camera [13]. This noise can include shot noise and readout noise, which are both discussed in Chapter 1. The shot noise will be independent of the camera exposure time if the intensity of the image is equalized across different exposure times. The readout noise will be constant for a given camera exposure time. Thus, an additional constant spatial variance, v_{noise}, should be added to Equation I.49, giving

$$K^2(T) = \beta\rho^2\left[\frac{e^{-2x}-1+2x}{2x^2}\right]+4\beta\rho(1-\rho)\left[\frac{e^{-x}-1+x}{x^2}\right]+\beta(1-\rho)^2+v_{noise} \ . \tag{I.50}$$

Now, taking the square root of the speckle variance K^2 gives the speckle contrast K,

$$\begin{aligned} K(T,\tau_c) &= \left(\beta\rho^2\frac{e^{-2x}-1+2x}{2x^2}+4\beta\rho(1-\rho)\frac{e^{-x}-1+x}{x^2}+\beta(1-\rho)^2+v_{noise}\right)^{1/2} \\ x &= T/\tau_c \\ \rho &= \frac{I_f}{I_f+I_s} \ . \end{aligned} \tag{I.51}$$

This is commonly known as the multi-exposure speckle imaging (MESI) model [11, 13, 14], and was originally derived by Parthasarathy *et al* [13]. This model is considered more robust than Equation I.31 because it is more widely applicable to imaging scenarios where static scattering may be present. If there are no static scatterers, then $\rho \to 1$ and Equation I.51 simplifies to Equation I.31, with the exception of the v_{noise} term. If there are only static scatterers, then $\rho \to 0$ and the speckle contrast reduces to a constant value

$\beta(1-\rho)^2 + v_{noise}$, which is independent of exposure time as expected [11]. This model is commonly used for MESI where multiple speckle images are recorded at various exposure times with equalized intensity to sample a broader range of flows within the sample. Because there are more unknowns (β, ρ, v_{noise}), multiple exposure times (T) are required to solve the expression for τ_c. The minimum number of exposures is 4, since there are 4 total unknowns including τ_c. Typically, 7 to 15 exposures times are recorded to improve fitting accuracy, and at least 6 exposure times spread across multiple decades (50 μs – 100 ms) are needed to maintain accuracy for microcirculatory flows [15].

It should be noted that the form of $g_1(\tau)$ used throughout this appendix assumes that particles are undergoing single dynamic scattering (Brownian motion, Lorentzian velocity distribution) [10], which is appropriate for parenchyma flows. A weighting factor proportional to the number of dynamic scattering events ($N_d \propto$ vessel caliber) should scale the x term in both Equation I.31 and I.51 for multiple dynamic scattering (bulk flow, Gaussian velocity distribution), which is expected for intravascular flows [14]. The use of this scaling factor is applied in Chapter 7 to demonstrate future directions for clinical data interpretation.

I.4 REFERENCES

[1] J. W. Goodman, "Statistical Properties of Laser Speckle Patterns," in *Laser Speckle and Related Phenomena*, J. C. Dainty, Ed., Berlin: Springer-Verlag, 1975, pp. 9-75.

[2] J. W. Goodman, *Statistical Optics*. New York: John Wiley & Sons, Inc., 1985.

[3] J. W. Goodman, "Some fundamental properties of speckle," *Journal of the Optical Society of America*, **66**(11), pp. 1145-1150 (1976).

[4] Bruce J. Berne and Robert Pecora, *Dynamic light scattering: with applications to chemistry, biology, and physics*, Dover ed. Mineola, N.Y.: Dover Publications, 2000.

[5] J. D. Briers, "Laser Doppler, speckle and related techniques for blood perfusion mapping and imaging," *Physiological Measurement,* **22**(4), pp. R35-66 (2001).
[6] A. F. Fercher and J. D. Briers, "Flow Visualization by Means of Single-Exposure Speckle Photography," *Optics Communications,* **37**(5), pp. 326-330 (1981).
[7] P. A. Lemieux and D. J. Durian, "Investigating non-Gaussian scattering processes by using nth-order intensity correlation functions," *Journal of the Optical Society of America A,* **16**(7), pp. 1651-1664 (1999).
[8] D. A. Boas and A. G. Yodh, "Spatially varying dynamical properties of turbid media probed with diffusing temporal light correlation," *Journal of the Optical Society of America A,* **14**(1), pp. 192-215 (1997).
[9] P. K. Dixon and D. J. Durian, "Speckle visibility spectroscopy and variable granular fluidization," *Physical Review Letters,* **90**(18), pp. 184302 (2003).
[10] R. Bandyopadhyay, A. S. Gittings, S. S. Suh, P. K. Dixon, and D. J. Durian, "Speckle-visibility spectroscopy: A tool to study time-varying dynamics," *Review of Scientific Instruments,* **76**(9), pp. 093110 (2005).
[11] D. A. Boas and A. K. Dunn, "Laser speckle contrast imaging in biomedical optics," *Journal of Biomedical Optics,* **15**(1), pp. 011109 (2010).
[12] D. Briers, D. D. Duncan, E. Hirst, S. J. Kirkpatrick, M. Larsson, W. Steenbergen, T. Stromberg, and O. B. Thompson, "Laser speckle contrast imaging: theoretical and practical limitations," *Journal of Biomedical Optics,* **18**(6), pp. 066018 (2013).
[13] A. B. Parthasarathy, W. J. Tom, A. Gopal, X. J. Zhang, and A. K. Dunn, "Robust flow measurement with multi-exposure speckle imaging," *Optics Express,* **16**(3), pp. 1975-1989 (2008).
[14] S. M. S. Kazmi, E. Faraji, M. A. Davis, Y. Y. Huang, X. J. Zhang, and A. K. Dunn, "Flux or speed? Examining speckle contrast imaging of vascular flows," *Biomedical Optics Express,* **6**(7), pp. 2588-2608 (2015).
[15] S. M. S. Kazmi, S. Balial, and A. K. Dunn, "Optimization of camera exposure durations for multi-exposure speckle imaging of the microcirculation," *Biomedical Optics Express,* **5**(7), pp. 2157-2171 (2014).

Appendix II: Speckle Size Theory and Experimental Measurements

Second-order statistics can be used to describe the spatial structure of the speckle pattern, such as the speckle size [1, 2]. The width of the intensity autocorrelation function provides an estimate of the "average width" of a speckle [2]. For intensities of two points in the image plane $I(x_1, y_1)$ and $I(x_2, y_2)$, the spatial autocorrelation function in the *(x, y)* plane for a free-space geometry is given by [2],

$$R_I(x_1, y_1; x_2, y_2) = \left\langle I(x_1, y_1) I(x_2, y_2) \right\rangle \ . \tag{II.1}$$

This corresponds to an average width of $\lambda z / L$, where z corresponds to the distance between the surface and the observation plane and L corresponds to size of the laser illumination spot [2]. In an imaging geometry, the autocorrelation function R_I of the speckle intensity is given by,

$$R_I(r) = \left\langle I \right\rangle^2 \left[1 + \left| 2 \frac{J_1\left(\frac{\pi D r}{\lambda z} \right)}{\frac{\pi D r}{\lambda z}} \right|^2 \right] , \tag{II.2}$$

where $\left\langle I \right\rangle$ is the mean intensity (spatial average), J_1 is a Bessel function of the first kind order one, $r = \sqrt{\left(\Delta x\right)^2 + \left(\Delta y\right)^2}$, $\Delta x = x_1 - x_2$, $\Delta y = y_1 - y_2$, D is the diameter of the circular lens pupil, λ is the laser wavelength, and z is the distance from the exit pupil to the imaging plane [2, 3]. By defining the first minimum of the Bessel function as the width of the autocorrelation function [4, 5], the speckle size is given by,

$$r = \frac{1.22 \lambda z}{D} \ , \tag{II.3}$$

since $J_1(x) = 0$ at $x = 1.22\pi$.

For a two-lens system, definitions of the speckle size have been suggested [4, 6]; however, the expressions involve parameters that are not easily defined for the Nikon Inc.

lenses used in this dissertation. For example, in Equation II.3, z is not easily defined, since the location of the exit pupil is unknown (part of the proprietary lens design). The speckle size can be estimated by defining z as the focal length of the lens closest to the camera, but experimental measurements are required to get a more accurate value for this particular imaging geometry.

II.1 MEASURING SPECKLE SIZE – THEORY

To measure the speckle size, the procedure outlined by Piederrière *et al* [7] and derived from Goodman [2] was used. The full width at half maximum (FWHM) of the spatial normalized autocovariance is calculated to measure the speckle width, which corresponds to the normalized autocorrelation function with unit amplitude and zero lag. The spatial intensity autocovariance function $C_I(x,y)$ is defined as the intensity autocorrelation function minus the mean intensity squared [8], given by

$$C_I(x,y) = R_I(x,y) - \left\langle I(x,y) \right\rangle^2 \ . \tag{II.4}$$

The spatial normalized autocovariance $c_I(x,y)$, which is also commonly called the correlation coefficient [9], is defined as the autocovariance function divided by the variance, given by

$$c_I(x,y) = \frac{R_I(x,y) - \left\langle I(x,y) \right\rangle^2}{\left\langle I(x,y)^2 \right\rangle - \left\langle I(x,y) \right\rangle^2} \ . \tag{II.5}$$

To calculate the intensity autocorrelation function experimentally, the Wiener-Khinchin theorem is used, which states that the intensity autocorrelation function and the power spectral density (PSD) form a Fourier transform pair [2, 8]. Thus, the spatial intensity autocorrelation can be defined as the inverse Fourier transform (FT^{-1}) of the PSD:

$$R_I(x,y) = FT^{-1}\left[PSD_I\left(\upsilon_x, \upsilon_y\right)\right] \ . \tag{II.6}$$

The PSD is defined as the squared magnitude of the Fourier transform (*FT*) of the speckle intensity [8, 10], given by

$$PSD_I\left(\upsilon_x,\upsilon_y\right)=\left|FT\left[I(x,y)\right]\right|^2 \quad . \tag{II.7}$$

Combining Equations II.5 – II.7, the spatial normalized autocovariance is given by Equation II.8, which can be calculated directly from the speckle pattern intensity distribution [7]:

$$c_I(x,y)=\frac{FT^{-1}\left[\left|FT\left[I(x,y)\right]\right|^2\right]-\left\langle I(x,y)\right\rangle^2}{\left\langle I(x,y)^2\right\rangle-\left\langle I(x,y)\right\rangle^2} \quad . \tag{II.8}$$

The speckle size in the *x*- and *y*- dimensions is defined as the FWHM of $c_I(x,y)$ calculated for horizontal (Δx) and vertical (Δy) profiles in the image.

II.2 Measuring Speckle Size – Experimental Procedure and Results

Using this procedure, the speckle size was measured for the tandem-lens setup used in this dissertation (Figure 2.8) using a reflectance standard (Ocean Optics Inc.). All lens apertures that produced a speckle size ≥1 pixel (*f*/# = 5.6, 8, 11, 16, 22) were recorded, and the raw image histogram was matched across apertures by controlling the laser power. This procedure was used to determine the relationship between speckle size and pixel size for correctly setting the apertures in the laboratory studies (Chapters 2 – 4).

A demonstration of the experimental procedure is shown in Figure II.1 for a single aperture (*f*/# = 22) using a CCD camera with 5.6 μm pixel size (Basler Ace acA640-100gm, Basler AG) and a 660 nm laser diode (HL6545MG, Thorlabs Inc.). The raw speckle image is shown in Figure II.1A, with an overlay of the 5 vertical and 5 horizontal profiles used to compute the speckle size. The procedure is then shown for a single representative profile (red vertical line) in Figure II.1B – II.1D. First, the raw image intensity profile is extracted from the image, shown in Figure II.1B. Then, the

normalized autocovariance from Equation II.8 is computed directly from this profile, as shown in Figure II.1C. The peak of the autocovariance curve, shown in the gray dashed box in Figure II.1C, was extracted and normalized so that the peak was at a value of 1. Then, this zoomed, normalized curve was fit to a Gaussian function using the Matlab *EzyFit* toolbox, with the fit curve and equation shown in red. The FWHM of a Gaussian function is given by ~2.3548σ. Thus, for this example with σ = 1.2119, the speckle size was approximately equal to 2.3548*1.2119 = 2.8538 pixels. This procedure was repeated for all 9 remaining profiles for this aperture size, and an average and standard deviation was computed.

An overview of the results for all apertures measured is shown in Figure II.2, where two data points are shown for each aperture. One data point represents the *f*/# setting on the top lens closest to the camera with the other lens was all the way open (f/# = 1.8), while the other data point represents the *f*/# setting on the bottom lens closest to the sample with the other lens all the way open. Both aperture options were tested to ensure that the both lenses could be used to set the aperture with equivalent performance. Both data points have overlapping errorbars, meaning that they are essentially equivalent for both aperture settings. This is an important finding, since the top lens closest to the camera must be used for the two-camera imaging setup in Chapter 4 to set the aperture individually for each camera arm. The theoretical value for the closest matching theoretical expression for the speckle size is shown in the red dashed line, given by 1.22*λ*M**f*/#, where λ is the laser wavelength (660 nm) and M is the magnification (M = 1). This shows a fairly close relationship, with errorbars from *f*/# $\geq$ 8 overlapping with the theoretical line. Thus, this expression for the speckle size was used for all laboratory studies in Chapters 2 – 4 to compute the required aperture setting for each camera to produce the desired speckle size ≥1 pixel.

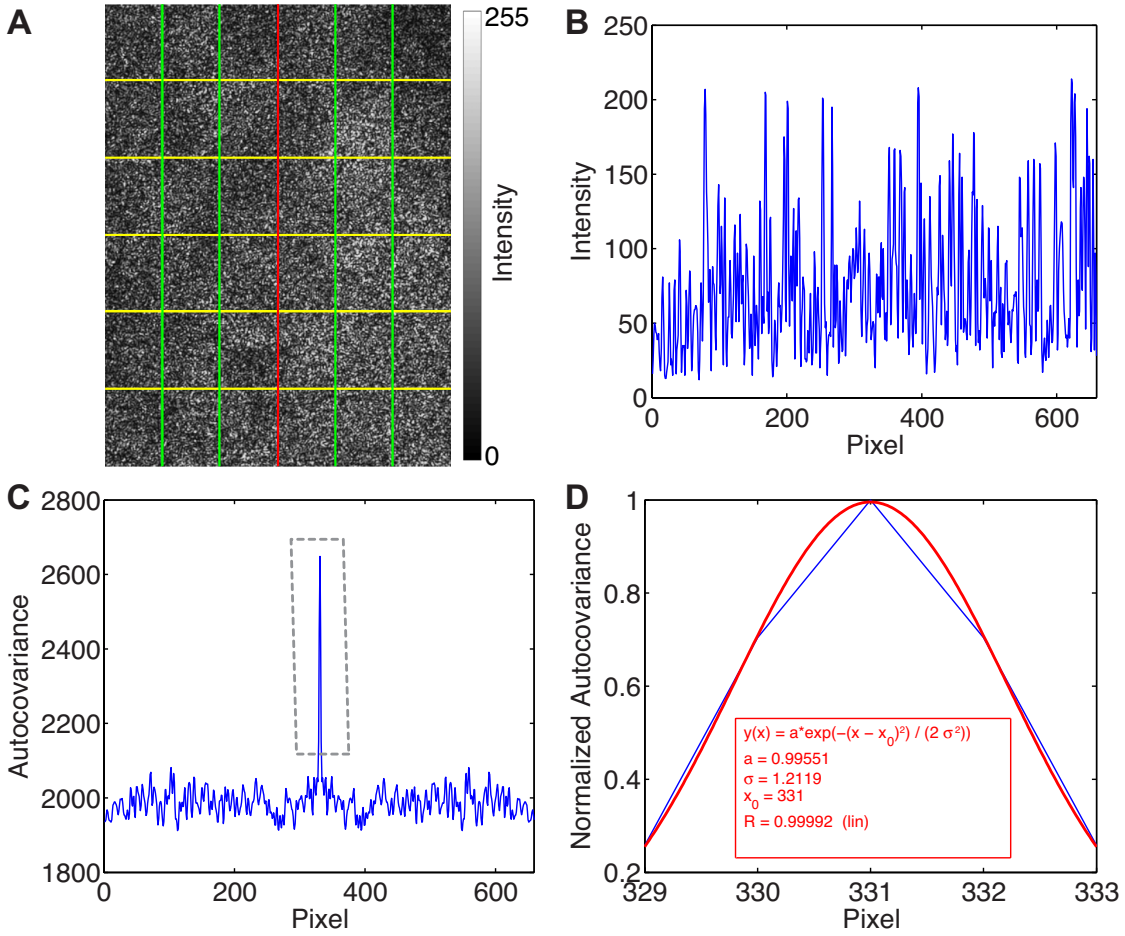

Figure II.1: (A) Raw speckle image of a reflectance standard recorded at *f*/# = 22, with an illustration of 5 vertical (green) and 5 horizontal (yellow) profiles used to calculate the speckle size. The result from the red vertical profile is shown in (B-D). The raw image intensity profile (B) and its corresponding autocovariance (C), which was calculated from Equation II.8. The gray dashed box represents the zoomed inset shown in (D), which was normalized and fit to a Gaussian using the Matlab *EzyFit* toolbox (www.fast.u-psud.fr/ezyfit/). The width of the Gaussian fit was used to compute the FWHM for calculation of the speckle size.

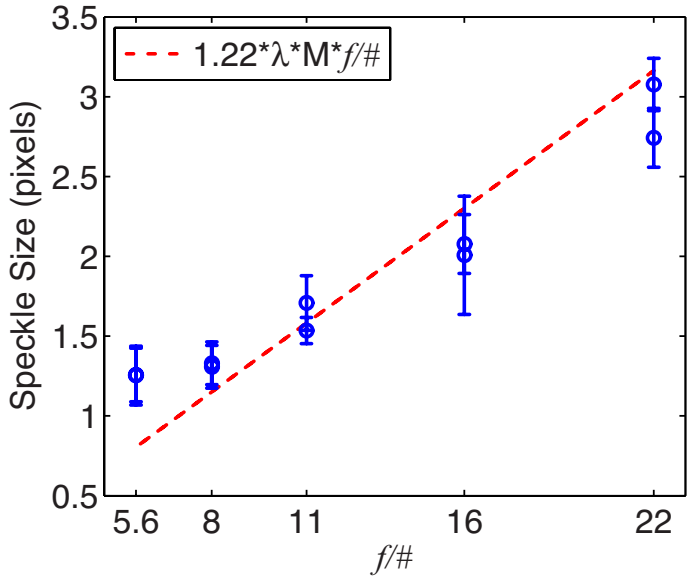

Figure II.2: Overview of the speckle size results (average and standard deviation over 10 image profiles) for *f/#* = 5.6, 8, 11, 16, 22 for both the top and bottom lens, with the other lens set to *f/#* = 1.8 (aperture all the way open). The red dashed line shows the closest matching speckle size expression, given by 1.22*λ*M**f/#*, where λ is the laser wavelength (660 nm) and M is the magnification (M = 1). This expression was normalized by the camera pixel size (5.6 μm) for display on this plot.

II.3 References

[1] L. I. Goldfischer, "Autocorrelation Function and Power Spectral Density of Laser-Produced Speckle Patterns," *Journal of the Optical Society of America,* **55**(3), pp. 247-253 (1965).

[2] J. W. Goodman, "Statistical Properties of Laser Speckle Patterns," in *Laser Speckle and Related Phenomena*, J. C. Dainty, Ed., Berlin: Springer-Verlag, 1975, pp. 9-75.

[3] J. W. Goodman, *Speckle Phenomena in Optics: Theory and Applications*. Englewood: Roberts and Company, 2007.

[4] J. E. Ward, D. P. Kelly, and J. T. Sheridan, "Three-dimensional speckle size in generalized optical systems with limiting apertures," *Journal of the Optical Society of America A,* **26**(8), pp. 1855-1864 (2009).

[5] Q. B. Li and F. P. Chiang, "Three-dimensional dimension of laser speckle," *Applied Optics,* **31**(29), pp. 6287-6291 (1992).

[6] T. Yoshimura, "Statistical properties of dynamic speckles," *Journal of the Optical Society of America A,* **3**(7), pp. 1032-1054 (1986).

[7] Y. Piederrière, J. Cariou, Y. Guern, B. Le Jeune, G. Le Brun, and J. Lotrian, "Scattering through fluids: speckle size measurement and Monte Carlo simulations close to and into the multiple scattering," *Optics Express,* **12**(1), pp. 176-188 (2003).
[8] J. W. Goodman, *Statistical Optics*. New York: John Wiley & Sons, Inc., 1985.
[9] Bernard Rosner, *Fundamentals of Biostatistics*, 6th ed. Belmont, CA: Thomson-Brooks/Cole, 2006.
[10] Bahaa E. A. Saleh and Malvin Carl Teich, *Fundamentals of Photonics*, 2nd ed. Hoboken, N.J.: Wiley Interscience, 2007.

References

R. J. Adrian and C. S. Yao, "Pulsed laser technique application to liquid and gaseous flows and the scattering power of seed materials," *Applied Optics,* **24**(1), pp. 44-52 (1985).

T. D. Alexander, R. L. Macdonald, B. Weir, and A. Kowalczuk, "Intraoperative angiography in cerebral aneurysm surgery: a prospective study of 100 craniotomies," *Neurosurgery,* **39**(1), pp. 10-17; discussion 17-18 (1996).

"American National Standard for the Safe Use of Lasers," in *ANSI Z136.1-2007*: Laser Institute of America, 2007.

S. Amin-Hanjani, G. Meglio, R. Gatto, A. Bauer, and F. T. Charbel, "The utility of intraoperative blood flow measurement during aneurysm surgery using an ultrasonic perivascular flow probe," *Neurosurgery,* **58**(4 Suppl 2), pp. ONS-305-312; discussion ONS-312 (2006).

J. R. Anderson, D. T. Chiu, R. J. Jackman, O. Cherniavskaya, J. C. McDonald, H. Wu, S. H. Whitesides, and G. M. Whitesides, "Fabrication of Topologically Complex Three-Dimensional Microfluidic Systems in PDMS by Rapid Prototyping," *Analytical Chemistry,* **72**(14), pp. 3158-3164 (2000).

C. Ayata, A. K. Dunn, Y. Gursoy-Özdemir, Z. Huang, D. A. Boas, and M. A. Moskowitz, "Laser speckle flowmetry for the study of cerebrovascular physiology in normal and ischemic mouse cortex," *Journal of Cerebral Blood Flow & Metabolism,* **24**(7), pp. 744-755 (2004).

C. Ayata, H. K. Shin, S. Salomone, Y. Ozdemir-Gursoy, D. A. Boas, A. K. Dunn, and M. A. Moskowitz, "Pronounced hypoperfusion during spreading depression in mouse cortex," *Journal of Cerebral Blood Flow & Metabolism,* **24**(10), pp. 1172-1182 (2004).

S. Bacigaluppi, M. Fontanella, P. Manninen, A. Ducati, G. Tredici, and F. Gentili, "Monitoring techniques for prevention of procedure-related ischemic damage in aneurysm surgery," *World Neurosurgery,* **78**(3-4), pp. 276-288 (2012).

R. Bandyopadhyay, A. S. Gittings, S. S. Suh, P. K. Dixon, and D. J. Durian, "Speckle-visibility spectroscopy: A tool to study time-varying dynamics," *Review of Scientific Instruments,* **76**(9), pp. 093110 (2005).

"Basler ace: User's Manual for GigE Vision Cameras," Basler AG, http://www.baslerweb.com, 2014.

Bruce J. Berne and Robert Pecora, *Dynamic light scattering: with applications to chemistry, biology, and physics*, Dover ed. Mineola, N.Y.: Dover Publications, 2000.

D. A. Boas and A. K. Dunn, "Laser speckle contrast imaging in biomedical optics," *Journal of Biomedical Optics,* **15**(1), pp. 011109 (2010).

D. A. Boas and A. G. Yodh, "Spatially varying dynamical properties of turbid media probed with diffusing temporal light correlation," *Journal of the Optical Society of America A,* **14**(1), pp. 192-215 (1997).

H. Bolay, U. Reuter, A. K. Dunn, Z. Huang, D. A. Boas, and M. A. Moskowitz, "Intrinsic brain activity triggers trigeminal meningeal afferents in a migraine model," *Nature Medicine,* **8**(2), pp. 136-142 (2002).

R. Bonner and R. Nossal, "Model for laser Doppler measurements of blood flow in tissue," *Applied Optics,* **20**(12), pp. 2097-2107 (1981).

J. D. Briers, "Laser Doppler, speckle and related techniques for blood perfusion mapping and imaging," *Physiological Measurement,* **22**(4), pp. R35-66 (2001).

D. Briers, D. D. Duncan, E. Hirst, S. J. Kirkpatrick, M. Larsson, W. Steenbergen, T. Stromberg, and O. B. Thompson, "Laser speckle contrast imaging: theoretical and practical limitations," *Journal of Biomedical Optics,* **18**(6), pp. 066018 (2013).

J. D. Briers and S. Webster, "Quasi real-time digital version of single-exposure speckle photography for full-field monitoring of velocity or flow fields," *Optics Communications,* **116**(1-3), pp. 36-42 (1995).

J. D. Briers and S. Webster, "Laser speckle contrast analysis (LASCA): a nonscanning, full-field technique for monitoring capillary blood flow," *Journal of Biomedical Optics,* **1**(2), pp. 174-179 (1996).

V. L. Chiang, P. Gailloud, K. J. Murphy, D. Rigamonti, and R. J. Tamargo, "Routine intraoperative angiography during aneurysm surgery," *Journal of Neurosurgery,* **96**(6), pp. 988-992 (2002).

B. Choi, N. M. Kang, and J. S. Nelson, "Laser speckle imaging for monitoring blood flow dynamics in the in vivo rodent dorsal skin fold model," *Microvascular Research,* **68**(2), pp. 143-146 (2004).

T. M. Cover and J. A. Thomas, *Elements of Information Theory*, 2nd ed.: John Wiley & Sons, Inc., 2006.

J. C. Dainty, *Laser speckle and related phenomena*. Berlin; New York: Springer-Verlag, 1975.

D. Dan, J. B. Hoag, K. A. Ellenbogen, M. A. Wood, D. L. Eckberg, and D. M. Gilligan, "Cerebral blood flow velocity declines before arterial pressure in patients with orthostatic vasovagal presyncope," *Journal of the American College of Cardiology,* **39**(6), pp. 1039-1045 (2002).

R. Dashti, A. Laakso, M. Niemela, M. Porras, and J. Hernesniemi, "Microscope-integrated near-infrared indocyanine green videoangiography during surgery of intracranial aneurysms: the Helsinki experience," *Surgical Neurology,* **71**(5), pp. 543-550; discussion 550 (2009).

M. M. da Silva, J. R. D. A. Nozela, M. J. Chaves, R. Alves Braga Jr., and H. J. Rabal, "Optical mouse acting as biospeckle sensor," *Optics Communications,* **284**(7), pp. 1798-1802 (2011).

M. A. Davis, S. M. S. Kazmi, and A. K. Dunn, "Imaging depth and multiple scattering in laser speckle contrast imaging," *Journal of Biomedical Optics,* **19**(8), pp. 086001 (2014).

R. H. Deckers, P. van Gelderen, M. Ries, O. Barret, J. H. Duyn, V. N. Ikonomidou, M. Fukunaga, G. H. Glover, and J. A. de Zwart, "An adaptive filter for suppression of cardiac and respiratory noise in MRI time series data," *NeuroImage,* **33**(4), pp. 1072-1081 (2006).

R. A. DeFazio, W. Zhao, X. Deng, A. Obenaus, and M. D. Ginsberg, "Albumin therapy enhances collateral perfusion after laser-induced middle cerebral artery branch occlusion: a laser speckle contrast flow study," *Journal of Cerebral Blood Flow & Metabolism,* **32**(11), pp. 2012-2022 (2012).

J. G. de Oliveira, J. Beck, V. Seifert, M. J. Teixeira, and A. Raabe, "Assessment of flow in perforating arteries during intracranial aneurysm surgery using intraoperative near-infrared indocyanine green videoangiography," *Neurosurgery,* **61**(3 Suppl), pp. 63-72; discussion 72-63 (2007).

T. Desmettre, J. M. Devoisselle, and S. Mordon, "Fluorescence properties and metabolic features of indocyanine green (ICG) as related to angiography," *Survey of Ophthalmology,* **45**(1), pp. 15-27 (2000).

P. K. Dixon and D. J. Durian, "Speckle visibility spectroscopy and variable granular fluidization," *Physical Review Letters,* **90**(18), pp. 184302 (2003).

M. Draijer, E. Hondebrink, T. van Leeuwen, and W. Steenbergen, "Review of laser speckle contrast techniques for visualizing tissue perfusion," *Lasers in Medical Science,* **24**(4), pp. 639-651 (2009).

S. Dufour, Y. Atchia, R. Gad, D. Ringuette, I. Sigal, and O. Levi, "Evaluation of laser speckle contrast imaging as an intrinsic method to monitor blood brain barrier integrity," *Biomedical Optics Express,* **4**(10), pp. 1856-1875 (2013).

D. D. Duncan and S. J. Kirkpatrick, "Can laser speckle flowmetry be made a quantitative tool?," *Journal of the Optical Society of America A,* **25**(8), pp. 2088-2094 (2008).

D. D. Duncan, S. J. Kirkpatrick, and R. K. Wang, "Statistics of local speckle contrast," *Journal of the Optical Society of America A,* **25**(1), pp. 9-15 (2008).

A. K. Dunn, "Laser speckle contrast imaging of cerebral blood flow," *Annals of Biomedical Engineering,* **40**(2), pp. 367-377 (2012).

A. K. Dunn, H. Bolay, M. A. Moskowitz, and D. A. Boas, "Dynamic imaging of cerebral blood flow using laser speckle," *Journal of Cerebral Blood Flow & Metabolism,* **21**(3), pp. 195-201 (2001).

A. K. Dunn, A. Devor, H. Bolay, M. L. Andermann, M. A. Moskowitz, A. M. Dale, and D. A. Boas, "Simultaneous imaging of total cerebral hemoglobin concentration, oxygenation, and blood flow during functional activation," *Optics Letters,* **28**(1), pp. 28-30 (2003).

A. K. Dunn, A. Devor, A. M. Dale, and D. A. Boas, "Spatial extent of oxygen metabolism and hemodynamic changes during functional activation of the rat somatosensory cortex," *NeuroImage,* **27**(2), pp. 279-290 (2005).

T. Durduran, M. G. Burnett, G. Yu, C. Zhou, D. Furuya, A. G. Yodh, J. A. Detre, and J. H. Greenberg, "Spatiotemporal quantification of cerebral blood flow during functional activation in rat somatosensory cortex using laser-speckle flowmetry," *Journal of Cerebral Blood Flow & Metabolism,* **24**(5), pp. 518-525 (2004).

A. E. Ennos, "Speckle Interferometry," in *Laser Speckle and Related Phenomena*, J. C. Dainty, Ed., Berlin: Springer-Verlag, 1975, pp. 203-253.

T. J. Essex and P. O. Byrne, "A laser Doppler scanner for imaging blood flow in skin," *Journal of Biomedical Engineering,* **13**(3), pp. 189-194 (1991).

A. F. Fercher and J. D. Briers, "Flow Visualization by Means of Single-Exposure Speckle Photography," *Optics Communications,* **37**(5), pp. 326-330 (1981).

K. R. Forrester, C. Stewart, J. Tulip, C. Leonard, and R. C. Bray, "Comparison of laser speckle and laser Doppler perfusion imaging: measurement in human skin and rabbit articular tissue," *Medical & Biological Engineering & Computing,* **40**(6), pp. 687-697 (2002).

K. R. Forrester, J. Tulip, C. Leonard, C. Stewart, and R. C. Bray, "A laser speckle imaging technique for measuring tissue perfusion," *IEEE Transactions on Biomedical Engineering,* **51**(11), pp. 2074-2084 (2004).

H. Girouard and C. Iadecola, "Neurovascular coupling in the normal brain and in hypertension, stroke, and Alzheimer disease," *Journal of Applied Physiology,* **100**(1), pp. 328-335 (2006).

L. I. Goldfischer, "Autocorrelation Function and Power Spectral Density of Laser-Produced Speckle Patterns," *Journal of the Optical Society of America,* **55**(3), pp. 247-253 (1965).

J. W. Goodman, "Statistical Properties of Laser Speckle Patterns," in *Laser Speckle and Related Phenomena*, J. C. Dainty, Ed., Berlin: Springer-Verlag, 1975, pp. 9-75.

J. W. Goodman, "Some fundamental properties of speckle," *Journal of the Optical Society of America,* **66**(11), pp. 1145-1150 (1976).

J. W. Goodman, *Statistical Optics*. New York: John Wiley & Sons, Inc., 1985.

J. W. Goodman, *Speckle Phenomena in Optics: Theory and Applications*. Englewood: Roberts and Company, 2007.

O. Goren, S. J. Monteith, M. Hadani, M. Bakon, and S. Harnof, "Modern intraoperative imaging modalities for the vascular neurosurgeon treating intracerebral hemorrhage," *Neurosurgical Focus,* **34**(5), pp. E2 (2013).

A. Gruber, C. Dorfer, H. Standhardt, G. Bavinzski, and E. Knosp, "Prospective comparison of intraoperative vascular monitoring technologies during cerebral aneurysm surgery," *Neurosurgery,* **68**(3), pp. 657-673; discussion 673 (2011).

Eugene Hecht, *Optics*, 4th ed. Reading, Mass.: Addison-Wesley, 2002.

N. Hecht, M-M. Müller, N. Sandow, A. Pinczolits, P. Vajkoczy, and J. Woitzik, "Infarct prediction by intraoperative laser speckle imaging in patients with malignant hemispheric stroke," *Journal of Cerebral Blood Flow & Metabolism,* pp. 1-11 (Published online before print, Oct 23, 2015).

N. Hecht, J. Woitzik, J. P. Dreier, and P. Vajkoczy, "Intraoperative monitoring of cerebral blood flow by laser speckle contrast analysis," *Neurosurgical Focus,* **27**(4), pp. E11 (2009).

N. Hecht, J. Woitzik, S. Konig, P. Horn, and P. Vajkoczy, "Laser speckle imaging allows real-time intraoperative blood flow assessment during neurosurgical procedures," *Journal of Cerebral Blood Flow & Metabolism,* **33**(7), pp. 1000-1007 (2013).

Gerald C. Holst and Terrence S. Lomheim, *CMOS/CCD sensors and camera systems*, 2nd ed. Winter Park, FL; Bellingham, WA: JCD Publishing; SPIE, 2011.

C. Iadecola, "Neurovascular regulation in the normal brain and in Alzheimer's disease," *Nature Reviews Neuroscience,* **5**(5), pp. 347-360 (2004).

M. A. Kamp, P. Slotty, B. Turowski, N. Etminan, H. J. Steiger, D. Hanggi, and W. Stummer, "Microscope-integrated quantitative analysis of intraoperative indocyanine green fluorescence angiography for blood flow assessment: first experience in 30 patients," *Neurosurgery,* **70**(1 Suppl Operative), pp. 65-73; discussion 73-64 (2012).

Y. J. Kang and S. Yang, "Fluidic low pass filter for hydrodynamic flow stabilization in microfluidic environments," *Lab on a Chip,* **12**(10), pp. 1881-1889 (2012).

E. Z. Kapsalaki, G. P. Lee, J. S. Robinson, 3rd, A. A. Grigorian, and K. N. Fountas, "The role of intraoperative micro-Doppler ultrasound in verifying proper clip placement in intracranial aneurysm surgery," *Journal of Clinical Neuroscience,* **15**(2), pp. 153-157 (2008).

S. M. S. Kazmi, S. Balial, and A. K. Dunn, "Optimization of camera exposure durations for multi-exposure speckle imaging of the microcirculation," *Biomedical Optics Express,* **5**(7), pp. 2157-2171 (2014).

S. M. S. Kazmi, E. Faraji, M. A. Davis, Y. Y. Huang, X. J. Zhang, and A. K. Dunn, "Flux or speed? Examining speckle contrast imaging of vascular flows," *Biomedical Optics Express,* **6**(7), pp. 2588-2608 (2015).

S. M. S. Kazmi, A. B. Parthasarathy, N. E. Song, T. A. Jones, and A. K. Dunn, "Chronic imaging of cortical blood flow using Multi-Exposure Speckle Imaging," *Journal of Cerebral Blood Flow & Metabolism,* **33**(6), pp. 798-808 (2013).

S. M. S. Kazmi, L. M. Richards, and A. K. Dunn, "Cerebral Blood Flow Imaging with Laser Speckle Contrast Imaging," in *Neurovascular Coupling Methods*, M. Zhao, H. Ma, and T. H. Schwartz, Eds., New York: Springer Science+Business Media, 2014, pp. 287-305.

S. M. S. Kazmi, R. K. Wu, and A. K. Dunn, "Evaluating multi-exposure speckle imaging estimates of absolute autocorrelation times," *Optics Letters,* **40**(15), pp. 3643-3646 (2015).

J. Kim, J. Oh, and B. Choi, "Magnetomotive laser speckle imaging," *Journal of Biomedical Optics,* **15**(1), pp. 011110 (2010).

H. J. Kirk, P. J. Rao, K. Seow, J. Fuller, N. Chandran, and V. G. Khurana, "Intra-operative transit time flowmetry reduces the risk of ischemic neurological deficits in neurosurgery," *British Journal of Neurosurgery,* **23**(1), pp. 40-47 (2009).

C. J. Kirkness, "Cerebral blood flow monitoring in clinical practice," *AACN Clinical Issues,* **16**(4), pp. 476-487 (2005).

S. J. Kirkpatrick, D. D. Duncan, and E. M. Wells-Gray, "Detrimental effects of speckle-pixel size matching in laser speckle contrast imaging," *Optics Letters,* **33**(24), pp. 2886-2888 (2008).

S. Klein, J. P. Pluim, M. Staring, and M. A. Viergever, "Adaptive Stochastic Gradient Descent Optimisation for Image Registration," *International Journal of Computer Vision,* **81**(3), pp. 227-239 (2009).

S. Klein and M. Staring, "Elastix: the manual," http://elastix.isi.uu.nl, 2014.

S. Klein, M. Staring, K. Murphy, M. A. Viergever, and J. P. Pluim, "elastix: a toolbox for intensity-based medical image registration," *IEEE Transactions on Medical Imaging*, **29**(1), pp. 196-205 (2010).

E. Klijn, H. C. Hulscher, R. K. Balvers, W. P. Holland, J. Bakker, A. J. Vincent, C. M. Dirven, and C. Ince, "Laser speckle imaging identification of increases in cortical microcirculatory blood flow induced by motor activity during awake craniotomy," *Journal of Neurosurgery*, **118**(2), pp. 280-286 (2013).

P. M. Korczyk, O. Cybulski, S. Makulska, and P. Garstecki, "Effects of unsteadiness of the rates of flow on the dynamics of formation of droplets in microfluidic systems," *Lab on a Chip,* **11**(1), pp. 173-175 (2011).

B. Kruijt, H. S. de Bruijn, A. van der Ploeg-van den Heuvel, H. J. Sterenborg, and D. J. Robinson, "Laser speckle imaging of dynamic changes in flow during photodynamic therapy," *Lasers in Medical Science,* **21**(4), pp. 208-212 (2006).

Y. Kubo, K. Ogasawara, N. Tomitsuka, Y. Otawara, S. Kakino, and A. Ogawa, "Revascularization and parent artery occlusion for giant internal carotid artery aneurysms in the intracavernous portion using intraoperative monitoring of cerebral hemodynamics," *Neurosurgery,* **58**(1), pp. 43-49 (2006).

M. L. Landsman, G. Kwant, G. A. Mook, and W. G. Zijlstra, "Light-absorbing properties, stability, and spectral stabilization of indocyanine green," *Journal of Applied Physiology,* **40**(4), pp. 575-583 (1976).

P. A. Lemieux and D. J. Durian, "Investigating non-Gaussian scattering processes by using nth-order intensity correlation functions," *Journal of the Optical Society of America A,* **16**(7), pp. 1651-1664 (1999).

M. Leutenegger, E. Martin-Williams, P. Harbi, T. Thacher, W. Raffoul, M. Andre, A. Lopez, P. Lasser, and T. Lasser, "Real-time full field laser Doppler imaging," *Biomedical Optics Express,* **2**(6), pp. 1470-1477 (2011).

Q. B. Li and F. P. Chiang, "Three-dimensional dimension of laser speckle," *Applied Optics,* **31**(29), pp. 6287-6291 (1992).

Z. Li, S. Y. Mak, A. Sauret, and H. C. Shum, "Syringe-pump-induced fluctuation in all-aqueous microfluidic system implications for flow rate accuracy," *Lab on a Chip,* **14**(4), pp. 744-749 (2014).

E. Marchese, A. Albanese, L. Denaro, A. Vignati, E. Fernandez, and G. Maira, "Intraoperative microvascular Doppler in intracranial aneurysm surgery," *Surgical Neurology,* **63**(4), pp. 336-342; discussion 342 (2005).

C. D. Meinhart and S. T. Wereley, "The theory of diffraction-limited resolution in microparticle image velocimetry," *Measurement Science and Technology,* **14**(7), pp. 1047-1053 (2003).

P. Miao, Z. Chao, Y. Zhang, N. Li, and N. V. Thakor, "Entropy analysis reveals a simple linear relation between laser speckle and blood flow," *Optics Letters,* **39**(13), pp. 3907-3910 (2014).

P. Miao, H. Lu, Q. Liu, Y. Li, and S. Tong, "Laser speckle contrast imaging of cerebral blood flow in freely moving animals," *Journal of Biomedical Optics,* **16**(9), pp. 090502 (2011).

P. Miao, A. Rege, N. Li, N. V. Thakor, and S. Tong, "High resolution cerebral blood flow imaging by registered laser speckle contrast analysis," *IEEE Transactions on Biomedical Engineering,* **57**(5), pp. 1152-1157 (2010).

K. Murari, N. Li, A. Rege, X. Jia, A. All, and N. Thakor, "Contrast-enhanced imaging of cerebral vasculature with laser speckle," *Applied Optics,* **46**(22), pp. 5340-5346 (2007).

P. Nakaji, "Laser speckle flow imaging of cerebral blood flow," *World Neurosurgery,* **82**(6), pp. e697-698 (2014).

H. Nakase, T. Kaido, S. Okuno, T. Hoshida, and T. Sakaki, "Novel intraoperative cerebral blood flow monitoring by laser-Doppler scanner," *Neurologia Medico-Chirurgica (Tokyo),* **42**(1), pp. 1-4 (2002).

S. Nomura, T. Inoue, H. Ishihara, H. Koizumi, E. Suehiro, F. Oka, and M. Suzuki, "Reliability of laser speckle flow imaging for intraoperative monitoring of cerebral blood flow during cerebrovascular surgery: comparison with cerebral blood flow measurement by single photon emission computed tomography," *World Neurosurgery,* **82**(6), pp. e753-757 (2014).

T. P. Obrenovitch, S. Chen, and E. Farkas, "Simultaneous, live imaging of cortical spreading depression and associated cerebral blood flow changes, by combining voltage-sensitive dye and laser speckle contrast methods," *NeuroImage,* **45**(1), pp. 68-74 (2009).

N. Ogata, J. Y. Fournier, H. G. Imhof, and Y. Yonekawa, "Thermal diffusion blood flow monitoring during aneurysm surgery," *Acta Neurochirurgica,* **138**(6), pp. 726-731 (1996).

A. B. Parthasarathy, S. M. S. Kazmi, and A. K. Dunn, "Quantitative imaging of ischemic stroke through thinned skull in mice with Multi Exposure Speckle Imaging," *Biomedical Optics Express,* **1**(1), pp. 246-259 (2010).

A. B. Parthasarathy, W. J. Tom, A. Gopal, X. J. Zhang, and A. K. Dunn, "Robust flow measurement with multi-exposure speckle imaging," *Optics Express,* **16**(3), pp. 1975-1989 (2008).

A. B. Parthasarathy, E. L. Weber, L. M. Richards, D. J. Fox, and A. K. Dunn, "Laser speckle contrast imaging of cerebral blood flow in humans during neurosurgery: a pilot clinical study," *Journal of Biomedical Optics,* **15**(6), pp. 066030 (2010).

Y. Piederrière, J. Cariou, Y. Guern, B. Le Jeune, G. Le Brun, and J. Lotrian, "Scattering through fluids: speckle size measurement and Monte Carlo simulations close to and into the multiple scattering," *Optics Express,* **12**(1), pp. 176-188 (2003).

S. A. Prahl. (1999). *Optical Absorption of Hemoglobin*. Available: http://omlc.ogi.edu/spectra/hemoglobin/index.html

V. Prinz, N. Hecht, N. Kato, and P. Vajkoczy, "Flow 800 Allows Visualization of Hemodynamic Changes After Extracranial-to-Intracranial Bypass Surgery but Not Assessment of Quantitative Perfusion or Flow," *Operative Neurosurgery,* **10**(2), pp. 231-239 (2013).

A. Raabe, J. Beck, R. Gerlach, M. Zimmermann, and V. Seifert, "Near-infrared indocyanine green video angiography: a new method for intraoperative assessment of vascular flow," *Neurosurgery,* **52**(1), pp. 132-139; discussion 139 (2003).

A. Raabe, P. Nakaji, J. Beck, L. J. Kim, F. P. Hsu, J. D. Kamerman, V. Seifert, and R. F. Spetzler, "Prospective evaluation of surgical microscope-integrated intraoperative near-infrared indocyanine green videoangiography during aneurysm surgery," *Journal of Neurosurgery,* **103**(6), pp. 982-989 (2005).

A. Raabe, D. Van De Ville, M. Leutenegger, A. Szelenyi, E. Hattingen, R. Gerlach, V. Seifert, C. Hauger, A. Lopez, R. Leitgeb, M. Unser, E. J. Martin-Williams, and T. Lasser, "Laser Doppler imaging for intraoperative human brain mapping," *NeuroImage,* **44**(4), pp. 1284-1289 (2009).

J. C. Ramirez-San-Juan, R. Ramos-Garcia, I. Guizar-Iturbide, G. Martinez-Niconoff, and B. Choi, "Impact of velocity distribution assumption on simplified laser speckle imaging equation," *Optics Express,* **16**(5), pp. 3197-3203 (2008).

E. H. Ratzlaff and A. Grinvald, "A tandem-lens epifluorescence macroscope: hundred-fold brightness advantage for wide-field imaging," *Journal of Neuroscience Methods,* **36**(2-3), pp. 127-137 (1991).

A. Rege, J. Senarathna, N. Li, and N. V. Thakor, "Anisotropic processing of laser speckle images improves spatiotemporal resolution," *IEEE Transactions on Biomedical Engineering,* **59**(5), pp. 1272-1280 (2012).

I. Remer and A. Bilenca, "Laser speckle spatiotemporal variance analysis for noninvasive widefield measurements of blood pulsation and pulse rate on a camera-phone," *Journal of Biophotonics,* **8**(11-12), pp. 902-907 (2015).

L. M. Richards, S. M. S. Kazmi, J. L. Davis, K. E. Olin, and A. K. Dunn, "Low-cost laser speckle contrast imaging of blood flow using a webcam," *Biomedical Optics Express,* **4**(10), pp. 2269-2283 (2013).

L. M. Richards, E. L. Towle, D. J. Fox, and A. K. Dunn, "Laser Speckle Imaging of Cerebral Blood Flow," in *Optical Methods and Instrumentation in Brain Imaging and Therapy*, S.J. Madsen, Ed.: Springer New York, 2013, pp. 117-136.

L. M. Richards, E. L. Towle, D. J. Fox, Jr., and A. K. Dunn, "Intraoperative laser speckle contrast imaging with retrospective motion correction for quantitative assessment of cerebral blood flow," *Neurophotonics,* **1**(1), pp. 015006 (2014).

L. M. Richards, E. L. Weber, A. B. Parthasarathy, K. L. Kappeler, D. J. Fox, and A. K. Dunn, "Intraoperative laser speckle contrast imaging for monitoring cerebral blood flow: results from a 10-patient pilot study," *Proceedings of SPIE, Photonic Therapeutics and Diagnostics VIII,* **8207**(82074L), pp. 1-12 (2012).

A. Roggan, M. Friebel, K. Dörschel, A. Hahn, and G. Müller, "Optical Properties of Circulating Human Blood in the Wavelength Range 400-2500 nm," *Journal of Biomedical Optics,* **4**(1), pp. 36-46 (1999).

Bernard Rosner, *Fundamentals of Biostatistics*, 6th ed. Belmont, CA: Thomson-Brooks/Cole, 2006.

P. Rousseau, G. Mahe, F. Haj-Yassin, S. Durand, A. Humeau, G. Leftheriotis, and P. Abraham, "Increasing the "region of interest" and "time of interest", both reduce the variability of blood flow measurements using laser speckle contrast imaging," *Microvascular Research,* **82**(1), pp. 88-91 (2011).

D. Rueckert, L. I. Sonoda, C. Hayes, D. L. Hill, M. O. Leach, and D. J. Hawkes, "Nonrigid registration using free-form deformations: application to breast MR images," *IEEE Transactions on Medical Imaging,* **18**(8), pp. 712-721 (1999).

Bahaa E. A. Saleh and Malvin Carl Teich, *Fundamentals of Photonics*, 2nd ed. Hoboken, N.J.: Wiley Interscience, 2007.

C. Schichor, W. Rachinger, D. Morhard, S. Zausinger, T. J. Heigl, M. Reiser, and J. C. Tonn, "Intraoperative computed tomography angiography with computed tomography perfusion imaging in vascular neurosurgery: feasibility of a new concept," *Journal of Neurosurgery,* **112**(4), pp. 722-728 (2010).

A. Serov, B. Steinacher, and T. Lasser, "Full-field laser Doppler perfusion imaging and monitoring with an intelligent CMOS camera," *Optics Express,* **13**(10), pp. 3681-3689 (2005).

I. Sigal, R. Gad, A. M. Caravaca-Aguirre, Y. Atchia, D. B. Conkey, R. Piestun, and O. Levi, "Laser speckle contrast imaging with extended depth of field for in-vivo tissue imaging," *Biomedical Optics Express,* **5**(1), pp. 123-135 (2013).

L. Song and D. S. Elson, "Effect of signal intensity and camera quantization on laser speckle contrast analysis," *Biomedical Optics Express,* **4**(1), pp. 89-104 (2013).

A. I. Srienc, Z. L. Kurth-Nelson, and E. A. Newman, "Imaging retinal blood flow with laser speckle flowmetry," *Frontiers in Neuroenergetics,* **2**(128), pp. 1-10 (2010).

R. M. Starke and A. S. Dumont, "Intraoperative imaging and assessment of cerebral blood flow in cerebrovascular surgery: hybrid operating rooms, intraoperative angiography and magnetic resonance imaging, Doppler ultrasound, cerebral blood flow probes, endoscopic assistance, indocyanine green videography, and laser speckle contrast imaging," *World Neurosurgery,* **82**(6), pp. e693-696 (2014).

A. J. Strong, E. L. Bezzina, P. J. B. Anderson, M. G. Boutelle, S. E. Hopwood, and A. K. Dunn, "Evaluation of laser speckle flowmetry for imaging cortical perfusion in experimental stroke studies: quantitation of perfusion and detection of peri-infarct depolarisations," *Journal of Cerebral Blood Flow & Metabolism,* **26**(5), pp. 645-653 (2005).

C. Studholme, D. L. G. Hill, and D. J. Hawkes, "An overlap invariant entropy measure of 3D medical image alignment," *Pattern Recognition,* **32**(1), pp. 71-86 (1999).

G. R. Sutherland, T. Kaibara, C. Wallace, B. Tomanek, and M. Richter, "Intraoperative assessment of aneurysm clipping using magnetic resonance angiography and diffusion-weighted imaging: technical case report," *Neurosurgery,* **50**(4), pp. 893-897; discussion 897-898 (2002).

C. Thome, P. Vajkoczy, P. Horn, C. Bauhuf, U. Hubner, and P. Schmiedek, "Continuous monitoring of regional cerebral blood flow during temporary arterial occlusion in aneurysm surgery," *Journal of Neurosurgery,* **95**(3), pp. 402-411 (2001).

W. J. Tom, A. Ponticorvo, and A. K. Dunn, "Efficient processing of laser speckle contrast images," *IEEE Transactions on Medical Imaging,* **27**(12), pp. 1728-1738 (2008).

M. Tomita, T. Osada, I. Schiszler, Y. Tomita, M. Unekawa, H. Toriumi, N. Tanahashi, and N. Suzuki, "Automated method for tracking vast numbers of FITC-labeled RBCs in microvessels of rat brain in vivo using a high-speed confocal microscope system," *Microcirculation,* **15**(2), pp. 163-174 (2008).

E. L. Towle, L. M. Richards, S. M. S. Kazmi, D. J. Fox, and A. K. Dunn, "Comparison of indocyanine green angiography and laser speckle contrast imaging for the assessment of vasculature perfusion," *Neurosurgery,* **71**(5), pp. 1023-1030; discussion 1030-1031 (2012).

Michael Unser. (1999) Splines: A Perfect Fit for Signal and Image Processing. *IEEE Signal Processing Magazine*, pp. 22-38.

M. Vannoni, M. Trivi, R. Arizaga, H. Rabal, and G. Molesini, "Dynamic speckle imaging with low-cost devices," *European Journal of Physics,* **29**(5), pp. 967-975 (2008).

T. W. Vitaz, M. Gaskill-Shipley, T. Tomsick, and J. M. Tew, Jr., "Utility, safety, and accuracy of intraoperative angiography in the surgical treatment of aneurysms and arteriovenous malformations," *American Journal of Neuroradiology,* **20**(8), pp. 1457-1461 (1999).

René von Fintel, "Comparison of the Most Common Digital Interface Technologies in Vision Technolog: Camera Link, USB3 Vision, GigE Vision, FireWire [White Paper]," Basler AG, http://www.baslerweb.com, 2013.

Z. Wang, S. Hughes, S. Dayasundara, and R. S. Menon, "Theoretical and experimental optimization of laser speckle contrast imaging for high specificity to brain microcirculation," *Journal of Cerebral Blood Flow & Metabolism,* **27**(2), pp. 258-269 (2007).

M. Wang, Y. Zeng, X. Liang, G. Feng, X. Lu, J. Chen, D. Han, and G. Yang, "In vivo label-free microangiography by laser speckle imaging with intensity fluctuation modulation," *Journal of Biomedical Optics,* **18**(12), pp. 126001 (2013).

J. E. Ward, D. P. Kelly, and J. T. Sheridan, "Three-dimensional speckle size in generalized optical systems with limiting apertures," *Journal of the Optical Society of America A,* **26**(8), pp. 1855-1864 (2009).

B. D. Watson, W. D. Dietrich, R. Busto, M. S. Wachtel, and M. D. Ginsberg, "Induction of reproducible brain infarction by photochemically initiated thrombosis," *Annals of Neurology,* **17**(5), pp. 497-504 (1985).

J. Woitzik, N. Hecht, A. Pinczolits, N. Sandow, S. Major, M. K. Winkler, S. Weber-Carstens, C. Dohmen, R. Graf, A. J. Strong, J. P. Dreier, and P. Vajkoczy, "Propagation of cortical spreading depolarization in the human cortex after malignant stroke," *Neurology,* **80**(12), pp. 1095-1102 (2013).

O. Yang and B. Choi, "Laser speckle imaging using a consumer-grade color camera," *Optics Letters,* **37**(19), pp. 3957-3959 (2012).

O. Yang, D. Cuccia, and B. Choi, "Real-time blood flow visualization using the graphics processing unit," *Journal of Biomedical Optics,* **16**(1), pp. 016009 (2011).

A. N. Yaroslavsky, P. C. Schulze, I. V. Yaroslavsky, R. Schober, F. Ulrich, and H. J. Schwarzmaier, "Optical properties of selected native and coagulated human brain tissues in vitro in the visible and near infrared spectral range," *Physics in Medicine and Biology,* **47**(12), pp. 2059-2073 (2002).

T. Yoshimura, "Statistical properties of dynamic speckles," *Journal of the Optical Society of America A,* **3**(7), pp. 1032-1054 (1986).

S. Yuan, A. Devor, D. A. Boas, and A. K. Dunn, "Determination of optimal exposure time for imaging of blood flow changes with laser speckle contrast imaging," *Applied Optics,* **44**(10), pp. 1823-1830 (2005).

P. Zakharov, F. Scheffold, and B. Weber, "Laser Speckle Analysis Synchronized with Cardiac Cycle," *Proceedings of SPIE, Novel Biophotonics Techniques and Applications III,* **9540**(954008), pp. 1-9 (2015).

S. Zhang and T. H. Murphy, "Imaging the impact of cortical microcirculation on synaptic structure and sensory-evoked hemodynamic responses in vivo," *PLoS Biology,* **5**(5), pp. e119 (2007).

J. Zhou, K. Ren, W. Dai, Y. Zhao, D. Ryan, and H. Wu, "Pumping-induced perturbation of flow in microfluidic channels and its implications for on-chip cell culture," *Lab on a Chip,* **11**(13), pp. 2288-2294 (2011).